Development and Application of a Numerical Simulation System to Evaluate the Impact of Anthropogenic Heat Fluxes on Urban Boundary Layer Climate

THÈSE N^{O} 4428 (2009)

PRÉSENTÉE LE 12 JUIN 2009
À LA FACULTÉ ENVIRONNEMENT NATUREL, ARCHITECTURAL ET CONSTRUIT
LABORATOIRE DE POLLUTION ATMOSPHÉRIQUE ET DU SOL
PROGRAMME DOCTORAL EN ENVIRONNEMENT

ÉCOLE POLYTECHNIQUE FÉDÉRALE DE LAUSANNE

POUR L'OBTENTION DU GRADE DE DOCTEUR ÈS SCIENCES

PAR

Andrea KRPO

acceptée sur proposition du jury:

Prof. A. Mermoud, président du jury
Dr A. Clappier, directeur de thèse
Dr A. Martilli, rapporteur
Prof. R. Perkins, rapporteur
Dr D. Robinson, rapporteur

ÉCOLE POLYTECHNIQUE
FÉDÉRALE DE LAUSANNE

Suisse
2009

to my parents

Every day I remind myself
that my inner and outer life
are based on the labors of other men,
living and dead,
and that I must exert myself
in order to give in the same measure
as I have received and am still receiving.

Albert Einstein

Abstract

Increasing economic development, and growing population, generated during the last decades a very important growth of cities. Urban regions include nowadays more than half of the global population and, by 2030, this proportion is forecasted to increase to three quarters. A consequent more and more extensive use of natural resources, together with increasing anthropogenic activities such as emissions from traffic and factories, or heating from air-conditioning facilities, modify local climate in many different ways, leading to a progressive degradation of life quality in urban areas.

Taking these facts into account, there is nowadays a real need for efficient urban planning guidelines and sustainability policies in order to improve life quality in urban areas. Different points should be considered including urban warming, air pollution, human health, economic, and cooling energy needs. The present work goes in this direction, aiming at developing a simulation system for the study of the complex interactions between buildings and the atmosphere.

The system of equations describing atmospheric flows is highly non linear and it is common to employ numerical techniques in order to solve them. Moreover, the representation of urban canopy climate, and related air pollution problems, requiree taking the interaction between urban scale (tens of kilometers), and mesoscale (hundreds of kilometers) processes into account.

At first, starting from previous studies, a mesoscale meteorological model has been developed as part of this work. Urban induced processes have been considered by implementing inside the model a detailed urban parameterization scheme developed in a previous work. The scheme is able to capture different urban processes, and reproduces the effects of cities in a more accurate way than traditional methods usually used in mesoscale models. However, the heat generated in buildings, and the way this heat is exchanged with the exterior, was not explicitly resolved. In particular, recent studies indicated that anthropogenic heat from air-conditioning facilities can play an important role and should be taken into account for more complete urban climate studies.

To this purpose, a Building Energy Model (BEM) has been developed, and coupled to the Urban Canopy Parameterisation (UCP). This building model takes into account the diffusion of heat through walls, roofs, and floors, the natural ventilation, the generation of heat from occupants and equipments, and the consumption of energy through air conditioning systems. Comparisons with other programs indicate that BEM is able to accurately simulate the basic heat transfer phenomena, and to reproduce the heat fluxes exchanged between buildings and the atmosphere.

In a second part of the work, the simulation system composed by the Mesoscale Model

(MM), UCP, and BEM is tested with respect to one, and two-dimensional configurations. In particular, the impact of BEM on the meteorological variables is analyzed, as well as the efficiency of different urban warming countermeasures, and cooling energy demands control strategies.

Two-dimensional results are then utilized as guidance for the application of MM-UCP-BEM over the realistic configuration including the city of Basel and the surrounding areas. At first, comparisons of urban and rural simulated temperatures with measures provided by the BUBBLE project (Basel Urban Boundary Layer Experiment), have shown that the model could reasonably well reproduce the variations in outdoor air temperature. In a second time, the simulations considered for the two-dimensional configuration are applied to the case of Basel. Numerical results confirm that anthropogenic fluxes from air-conditioning facilities can have a non negligent impact on the urban meteorology. Typically, they modify the outdoor temperature and increase the Urban Heat Island (UHI) phenomenon.

In the last part of the study, the applicability of the model in performing urban warming countermeasures, and cooling energy demands control strategies, is evaluated. In this purpose in mind, a sensitivity analysis is carried out indicating that appropriate physical properties of built materials, efficient air-conditioning systems, and the application of simple energy saving policies, can lead to very important cooling energy savings.

In general, the application of BEM inside the UCP allows computing the heat released into the atmosphere by air-conditioning facilities, as well as the corresponding feedbacks produced on the different meteorological variables. It also increases the capability of the urban parameterisation to provide more detailed studies of urban warming countermeasures, and cooling energy demands in real cities.

Keywords: *Mesoscale Model, Urban Canopy Parameterisation, Building Energy Model, Urban Heat Island, cooling energy needs, thermal modeling, air-conditioning fluxes, BUBBLE.*

Résumé

Durant ces dernières décennies le développement économique et l'augmentation de la population mondiale ont conduit à une forte croissance des villes. De nos jours, plus de la moitié des personnes vivent en milieu urbain, et d'ici 2030 il est prévu que trois quarts des habitants de la planète seront citadins. L'augmentation et la concentration des activités anthropogéniques induisent une modification du climat local urbain qui mène à une dégradation progressive de la qualité de vie de nos villes.

En partant de cette constatation, il est, de nos jours, important d'établir des outils d'aide à la décision efficaces afin de planifier durablement le développement des villes pour y préserver la qualité de vie. Le présent travail s'inscrit dans cette logique en ayant pour objectif le développement d'un système de simulation pour l'étude des interactions complexes entre les bâtiments et l'atmosphère.

Le système d'équations décrivant les flux atmosphériques est fortement non linéaire et il est commun d'appliquer des méthodes numériques pour le résoudre. De plus, la représentation de la canopée urbaine ainsi que de la qualité de l'air dans ces milieux font intéragir différentes échelles (urbaine (quelques kilomètres) et méso-échelle (une centaine de kilomètres)) que seuls les modèles numériques peuvent prendre en compte.

En se basant sur une étude précédente, un modèle météorologique méso-échelle a été développé dans la première partie de ce travail. Les effets induits par la présence d'une ville ont été pris en compte en implémentant une paramétrisation urbaine détaillée développée ultérieurement. Le schéma urbain reproduit un grand nombre des effets induits par les villes et il est ainsi mieux adapté que les méthodes généralement utilisées dans les modèles méso-échelles. Cependant, la chaleur générée par les bâtiments et les flux de chaleur entre les bâtiments et l'atmosphère urbaine n'étaient pas explicités. Alors que de récentes études ont montré que pour une représentation complète du climat urbain, il est important de prendre en compte les flux de chaleur anthropogénique comme par exemple ceux générés par les systèmes d'air conditionné.

Ainsi, un modèle d'énérgie des bâtiments (Building Energy Model, BEM) a été développé et couplé à une paramétrisation de la canopée urbaine (Urban Canopy Parameterisation, UCP). Ce modèle des bâtiments prend en compte la diffusion de chaleur au travers des murs, des toits et des étages, la ventilation naturelle, la production de chaleur des occupants et des équipements ainsi que la consommation d'énergie dans les systèmes d'air conditionné. La comparaison avec d'autres modèles de thermique des bâtiments à montré que BEM simule bien les phénomènes de transfert de chaleur et les échanges entre les bâtiments et l'atmosphère.

Dans une deuxième partie de ce travail, le système complet de simulation, composé du modèle a méso-échelle (MM), d'UCP et de BEM, est testé en une et deux dimensions. Les impacts de BEM sur les variables météorologiques sont plus particulièrement analysés, tel que l' efficacité de mesures d'abattement du réchauffement urbain ou des stratégies de contrôle de la demande en énergie.
Les résultats en 2 dimensions ont ensuite servi de guide dans l'application du système MM-UCP-BEM sur le cas réel de la Ville de Bâle et de sa région. Dans un premier temps, les résultats ont montré que le modèle reproduit raisonnablement l'évolution des temperatures extérieures qui ont été mesurées durant la campagne de mesure BUBBLE. Dans un deuxième temps, les résultats numériques confirment que les systèmes d'air conditionné, qui modifient la température extérieure et augmentent le phénomène d'ilôt de chaleur urbain (Urban Heat Island, UHI), ont un effet non négligeable.
Finalement, dans la dernière partie de ce travail, la capacité du modèle à être utilisé comme outil de planification énergétique est évaluée. L'étude de sensibilité aux différents paramètres montre qu'avec l'utilisation de matériaux adéquats, de systèmes d'air conditionné efficaces, ainsi qu'avec une politique simple d'utilisation rationnelle de l'énergie, des économies d'énergie importantes peuvent être faites.

L'application de BEM dans une UCP permet de modéliser l'énergie relâchée dans l'atmosphère par les systèmes d'air conditionné ainsi que son impact sur les différentes variables météorologiques. Elle permet également de mieux évaluer des stratégies de planification urbaines en matière de demande en énergie.

Mots Clés: *Modèle Mésoechelle, Paramétrisation urbaine, Canopée Urbaine, Modèle d'énergie du bâtiment, Ilôt de chaleur urbain, besoins énergetiques, flux d'air conditionné, BUBBLE.*

Acknowledgements

It is not possible to carry out a thesis alone, and here, I would like to thank all the people that with their encouragements, friendship, and love, made this work possible. I will mention only some, even if my thoughts go to all of them.

First, I would like to thank Prof. H. van den Bergh for giving me the opportunity to start this work at the Air and Soil Pollution Laboratory (LPAS) at EPFL. A very special thank goes to Alain Clappier, my thesis supervisor, for his essential scientific support, his friendship, and his constant encouragements during all these years. I would also like to thank all the members of the jury, Prof. A. Mermoud, Prof. R. Perkins, Dr. D. Robinson, for his help in the physics of buildings, and Dr. A. Martilli, for giving me the opportunity to work at the Centro de Investigationes Energéticas Medioambientales y Technológicas (CIEMAT) in Madrid, and for all the time he spent for me, putting his great experience in urban modeling at my disposal. Without his collaboration, this work would not have been possible. I am very grateful to all the people of CIEMAT for their hospitality and kindness. A very special thank goes to Francisco Salamanca, for his friendship, and the essential scientific collaboration for Chapters 3 and 4 of this thesis.
I would also like to thank all the group at the Centre d'Enseignement et de Recherche en Environnement Atmosphérique (CEREA) in Paris, and especially Hossein Malakooti, for his friedship, scientific collaboration, and for putting his experience with the MM5 mesoscale model at my disposal.

I am very grateful to all my colleagues and friends at the numerical group of LPAS with whom we formed a very knit and international team:
- Clive Muller and Erika Zarate for their very important help since my first day at the LPAS
- Oliver Fuhrer, for the important scientific support, his eternal good humor and dynamism without whom these years at the LPAS would not have been the same
- Luis Carlos Belalcazár Ceron (my ”parilladas” partner) for his enthusiasm, and his very important support during the last period of this work
- Ho Quoc Bang, Ho Minh Dung, and Sandra Angarita for their kindness and for giving me the opportunity to discover Vietnamese and Colombian culture
- Tristan Mariethoz, Anne Roches and Samuel Pantet, for the important collaboration in this work, their good humor and friendship.

I would also like to thank David Meylan for helping me in many informatic problems, Veronique Bauler, as well as Silvette Renfer from the Solar Energy and Building Physics

Laboratory (LESO) for their availability. I am grateful to all the members of the LESO, especially to Adil Rasheed who "accompanied" me in this project during all these years, and Jerome Kämpf for his very important help in the physics of buildings.

I would like to thank all my friends who supported me in many different ways during these years. A special thought goes to my "sport partner" Fabrizio Patuzzo for helping me with english corrections of the thesis, and Chantal Landry, my flatmate, with whom it has been a pleasure to share our PhD experience.

A very special thank goes to my parents for their love, and their priceless support during all my life. My final thoughs go to Maria. I would like to thank you for all your constant support, for giving me the privilege to share these important years with you, and making this period unforgettable.

The financial support for this study from the Swiss National Science Foundation under the auspices of National Research Program 54 ”Sustainable Development of the Built Environment” is gratefully acknowledged.

Contents

List of Figures

List of Tables

List of Symbols

ρ	air density $[\frac{Kg}{m^3}]$
ρ_0	air density at hydrostatic reference state $[\frac{Kg}{m^3}]$
ρ'	air density perturbation $[\frac{Kg}{m^3}]$
P	air pressure $[Pa]$
P_0	air pressure at hydrostatic reference state $[Pa]$
P'	air pressure perturbation $[Pa]$
$\mathbf{U}$	wind velocity $[\frac{m}{s}]$
g	gravity acceleration $[\frac{m}{s^2}]$
δ_{ij}	Kroenecker symbol
ε_{ijk}	Levi-Civita symbol
$\mathbf{\Omega}$	angular acceleration of the earth $[\frac{\text{rad}}{s}]$
$\mathbf{U}^G$	geostrophic wind $[\frac{m}{s}]$
θ	air potential temperature $[K]$
θ_0	air potential temperature at hydrostatic reference state $[K]$
θ'	air potential temperature perturbation $[K]$
θ	air potential temperature $[K]$
T	air temperature $[K]$
C_p	specific heat at constant pressure $[\frac{J}{Kg \cdot K}]$
g	gravity acceleration $[\frac{m}{s^2}]$
R	specific gas constant for dry air $[\frac{J}{Kg \cdot K}]$
R_{lw}	long wave radiation flux $[\frac{W}{m^2}]$
$\mathcal{H}$	absolute humidity $[\frac{g}{m^3}]$
c	speed of sound $[\frac{m}{s}]$
$\mathbf{K}$	eddy diffusivity $[\frac{m^2}{s}]$
E	turbulent kinetic energy $[\frac{m^2}{s^2}]$

l_ε	characteristic length scale [m]
l_k	characteristic length scale [m]
$\mid \Omega_{IJK} \mid$	volume of the domain IJK [m^3]
$\mathcal{S}_{IJK}$	surfaces of the domain IJK [m^2]
$\mathbf{xc}_{IJK}$	coordinate of the centers of the cell IJK [m]
$\mathbf{xn}_{IJK}$	coordinate of the nodes of the cell IJK [m]
λ	latitude [deg]
Φ	longitude [deg]
R_e	radius of the earth [m]
r	mixing ratio
Q_B	overall heat capacity [$\frac{J}{K}$]
V_B	total volume of the indoor air [m^3]
T_r	indoor air temperature [K]
T_a	outdoor air temperature [K]
l	latent heat of evaporation [$\frac{J}{Kg}$]
q_{V_r}	specific humidity of the indoor air [$\frac{Kg}{Kg}$]
q_{V_a}	specific humidity of the outdoor air [$\frac{Kg}{Kg}$]
A_j^{wall}	surface area of the wall j [m^2]
A_j^{wind}	surface area of the window in the wall j [m^2]
$h_{wall,j}$	convective heat transfer coefficient between the indoor air and the wall j [$\frac{W}{m^2 \cdot K}$]
$h_{wind,j}$	convective heat transfer coefficient between the indoor air and the window in the wall j [$\frac{W}{m^2 \cdot K}$]
A_f	floor area [m^2]
K_s	thermal diffusivity [$\frac{m^2}{s}$]
$T_{wall,j}$	indoor surface temperature of the wall j [K]
$T_{wind,j}$	temperature of the window in the wall j [K]
q_E	sensible heat gain from equipments per floor area [$\frac{W}{m^2}$]
q_{hl}	latent heat generation from occupants [$\frac{W}{\text{person}}$]
q_{hs}	sensible heat generation from occupants [$\frac{W}{\text{person}}$]
V_a	total ventilation rate [$\frac{m^3}{s}$]
β	control coefficient for ventilation rate $0 \leq \beta \leq 1$
φ_P	ratio of hourly occupants $0 \leq \varphi_P \leq 1$
σ	Stefan-Bolzmann constant [$\frac{W}{m^2 \cdot K^4}$]
Rs_{ext}	incoming external short wave radiation [$\frac{W}{m^2}$]

Rl_{ext}	incoming external long wave radiation $[\frac{W}{m^2}]$
α_{ext}	albedo of the external layer of the wall
ε_{ext}	emissivity of the external layer of the wall
C_s	specific heat of the layer of the wall $[\frac{J}{m^3 \cdot K}]$
η_{ext}	external transfer coefficient $[\frac{m}{s}]$
η_{int}	internal transfer coefficient $[\frac{m}{s}]$
p_{win}	window proportion $0 \leq p_{win} \leq 1$
α_{wal_j}	albedo of the indoor surface of the wall j
α_{win}	albedo of the window
$\varepsilon_{\text{wal}_j}$	emissivity of the indoor surface of the wall j
ε_{win}	emissivity of the window
α_{wal_j}	albedo of the indoor surface of the wall j
$\rho_{\text{wind,i}}$	density of the glass i $[\frac{Kg}{m^3}]$
α_{wal_j}	albedo of the indoor surface of the wall j
Rs^i_{int}	short wave radiation reaching the internal wall i $[\frac{W}{m^2}]$
Rl^i_{int}	long wave radiation reaching the internal wall i $[\frac{W}{m^2}]$
Rs_{tr}	short wave radiation transmitted through the window $[\frac{W}{m^2}]$
T_n	temperature of the most external layer of the material $[K]$
$\Delta_{\text{wind,i}}$	thickness of the window i $[m]$
δ	maximum power of cooling/heating $[\frac{°C}{s}]$
$\Gamma(z_{iu})$	probability to have a building of height z_{iu} or higher $0 \leq \Gamma(z_{iu}) \leq 1$
$\gamma(z_{iu})$	probability to have a building of height z_{iu} $0 \leq \gamma(z_{iu}) \leq 1$
ΔZ_{IU}	height of the urban level IU $[m]$
B_{WE}	building width in the west/east direction $[m]$
B_{SN}	building width in the south/north direction $[m]$
W_{WE}	street width in the west/east direction $[m]$
W_{SN}	street width in the south/north direction $[m]$
B_{WE}	building width in the west/east direction $[m]$
k	von Karmann constant
R_{i_B}	bulk Richardson number $[m]$
h_c	convective heat transfer coefficient $[\frac{W}{m^2 \cdot K}]$
T^{wal}_M	average temperature of the wall $[K]$
$T^{wal}_{i,IU}$	external surface wall temperature of the building type i at the level IU $[K]$

V_{tot_I}	total volume of the cell I (building+air) $[m^3]$
V_I^A	volume of air of the cell I $[m^3]$
λ_P^I	plane area density
$\psi_{[-]}$	view factor
Rs	short wave radiation $[\frac{W}{m^2}]$
Rl	long wave radiation $[\frac{W}{m^2}]$
$N_{\mathrm{city}}^{\mathrm{people}}$	total number of people in the city
ρ_P	average population density in the city $[\frac{\mathrm{inhab.}}{m^2}]$

List of Abbreviations

AC	**A**ir-**C**onditioning
BEM	**B**uilding **E**nergy **M**odel
BLAST	**B**uilding **L**oads **A**nalysis and **S**ystem **T**hermodynamics
BUBBLE	**B**asel **U**rban **B**oundary **L**ayer **E**xperiment
CDD	**C**ooling **D**egree-**D**ays
CIBSE	**C**hartered **I**nstitution of **B**uilding **S**ervices **E**ngineers
COP	**C**oefficient **O**f **P**erformance
CPU	**C**entral **P**rocessing **U**nit
DEM	**D**igital **E**levation **M**odel
HDD	**H**eating **D**egree-**D**ays
IDW	**I**nverse **D**istance **W**eighted
IOP	**I**ntensive **O**bservation **P**eriod
FVM	**F**inite **V**olume **M**odel
KABA	Climate Analysis of the Region of Basel
LM	**L**ocal **M**odel
LT	**L**ocal **T**ime
MM	**M**esoscale **M**odel
MOST	**M**onin **O**bukhov **S**imilarity **T**heory
NAC	**N**on **A**ir-**C**onditioning
NCAR	**N**ational **C**enter for **A**tmospheric **R**esearch
NCEP	**N**ational **C**enters for **E**nvironmental **P**redictions
PBL	**P**lanetary **B**oundary **L**ayer
PDE	**P**artial **D**ifferential **E**quation
RAMS	**R**egional **A**tmospheric **M**odeling **S**ystem
SBL	**S**urface **B**oundary **L**ayer

TARP	**T**hermal **A**nalysis **R**esearch **P**rogram
TKE	**T**urbulent **K**inetik **E**nergy
TVM	**T**hermal **V**orticity **M**odel
UCP	**U**rban **C**anopy **P**arameterization
UHI	**U**rban **H**eat **I**sland
UBL	**U**rban **B**oundary **L**ayer
UN	**U**nited **N**ations
WRF	**W**eather **R**esearch & **F**orecasting

Chapter 1

Introduction

Nowadays approximately half of the global population is urbanised and this proportion is expected to increase to three quarters during the next twenty-five years. According to the United Nations population projections (UN, 2006), by 2030 4.9 billion people, representing 60% of the World's population, are expected to live in cities. The welfare of the majority of the population is therefore linked to urban environment.

Geometrical and physical properties of urban regions, the topographical location, as well as anthropogenic activities in cities (traffic emissions, heating from air-conditioning facilities, etc.) can modify local climate in rather complex ways often causing the city to be an unhealthy ambient to live in. A significant example is represented by the Mexico City Metropolitan area (cf. Figure 1.1) with more than 19 million inhabitants, about 3.5 million motor vehicles (Molina et al., 2002), about 20 million liters of gasoline used every day (Bravo et al., 2002) and a topographical situation which does not allow an efficient ventilation of the basin (Roulet, 2004, Muller, 2007).

Figure 1.1: View of the Mexico City area.

Taking this into consideration, it is not surprising that the effects produced on local climate by the presence of cities have been extensively studied during the last decades and remain nowadays a very important issue for atmospheric scientists. In this context the aim of the present work is to develop a numerical simulation system which allows, on one hand, an efficient study of those impacts, and on the other hand, identifies possible long and short term strategies that could generate healthier and more comfortable cities.

1.1 Urban climate and the Planetary Boundary Layer (PBL)

In the vertical direction, the atmosphere can be divided into four distinct layers of different thickness, usually associated with a specific vertical temperature distribution (Jacobson, 1999): the troposphere, the stratosphere, the mesosphere and the thermosphere. In particular with a thickness of around $10km$ ($16km$ at the Equator and $7km$ at the Poles according to Seinfeld and Pandis, 1998), the troposphere represents the lowest portion of the Earth's atmosphere and contains almost 80% of the atmosphere mass and almost all the water vapor. In this layer one can furthermore distinguish two different parts (Oke, 1987): the Planetary Boundary Layer (PBL) from the ground to about $1km$ and the Free Atmosphere from $1km$ above the ground to the tropopause. As explained by Stull (1988), the PBL is 'that part of the atmosphere which is directly influenced by the presence of the earth's surface'. In particular physical and chemical processes in the PBL can be deeply modified by the presence of urban surfaces which in turn affect meteorological conditions, air quality and consequently human comfort.

As we can observe in Figure 1.2 there are *mechanical* and *thermal* factors with which urban regions can modify the local microclimate and the vertical structure of the atmosphere.

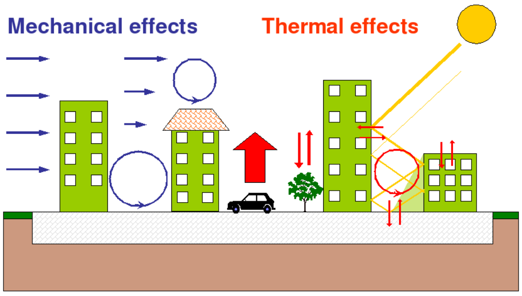

FIGURE 1.2: Mechanical and thermal effects produced by a city.

Mechanical effects are induced by the high roughness of the urban surfaces. Buildings produce, in fact, an intense drag as well as a shear layer at the top of the canopy where mean kinetic energy is transformed into turbulent kinetic energy. Cities also generate a turbulent wake diffusion and decrease wind speed (Roth, 2000).

Thermal effects are produced as geometrical and physical properties of urban areas generate a relatively dry environment and a differential heating/cooling compared to rural regions. Radiation trapping effects in street canyons and heat storage in buildings are observed and modify the radiative and energy budget often causing a city to be warmer than the surrounding areas. This is one of the most important phenomena generated by the presence of cities and is called the Urban Heat Island (UHI).

1.2 Causes and effects of the UHI

The UHI has been observed in numerous cities of different latitudes, sizes, densities, and remains nowadays one of the most studied phenomena by atmospheric scientists. According to Chow and Roth (2006), the UHI intensity can vary between 0 to $7°C$ depending on season, solar radiation and city characteristics. For example it has been observed (cf. Figure 1.3) that under clear skies and light winds, temperature in central London during the spring can reach a minimum of $11°C$, whereas in the suburbs it drops to $5°C$. The UHI can occur during the day or at night, but urban-rural temperature differences are often largest during calm, clear evenings (Oke, 1982, Arnfield, 2003). This is because rural areas cool off faster at night than cities, which retain large amounts of heat stored in roads, buildings and other infrastructures.

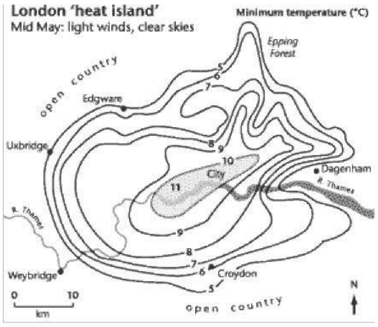

FIGURE 1.3: Nocturnal heat island over London (*www.london.gov.uk*).

Figure 1.3 indicates that when isotherms are plotted on the surface weather map, the pattern looks like the topographic contours of an island, whence the term "heat island" (Stull, (1988)). It should also be noted that for certain cities in arid regions, a negative UHI can instead be dominant (Grimmond, 2007).

The heat island forms as cities replace natural land cover with pavement, buildings, and other infrastructures. In particular, materials commonly used in urban areas such as asphalt, have different thermal properties (heat capacity, thermal conductivity) and surface radiative properties (albedo, emissivity) than the surrounding rural areas. Those materials change the energy balance inside cities, often causing it to reach higher temperatures than its surroundings. The energy balance is also affected by a reduction of trees and vegetation, which minimizes the natural cooling effects of shading and evapotranspiration.

As previously mentioned, the presence of tall buildings leads to a decrease in wind speed and can generate a heat storage as well as a radiation trapping effect in street canyons (canyon effect). All these geometric factors inhibit cooling inside urban areas and contribute to exacerbate the UHI. This phenomenon is also increased by human activities like heat from vehicles, factories, and air-conditioning facilities. According to the study of Kikegawa et al. (2003) over a central area of Tokyo (Japan), the cut-off of anthropogenic air-conditioning heat could produce a cooling energy saving up to 6% with an outdoor air-temperature decrease by more than $1°C$. Moreover as the daily maximum temperature increases by $1°C$, about $1.5GW$ of new cooling energy-demands are requested.

One of the most negative effects produced by the UHI lies in the intensification of the strength and the duration of excessively hot weather and high humidity periods (heat waves) which result in an increase in mortality rate due to overheating (Davies et al., 2008). On the other hand, it is important to observe that this general warming can also have positive effects. For example in the wintertime, some cities in the cold climates may benefit from the UHI. Warmer temperatures can reduce heating energy needs and may help melt ice and snow on roads. According to Davies et al. (2008), positive and negative factors should be taken into account for large-scale urban modification strategies.

Urban heat island produces effects on local meteorology, including the altering of local wind patterns. In particular the temperature increase in an urban area can lead to wind convergence formation above the city and to the generation of a higher wind speed opposed to the decrease generated by mechanical effects. Different studies indicate that this phenomenon can also lead to clouds and fog development, as well at to an increase in precipitation rates (Collier, 2006, Bornstain and Lin, 2000, Shi et al., 2008). An observed increase in smog production can also have further negative effects on air quality and health, especially in children and seniors (Rizwan et al., 2008).

Due to the important consequences generated by this urban areas warming up on human health, air pollution, local meteorology, economic and cooling-energy needs, there is nowadays an outgoing effort focused on identifying different UHI mitigation stategies. For instance in the work Smith et al. (2008), a large list of possible countermeasures is summarised:

- modify the thermo-physical properties of the urban surfaces (walls, roofs, streets) through urban greening or the use of high-reflective materials;

- increase openness in order to minimize the canyon effect and allow cooling winds;
- improve the buildings design in order to optimize the internal comfort (e.g. taking advantage of glazings and natural ventilation);
- minimize anthropogenic heat emissions by changing building occupants' behaviour.

According to Smith et al. (2008), nowadays a real need is left for complementary policy and urban planning commitments in order to be able to implement different countermeasures, especially in existing buildings and urban areas. The present work aims to give its contribution by developping a numerical simulation system capable of reproducing the physical processes generated by urban canopy climate. A particular interest will be given to UHI processes and the optimisation of buildings' energy demand. This kind of tool can become in the near future an important support for urban planners in evaluating the impact of different possible countermeasures.

1.3 Urban and mesoscale modelling

The system describing the UHI is highly non-linear and it is commun to use numerical models to handle this kind of problem. We also remark that a city is probably one of the most complex surfaces and that (due to the limited CPU power of computers and the lack of measured data), a complete representation of all buildings in a "real" urban area would be too complex and hardly realisable. Moreover one of the major complexities that numerical models representing urban canopy climate and air pollution problems have to handle lies in the diversity of spatio-temporal scales over which the different physical processes occur:

- an **urban** scale of few tens of kilometers (i.e. a normal city size) where large part of primary pollutants are emitted;
- a **meso** scale of few hundreds of kilometers where secondary pollutants are formed and dispersed.

According to Martilli (2001), these two scales are strictly linked and interactions between them must be taken into account. Mesoscale models cover a relatively large area with a horizontal extension of 100-200km. Thus, in order to keep the number of grid points reasonable with respect to CPU time cost, the horizontal grid resolution, generally, ranges between several hundreds of meters and few kilometers. This means that it is not possible to represent the city structure in detail (buildings or blocks) but the effects generated by urban areas have to be *parametrised*. In particular according to Masson (2006), different parameterisation techniques can be considered: *Empirical Models, adapted vegetation schemes, urban canopy parameterisations.*

Empirical Models are based on observations of the urban surface energy balance (Grimmond and Oke, 1999): the energetics generated by urban canopies is reproduced using statistical relations derived from observations. As explained by Muller (2007), these models use extremely simples schemes, but they need many measurement data and are limited to the range of those data conditions (city, meteorological conditions, land cover,$\cdots$).

The most common way to treat the interactions between the ground surface and the atmosphere in mesoscale models is based on the Monin Obukhov Similarity Theory (MOST) which assumes a *constant flux layer* in the lowest tens of meters of the atmosphere (the so-called Surface Boundary Layer (SBL)). The adapted vegetation schemes are based on MOST and the dynamical effects generated by the presence of buildings are generally reproduced by increasing the surface roughness (Grimmond et al., 1998) or by deriving the drag force from forest canopy models. In order to have a better representation of the physical properties of urban surfaces, surface albedo is generally decreased, ground is “dried”, soil heat capacity is modified and anthropogenic fluxes are taken into account by adding additional energy sources (Makar et al., 2006). However this approach is not able to represent the complex geometries and the radiative interactions between different buildings (e.g. radiation trapping). In addition, field measurements indicated that MOST is not able to reproduce urban canopy climate (Rotach, 1993).

Thanks to the increasing CPU power of computers, atmospheric scientists began in the $70's$ and $80's$ to introduce urban parameterisations in numerical mesoscale models. The aim was to study the impact of urban areas on the meteorological fields, as well as on the boundary layer structure. Nevertheless the physics of these first parameterisations was still to simplified, and it is only during the second part of the $90's$ and the beginning of the 21^{st} century that more realistic urban parameterisations appeared (Masson, 2000, Kusaka et al. 2001, Martilli et al. 2002). These models aim to solve the urban surface energy balance for a realistic $3D$ urban canopy by representing a city with a simplified geometry reasonably close to reality. The different surfaces composing urban areas are considered (street, roof, wall) taking into account the interactions between them, as well as the corresponding effects produced on the solar radiation.

Based on the above background, the aim of the present work is to develop a $3D$ mesoscale model coupled with an urban canopy parameterisation for urban canopy climate study. In this context a particular interest will be given to the identification of UHI control strategies and to air-conditioning cooling energy demands optimisation.

1.4 Structure of the thesis

Starting from the work of Clappier et al. (1996), a finite volumes non hydrostatic mesoscale model is developped as part of this thesis. The description and the numerical treatment of the basic equations is presented in *chapter 2*. Different numerical tests are also considered with the purpose to test and verify the model.

In order to enable the impact of urban surfaces to be taken into account, the urban canopy parameterisation, developped by Martilli et al. (2002), is coupled to the mesoscale model. This parameterisation accounts for the impact of the urban surfaces (roof, wall, street) on wind speed, temperature, turbulent kinetic energy, shadowing and radiation trapping induced by urban canyons. On the other hand anthropogenic heat sources are only partially taken into account by fixing the temperature inside buildings to a constant value. In this context, recent studies indicate that the heat released from air-contitioning facilities can have a non negligent impact on external air temperature and should be considered in a more complete UHI mitigation study, as well as for an evaluation of cooling energy demands (Kikegawa et al., 2003, 2006). In this purpose, a Building Energy Model (BEM) is developped as part of this work, and the complete description is presented in *chapter 3*. Sensitivity and validation tests are also considered in order to verify the model and evaluate the impact of different physical parameters.

In a second time the Building Energy Model has been coupled to the Urban Canopy Parameterisation (UCP) of Martilli et al. (2002) and introduced inside the Mesoscale Model (MM). The coupling procedure is detailed in *chapter 4* in which the whole simulation system (MM-UCP-BEM) is tested with respect to one and two-dimensional idealised cases. In particular the impact of BEM on the meteorological variables is analysed, as well as the efficiency of different UHI mitigation strategies on external temperature and cooling energy demands.

Finally, *chapter 5* focuses on a real case simulation where the whole model is applied to the city of Basel. Different numerical simulations are considered in order to verify the model, to study urban canopy climate, and to evaluate the impact of long/short term strategies for UHI mitigation and cooling energy savings.

Conclusions and perspectives are given in *chapter 6*.

Bibliography

[1] Arnfield, A.J.: 2003, 'Two decades of urban climate research: A review of turbulence, exchanges of energy and water, and the urban heat island', *Int. J. Climatol.*, **23**, 1-26.

[2] Bravo, H., Sosa, R., Sánchez, P., Bueno, E., González, L.: 2002, 'Concentrations of benzene and toluene in the atmosphere of the southwestern area at the Mexico City Metropolitan Zone', *Atmos. Environ.*, **36**, 3843-3849.

[3] Bornstain, R., Lin, Q.: 2000, 'Urban heat island and summertime convective thunderstorms in Atlanta: three cases studies', *Atmos. Environ.*, **34**, 507-516.

[4] Clappier, A., Perrochet, P., Martilli, A., Muller, F., Krueger, B.C.: 1996, 'A new non-hydrostatic mesoscale model using a CVFE (control volume finite element) Discretisation technique', in *Proceedings of EUROTRAC Symposium '96.*, Editors: P.M. Borrell et al., Computational Mechanics Publications, Southampton, 527-531, 1996.

[5] Chow, W.T.L., Roth, M.: 2006, 'Temporal dynamics of the urban heat island of singapore', *Int. J. Climatol.*, **26**, 2243-2260.

[6] Collier, C.G.: 2006, 'The impact of urban areas on weather', *Q.J.R. Meteorol. Soc.*, **132**, 1-25.

[7] Davies, M., Steadman, P., Oreszczyn, T.: 2008, 'Strategies for the modification of the urban climate and the consequent impact on building energy use', Energy Policy **36**, 4548-4551.

[8] Grimmond, C.S.B., Oke, T.R.: 1999, 'Heat storage in urban areas: local-scale observations and evaluation of a simple model', *J. Appl. Meteor.*, **38**, 922-940.

[9] Grimmond, C.S.B., King, T.S., Roth, M., Oke, T.R.: 1998, 'Aerodynamic roughness of urban areas derived from wind observations', *Bound.-Layer Meteor.*, **89**, 1-24.

[10] Grimmond, S.: 2007, 'Urbanization and global environmental change: local effects of urban warming', Geographical journal, **173**, 83-88.

[13] Jacobson, M.Z.: 1999, 'Fundamentals of atmospheric modeling', Cambridge University Press, Cambridge, UK.

[12] Kikegawa, Y., Genchi, Y., Yoshikado, H., Kondo, H.: 2003, 'Development of a numerical simulation system toward comprehensive assessments of urban warming countermeasures including their impact upon the urban buildings energy-demands', *Applied Energy*, **76**, 449-466.

[13] Kikegawa, Y., Genchi, Y., Kondo, H., Hanaki, H.: 2006, 'Impacts of city-block-scale countermeasures against urban heat island phenomena upon a building's energy-consumption for air conditioning', *Applied Energy*, **83**, 649-668.

[14] Kusaka, H., Kondo, H., Kikegawa, Y., Kimura, F.: 2001, 'A simple single-layer urban canopy model for atmospheric models: Comparison with multi layer and slab models', *Boundary-Layer Meteorology*, **101**, 329-358.

[15] Makar, P.A., Gravel, S., Chirkhov, V., Strawbridge, K.B., Froude, F., Arnold, J., Brook, J.: 2006, 'Heat flux, urban properties, and regional weather', *Atmos. Environ.*, **40**, 2750-2766.

[10] Martilli, A.; 2001, 'Development of an urban turbulence parameterisation for mesoscale atmospheric models', Phd Thesis $N°$, **2445**, Swiss Federal Institute of Technology, Lausanne.

[20] Martilli, A., Clappier, A., Rotach, MW.: 2002, 'An urban surface exchange parameterization for mesoscale models', *Boundary-Layer Meteorology*, **104**, 261-304.

[18] Masson, V.: 2000, 'A physically-based scheme for the urban energy budget in atmospheric models', *Boundary-Layer Meteorology*, **94**, 357-397.

[19] Masson, V.: 2006, 'Urbansurface modeling and the meso-scale impact of cities', *Theor. Appl. Climatol.*, **84**, 35-45.

[20] Molina, L.T., Molina, M.J.: 2002, 'Air Quality in the Mexico Megacity: an Intergraduated Assessment ', (Eds.) Kluwer Acad., Norwell. Mass., 384 pp.

[12] Muller, C.: 2007, 'Improvement of an urban turbulence parameterization for meteorological operational forecast and air quality modeling', Phd Thesis $N°$, **3766**, Swiss Federal Institute of Technology, Lausanne.

[22] Oke, T.R.: 1987, 'Boundary Layer Climates', 2nd edn. London: Methuen, 384 pp.

[23] Oke, T.R.: 1982, 'The energetic basis of the urban heat island', *Q.J.R. Meteorol. Soc.*, **108**, 1-24.

[24] Rizwan, A.M., Leung, D.Y.C., Chunho, L.: 2008, 'A rewiev on the generation, determination and mitigation of Urban Heat Island', *Journal of Environmental Sciences* **20**, 120-128.

[15] Rotach, M.W.: 1993, 'Turbulence close to a rough urban surface Part II: variances and gradients', *Bound.-Layer Meteor.*, **66**, 75-92.

[26] Roth, M.: 2000, 'Review of atmospheric turbulence over cities', Q.J.R. *Meteorol. Soc.*, **126**, 941-990.

[26] Roulet, Y.-A.: 2004, 'Validation and application of an urban turbulence parameterisation for mesoscale atmospheric models', Phd Thesis $N°$, **3032**, Swiss Federal Institute of Technology, Lausanne.

[28] Seinfeld, J.H. and Pandis, S.N.: 1998, 'Atmospheric chemistry and physics from air pollution to climate change', John Wiley and Sons, 1326 pp.

[29] Shi, C., Roth, M., Zhang, H., Li, Z.: 2008, 'Impacts on urbanization on long-term fog variation in Anhoi Province, China', *Atmos. Environ.* **42**, 8484-8492.

[30] Smith, C., Levermore, G.: 2008, 'Designing urban spaces and buildings to improve sustainability and quality of life in a warmer world', Energy Policy, **36**, 4558-4562.

[33] Stull, R.B.: 1988, 'An Introduction to Boundary Layer Meteorology', *Kluwer Academic Publisher*, Dordrecht, 670 pp.

[32] United Nations: 2006, 'World Urbanization Prospects. The 2005 Revision', *Departement of Economic and Social Affairs*, *Population Division*, New York.

Chapter 2

Development of a Finite Volume non-hydrostatic Mesoscale model (FVM)

Abstract

The governing equations of atmospheric flows are highly non linear and it is commun to use numerical techniques in order to solve them. In this context, a non hydrostatic numerical mesoscale atmospheric model has been developped in the following study. It is based on a finite volume method and considers a cartesian structured and deformable mesh.
With a horizontal extension ranging between few kilometers and hundreds of kilometers, mesoscale models can for example simulate local winds (land and see breeze) and mountain waves. These models play also an essential part in the study of urban climate and air pollution as the feedbacks that the corresponding atmospheric processes generate over cities cannot be neglegted.

In this study we present the basic equations handled by the model and the corresponding finite volume resolution techniques. Benchmark tests are also performed showing some characteristics of the numerical schemes, and the effectiveness of the model to simulate different physical processes.

2.1 Introduction

The governing equations of atmospheric flows are highly non linear, and therefore, the dawn of computer machines represented a great opportunity for the development of numerical techniques focused on their resolution. In this context, the first mesoscale models started to be developped in the 1970s (Pielke, 1974), but the lack of CPU power limited the possible applications and forced to treat the equations in simplified forms (e.g. hydrostaticity, incompressibility). In recent decades, the exponential growth of computer power allowed a rapid development of the complexity and of the applicability of mesoscale models which are nowadays currently used for weather forecasting. With a horizontal extension of few hundreds of kilometers and a horizontal resolution ranging between hundreds of meters and few kilometers, they can for example simulate gravity waves and local winds like land/see breezes, slope winds and mountain-valley flows (Jacobson, 1999). In the vertical direction, the computational domain is typically stretched up to the troposphere with a more refined resolution near the ground surface.
Nowadays different types of mesoscale models exist, and more and more detailed and complex physical processes are taken into account (cloud formation, surface energy exchanges). Among them, RAMS (Pielke et al., 1992), TVM (Thunis, 1995), $MM5$ (Grell et al., 1994), LM and WRF[1]should be mentioned.

Following the work of Clappier et al. (1996) a three-dimensional non-hydrostatic mesoscale model has been developped as part of this thesis. The basic *mass*, *momentum*, *humidity*, *energy*, and *turbulent kinetic energy* conservation equations are solved considering a finite volumes approach (Leveque, 2004), with a cartesian structured and deformable mesh.
The system of equations treated by the mesoscale model is first presented in section 2.2. The characteristics of the numerical grid are discussed in paragraph 2.3. The finite volumes techniques adopted for the resolution of the mesoscale system are detailed in section 2.4, and the general algorithm is described in paragraph 2.5. Numerical benchmark tests are considered in section 2.6 in order to evaluate the capability of the model to simulate some physical processes (e.g. mountain waves). Conclusions are finally given in section 2.7.

---

[1] A detailed description of LM and WRF can be found respectively on the COSMO and the WRF model website.

2.2 The mesoscale model equations

One of the major difficulties in the treatment of atmospheric flows lies in the number of different physical processes having to be taken into account. These phenomena are strictly linked one to another and occur over different spatio-temporal scales (cf. Table 2.1).

Scale Name	**Scale Dimension**	**Examples**
Molecular scale	<< 2mm	Molecular diffusion, molecular viscosity
Microscale	2mm-2km	Eddies, small plumes, car exhaust, cumulus clouds
Mesoscale	2-2’000km	Gravity waves, thunderstorms, tornados, cloud clusters, local winds, urban air pollution
Synoptic scale	500-10’000km	High- and low- pressure systems, weather fronts, tropical storms, hurricanes, Antartic ozone hole
Planetary scale	>10’000km	Global winds systems, Rosbby (planetary) waves, stratospheric ozone reduction, global warming

Table 2.1: Scales of atmospheric motion (Jacobson, 1999)

Typically, microscale processes can last few seconds while synoptic and planetary scale phenomena last even several month (Stull, 1988). Atmospheric models, thus, have to simulate many physical processes by taking the corresponding feedbacks among them into account.

In the present work we are mainly interested in studing physical processes and interactions between earth surface and the atmosphere (e.g. urban heat island in urban areas). In this contribution, starting from the work of Clappier et al. (1996), a mesoscale model has been worked up. For real case simulations, the feedbacks produced by higher scale phenomena are taken into account by forcing the boundaries of the mesoscale domain with the results of global models (Roulet, 2004).
The primary meteorological variables considered in the mesoscale model are wind speed and direction, air temperature, density, pressure, and water content (humidity). These quantities are strictly linked and a system of partial differential equations is considered in order to simulate them. It includes the **mass**, **momentum**, **energy**, **humidity** conservation equations, as well as the equation of **state**.

One of the most important physical processes taking place while treating the interactions between earth surface and the atmosphere concerns the formation of turbulence. As explained by Jacobson (1999), this can be linked to mechanical (wind blowing over objects like trees, buildings), and thermal effects (temperature gradient produced by solar heating of the ground). Considering the purposes of this study, the present mesoscale model has to take these kind of processes into account. In particular, turbulence is considered with a Reynolds Averaging approach (Stull, 1988) in which the different meteorological variables are divided into a mean and turbulent contribution. In the following, capital letters will refer to mean quantities while small letters refer to the corresponding turbulent perturbations. The different conservation equations treated by the mesoscale model, as well as the approximation used, are presented in detail in the following part of the section.

2.2.1 Conservation of mass

The mass conservation equation states that when air circulates in an enclosed volume, without any external process (physical or chemical) affecting it, the total mass of air in the volume remains constant. In differential form this can be written as (Jacobson, 1999):

$$\underbrace{\frac{\partial \rho}{\partial t}}_{\mathbf{A}} + \underbrace{\frac{\partial \rho U_i}{\partial x_i}}_{\mathbf{B}} = 0 \tag{2.1}$$

where ρ is the air density and U_i the wind velocity components in the three space directions ($i = 1 \cdots, 3$). Term A describes the storage of mass, while term B the mean transport.

2.2.2 Conservation of momentum

The momentum conservation equation is derived from Newton's second law of motion stating that the acceleration of a body due to a force is proportional to the force, inversely proportional to the mass of the body, and in the direction of the force. In differential form, the momentum equation can be written as:

$$\underbrace{\frac{\partial \rho U_i}{\partial t}}_{\mathbf{A}} = -\underbrace{\frac{\partial \rho U_i U_j}{\partial x_i}}_{\mathbf{B}} - \underbrace{\frac{\partial \rho \overline{u_i u_j}}{\partial x_j}}_{\mathbf{C}} - \underbrace{\frac{\partial P}{\partial x_i}}_{\mathbf{I}} - \underbrace{\rho g \delta_{i3}}_{\mathbf{II}} - \underbrace{2\varepsilon_{ijk}\varOmega_j U_k}_{\mathbf{III}} + \underbrace{\mathcal{D}_{ui}}_{\mathbf{D}} \tag{2.2}$$

where P is the air pressure, g the gravity acceleration, and $\varOmega_j$ the rotation angular velocity of the earth. Term A describes the storage of momentum, term B the mean, and term C the turbulent transport. Source term D indicates the forces induced by the interactions between the earth surface (rural or urban) and airflow, term I the pressure-gradient force, term II the impact of the vertical action of gravity. Finally, term III corresponds to the Coriolis force describing the influence of the Earth's rotation.

The present mesoscale model is *non-hydrostatic* and assumes that the air pressure (P) and density (ρ) can be decomposed as:

$$\begin{aligned} P &= P_0 + P';\; P' << P_0 \\ \rho &= \rho_0 + \rho';\; \rho' << \rho_0 \end{aligned} \tag{2.3}$$

where P_0 and ρ_0 are the air pressure and density in the hydrostatic equilibrium, and P', ρ' the corresponding perturbations.

Concerning the reference hydrostatic state, the following hydrostatic balance equations can be considered (Jacobson, 1999):

$$\frac{\partial P_0}{\partial x_3} = -\rho_0 g \tag{2.4}$$

$$\frac{\partial P_0}{\partial x_i} = -2\Omega_{ijk} U_k^G \; i = 1,2 \tag{2.5}$$

where U_k^G represents the geostrophic wind.

Taking (2.4) and (2.5) into account, the pressure-gradient term (I) in the equation (2.2) can be written as:

$$\begin{aligned} -\frac{\partial P}{\partial x_3} &= -\frac{\partial P_0}{\partial x_3} - \frac{\partial P'}{\partial x_3} = \rho_0 g - \frac{\partial P'}{\partial x_3} \\ -\frac{\partial P}{\partial x_i} &= -\frac{\partial P_0}{\partial x_i} - \frac{\partial P'}{\partial x_i} = 2\Omega_{ijk} U_k^G - \frac{\partial P'}{\partial x_i} \; i = 1,2 \end{aligned} \tag{2.6}$$

Substituting (2.6) into (2.2) leads to the following momentum conservation equation:

$$\underbrace{\frac{\partial \rho U_i}{\partial t}}_{\textbf{A}} = -\underbrace{\frac{\partial \rho U_i U_j}{\partial x_j}}_{\textbf{B}} - \underbrace{\frac{\partial \rho \overline{u_i u_j}}{\partial x_j}}_{\textbf{C}} - \underbrace{\frac{\partial P'}{\partial x_i}}_{\textbf{I}} - \underbrace{\rho' g \delta_{i3}}_{\textbf{II}} - \underbrace{2\varepsilon_{ijk}\Omega_j \left(U_k - U_k^G\right)}_{\textbf{III}} + \underbrace{\mathcal{D}_{ui}}_{\textbf{D}} \tag{2.7}$$

In the following, the pressure-gradient force will always be referred to the spatial variation of the pressure perturbation. The term $\rho' g$ corresponds to the **buoyancy** contribution. In particular considering the equation of state and the definition of potential temperature ($\theta := T \left(\frac{P_{z=0}}{P}\right)^{\frac{R}{C_P}}$), one can derive that this term can be written in the following form (Marardel, 2005):

$$\rho' g = -\rho_0 \frac{\theta'}{\theta_0} g \tag{2.8}$$

where θ_0 is the potential temperature of the reference hydrostatic state, and $\theta' = \theta - \theta_0$ the corresponding fluctuation.

Taking (2.8) into account, the momentum conservation law (2.7) is finally written as:

$$\underbrace{\frac{\partial \rho U_i}{\partial t}}_{\textbf{A}} = -\underbrace{\frac{\partial P'}{\partial x_i}}_{\textbf{I}} + F_i \tag{2.9}$$

where:

$$F_i = -\underbrace{\frac{\partial \rho U_i U_j}{\partial x_i}}_{\textbf{B}} - \underbrace{\frac{\partial \rho \overline{u_i u_j}}{\partial x_j}}_{\textbf{C}} - \underbrace{\rho \frac{\theta'}{\theta_0} g \delta_{i3}}_{\textbf{II}} - \underbrace{2\varepsilon_{ijk}\Omega_j \left(U_k - U_k^G\right)}_{\textbf{III}} + \underbrace{\mathcal{D}_{ui}}_{\textbf{D}} \tag{2.10}$$

2.2.3 Conservation of energy

The energy conservation equation is derived from the first law of thermodynamic which states that the energy par unit of mass $[\frac{J}{kg}]$ transferred between an air parcel and its environment (dQ) is equal to the change in internal energy of the parcel (dI) and the work done by or on the parcel (dW):

$$dQ = dI + dW. \tag{2.11}$$

Using the definition of entropy (dS), we have that:

$$\begin{aligned} dS &= \frac{dQ}{T} \\ \Rightarrow dS &= \frac{1}{T}(dI + dW) \end{aligned} \tag{2.12}$$

where $T\,[K]$ is the air temperature.

Furthermore, starting from the definition of potential temperature (θ), one can derive that the entropy function can be written as (Bougeault, 2001, Pielke, 2002):

$$dS = C_p \frac{d\theta}{\theta} \tag{2.13}$$

where C_p is the specific heat at constant pressure of the air.
Considering (2.12) and (2.13) it is possible to transform the energy conservation law in

an equation which directly describes the temporal evolution of potential temperature. In the present mesoscale model, the following conservation equation is considered:

$$\underbrace{\frac{\partial\rho\theta}{\partial t}}_{\mathbf{A}} = -\underbrace{\frac{\partial\rho\theta U_i}{\partial x_i}}_{\mathbf{B}} - \underbrace{\frac{\partial\rho\overline{u_j\theta}}{\partial x_j}}_{\mathbf{C}} - \underbrace{\frac{1}{C_p}\left(\frac{P_{z=0}}{P}\right)^{\frac{R}{C_P}}\frac{\partial R_{lw}}{\partial z}}_{\mathbf{I}} + \underbrace{\mathcal{D}_\theta}_{\mathbf{D}} \tag{2.14}$$

where R is the gas constant, R_{lw} the long wave radiation flux, and $P_{z=0}$ the reference pressure at 1000 $[mbar]$. Similarly to the momentum equation, term A indicates the storage of heat (potential temperature), term B the mean transport, term C the turbulent transport, and term D the impact of sensible heat fluxes from solid surfaces. Finally, the source term I describes the loss through long wave emissions.

Remark that changes in temperature affect atmospheric stability, pressure, density, turbulence, and other parameters. Furthermore, the study of the evolution of air temperature will play a central part in the present work as it is directly linked to the urban heat island formation, and more in general to human comfort in urban areas.

2.2.4 Conservation of humidity

The humidity conservation law describes how the air moisture varies with time. In particular, as one can see in the equation (2.15), the humidity stored by an air parcel in given period of time (term A), is equal to the mean (term B) and turbulent (term C) transport of moisture, and to the impact of latent heat fluxes from solid surfaces (term D).

$$\underbrace{\frac{\partial\rho\mathcal{H}}{\partial t}}_{\mathbf{A}} = -\underbrace{\frac{\partial\rho\mathcal{H}U_i}{\partial x_i}}_{\mathbf{B}} - \underbrace{\frac{\partial\rho\overline{u_j h}}{\partial x_j}}_{\mathbf{C}} + \underbrace{\mathcal{D}_h}_{\mathbf{D}} \tag{2.15}$$

where $\mathcal{H}$ is the absolute humidity of the air.

Remark that in the present mesoscale model condensation and cloud formation are not taken into account.

2.2.5 The equation of state

It is important to remark now that the system describing the mass (2.1), momentum (2.9), energy (2.14) and humidity (2.15) conservation is not closed as we have 6 partial differential equations for 7 meteorological variables (ρ, U_1, U_2, U_3, P', θ, $\mathcal{H}$), and 3 turbulent fluxes (terms C in (2.9), (2.14), (2.15)). Thus, in order to close the system, a further relation is first needed linking the air pressure with the other meteorological quantities. In this context, the equation of state is considered:

$$P = \rho R T \tag{2.16}$$

where T is the air temperature.

Setting $c = \sqrt{RT}$ as the speed of sound in the air, the equation of state is finally written as:

$$P = \rho c^2 \tag{2.17}$$

2.2.6 Computation of turbulent transport

The computation of turbulent transport is a complex problem known in the literature as **closure problem** (Stull, 1988). It comes from the fact that the number of unknowns in the set of equations for turbulent flow is larger than the number of equations. When equations are included for these unknowns (changing them to known variables), one discovers even more unknowns. Thus, for any finite set of those equations the description of turbulence is not closed. In order to overcome this kind of problem, the vertical turbulent transport cannot be directly computed, but has to be parametrised. In other words, we have to replace the true equation describing a value with some artificially constructed approximation. In the present mesoscale model the vertical turbulent transport has been parametrised using the closure approximation called K-theory or gradient-transport theory. This closure varies with respect to diffusion coefficients K_j (eddy diffusivity), and for a given variable $\mathit{\Gamma}$ (wind temperature, humidity) we have:

$$\overline{u_j \gamma} = -K_j \frac{\partial \Gamma}{\partial x_j} \; ; j = 1, \cdots, 3 \tag{2.18}$$

In order to compute the diffusion coefficients K_j, a prognostic equation for turbulent kinetic energy (E in the following equation) is first considered:

$$\begin{aligned}\underbrace{\frac{\partial \rho E}{\partial t}}_{\mathbf{A}} = -\underbrace{\frac{\partial \rho E U_i}{\partial x_i}}_{\mathbf{B}} - \underbrace{\frac{\partial \rho \overline{u_j e}}{\partial x_j}}_{\mathbf{C}} + \underbrace{\rho K_z \left[\left(\frac{\partial U_1}{\partial x_3} \right)^2 + \left(\frac{\partial U_2}{\partial x_3} \right)^2 \right]}_{\mathbf{I}} - \underbrace{\frac{g}{\theta_0} \rho K_z \frac{\partial \theta}{\partial x_3}}_{\mathbf{II}} \\ - \underbrace{\rho C_\varepsilon \frac{E^{\frac{3}{2}}}{l_\varepsilon}}_{\mathbf{III}} + \underbrace{\mathcal{D}_E}_{\mathbf{D}}\end{aligned} \tag{2.19}$$

Similarly to the previous equations, term A represents the storage of turbulent kinetic energy (*TKE*), terms B and C represent the mean and turbulent transport of *TKE*, while the term D represents the impact of solid surfaces on the *TKE* budget. Furthermore, sources terms I and II represent the buoyant and shear production of *TKE*, while source term III describes the *TKE* dissipation term. Note that expressions for the source terms I and II are derived from the K-theory approach given by (2.18).
The value of *TKE* is then used to compute the diffusion coefficients K_j thanks to the following expression:

$$K_j = C_j l_j \sqrt{E} \; ; j = 1, \cdots, 3 \tag{2.20}$$

where C_j and C_ε in (2.19) are numerical constanst, while l_j and l_ε in (2.19) are characteristic length scales. Finally, E refers to the turbulent kinetic energy.

In the vertical direction (k), the parameters C_k and l_k are computed following the k-l closure technique of Bougeault and Lacarre (1989). In this case, the characteristic length l_k refers to the vertical distance that an air parcel can travel before being stopped by the buoyancy effect. The computation of l_k, l_ε with the corresponding model parameters C_k and C_ε is described in detail in Martilli et al. (2002).
Generally, in mesoscale models the horizontal resolution is very low compared to the vertical. Thus, vertical turbulence dominates the horizontal fluxes and represents the most important term in (2.18). In that case, horizontal turbulence can be neglected (Masson et al., 2002). However, when higher horizontal resolutions are considered (this is important in order to have a more detailed representation of the city), horizontal diffusion should also be considered. In that particular case the magnitude of characteristic length scales is in the order of the horizontal resolution of the mesoscale grid.

2.2.7 Equation for the pressure

In the present mesoscale model the pressure perturbation is solved with an implicit method. In particular, a partial differential equation is built up by combining the mass, momentum, and the equation of state.

Deriving in space the momentum equation (2.9) and assuming that the spatial and temporal derivatives commute, we have that:

$$\frac{\partial}{\partial t}\left(\frac{\partial \rho U_i}{\partial x_i}\right) = -\frac{\partial^2 P'}{\partial x_i^2} + \frac{\partial F_i}{\partial x_i} \tag{2.21}$$

where F_i is given by (2.10).

Combining (2.21) with the mass conservation equation (2.1) we derive that:

$$-\frac{\partial^2 \rho}{\partial t^2} = -\frac{\partial^2 P'}{\partial x_i^2} + \frac{\partial F_i}{\partial x_i} \tag{2.22}$$

Finally, with the equation of state (2.17), we can obtain the following **acoustic equation**:

$$-\frac{\partial^2}{\partial t^2}\left(\frac{P}{c^2}\right) + \frac{\partial^2 P'}{\partial x_i^2} = \frac{\partial F_i}{\partial x_i} \tag{2.23}$$

Remark 1 (Barotropic assumption)

One possible simplification of (2.23) can be obtained by assuming barotropic atmospheric conditions. In that case the pressure is assumed to be only density dependent and the speed of sound c in (2.17) is set to a constant value. Thus, equation (2.23) is written as:

$$\frac{1}{c^2}\frac{\partial^2 P}{\partial t^2} + \frac{\partial^2 P'}{\partial x_i^2} = \frac{\partial F_i}{\partial x_i} \tag{2.24}$$

Remark 2 (Anelastic approximation)

Acoustic (or sound) waves are a solution of (2.23) but, sometimes, these processes are not taken into account in meteorological applications (Marardel, 2005, Pielke, 2002). In particular, an anelastic condition is assumed by setting $c^2 >> P$ and therefore neglegting the first term in (2.23). Taking this into account, the following *Poisson equation* is considered for pressure perturbation:

$$\frac{\partial^2 P'}{\partial x_i^2} = \frac{\partial F_i}{\partial x_i} \tag{2.25}$$

2.2.8 The system of partial differential equations (PDE)

Taking the previous discussion into account, one can observe that the present mesoscale model aims to compute the following meteorological variables: air density (ρ), wind speed (U_1, U_2, U_3), air pressure perturbation (P'), potential temperature (θ), *TKE* (E), and absolute humidity ($\mathcal{H}$). In order to resolve these different quantities the following system of eight *PDE* has been obtained:

$$\begin{cases} \textit{acoustic equation for } P' \text{ (2.23);} \\ \textit{momentum conservation for } U_i \ i = 1, \cdots, 3 \text{ (2.9);} \\ \textit{energy conservation} \text{ (2.14);} \\ \textit{humidity conservation} \text{ (2.15);} \\ \textit{TKE conservation} \text{ (2.19)} \\ \textit{equation of state} \text{ (2.17).} \end{cases} \tag{2.26}$$

Turbulent transport of the different quantities (terms C in the system (2.26)) is parametrised by a diffusion process (cf. (2.18)), with the corresponding diffusion coefficient computed as in (2.20). The calculation of the source terms produced by the impact of earth's surface (terms D in the system (2.26)) is computed following the work of Martilli et al. (2002) and will be discussed more in detail in chapter 4. A more complete description of the algorithm used to solve the system (2.26) is presented in section 2.5.

In conclusion, one can observe that the mesoscale model system (2.26) is closed as for a set of 8 meteorological unknowns, a corresponding number of PDE is considered. A numerical method is adopted in order to solve the present problem, with the spatial discretisation technique following the finite volumes approach (Leveque, 2002). In particular, the corresponding Finite Volume based Mesoscale model (FVM) estimates the pressure gradient and the velocity fluxes at the faces of the cells, while the velocity components, the potential temperature, air humidity, turbulent kinetic energy and pressure, are computed at the center.

In the following part of the chapter, we will focus on describing the properties of the numerical mesh (section 2.3), the resolution of the different terms composing the FVM system (section 2.4), and on the presentation of the general algorithm adopted for the resolution of the whole model (section 2.5). Finally, a serie of numerical benchmark tests will be discussed in section 2.6.

2.3 The numerical grid

Mesoscale models are applied to relatively large areas with an extension of $100km$-$200km$ in the horizontal, and up to $10km$ above the earth's surface in the vertical direction (the entire troposphere is coverred). In the present finite volume model (FVM) the whole domain is discretised into $\mathcal{N}$ different cells (finite volumes) characterised by a horizontal resolution of $1km$ to $10km$, and a vertical one ranging between tens of meters near the ground and $1km$ at the upper levels. The mesh is structured meaning that every finite volume is composed by six faces and is connected with six neighbours. Furthermore, the grid can be deformed by modifying the position of the cell corners (deformable mesh). Note that this is an essential point as terrain-influenced processes generated by topography have to be considered for mesoscale applications (cf. Figure 2.1).

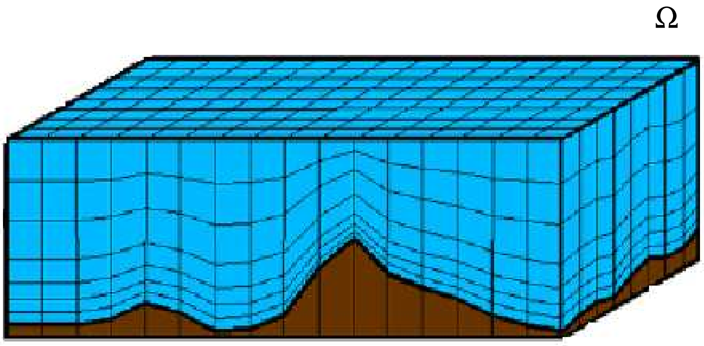

FIGURE 2.1: Genaral view of a typical domain (Ω) treated by the FVM mesoscale model (Roulet, 2004).

The domain Ω is divided into $\mathcal{N}$ finite volumes Ω_{IJK}, where (I, J, K) defines the location of the corresponding centers in the cartesian reference frame (cf. Figure 2.2).

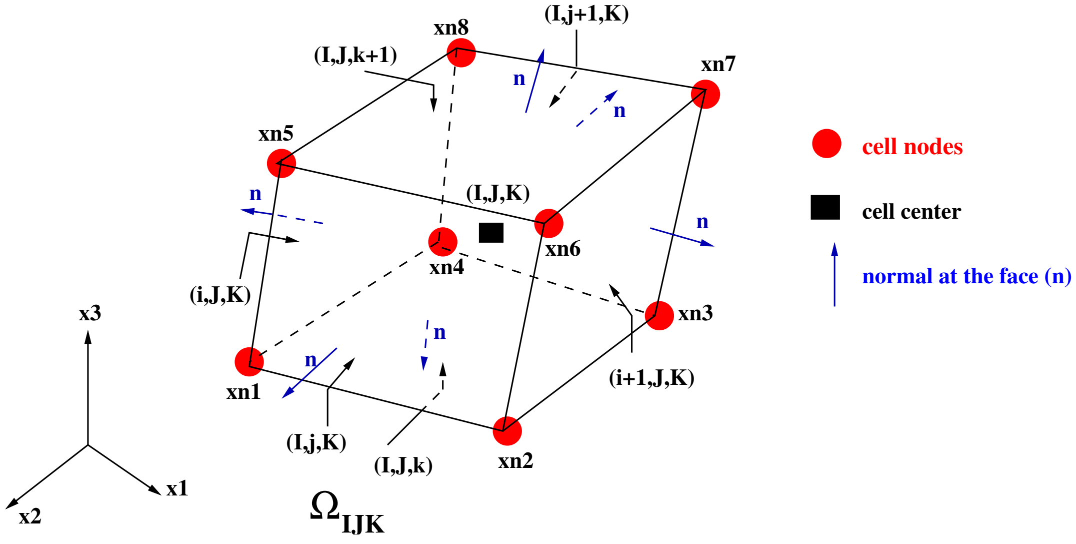

FIGURE 2.2: Description of a typical finite volume Ω_{IJK}. It is a structured domain determined by eight nodes $\mathbf{xn^i_{IJK}} = (xn_1, xn_2, xn_3)^i_{IJK}$ $i = 1, , 8$ defining the size and orientation of the six corresponding faces: (i, J, K), $(i+1, J, K)$, (I, j, K), $(I, j+1, K)$, (I, J, k), $(I, J, k+1)$. At every face we associate a corresponding normal unit vector $\mathbf{n} = (n_1, n_2, n_3)$ defining the orientation. All the coordinates are considered with respect to the cartesian reference frame.

It is important to note that the characteristics of Ω_{IJK} (volume, surfaces and orientations of the faces) can be completely determined from the coordinates of the eight nodes delimitating the domain. In particular the volumes are computed with respect to the center of the cells, while the surfaces and the normal vectors refer to the specific faces. Thus, for a given volume Ω_{IJK} we define:

• $\mid \Omega_{IJK} \mid$ as the volume of the domain;
• $\mathcal{S}_{IJK} := \left\{S^1, \cdots, S^6\right\}_{IJK}$ the set including the six faces of the cell,
and $\mathbf{n}_{IJK} := \{\mathbf{n}^1, \cdots, \mathbf{n}^6\}_{IJK}$ the corresponding set of normal vectors;
• when a specific face of Ω_{IJK} is considered, the surface and the normal are defined following the Figure 2.2. For example the face (i, J, K) has a corresponding surface S_{iJK} and normal vector $\mathbf{n_{iJK}}$.

The calculation of the surfaces, volumes and normal vectors is presented in the Appendix A.

Finally, the coordinates of the center of the cells Ω_{IJK} $(\mathbf{xc}_{IJK} = (xc_1, xc_2, xc_3)_{IJK})$ are also derived from the position of the eight nodes $\mathbf{xn}^i_{IJK}$ $i = 1, \cdots, 8$. In particular this is performed by a simple average calculation:

$$\mathbf{xc}_{IJK} = \frac{1}{8}\sum_{i=1}^{8} \mathbf{xn}^i_{IJK} \ \forall \ cells \ IJK \tag{2.27}$$

Remark 1

When a terrain-influenced grid is considered the xc_3 coordinate at ground level (cells $IJ1$) is set equal to the corresponding input topography altitude:

$$[xc_3]_{IJ1} = topo_{IJ} \ \forall \ cells \ IJ1 \tag{2.28}$$

where $topo_{IJ}$ is the topography altitude of the finite volume $IJ1$.

Remark 2

In the horizontal direction the position of the different cells is also identified with respect to a longitude (λ) - latitude (Φ) reference frame. In particular starting from the increment of distance in cartesian coordinates $(\Delta x, \Delta y)$, the corresponding arc-length increment in the spherical system $(\Delta\lambda, \Delta\Phi)$ is computed as (Jacobson, 1999):

$$\Delta\Phi = \frac{\Delta y}{R_e}; \ \Delta\lambda = \frac{\Delta x}{R_e \cos \Phi_{IJK}} \tag{2.29}$$

where R_e is the earth radius, and Φ_{IJK} the latitude of the finite volume Ω_{IJK}.

Starting from the present finite volumes grid, the numerical resolution of the mesoscale system computes average values of the meteorological quantities $(\rho, \theta, U_1, U_2, U_3, P', E)$ at the center of the different cells Ω_{IJK}. On the other hand, pressure-gradients and velocity fluxes are determined at the corresponding faces (cf. Figure 2.2). The numerical treatment of the different terms composing the mesoscale system (2.26) is detailed in the following section.

2.4 Resolution of hyperbolic and parabolic PDE

Most of the governing equations in fluid dynamics are second order partial differential equations. In particular, a general second order PDE in a two-dimensional domain can be written as (Sneddon, 1957):

$$A\frac{\partial^2 r}{\partial x^2} + B\frac{\partial^2 r}{\partial x \partial y} + C\frac{\partial^2 r}{\partial y^2} + D\frac{\partial r}{\partial x} + E\frac{\partial r}{\partial y} + Fr + G = 0 \tag{2.30}$$

where r is the unknown quantity and $A, \cdots, G$ can be constant or function of both independent and/or dependent variables.

Using the similitude between (2.30) and the expression of a conic section, second order PDE can be classified with respect to the sign of the discriminant $B^2 - 4AC$. In particular, three different types of PDE are identified (Chung, 2002):

- **Elliptic**: $B^2 - 4AC < 0$;
- **Parabolic**: $B^2 - 4AC = 0$;
- **Hyperbolic**: $B^2 - 4AC > 0$;

As explained by Chung (2002), elliptic PDE approximate subsonic flows, parabolic consider transonic flows, and hyperbolic equations model supersonic speeds.

Examples

- Elliptic 2D equation

$$\frac{\partial^2 r}{\partial x^2} + \frac{\partial^2 r}{\partial y^2} = 0 \tag{2.31}$$

- *Parabolic 1D equation*

$$\frac{\partial r}{\partial t} - a\frac{\partial^2 r}{\partial x^2} = 0 \ \ (a > 0) \tag{2.32}$$

- *Hyperbolic 1D equation*

$$\frac{\partial^2 r}{\partial t^2} - a^2\frac{\partial^2 r}{\partial x^2} \ \ (a > 0) \tag{2.33}$$

Remark

Equation (2.33) can be written as a combination of the following 1D Second Order Wave equations:

$$\frac{\partial^2 r}{\partial t \partial x} + a\frac{\partial^2 r}{\partial x^2} = 0 \tag{2.34}$$

$$\frac{\partial^2 r}{\partial t^2} + a\frac{\partial^2 r}{\partial t \partial x} = 0 \tag{2.35}$$

In fact, multiplying (2.34) by the factor a, and replacing the term $a\frac{\partial^2 r}{\partial t \partial x}$ with $-a^2\frac{\partial^2 r}{\partial x^2}$ in (2.35), one can directly obtain the hyperbolic equation (2.33).
We also remark that equations (2.34), (2.35) are obtained from the 1D First Order Wave equation

$$\frac{\partial r}{\partial t} + a\frac{\partial r}{\partial x} = 0, \tag{2.36}$$

by differentiating with respect to x ant t.

This derivation indicates that first and second order wave equations can be classified as hyperbolic PDE.

The system of equations describing the mesoscale model (2.26) is characterised by a combination of parabolic and hyperbolic PDE. In particular hyperbolic processes (terms A and B in the mesoscale system) describe the mean transport of the meteorological quantities, while parabolic phenomena (terms A and C in the mesoscale system) indicate the turbulent transport which is parametrised as a diffusion process. Finally, note that the general Acoustic equation for pressure perturbation (2.23) is also a parabolic PDE.

As already mentioned, in the present mesoscale model all these processes are computed with a finite volume technique. The corresponding numerical resolution schemes with some correlated tests are presented in sections 2.4.1 and 2.4.2.

2.4.1 The advection process

Let $r = r(\mathbf{x}, t)$ be the mixing ratio. Following the same notations of section 2.2, the **transport problem** can be witten as:

$$\begin{aligned} \frac{\partial \rho}{\partial t} + \frac{\partial}{\partial x_i}(\rho U_i) &= 0 \\ \frac{\partial r}{\partial t} + U_i \frac{\partial r}{\partial x_i} &= 0 \end{aligned} \tag{2.37}$$

Remark that the second equation in the system (2.37) is not conservative. The following computation shows that a **conservative form** can be obtained by multiplying by r the first equation in (2.37), by ρ the second, and then adding them together:

$$\begin{aligned} 0 &= r\frac{\partial \rho}{\partial t} + r\frac{\partial}{\partial t}(\rho U_i) + \rho\left(\frac{\partial r}{\partial t}\right) + \rho U_i \frac{\partial r}{\partial x_i} \\ &= \frac{\partial \rho r}{\partial t} + \frac{\partial}{\partial x_i}(U_i \rho r) \end{aligned}$$

Finally, the problem (2.37) can be written in the following conservative form:

Let $\Omega \subset \mathbb{R}^3 \times \mathbb{R}$, find a solution $\rho(\mathbf{x}, t)$, $r(\mathbf{x}, t)$ $\forall$ $\mathbf{x} \in \Omega$, $\forall$ $t \geq 0$ s.t.:

$$\begin{aligned} \frac{\partial \rho}{\partial t} + \frac{\partial}{\partial x_i}(\rho U_i) &= 0 \\ \frac{\partial \rho r}{\partial t} + \frac{\partial}{\partial x_i}(\rho r U_i) &= 0 \end{aligned} \tag{2.38}$$

with the initial conditions: $\rho(\mathbf{x}, 0) = f(\mathbf{x})$, $r(\mathbf{x}, 0) = g(\mathbf{x})$.

Thus, one can observe that the resolution of the transport of a given physical quantity in the atmosphere leads to the treatment of the following **pure advection problem**:

$$\begin{aligned} \frac{\partial q}{\partial t} + \frac{\partial}{\partial x_i}(q U_i) &= 0 \\ q(\mathbf{x}, 0) = g(\mathbf{x}) & \end{aligned} \tag{2.39}$$

In the present mesoscale model the treatment of (2.39) is based on a finite volumes approach and a fifth order Crowley interpolation method (Crowley, 1968) with a universal limiter (Thuborn, 1996). Its resolution is discussed in the following section. Numerical simulations are also carried out in order to show the characteristics of the corresponding numerical scheme.

2.4.1.1 Numerical treatment of the Transport Equation

Let $\Omega \subset \mathbb{R}^3$ be a mesoscale domain as the one of the Figure 2.1. In the following derivation we consider the same finite volume grid presented in the section 2.3. In particular, integrating (2.39) over Ω we get:

$$\int_{\Omega} \left[\frac{\partial q}{\partial t} + \frac{\partial q U_i}{\partial x_i} \right] d\Omega = 0 \tag{2.40}$$

Discretising Ω into $\mathcal{N}$ finite volumes Ω_{IJK} (cf. Figure 2.2) the integral (2.40) can be written as:

$$\sum_{(IJK)=1}^{\mathcal{N}} \left[\int_{\Omega_{IJK}} \frac{\partial q}{\partial t} + \frac{\partial q U_i}{\partial x_i} \right] d\Omega_{IJK} = 0 \tag{2.41}$$

In particular for every Ω_{IJK} this leads to:

$$\int_{\Omega_{IJK}} \left(\frac{\partial q}{\partial t} + \frac{\partial q U_i}{\partial x_i} \right) d\Omega_{IJK} = 0 \tag{2.42}$$

Applying the Gauss (or divergence) theorem, equation (2.42) can be written as:

$$\int_{\Omega_{IJK}} \frac{\partial q}{\partial t} d\Omega_{IJK} + \int_{\mathcal{S}_{IJK}} (qU_i n_i)_{IJK} \, d\mathcal{S}_{IJK} = 0 \tag{2.43}$$

Discretising in time and dividing by the magnitude of the finite volume Ω_{IJK} we get:

$$\begin{aligned} &\frac{\frac{1}{|\Omega_{IJK}|} \int_{\Omega_{IJK}} q^{n+1} d\Omega_{IJK} - \frac{1}{|\Omega_{IJK}|} \int_{\Omega_{IJK}} q^{n} d\Omega_{IJK}}{\Delta t} + \\ &\qquad \frac{1}{\mid \Omega_{IJK} \mid} \int_{\mathcal{S}_{IJK}} (qU_i n_i)_{IJK} \, d\mathcal{S}_{IJK} = 0 \end{aligned} \tag{2.44}$$

where Δt is the time step.

Defining

$$\overline{q}^{n}_{IJK} := \frac{1}{\mid \Omega_{IJK} \mid} \int_{\Omega_{IJK}} q^{n} d\Omega_{IJK} \tag{2.45}$$

as the average value of q in the volume Ω_{IJK}, equation (2.44) can be written as:

$$\overline{q}^{n+1}_{IJK} = \overline{q}^{n}_{IJK} - \frac{\Delta t}{\mid \Omega_{IJK} \mid} \int_{\mathcal{S}_{IJK}} (qU_i n_i)_{IJK} \, d\mathcal{S}_{IJK} \tag{2.46}$$

Substituting q by ρ and ρr in (2.46), the advection problem (2.38) can be written as:

$$\begin{aligned}\overline{\rho}_{IJK}^{n+1} &= \overline{\rho}_{IJK}^{n} - \frac{\Delta t}{\mid \Omega_{IJK} \mid}\int_{\mathcal{S}_{IJK}} (\rho U_i n_i)_{IJK}\, d\mathcal{S}_{IJK} \\ (\overline{\rho r})_{IJK}^{n+1} &= (\overline{\rho r})_{IJK}^{n} - \frac{\Delta t}{\mid \Omega_{IJK} \mid}\int_{\mathcal{S}_{IJK}} ((\rho r)\, U_i n_i)_{IJK}\, d\mathcal{S}_{IJK}\end{aligned} \tag{2.47}$$

The integrals over $\mathcal{S}_{IJK}$ in (2.47) are computed by summing over the corresponding surfaces $S_{IJK}^1, \cdots S_{IJK}^6$. For instance, for the quantity ρr this leads to:

$$\int_{\mathcal{S}_{IJK}} ((\rho r)\, U_i n_i)_{IJK}\, d\mathcal{S}_{IJK} = \sum_{\alpha=1}^{6} \rho_{IJK}^{n} \overline{r}_{IJK}^{\alpha} \left(U_i n_i\right)_{IJK}^{\alpha} S_{IJK}^{\alpha} \tag{2.48}$$

where $\mathbf{U}_{IJK}^{\alpha}$ is the interpolated wind speed at the face α of the finite volume Ω_{IJK} ($\forall \quad \alpha = 1, \cdots, 6$) and $\overline{r}_{IJK}^{\alpha}$ is the average of r crossing the face α of the finite volume Ω_{IJK} during the time interval Δt. This value is computed by an *interpolation* of the values of r located at the center of the neighbouring cells. In particular, the type of interpolation will generate a corresponding numerical scheme. In the present mesoscale model the values of $\overline{r}_{IJK}^{\alpha}$ are approached by a Taylor series expansion of order five leading to a *fifth order Crowley method* (Crowley, 1968, Tremback et al., 1986). As we will see in the numerical tests of section 2.4.1.3, this interpolation method can generate non physical oscillations. In order to avoid this kind of problem, a *universal limiter* is added to the model following the work of Thuborn (1996). The complete derivation of the term $\overline{r}_{IJK}^{\alpha}$ is presented in the following section.

Defining (for every Ω_{IJK}) the **mass flow** crossing the face α during the time interval Δt as

$$\mathcal{F}_{IJK}^{\alpha} := (\rho_{IJK}^{n} (U_i n_i)_{IJK}^{\alpha})\, S_{IJK}^{\alpha}, \tag{2.49}$$

the system of equations (2.47) can be finally written as:

$$\begin{aligned}\overline{\rho}_{IJK}^{n+1} &= \overline{\rho}_{IJK}^{n} - \frac{\Delta t}{\mid \Omega_{IJK} \mid}\sum_{\alpha=1}^{6} \mathcal{F}_{IJK}^{\alpha} \\ (\overline{\rho r})_{IJK}^{n+1} &= (\overline{\rho r})_{IJK}^{n} - \frac{\Delta t}{\mid \Omega_{IJK} \mid}\sum_{\alpha=1}^{6} \overline{r}_{IJK}^{\alpha} \mathcal{F}_{IJK}^{\alpha}\end{aligned} \tag{2.50}$$

Remark that (2.50) indicates that the evolution of the mean values of ρ and ρr during the time interval Δt over the finite volume Ω_{IJK} depends on the corresponding fluxes crossing the faces of the domain during this period.

Following the work of Clappier (1998), the problem (2.50) is solved with a *time splitting* technique corrected for multidimensional applications. In particular, as one can see in the following, the one-dimensional transport problem is progressively considered in the x_1, x_2 and x_3 directions (cf. Figure 2.2 for the different notations).

- Faces in x1-direction

$$\begin{aligned}
(\overline{\rho r})^{\star}_{IJK} = (\overline{\rho r})^{n}_{IJK} - \frac{\Delta t}{\mid \Omega \mid_{IJK}} \left(\overline{r}_{i,J,K}\mathcal{F}_{i,J,K} - \overline{r}_{i+1,J,K}\mathcal{F}_{i+1,J,K}\right) \\
(\overline{\rho})^{\star}_{IJK} = (\overline{\rho})^{n}_{IJK} - \frac{\Delta t}{\mid \Omega \mid_{IJK}} \left(\mathcal{F}_{i,J,K} - \mathcal{F}_{i+1,J,K}\right) \\
\Rightarrow \overline{r}^{\star}_{IJK} = \frac{(\overline{\rho r})^{\star}_{IJK}}{\overline{\rho}^{\star}_{IJK}}
\end{aligned}$$

- Faces in x2-direction

$$\begin{aligned}
(\overline{\rho r})^{\star\star}_{IJK} = (\overline{\rho r})^{\star}_{IJK} - \frac{\Delta t}{\mid \Omega \mid_{IJK}} \left(\overline{r}_{I,j,K}\mathcal{F}_{I,j,K} - \overline{r}_{I,j+1,K}\mathcal{F}_{I,j+1,K}\right) \\
(\overline{\rho})^{\star\star}_{IJK} = (\overline{\rho})^{\star}_{IJK} - \frac{\Delta t}{\mid \Omega \mid_{IJK}} \left(\mathcal{F}_{I,j,K} - \mathcal{F}^{4}_{I,j+1,K}\right) \\
\Rightarrow \overline{r}^{\star\star}_{IJK} = \frac{(\overline{\rho r})^{\star\star}_{IJK}}{\overline{\rho}^{\star\star}_{IJK}}
\end{aligned}$$

- Faces in x3-direction

$$\begin{aligned}
(\overline{\rho r})^{n+1}_{IJK} = (\overline{\rho r})^{\star\star}_{IJK} - \frac{\Delta t}{\mid \Omega \mid_{IJK}} \left(\overline{r}_{I,J,k}\mathcal{F}_{I,J,k} - \overline{r}_{I,J,k+1}\mathcal{F}_{I,J,k+1}\right) \\
(\overline{\rho})^{n+1}_{IJK} = (\overline{\rho})^{\star\star}_{IJK} - \frac{\Delta t}{\mid \Omega \mid_{IJK}} \left(\mathcal{F}_{I,J,k} - \mathcal{F}_{I,J,k+1}\right) \\
\Rightarrow \overline{r}^{n+1}_{IJK} = \frac{(\overline{\rho r})^{n+1}_{IJK}}{\overline{\rho}^{n+1}_{IJK}}
\end{aligned} \tag{2.51}$$

Moreover, the order of resolution of (2.51) is reversed each time step in order to improve accuracy (Yaneko, 1971, Jacobson, 1999).

Remark (Constancy property)
Suppose $\overline{r}^{i}_{IJK}$ equal to a constant r^0 $\forall$ time step $i = 1 \cdots, n$. Applying (2.51) in the $x1$-direction leads to:

$$\begin{aligned}
(\overline{\rho r})^{\star}_{IJK} = r^0 \, (\overline{\rho})^{n}_{IJK} - \frac{\Delta t}{\mid \Omega \mid_{IJK}} \left(\mathcal{F}_{i,J,K} - \mathcal{F}_{i+1,J,K}\right) r^0 \\
(\overline{\rho})^{\star}_{IJK} = (\overline{\rho})^{n}_{IJK} - \frac{\Delta t}{\mid \Omega \mid_{IJK}} \left(\mathcal{F}_{i,J,K} - \mathcal{F}_{i+1,J,K}\right) \\
\Rightarrow \overline{r}^{\star}_{IJK} = r^0
\end{aligned}$$

Considering a similar development in the *x2* and *x3* directions one can conclude that:

$$\overline{r}_{IJK}^{n+1} = r^0$$

This illustrates that if the initial perturbation is constant, it remains constant after every time step. In that case we can say that the numerical method has the *constancy property.*

Remark (Courant-Friedrich-Levy (CFL) condition)
In order to ensure the stability of the numerical method, the following CFL condition must be satisfied:

$$CFL = \frac{\Delta t \sum_{\alpha=1}^{6} \left(\tilde{U}_i\right)_{IJK}^{\alpha} S_{IJK}^{\alpha}}{\mid \Omega_{IJK} \mid} < 1. \; \forall \; cell \; IJK \tag{2.52}$$

where Δt is the time step, and $\left(\tilde{U}_i\right)_{IJK}^{\alpha} := \max\left(0, (U_i n_i)_{IJK}^{\alpha}\right)$.

Remark that this condition states that the "physical wind velocity" **U** cannot be greater than the one imposed by the spatial and temporal discretisation. This, in turn, can have important consequences on the CPU calculation time.

2.4.1.2 Crowley method and the Universal Limiter

Following (2.51), three one-dimensional advection problems are solved corresponding to the faces in the *x1*, *x*2, and *x3* directions. In the following development only the faces along *x1* are taken into account, but an equivalent procedure can be considered with respect to the other directions. Furhemore, it is assumed that the flow is moving upstream from the cell *IJK* to the cell *I* + *1JK* (cf. Figure 2.3), but the other direction can also be treated in a similar way.

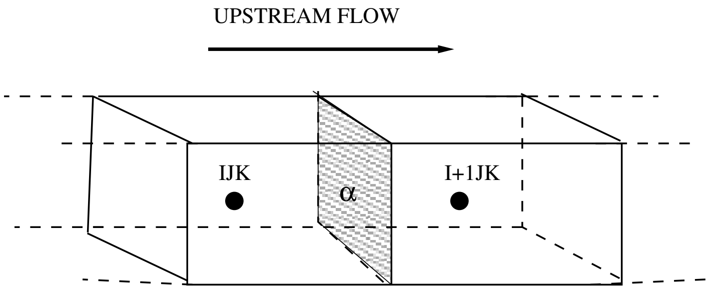

FIGURE 2.3: Representation of the face α utilised for the derivation of the term $\overline{r}_{IJK}^{\alpha}$. The flow is supposed to move from the cell *IJK* to the cell *I* + *1JK*.

Starting from these assumptions, we first define the adimensional *volume fraction* crossing the face α during the time interval Δt as:

$$\mathcal{V}f^{\alpha}_{IJK} := \frac{\Delta t \mathcal{F}^{\alpha}_{IJK}}{\rho_{IJK} \mid \Omega_{IJK} \mid} \tag{2.53}$$

Taking (2.53) into account, the advection flux $\overline{r}^{\alpha}_{IJK}$ is computed following the formulation of Bott (1989):

$$\overline{r}^{\alpha}_{IJK} = \int_{\frac{1}{2}-\mathcal{V}f^{\alpha}_{IJK}}^{\frac{1}{2}} \tilde{r}_{IJK}(x)dx \tag{2.54}$$

where $\tilde{r}$ is the polynomial interpolation of $\overline{r}$ of a given degree M:

$$\tilde{r}_{IJK}(x) = \sum_{j=0}^{M} a_j x^j \tag{2.55}$$

In general, the different numerical methods are defined by the degree of this polynomial and the way with which the a_j coefficients are computed. In the present mesoscale model a fifth-order Crowley scheme is considered ($M = 5$ in (2.55)). The method used for the calculation of the coefficients a_j employes the value of $\overline{r}_{IJK}$ and that at the neighbouring cells. The complete derivation is presented in the Appendix B.

Introducing (2.55) inside (2.54) one can derive the following expression for $\overline{r}^{\alpha}_{IJK}$:

$$\overline{r}^{\alpha}_{IJK} = \sum_{j=0}^{M} a_j \left(\frac{1}{2}^{j+1} - \left(\frac{1}{2} - \mathcal{V}f^{\alpha}_{IJK} \right)^{j+1} \right) \tag{2.56}$$

Expression (2.56) is finally used to compute $\overline{r}^{\alpha}_{IJK}$ for every face α and the corresponding values are introduced inside the splitting procedure (2.51).

In general, a great advantage of the fifth-order Crowley method lies in the fact that the solution is subject to a very small diffusion error. On the other hand, it has been observed that the transported function can present non physical oscillations which are generated by the dispersion error. This problem has been exstensivly studied in the literature (Harten, 1983, Sweby, 1985, Hundsdorfer et al., 1995, Leonard, 1991, Thuborn, 1996) with the aim to implement an advection scheme which does not create spurious extrema or amplify existing extrema. It has been found that this property (called monotonicity-preserving) can be achieved by limiting the advective flux to physical values. This can be performed by different techniques and in the present model the one based on the *Universal Limiter* has been considered (Leonard, 1991, Thuborn, 1996). In particular for an upstream flow as the one in Figure 2.3, the universal limiter aims to ensure the following local bounding property:

$$r\min_{IJK} \leq \overline{r}^{n+1}_{IJK} \leq r\max_{IJK} \tag{2.57}$$

where

$$r\max_{IJK} = \max\left(\overline{r}^{n}_{IJK}, \overline{r}^{n}_{I-1JK}\right);\; r\min_{IJK} = \min\left(\overline{r}^{n}_{IJK}, \overline{r}^{n}_{I-1JK}\right). \tag{2.58}$$

As described in detail in Thuborn (1996), this property is achieved by placing constraints on the value of the outflow edge ($\overline{r}^{\alpha}_{IJK}\mathcal{F}^{\alpha}_{IJK}$). In practise, the universal limiter is performed by first calculating preliminary values of $\overline{r}^{\alpha}_{IJK}\mathcal{F}^{\alpha}_{IJK}$ using the fifth-order Crowley advection scheme, and then adjusting them in order to satisfy the bounding property (2.57) – (2.58).

2.4.1.3 Numerical tests

A set of one and two-dimensional simulations is considered in order to test and study some characteristics of the advection scheme.

Part I: One-dimensional results

We consider a domain $\mathcal{D} = [0, 120] \times [0, \infty) \subset \mathbb{R} \times \mathbb{R}$ with $\Delta x = 1m$. As one can see in the Figure 2.4 the initial perturbation $r(x, 0)$ describes a one-dimensional cone with a peak value $r(14, 0) = 2$. A constant wind velocity $u = 1\frac{m}{s}$ is considered with a time step $\Delta t = 0.4s$.

Figure 2.4 first compares the initial perturbation with the transported solution after $80s$. In this test the fifth-order Crowley method has been applied without any limiter.

Remark first that the transported solution is subject to a small diffusion error resulting in a decrease of the peak perturbation value. In addition, as previously mentioned, one of the major problems of this kind of interpolation scheme lies in the formation of non physical oscillations, which can be clearly observed in the Figure 2.4.

Figure 2.5 illustrates that the application of the Universal Limiter is able to counteract this problem. Also observe that a related negative effect is to generate an additional smoothing of the transported solution. In this context, Figure 2.5 indicates that higher order interpolation functions lead to more accurate solutions with better preserved peak of the transported solution.

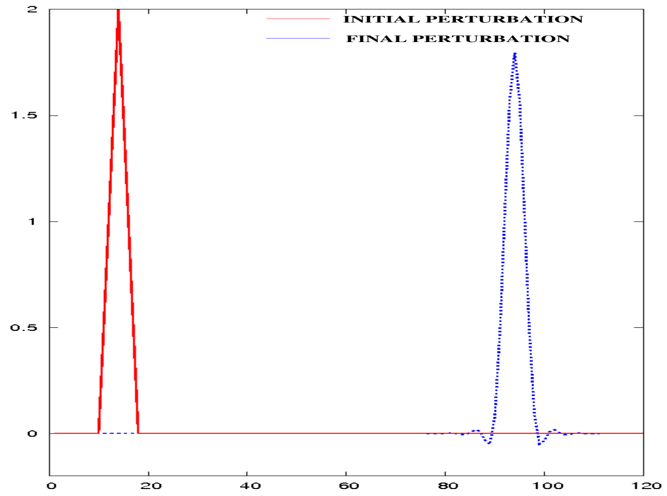

FIGURE 2.4: Comparison between the initial perturbation (left) and the transported solution after 80s (right).

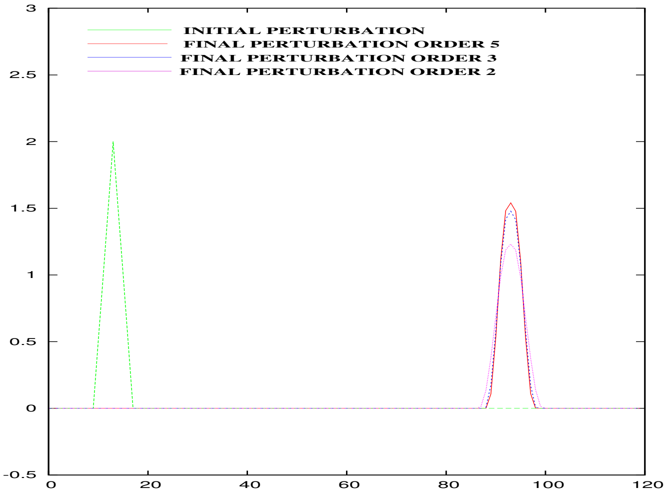

FIGURE 2.5: Comparison between the initial perturbation (left) and the transported solutions after 80s (right). The Universal Limiter is applied, and interpolation functions of different orders are considered.

Part II: Two-dimensional results

Consider a general wind field of the form:

$$\mathbf{U}(x,y) = \left(-\overline{\omega}y + (\omega_{\max} - \omega_{\min})\,x, \overline{\omega}x - (\omega_{\max} - \omega_{\min})\,y\right) \tag{2.59}$$

where $\overline{\omega}$ describes the mean, and $\omega_{\max}$, $\omega_{\min}$ maximal and minimal angular velocity values.

Note that $\nabla.\mathbf{U} = 0$, which corresponds to a zero divergence wind field. On the other hand, it is important to remark that in general, the flow field is not monodimensionally divergence free as $\frac{\partial U_1}{\partial x_1} = -\frac{\partial U_2}{\partial x_2} = \omega_{\max} - \omega_{\min}$.

A: Rotational wind field

We first consider a particular case of (2.59) where $\omega_{\max} = \omega_{\min} = \varpi$. This is a zero divergence rotational wind field with constant angular velocity ϖ. In this test the flow field velocities are defined over a 100×100 grid cell domain with an angular velocity $\varpi = 0.1$. The initial perturbation is defined by a cone of radius 10 grids and height 5, above a background of base value 1. Similar initial perturbations and wind field are often used in order to evaluate the performances of the different advection schemes (Clappier, 1996, Crowley, 1968, Smolarkevicz, 1984, Bott, 1992). The cone is centered in $(15, 75)$ and the initial perturbation is compared to the solution obtained after one complete rotation (cf. Figure 2.6).

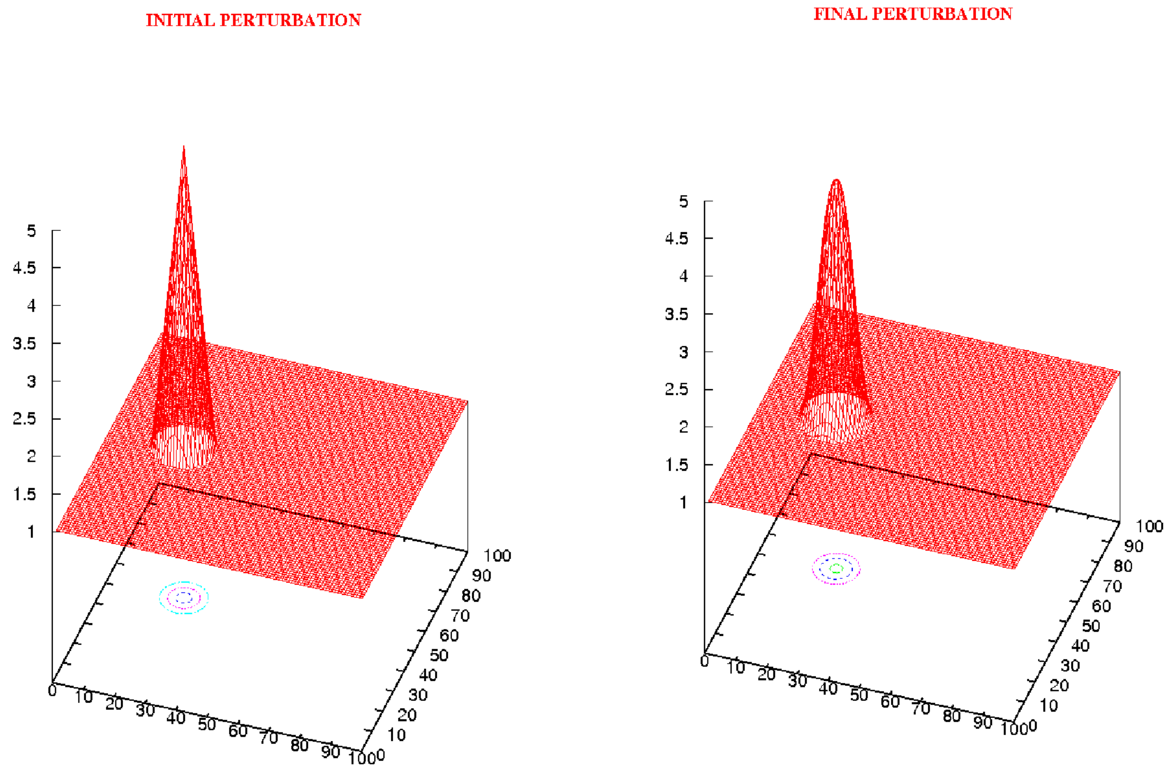

Figure 2.6: Comparison between the initial perturbation (left) and the solution after 1 rotation (right). The fifth order Crowley method with the Universal Limiter is considered. The courant number (CFL) is set to 0.15.

It is known that for this test the cone should rotate around the domain keeping the same shape. As one can see in Figure 2.6 the shape is well preserved by the numerical advection scheme. Similarly to one-dimensional results, the method leads to a small diffusion error with a truncated peak of the rotated cone.

Remark (Constancy condition)
The following result illustrates the importance of the constancy condition. In particular the Figure 2.7 indicates that if in the splitting procedure (2.51), $\overline{\rho}$ is not transported in correspondance to $\overline{\rho r}$, the constant base value of 1 is not maintained and non physical background oscillations appear.

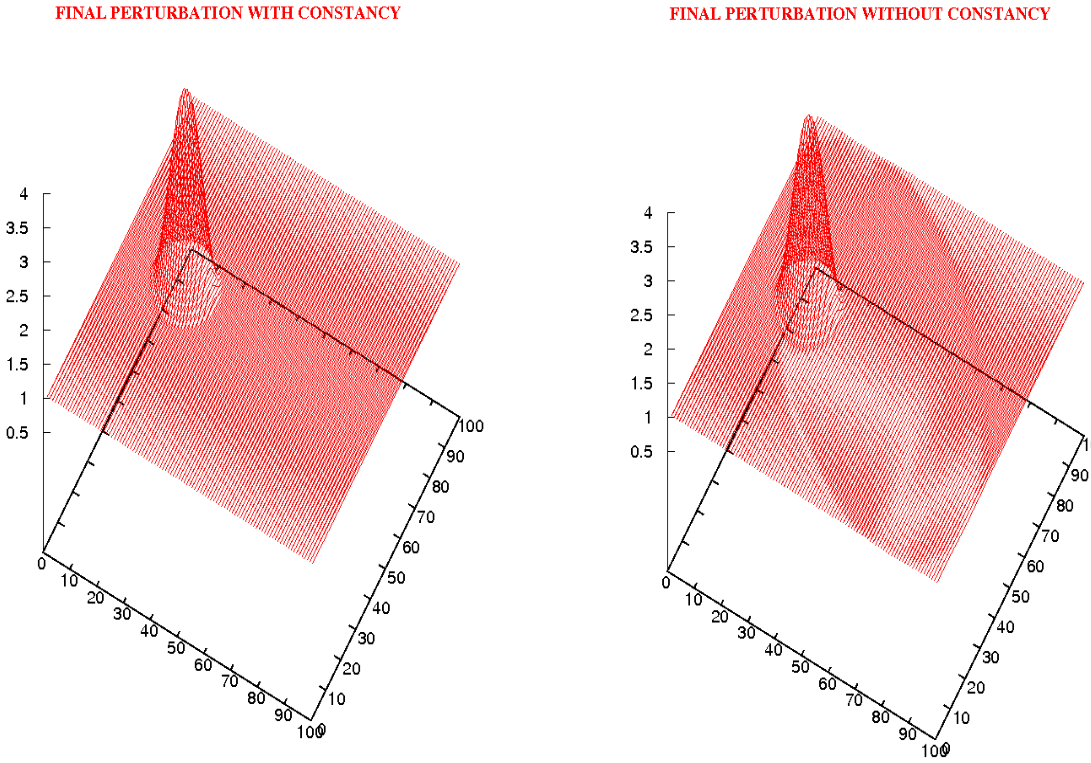
FINAL PERTURBATION WITH CONSTANCY

FINAL PERTURBATION WITHOUT CONSTANCY

FIGURE 2.7: Perturbation after one rotation with (left) and without (right) the constancy condition in the splitting procedure.

Remark (CFL condition)
As previously mentioned, the CFL stability condition (2.52) has to be satisfied at each time step by the numerical scheme. For instance, Figure 2.8 illustrates the shape of the transported solution for a CFL of 1.94. Remark that non physical instabilities can clearly be observed.

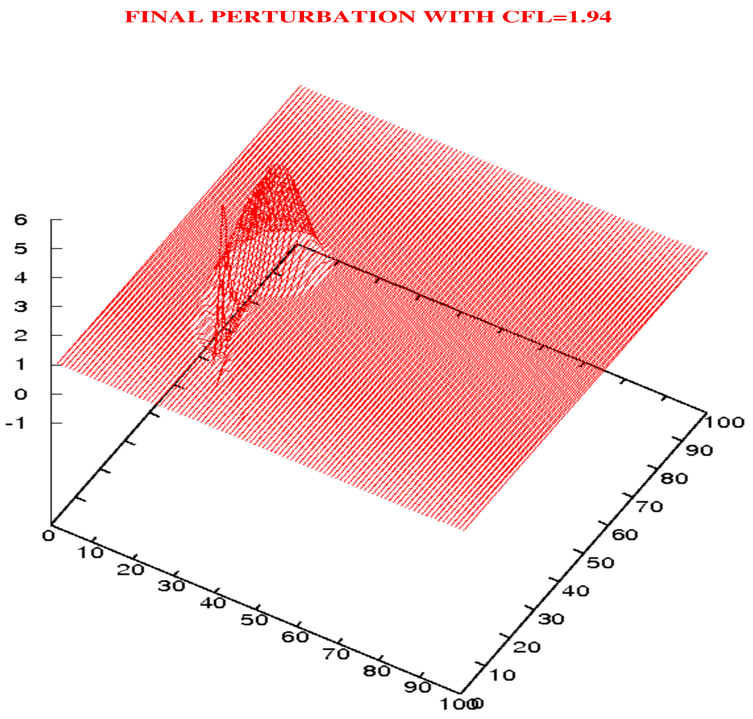

FIGURE 2.8: Perturbation after one rotation with a $CFL > 1$.

B: Convergent and divergent wind field

For this last test we consider a general wind field of the form (2.59) with $\varpi = 0.1$, $\omega_{\max} = 0.2$, and $\omega_{\min} = 4.9.10^{-2}$. Remark that the corresponding flow is divergent in the x-direction ($\frac{\partial U_1}{\partial x_1} = \omega_{\max} - \omega_{\min} > 0$) and convergent in the y-direction ($\frac{\partial U_2}{\partial x_2} = \omega_{\min} - \omega_{\max} < 0$). During the rotation the initial perturbation will therefore be submitted to a serie of divergences and compressions. As can observe in Figure 2.9, the shape of the initial perturbation is still well preserved by the numerical scheme, but the peak of the cone is more truncated compared to the simple rotational wind field.

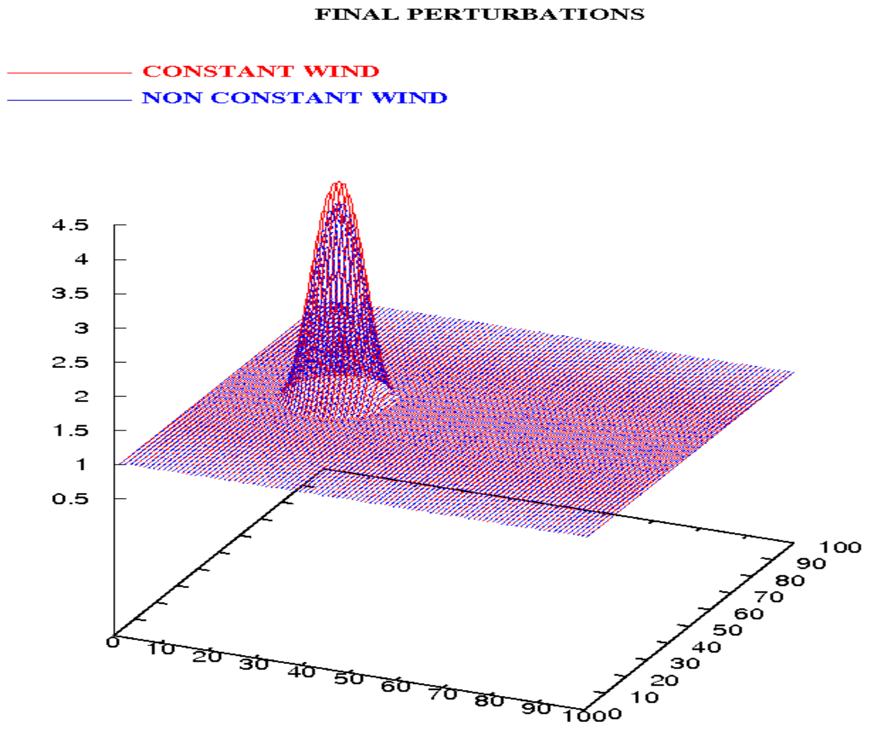

Figure 2.9: Comparison between the perturbation after one rotation obtained with a constant ($\omega_{\max} = \omega_{\min}$), and a non constant ($\omega_{\max} \neq \omega_{\min}$) wind field in the x and y directions.

2.4.2 The diffusion process

As mentioned at the beginning of section 2.4, the diffusion process is described by a parabolic PDE which can be written in the following general form:

$$\frac{\partial q}{\partial t} - \frac{\partial}{\partial x_i} K_j \frac{\partial q}{\partial x_j} = \mathcal{S}_{rc} \quad i, j = 1, \cdots, 3 \tag{2.60}$$

where $q(\mathbf{x})$ is the unknown quantity, $\mathbf{K}$ the vector of the diffusion coefficients at the different directions, and $\mathcal{S}_{rc}$ a source term.

2.4.2.1 Numerical treatment of the Diffusion Equation

Following a similar procedure as for hyperbolic problems, equation (2.60) is treated with a finite volume approach. In particular integrating it over the mesoscale domain $\Omega \subset \mathbb{R}^3$

we get:

$$\int_{\Omega}\left[\frac{\partial q}{\partial t}-\frac{\partial}{\partial x_i}K_j\frac{\partial q}{\partial x_j}-\mathcal{S}_{rc}\right]d\Omega=0. \tag{2.61}$$

Discretising Ω into $\mathcal{N}$ finite volumes Ω_{IJK} (cf. Figure 2.2), the integral (2.61) can be written as:

$$\sum_{\Omega_{IJK}=1}^{\mathcal{N}}\int_{\Omega_{IJK}}\left[\frac{\partial q}{\partial t}-\frac{\partial}{\partial x_i}K_j\frac{\partial q}{\partial x_j}-\mathcal{S}_{rc}\right]d\Omega_{IJK}=0. \tag{2.62}$$

In particular for every Ω_{IJK} this leads to:

$$\int_{\Omega_{IJK}}\left[\frac{\partial q}{\partial t}-\frac{\partial}{\partial x_i}K_j\frac{\partial q}{\partial x_j}-\mathcal{S}_{rc}\right]d\Omega_{IJK}=0. \tag{2.63}$$

In the present mesoscale model the diffusion term $\frac{\partial}{\partial x_i}K_j\frac{\partial q}{\partial x_j}$ is treated with an implicit method. Furthermore, dividing (2.63) by $\mid\Omega_{IJK}\mid$, using the divergence theorem, and the definition of $\overline{q}^n_{IJK}$ (cf. (2.45)), one can write (2.63) in the following form:

$$\frac{\overline{q}^{n+1}_{IJK}}{\Delta t}-\frac{1}{\mid\Omega_{IJK}\mid}\int_{\mathcal{S}_{IJK}}K_j\left[\frac{\partial q^{n+1}}{\partial x_j}\right]dS=\frac{\overline{q}^n_{IJK}}{\Delta t}+\left[\overline{\mathcal{S}_{rc}}\right]^n_{IJK} \tag{2.64}$$

where Δt is the time step and $\left[\overline{\mathcal{S}_{rc}}\right]^n_{IJK}$ is the average source term over the finite volume Ω_{IJK} at time n.

Computing the integral over $\mathcal{S}_{IJK}$ with a summation over the corresponding surfaces $S^1_{IJK},\cdots,S^6_{IJK}$ (cf. Figure 2.2) we can write (2.64) as:

$$\frac{\overline{q}^{n+1}_{IJK}}{\Delta t}-\frac{1}{\mid\Omega_{IJK}\mid}\sum_{\alpha=1}^{6}\left[K_j\frac{\partial q^{n+1}}{\partial x_j}\right]^{\alpha}_{IJK}.\,(Sn_j)^{\alpha}_{IJK}=\frac{\overline{q}^n_{IJK}}{\Delta t}+\left[\overline{\mathcal{S}_{rc}}\right]^n_{IJK} \tag{2.65}$$

where the symbol "**.**" describes the dot product.

Remark that ($\forall\ \alpha=1,\cdots,6$) the term $\left[\frac{\partial q}{\partial x_j}\right]^{\alpha}_{IJK}$ describes the gradient of q at the face α of the finite volume IJK. In general, there are different numerical techniques that one can utilise in order to approximate this value. In any case, this will be finally determined by a linear combination of the values of q at the neighbouring cells:

$$\frac{\partial q}{\partial x_j}=\sum_{\beta=1}^{M}\xi^j_{\beta}q_{\beta};\ \sum_{\beta=1}^{M}\xi^j_{\beta}=1\ \forall\ j=1,\cdots,3. \tag{2.66}$$

where M is the number of neighbouribg cells that is considered, and ξ^i_β are ponderation coefficients depending on the numerical method being in use.

In the present mesoscale model the gradient of q at the different faces is approximated by a finite volume technique. Furthermore, as one can see inFigure 2.10 for the face $(i+1, J, K)$, this is determined by a linear combination of the mean values of q over ten neighbouring cells ($M = 10$ in (2.66)). The calculation of the corresponding ponderation coefficients ξ^j_β is detailed in the Appendix C.

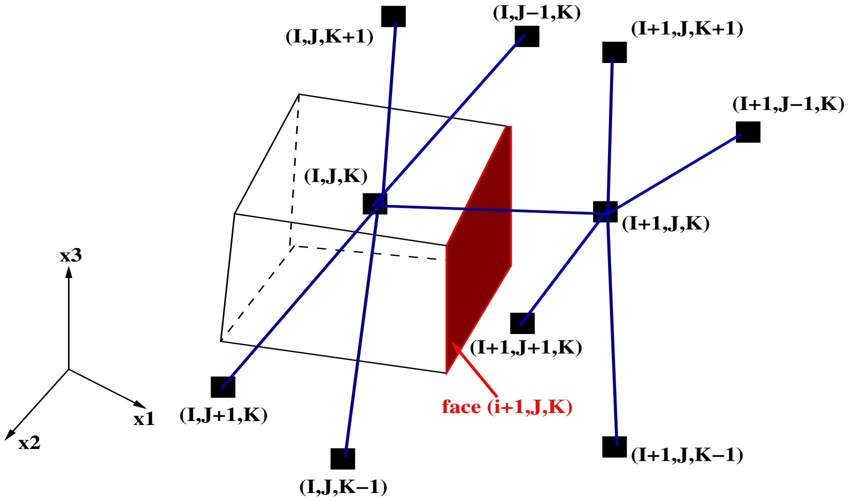

FIGURE 2.10: Representation of the domain of dependence for the computation of the gradient at the face.

Taking (2.66) into account, expression (2.65) can be finally written as:

$$\frac{\overline{q}^{n+1}_{IJK}}{\Delta t} - \frac{1}{\mid \Omega_{IJK} \mid} \sum_{\alpha=1}^{6} \left\{ \left[K_j \sum_{\beta=1}^{M} \xi^j_\beta \overline{q}^{n+1}_\beta \right]^\alpha_{IJK} . (Sn_j)^\alpha_{IJK} \right\} = \frac{\overline{q}^n_{IJK}}{\Delta t} + \left[\overline{\mathcal{S}_{rc}}\right]^n_{IJK} \tag{2.67}$$

Remark that at the left hand side of (2.67) we consider the values of $\overline{q}$ at time $n+1$, while at the right hand side the values at time n are grouped together. In particular, applying (2.67) at every finite volume $\Omega_{IJK} = 1, \cdots, \mathcal{N}$ (i.e. introducing (2.67) inside (2.62)), we finally obtain the following linear system:

$$\left[\frac{1}{\Delta t}\mathbb{I} - \mathcal{L}\right] \overline{\mathbf{Q}}^{n+1} = \left[\frac{1}{\Delta t} I\right] \overline{\mathbf{Q}}^{n} + \overline{\mathbb{S}_{\mathbf{rc}}}^{n} \tag{2.68}$$

where $\mathbb{I}$ represents the Identity matrix, and $\mathcal{L}$ is called the Laplacian matrix. The term $\overline{\mathbb{S}_{\mathbf{rc}}}^{n}$ is the vector of all the source terms at time n, while $\overline{\mathbf{Q}}^{n}$ and $\overline{\mathbf{Q}}^{n+1}$ are the vectors including all the unknown quantities (i.e. at every finite volume Ω_{IJK}) at time n and

$n + 1$. In the present mesoscale model the system (2.68) is treated with a biconjugate gradient iterative method (Numerical Recipes, 1986 – 1992).

2.4.2.2 Numerical tests

In the simple case when the initial perturbation is a step function and the mesh is not deformed, it is possible to find the analytical solution of the one-dimensional diffusion problem:

$$q(x,t) = \frac{q_{ini}}{2}\left(erf\left(\frac{x+e}{2\sqrt{Kt}}\right) - erf\left(\frac{x-e}{2\sqrt{Kt}}\right)\right) \tag{2.69}$$

where q_{ini} is the initial perturbation (step function), e corresponds to half of the step width, K is the diffusion coefficient, and x the distance with respect to the center of the initial step. The erf function is given by:

$$erf(x) = \frac{2}{\sqrt{\pi}}\int_0^x \exp(-\xi^2)d\xi \tag{2.70}$$

The comparison between the analytical and the numerical solution for this particular one-dimensional problem is presented in Figure 2.11. The parameters adopted for the test are: $e = 15cm$, q_{ini} a step function of height 1, and $Kt = 0.001$.

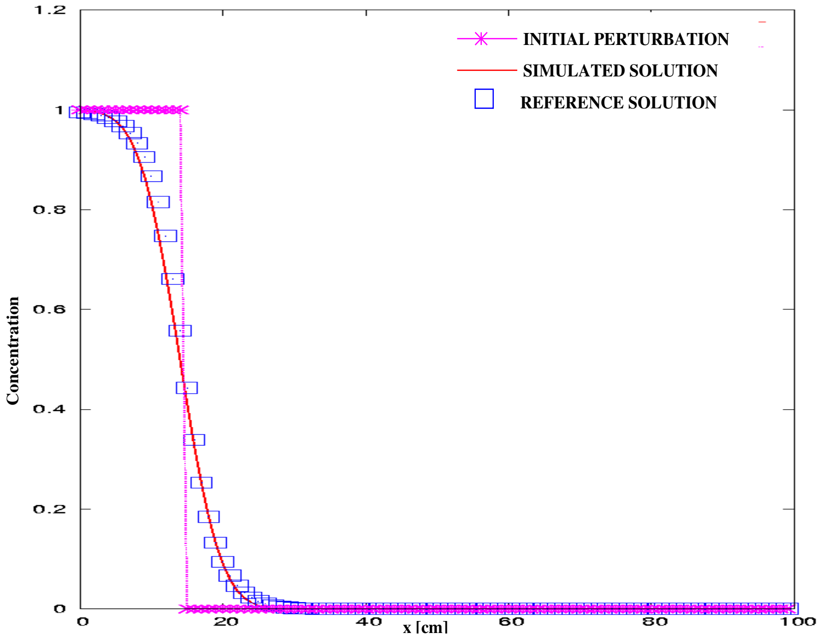

FIGURE 2.11: Comparison between the numerical and the analytical solution for the one-dimensional diffusion problem and an initial step perturbation.

In Figure 2.12 we present a direct generalisation of this test to the two-dimensional diffusion problem. Observe that the initial "box" perturbation is diffused along the x and y directions.

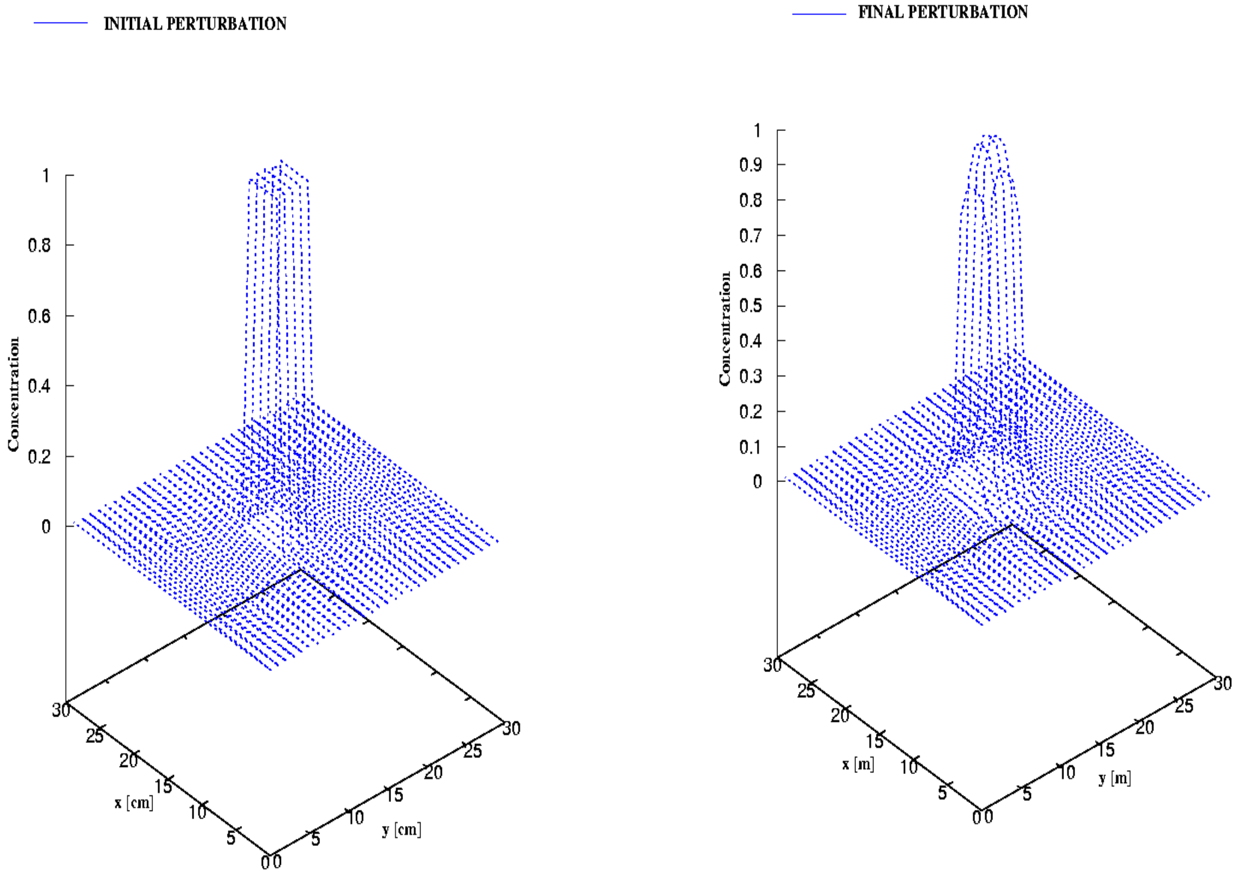

FIGURE 2.12: Representation of the initial (left) and final (right) perturbations after a two-dimensional diffusion process and an initial "box" distribution.

2.5 Description of the FVM algorithm

As presented in the section 2.2, the system of PDE describing the mesoscale model is composed by a combination of hyperbolic (mean wind transport), and parabolic (turbulent transport and acoustic equation for pressure perturbation) PDE, to which some source terms are added. In the present paragraph we illustrate how these different processes are linked in order to form the general algorithm used for the resolution of the Finite Volumes Mesoscale model (FVM). In the following, the different parts of the algorithm are enphasized with a box.

MESH

In this routine the Finite Volume Mesoscale grid is generated following the same procedure detailed in the paragraph 2.3.

Then, the following set of routines are considered at every time step until the end of the simulation period.

ADVECTION

In this part of the algorithm the hyperbolic equation describing the mean transport of the different meteorological quantities (terms A and B in the mesoscale system (2.26)) is computed following the numerical technique detailed in the section 2.4.1. In particular, starting from the values at the time step n and the mass flow crossing the different faces during the time interval $[t^n, t^{n+1}]$ (cf. (2.49)), we compute the corresponding meteorological variables $\Big(\rho, (U_i)_{i=1,\cdots,3}, \mathcal{H}, \theta, E\Big)$ after the advection process.

RADIATION

In this routine, we first compute the amount of short and long wave radiation fluxes. Details concerning these calculations can be found in Schayes, (1982), and Sasamori, (1968). The long wave radiation is then used to compute explicitly the source term I in the energy equation (2.14).

TURBULENCE

The expression (2.20) is first used in order to compute the turbulent diffusion coefficient. Then, the shear (I), buoyant (II), and dissipation (III) source terms in (2.19) are calculated. In particular, terms I and II represent explicit source contributions, while the dissipation (III) is treated numerically in an implicit form:

$$\mathrm{III} = -\rho^{n+1} C_\varepsilon \frac{\sqrt{E^n}}{l_\varepsilon} E^{n+1} \tag{2.71}$$

SURFACE FLUXES

In this part of the algorithm we compute the source terms generated by the presence of urban and rural surfaces (terms $\mathcal{D}$ in the mesoscale system (2.26)). As in standard mesoscale models, rural soil sources are treated using the MOST theory according to the formulation of Louis, (1979). More details concerning this calculation are given in Martilli (2002), and Roulet (2004). The computation of the urban sources on the momentum, and turbulent kinetic energy budget are described in detail in Martilli et al. (2002). The sensible and latent heat sources are treated in chapter 4 of the present thesis. As for the other sources, urban and rural terms generate both, implicit and explicit contributions. In particular, these different quantities are finally taken into account as source terms in the diffusion equation resolving the turbulent transport.

DIFFUSION

This step of the mesoscale model resolution is focused on the computation of the turbulent transport. As already detailed in the paragraph 2.2.5 this is treated with the K-theory approach which parametrises the turbulent transport by a diffusion process. The air density remains constant in this part of the algorithm. In particular, for a mesoscale variable Γ (wind speed, temperature, humidity, TKE), and following the expression (2.18), the diffusion process can be written as:

$$\frac{\partial \Gamma}{\partial t} = \frac{1}{\rho}\frac{\partial}{\partial x_i}\left(K_j \frac{\partial \Gamma}{\partial x_j}\right) + a\Gamma + b \tag{2.72}$$

where a and b represent respectively implicit and explicit source terms.

Equation (2.72) is treated numerically following the same procedure detailed in the paragraph 2.4.2. In particular, this leads to the following linear system which is solved again with a biconjugate gradient iterative method (Numerical Recipes, 1986 – 1992):

$$\left[\mathcal{L} + \mathrm{DIAG}\left(\overline{\rho}\;\overline{a} - \frac{\overline{\rho}}{\Delta t}\right)_{\mathrm{IJK}}\right]\overline{\mathbf{\Gamma}}^{n+1} = \frac{1}{\Delta t}\overline{\rho \mathbf{\Gamma}}^{n} - \overline{\rho}\overline{\mathbf{B}} \tag{2.73}$$

where DIAG is the diagonal matrix having the same dimensions of the Laplacian $\mathcal{L}$ and the terms $\left(\overline{\rho}\;\overline{a} - \frac{\overline{\rho}}{\Delta t}\right)_{\mathrm{IJK}}$ in the different diagonals. The term $\mathbf{B}$ is the vector of all the explicit source terms, while $\overline{\mathbf{\Gamma}}^{\mathbf{n}}$ and $\overline{\mathbf{\Gamma}}^{\mathbf{n+1}}$ include the meteorological quantity under consideration (at time n and $n+1$) for the different finite volumes. Finally, $\overline{\rho}$ is the vector including all the air densities.

DYNAMIC

This is the "non hydrostatic" step of the algorithm, in which the mass (2.1), momentum (2.9), state (2.17), and acoustic (2.23) equations are grouped together in order to compute the pressure perturbation which, in turn, affects the density and the velocity field.

At first, an explicit method is considered in order to compute and add to F_i in (2.10) the source terms generated by buoyancy (source I in (2.11)), and Coriolis (source II in (2.11)), to the advective, diffusive, and urban-rural sources. In that way, the terms F_i given by (2.10) are updated at the center of the different finite volumes Ω_{IJK}.
Then, the acoustic system (2.23) is solved with a finite volumes approach. In particular, integrating (2.23) over the mesoscale domain Ω we obtain:

$$\int_{\Omega}\left[-\frac{\partial^2}{\partial t^2}\left(\frac{P}{c^2}\right)+\frac{\partial^2 P'}{\partial x_i^2}-\frac{\partial F_i}{\partial x_i}\right]d\Omega = 0 \tag{2.74}$$

Summing (2.74) over the finite volumes Ω_{IJK} and dividing by $\mid \Omega_{IJK} \mid$ we have:

$$\frac{1}{\mid \Omega_{IJK} \mid}\int_{\Omega_{IJK}}\left[-\frac{\partial^2}{\partial t^2}\left(\frac{P}{c^2}\right)+\frac{\partial^2 P'}{\partial x_i^2}-\frac{\partial F_i}{\partial x_i}\right]d\Omega_{IJK} = 0 \ \forall \Omega_{IJK} \tag{2.75}$$

Considering the barotropic assumption (2.24) and discretising the time derivative we can write the first term of (2.75) as:

$$\frac{\partial^2}{\partial t^2}\left(\frac{P}{c^2}\right) = \frac{1}{\Delta t}\left[\frac{1}{c^2}\frac{\partial}{\partial t}P^{n+1} - \frac{1}{c^2}\frac{\partial}{\partial t}P^{n}\right] \tag{2.76}$$

where Δt is the time step.

In particular, using the equation of state (2.17) and the mass conservation (2.1) we can write $-\frac{1}{c^2}\frac{\partial}{\partial t}P^n$ as:

$$-\frac{1}{c^2}\frac{\partial}{\partial t}P^n = -\frac{\partial}{\partial t}\rho^n = \frac{\partial}{\partial x_i}(\ \rho U_i)^n \tag{2.77}$$

Replacing (2.77) in (2.76), and discretising in time we finally obtain:

$$\frac{\partial^2}{\partial t^2}\left(\frac{P}{c^2}\right) = \frac{1}{\Delta t^2 c^2}P'^{n+1} - \frac{1}{\Delta t^2 c^2}P'^{n} + \frac{\partial}{\partial x_i}(\ \rho U_i)^n \tag{2.78}$$

where we used the fact that the reference state P_0 is constant in time.

Taking (2.78) into account, and treating the second space derivative of P' in an implicit form, the acoustic system (2.75) can be written as:

$$-\frac{1}{\Delta t^2 c^2}\left[\overline{P'}\right]_{IJK}^{n+1}+\frac{1}{\mid \Omega_{IJK}\mid}\int_{\Omega_{IJK}}\frac{\partial^2 P'^{n+1}}{\partial x_i^2}d\Omega_{IJK}= \frac{1}{\Delta t}\left[\Delta t\frac{\partial \overline{F}_i}{\partial x_i}+\frac{\partial}{\partial x_i}\left(\overline{\rho U_i}\right)\right]_{IJK}^{n}-\frac{1}{\Delta t^2 c^2}\left[\overline{P'}\right]_{IJK}^{n} \tag{2.79}$$

where we used the definitions of average value (2.45).

The divergence term $\left[\frac{\partial F_i}{\partial x_i}\right]_{IJK}^n$ in (2.79) is calculated by computing the fluxes of $\mathbf{F}_{IJK}^n = (F_1, F_2, F_3)_{IJK}^n$ at the different faces α of Ω_{IJK} (for every finite volume Ω_{IJK}). The corresponding quantities F_{IJK}^α are obtained by a linear interpolation technique which is detailed in the Appendix D. Then, the divergence term is calculated with the following averaging procedure:

$$[\text{div}_F]_{IJK}^n := \left[\frac{\partial F_i}{\partial x_i}\right]_{IJK}^n = \frac{1}{\mid \Omega_{IJK}\mid}\sum_{\alpha=1}^{6} F_{IJK}^\alpha \ \forall\ \Omega_{IJK} \tag{2.80}$$

Similarly, the divergence term $\left[\frac{\partial}{\partial x_i}\left(\rho U_i\right)\right]_{IJK}^n$ in (2.79) is calculated by averaging the fluxes of (ρU_i) at the different faces. Remark in particular that for every finite volume Ω_{IJK} the flux of (ρU_i) at a face α corresponds to $\mathcal{F}_{IJK}^\alpha$ given by (2.49). Therefore, similarly to (2.80), we define for every cell (I, J, K):

$$[\text{div}_{\mathcal{F}}]_{IJK}^n := \left[\frac{\partial}{\partial x_i}\left(\rho U_i\right)\right]_{IJK}^n \tag{2.81}$$

Replacing (2.80) and (2.81) inside (2.79) we obtain:

$$-\frac{1}{\Delta t^2 c^2}\left[\overline{P'}\right]_{IJK}^{n+1}+\frac{1}{\mid \Omega_{IJK}\mid}\int_{\Omega_{IJK}}\frac{\partial^2 P'^{n+1}}{\partial x_i^2}d\Omega_{IJK}= \frac{1}{\Delta t}\left[\Delta t\overline{\text{div}_F}+\overline{\text{div}_{\mathcal{F}}}\right]_{IJK}^{n}-\frac{1}{\Delta t^2 c^2}\left[\overline{P'}\right]_{IJK}^{n} \tag{2.82}$$

Remark that $\frac{1}{|\Omega_{IJK}|}\int_{\Omega_{IJK}}\frac{\partial^2 P'^{n+1}}{\partial x_i^2}d\Omega_{IJK}$ in (2.82) is a diffusive term which is treated following the same procedure detailed in the section 2.4.2. In particular, applying (2.82) to every finite volume Ω_{IJK} we obtain a linear system similar to (2.68) for the pressure perturbation P':

$$\left[-\frac{1}{\Delta t^2 c^2}\mathbb{I}+\mathcal{L}\right]\overline{\mathbf{P}'}^{n+1}=\frac{1}{\Delta t}\overline{\text{DIV}}_{\Delta tF+\mathcal{F}}^{n}-\frac{1}{\Delta t^2 c^2}\overline{\mathbf{P}'}^{n} \tag{2.83}$$

where $\overline{\mathrm{DIV}}^{n}_{\Delta tF+\mathcal{F}}$ is the vector including the divergences at time n, while $\overline{\mathbf{P}'}^{n}$ and $\overline{\mathbf{P}'}^{n+1}$ correspond to the pressure perturbations at time n and $n+1$. As already mentioned in the section 2.4.2, this type of linear system is solved with a biconjugate gradient method (Numerical Recipes, 1986-2002).

Knowing the pressure effects P' at the time step $n+1$, the corresponding pressure gradient $-\frac{\partial P'}{\partial x_i}$ (source I in (2.9)) is computed following (2.66). Then, considering the momentum equation (2.9), the mass flows crossing the faces α of the finite volumes Ω_{IJK} at the next time step can be updated as:

$$\mathcal{F}^{\alpha}_{IJK} = \left[\mathcal{F} + \Delta tF - \frac{\partial P'}{\partial x_i} Sn_i\right]^{\alpha}_{IJK} \tag{2.84}$$

The fluxes calculated by (2.84) are finally interpolated at the center of the different finite volumes in order to compute the momentum contributions at the following time step $\left((\overline{\rho}\overline{U}_i)^{n+1}_{IJK} \;\; i = 1, \cdots, 3\right)$. The interpolation procedure from the face to the center of the different volumes is also detailed in the Appendix D.

Furthermore, starting from the pressure perturbation P' at the time step $n+1$, and using the equation of state (2.17), the air density at the following time step can by computed as:

$$\overline{\rho}^{n+1}_{IJK} = \rho_0 + \left[\frac{P'}{c^2}\right]^{n+1}_{IJK} \tag{2.85}$$

where ρ_0 is the air density at the hydrostatic reference state (cf. (2.3)).

The velocities evolutions after the "dynamic" routine can finally be obtained by dividing $\overline{\rho}\overline{U}_i$ by $\overline{\rho}$ given by (2.85).

Remark 1

Equation (2.84) indicates that a particularity of the present algorithm lies in the fact that the "history" is kept by the fluxes ($\mathcal{F}$). Remark in fact that the variables which are updated from one time step to the other are the fluxes at the faces and not the velocities and densities at the center of the cells. In fact, these meteorological quantities are interpolated at the center once the fluxes at the next time step are known.

Remark 2

The fluxes F^{α} in (2.84) have been obtained by interpolating the source vector $\mathbf{F}$ given by (2.10) from the center to the face. Then, the velocities at the next time step (used for the calculation of these sources) are also computed by interpolating the fluxes F^α, this time, from the faces to the center. Thus, from one time step to another, the total fluxes $\mathcal{F}^\alpha$ in (2.84) are always subject to two interpolations. In particular, as presented in the Appendix D, this calculation is linear and leads to a loss of information with a consequent "smoothing" of the solution from one time step to another.

2.6 Applications

The simulations presented in the previous paragraphs were focused on behaviour study of numerical schemes resolving the advection and the diffusion processes. In the present section, a set of benchmark tests is proposed in order to evaluate the performance of the whole mesoscale algorithm. As explained by Pielke (2002), there are different techniques that can be employed in order to evaluate a numerical model:

1. comparison with known analytical solutions;
2. comparison with other numerical models;
3. comparison with field observations.

Case 1., is considered when the model is subject to very small perturbations, so that linearised analytical results can be produced. In this context, the formation of *2D mountain waves* is studied (Smith, 1979, Klemp and Lilly, 1978, Thunis, 1995), and results are presented in the section 2.6.1.

In most real situations, non linearity becomes important and no analytical solutions can be considered. Thus, the comparison with other numerical models may be used. In this work, the present mesoscale model is compared to a standard non-linear problem of a cold bubble of air that subsequently descends to the ground (Straka et al., 1993). Results are presented in the section 2.6.2.

Finally, test 3 is used in order to verify if the model is capable to reproduce the behaviour of the flow for real atmospheric circulations. As an example, the Boulder windstorm is considered (Klemp and Lilly, 1978), and results are presented in the section 2.6.3.

2.6.1 The formation of 2D Mountain Waves

Mountains are relatively small compared to the Earth dimensions but they can strongly modify the atmosphere on both local and larger scales. As explained by Thunis (1995), there are two main factors explaining the impact of mountains on local climate:

- the stable stratification of the atmosphere gives a resistance to vertical displacement.

In particular, buoyancy will always try to return vertically displaced air parcels to their equilibrium level.
• the water vapor contained in the atmosphere is subject to a slight adiabatic ascent which can consequently generate saturation, leading to condensation and possible precipitations.

In general, the way with which mountains affect atmospheric circulations can depend on different factors: the dimension of the hill, the vertical stability of the atmosphere, the wind speed and magnitude.
In the present work, we apply our finite volume mesoscale model in order to study the flow generated over a 10km wide, 50m height mountain, as the one presented in Figure 2.13. For this kind of hill the Coriolis force can be neglegted, but the buoyancy contribution plays a very important role. This force will tend to bring back to the equilibrium level an air parcel lifted up after its forced mountain ascent. During the descent the parcel may acquire enough speed to come down to a lower height with respect to its equilibrium level. Buoyancy will then force the air parcel to rise back generating a vertical oscillation known as *internal gravity wave*.
This perturbation may be advected by the mean wind, but for strong stability and weak winds, perturbations propagate mainly vertically. In this case the flow is hydrostatic: perturbations are located above the mountain itself and are referred to as *Mountain waves*.

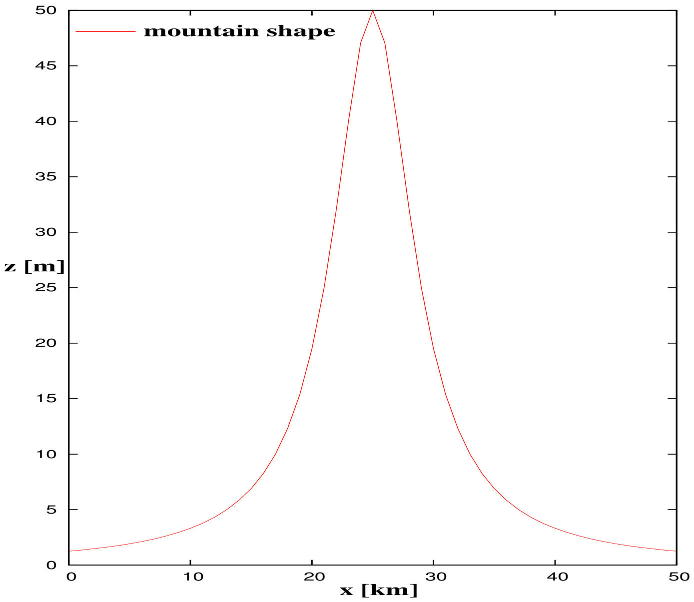

FIGURE 2.13: Representation of the 50m height, 10km wide mountain considered for the simulation.

Solutions for hydrostatic mountain waves can be analytically evaluated. This study, called linear theory, is performed by assuming two-dimensional, non-viscous, adiabatic flows. The derivation of the exact solutions will not be discussed in this work, but a complete description can be found in Smith (1979), Thunis (1995).

In general, the comparison with analytical solutions has become a standard way to evaluate a mesoscale model (Klemp and Lilly, 1978, Thunis, 1995). In the present work, the flow over the 10km wide mountain represented in Figure 2.13 is simulated by considering a domain of 51 points in the horizontal with a resolution of 2.5km. In the vertical, a stretched grid is considered with a resolution ranging from 100m at the first level, and 1000m at the top boundary, with a corresponding total height of 19200m. A strong stability of $3.5\frac{K}{m}$ is considered with a geostrophic wind of $10\frac{m}{s}$. No vertical damping filter is taken into account in order to preserve the full number of vertical levels.

As indicated in Figure 2.14, the solution after the first time step corresponds to a simmetric flow field in respect to the middle of the hill. As indicated in the Appendix E, this behaviour is in agreement with reference results that one can find in the literature (Thunis, 1995).

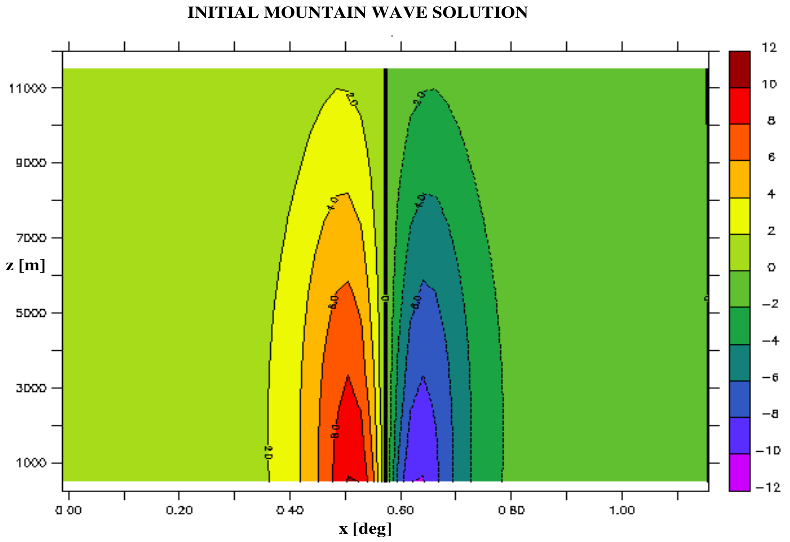

FIGURE 2.14: Initial vertical wind field in $[\frac{cm}{s}]$ for the 10km wide, 50m height mountain.

Note that if there are no buoyancy forces affecting the flow, the solution of Figure 2.14 will be stationary. Typically, this is the case for near-neutral thermal stabilities, and low and narrow hills. We also point out that the result of Figure 2.14 cannot be generated with a hydrostatic model. In particular, in that case the vertical velocity field propagates vertically up to the domain top (Thunis, 1995).

For the present simulation, the solution in Figure 2.14 is not stationary as the strong stability and the dimensions of the hill generate an important buoyancy force. As one can see in Figure 2.15, this leads to the formation of mountain waves above the hill with the typical superposition of positive and negative velocity cells (Klemp and Lilly, 1978, Smith, 1979, Thunis, 1995). The analytical solution for the same type of mountain is presented in the Appendix E for comparison. Remark that the solution presents sporious reflection from the lateral boundaries which could be eliminated with the application of a vertical damping filter (Thunis, 1995).

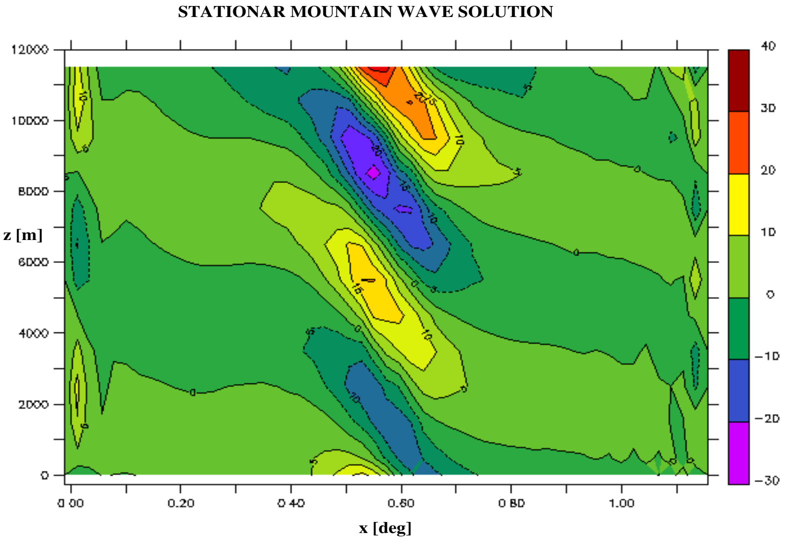

FIGURE 2.15: Stationar vertical wind field in $\left[\frac{cm}{s}\right]$ for the 10km wide, 50m height mountain.

2.6.2 The buoyant bubble test

A standard non-linear test problem for the behaviour study of a numerical model is the one designed by Straka et al. (1993). It consists in a two-dimensional problem initiated as a cold bubble of air that subsequently descends to the ground. Then, as the density current spreads out laterally at the bottom boundary, Kelvin-Helmolts shear instability rotors form along the top of the cold air boundary, with maximal wind speeds of the order of 30 $\left[\frac{m}{s}\right]$. Reference solutions for this test problem can be found in the literature (Straka et al., 1993).

The initial conditions for the simulation are a hydrostatic reference state ($P' = 0\,[\mathrm{Pa}]$)

and a potential temperature field described by the following function:

$$\theta\,(x,z) = \begin{cases} 300\;\;[K] & \text{if } L > 1 \\ 300 - 15\frac{\cos(\pi L)+1}{2}\;\;[K] & \text{if } L \leq 1 \end{cases} \tag{2.86}$$

where

$$L = \sqrt{\left(\frac{x - x_c}{x_r}\right)^2 \left(\frac{z - z_c}{z_r}\right)^2},$$

and $(x_c, z_c) = (0m, 3000m)$, $(x_r, z_r) = (4000m, 2000m)$ are respectively the coordinates of the center and the radius of the bubble.
In the horizontal direction the domain is 19.2km wide with a resolution of $200m$ (96 grid points). In the vertical, the grid has a height of 6.4km with a resolution of 200m (32 grid points). A time step of 3s has been considered.

Figures 2.16 and 2.17 show simulation result from time t=0s to t=900s. Remark that Kelvin-Helmoltz shear instabilities are well reproduced and, more in general, that the solution has a similar behaviour compared to the one presented in the literature by Straka et al., 1993 (cf. Appendix E).

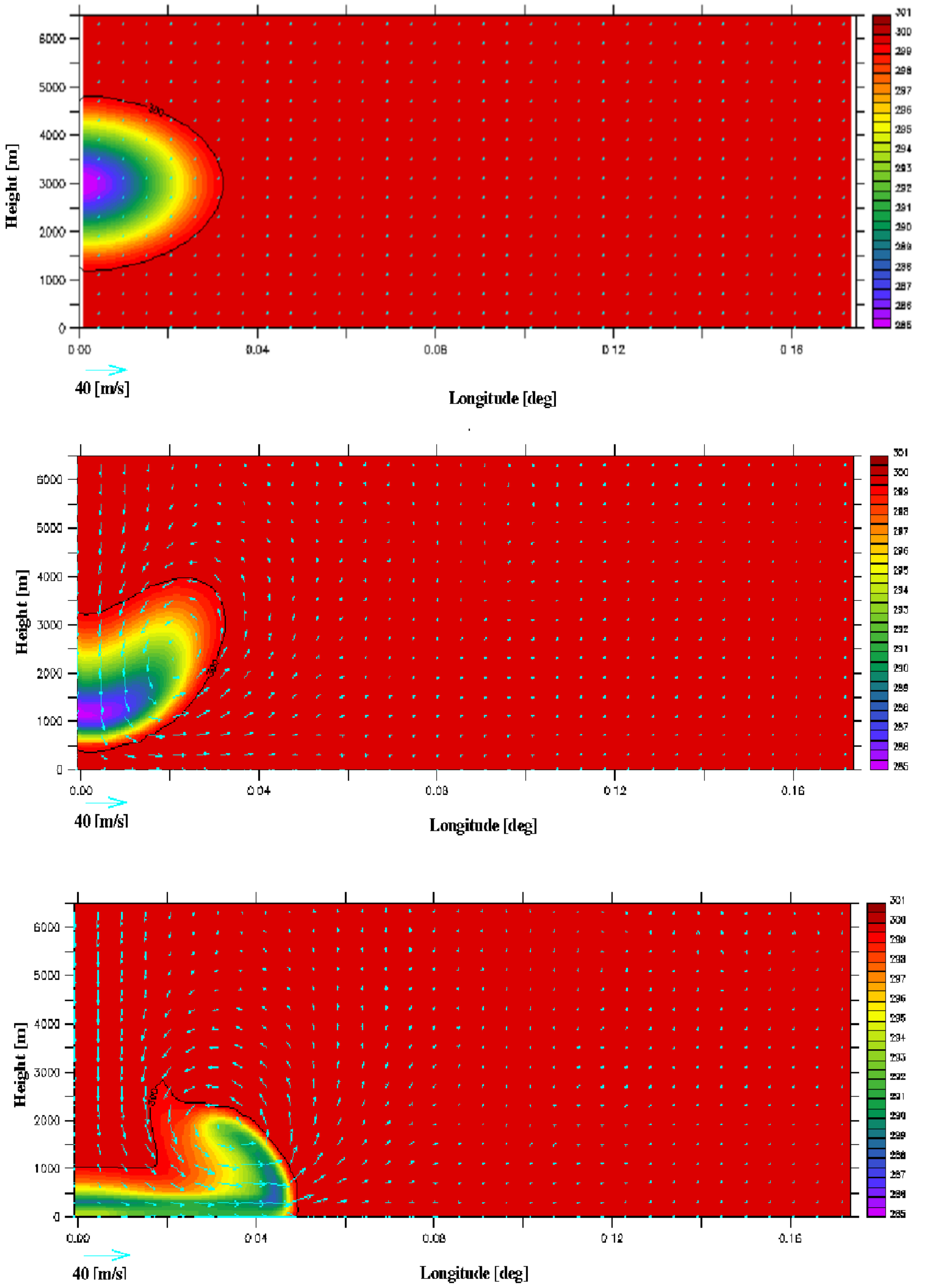

FIGURE 2.16: Evolution of the cold bubble at time $t = 0s$, $t = 180s$, $t = 360s$.

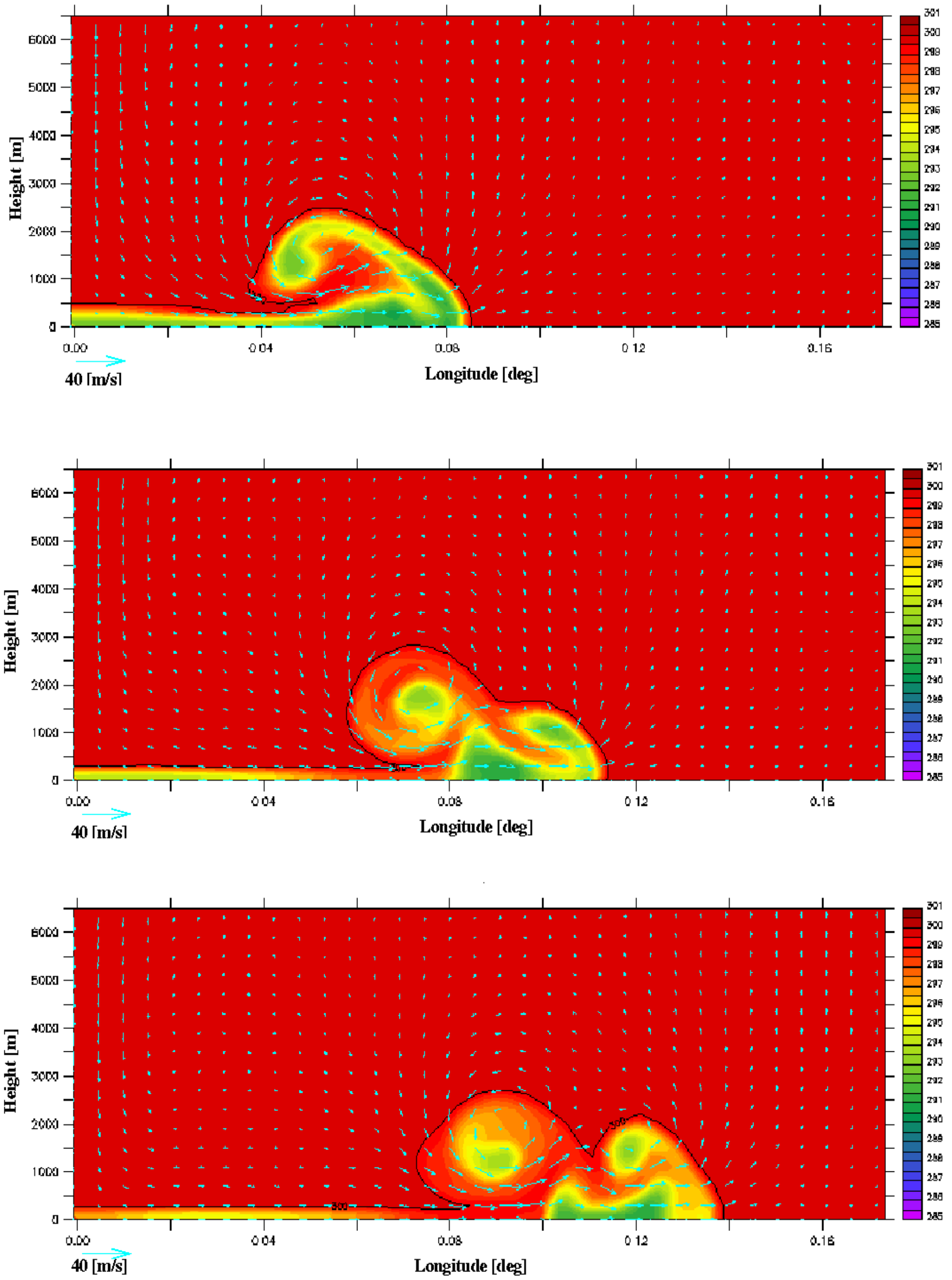

FIGURE 2.17: Evolution of the cold bubble at time $t = 540s$, $t = 720s$, $t = 900s$.

2.6.3 The Boulder windstorm

In January 1972, in Boulder (Colorado), a city located at the eastern slope of the Rocky mountains, a very important windstorm took place with observed peak gusts of $60\frac{m}{s}$. The uniqueness of this phenomenon lies in the large amount of experimental in-situ data which represented a great opportunity to compare mesoscale models with real observations (Klemp and Lilly, 1978, Thunis, 1995). For instance, a reproduction of the corresponding horizontal wind field for this Boulder episode is represented in Figure 2.18. We point out that this figure is based on observations, and is not representative of a fixed point in time (observations are not simultaneous).

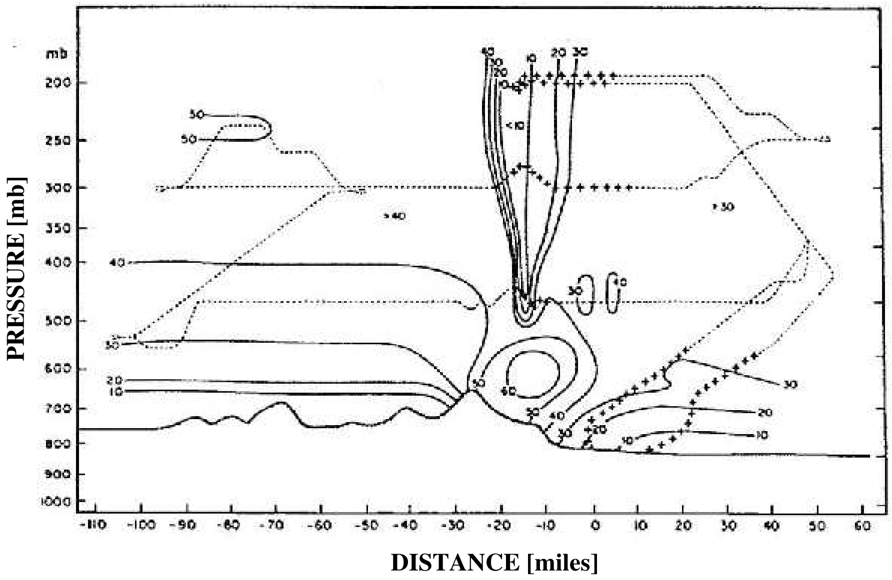

FIGURE 2.18: Cross section of horizontal wind speed $[\frac{m}{s}]$ along an east west line through Boulder, as obtained from aircraft measurements (Klemp and Lilly, 1978).

Observe that perturbations propagate both vertically and horizontally, and affect the atmosphere not only through its depth but also in the lee of the obstacle. This phical phenomenon, called *lee waves* (Atkinson, 1981), is typically observed when the flow starts to have non hydrostatic features (buoyancy is important, but not enough to suppress vertical acceleration).

In Figure 2.19 we present the numerical result for the Boulder windstorm generated by the FVM mesoscale model. The initial conditions for the simulations are taken from the work of Thunis (1995), and correspond to a simplified bell shape mountain of $2000m$ height. The vertical structure of the atmosphere is characterised by two stable layers: the first from 0 to 10km, and a second very stable layer (isothermal) above 10km.

The result in Figure 2.19 indicates that the FVM model has correctly represented the main features of the flow with the corresponding lee waves that propagate from the west to the east part of the domain. On the other hand, the peak gusts are a little overestimated with simulated values reaching more that $70\frac{m}{s}$. Also observe that, with respect to observed velocities, the simulated result leads to an additional diffusion.

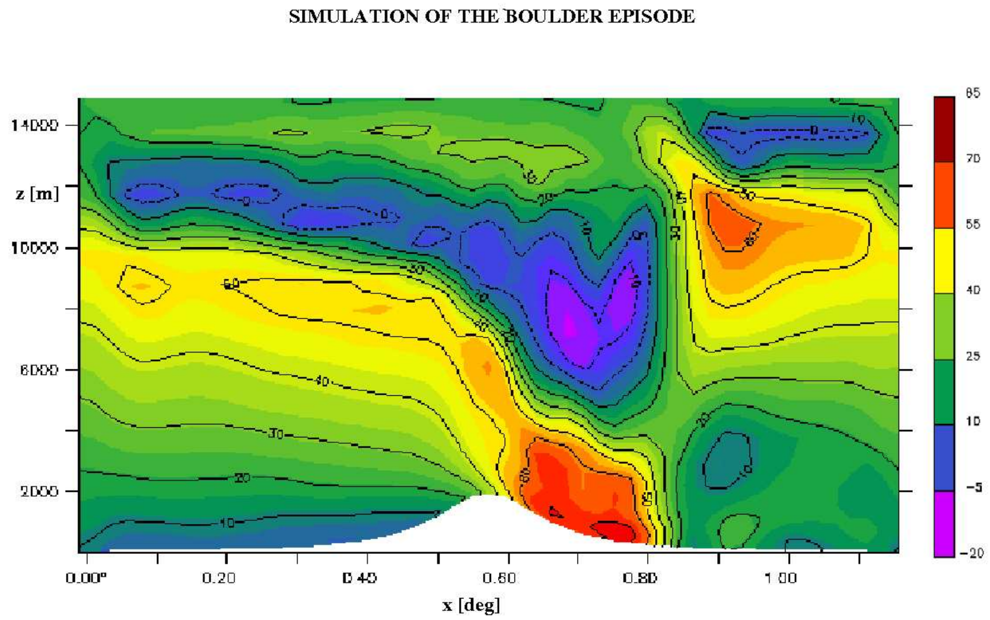

FIGURE 2.19: Countour of the west wind component $\left[\frac{m}{s}\right]$ for the Boulder case simulation.

2.7 Conclusions

The objective of this chapter was to present the finite volumes non hydrostatic mesoscale model that will be used in the following part of the thesis as part of the simulating tool for the study of urban canopy climate and Urban Heat Island processes.

Firstly, the system of partial differential equations composing the mesoscale model was introduced. It includes the basic conservation equations of mass, momentum, and energy, as well as the equation of state used to couple the air pressure and density. The turbulent transport is parametrised following the gradient transport theory, and the corresponding diffusion coefficients are computed as a function of turbulent kinetic energy.

We observed that the mesoscale system can be finally represented as a combination of advective and diffusive processes, which were treated following a finite volumes approach. In particular, the mososcale domain was divided into a finite set of control volumes characterising a structured and deformable mesh (terrain-following grid is needed in order to take topographic features into account). The corresponding resolution techniques were detailed in the second part of the chapter, and different simulations were performed in order to illustrate the properties and the effectiveness of the numerical schemes.

Then, the general algorithm resolving the mesoscale system was presented. We observed that in the numerical resolution, the mass, momentum, and state equations are combined yelding to an acoustic partial differential equation for the pressure perturbation, which is treated with an implicit method. It was pointed out that in this procedure, the "history" is kept by the fluxes at the faces which are then interpolated in order to compute the values of the corresponding meteorological variables at the centers.
More in general, in all the algorithm, the velocity fluxes and the pressure gradients are computed at the faces, while the velocity components, the potential temperature, the air humidity, the turbulent kinetic energy, and the pressure are located at the center of the different finite volumes.

The whole mesoscale algorithm was finally tested with respect to a set of benchmark tests including the comparison with analytical, numerical, and observed results. In this context, the model has shown his capability to correctly reproduce different physical processes like the formation of mountain waves, the generation of lee waves observed in the Boulder windstorm, and the production of Kelvin-Helmolts instabilities corresponding to the buoyant bubble test.

As it will be emphasized in the following of this thesis, the present mesoscale model represents a very important part of the general modelling tool considered for the study of urban climate. In fact, when coupled with an urban canopy parameterisation, it will allow to take the different interactions and feedbacks between meso, and the urban scale processes into account.

Appendix A: Surfaces, normal vectors, and volumes calculation

Consider a typical finite volume Ω_{IJK} as the one presented in the Figure 2.2.

Surface and normal calculation

Consider as an example the face (i, J, K) (for the other faces a similar calculation is performed). Let $\mathbf{v_{16}}$ and $\mathbf{v_{25}}$ be the vectors connecting the corresponding nodes of that face. The normal vector $\mathbf{n}_{iJK}$ is then given by:

$$\mathbf{n}_{iJK} = \frac{1}{2} \frac{\mathbf{v}_{16} \times \mathbf{v}_{25}}{\| \mathbf{v}_{16} \times \mathbf{v}_{25} \|_2} \tag{2.87}$$

where "×" defines the cross product and $\| \, . \, \|_2$ the euclidean norm.

Similarly, the surface S_{iJK} is computed by:

$$S_{iJK} = \frac{1}{2} \| \mathbf{v}_{16} \times \mathbf{v}_{25} \|_2 \tag{2.88}$$

Volume calculation

The volume calculation is performed by using the fact that the cell Ω_{IJK} is given by the sum of the following six pyramides (the numbers refer to the corresponding nodes of the Figure 2.2):

- $\{4,6,7,8\}$; $\{4,5,6,8\}$; $\{3,4,6,7\}$; $\{1,4,5,6\}$; $\{1,2,4,6\}$; $\{2,3,4,6\}$.

The volume ($\mathcal{V}$) of the different pyramides is then easily computed with a box product operation. For example, for the pyramide $\{4,6,7,8\}$ this is given by:

$$\mathcal{V}_{\{4,6,7,8\}} = \frac{1}{6} \| \left(\mathbf{v_{84}} \times \mathbf{v_{86}} \right) . \mathbf{v_{87}} \|_2 \tag{2.89}$$

Appendix B: Computation of the polynomial coefficients for the fifth-order Crowley method

Consider $\tilde{r}_{IJK}$ given by (2.55) with M equal to 5. Following the formulation of Bott (1989), one can first observe that:

$$\int_{-\frac{1}{2}}^{\frac{1}{2}} \tilde{r}(x) dx = \overline{r}^n_{IJK} \tag{2.90}$$

Furthemore, integrating (2.55) from $-\frac{1}{2}$ to $\frac{1}{2}$ and deriving it five times we obtain:

$$a_5 = \frac{1}{120}\frac{\partial^5}{\partial x^5}\left(\overline{r}^n_{IJK}\right) \tag{2.91}$$

Similarly, deriving with respect to the lower orders the following coefficients are obtained:

$$\begin{aligned} a_4 = \frac{1}{24}\frac{\partial^4}{\partial x^4}\left(\overline{r}^n_{IJK}\right); \quad a_3 = \frac{1}{6}\left[\frac{\partial^3}{\partial x^3}\left(\overline{r}\right)^n_{IJK} - 5a_5\right] \\ a_2 = \frac{1}{2}\left[\frac{\partial^2}{\partial x^2}\left(\overline{r}\right)^n_{IJK} - a_4\right]; \quad a_1 = \frac{\partial}{\partial x}\left(\overline{r}\right)^n_{IJK} - \frac{a_3}{4} - \frac{a_5}{16} \\ a_0 = \overline{r}^n_{IJK} - \frac{a_2}{12} - \frac{1}{80}a_4 \end{aligned} \tag{2.92}$$

The different derivatives in (2.91) and (2.92) are approximated by a central difference scheme.

Appendix C: Calculation of the ponderation coefficients for the approximation of the gradient at the face

In the following we will focus on the face $(i+1, J, K)$. All the gradients at the other faces are computed with a similar method.

As one can see in Figure 2.20, we first define Ω_{i+1JK} as the finite volume centered in the face $(i+1, J, K)$. In particular, the magnitude of Ω_{i+1JK} is computed by a simple average of the values of the neighbouring volumes:

$$\mid \Omega_{i+1JK} \mid = \frac{\mid \Omega_{IJK} \mid + \mid \Omega_{I+1JK} \mid}{2} \tag{2.93}$$

Starting from Ω_{i+1JK}, we also define $\mathcal{S}_{i+1JK} = \{S_{up}, S_{do}, S_{le}, S_{ri}, S_{bot}, S_{top}\}$ as the set of the corresponding surfaces (cf. Figure 2.20 for the different notations).

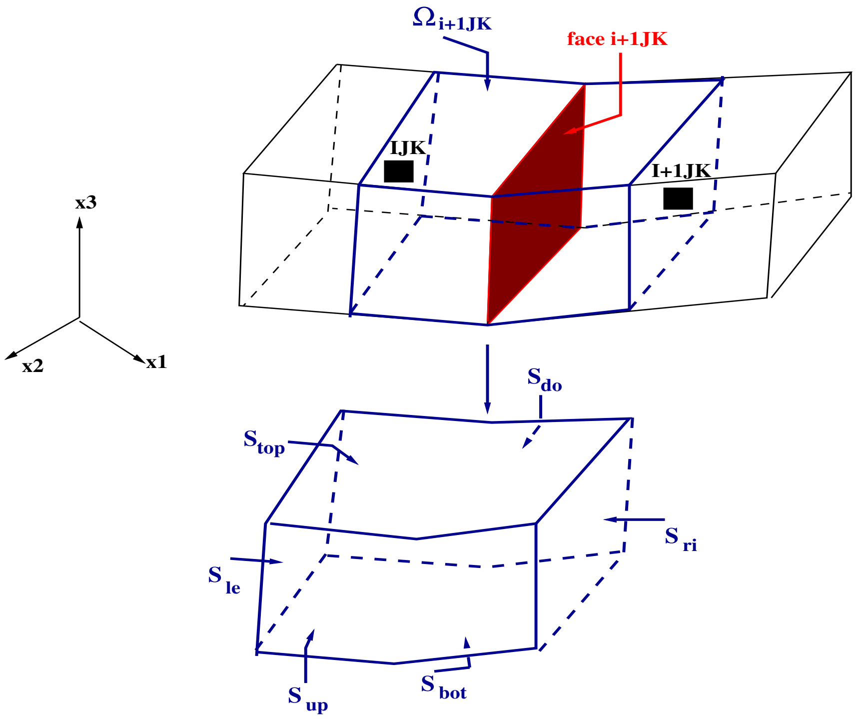

Figure 2.20: Representation of the domain Ω_{i+1JK} with the corresponding set of surfaces $\mathcal{S}_{i+1JK} = \{S_{up}, S_{do}, S_{le}, S_{ri}, S_{bot}, S_{top}\}$

Starting from these assumptions, the gradient of q at the face $(i+1, J, K)$ is computed as:

$$\left[\frac{\partial q}{\partial x_j}\right]_{i+1JK} = \frac{1}{\mid \Omega_{i+1JK} \mid} \int_{\mathcal{S}_{i+1JK}} q n_j dS \quad j = 1, \cdots, 3 \tag{2.94}$$

The integral in (2.94) is computed with a summation over the different faces of Ω_{i+1JK}. In particular, following the notations of Figure 2.20 this can be written as:

$$\begin{aligned} \int_{\mathcal{S}_{i+1JK}} q n_j dS = & \underbrace{q_{ri}\left(S n_j\right)_{ri} - q_{le}\left(S n_j\right)_{le}}_{\mathbf{A}} + \\ & \underbrace{q_{up}\left(S n_j\right)_{up} - q_{do}\left(S n_j\right)_{do}}_{\mathbf{B}} + \\ & \underbrace{q_{top}\left(S n_j\right)_{top} - q_{bot}\left(S n_j\right)_{bot}}_{\mathbf{C}} \end{aligned} \tag{2.95}$$

Remark

When the mesh is not deformed (flat terrain), the normal vectors at the different faces α have the same orientation as the axis of the cartesian reference frame. Thus, the contribution of the gradient of q at the face $(i+1, J, K)$ in the Laplacian matrix (cf. (2.67), (2.68)) will only be that of the term A in (2.95). In that case the Laplacian matrix has a tridiagonal form along the three main directions.

A : Computation of the left and right terms

Following Figure 2.20, first remark that $q_{ri} := \overline{q}_{I+1JK}$ and $q_{le} := \overline{q}_{IJK}$. The left and right surfaces are calculated by averaging the values at the neighbouring faces:

$$\begin{aligned} (Sn_j)_{ri} &= \frac{(Sn_j)_{i+1JK} + (Sn_j)_{i+2JK}}{2} \\ (Sn_j)_{le} &= \frac{(Sn_j)_{iJK} + (Sn_j)_{i+1JK}}{2} \end{aligned} \tag{2.96}$$

Therefore, the term $\mathbf{A}$ in (2.95) can be written as:

$$\mathbf{A} = \frac{1}{2}\overline{q}_{I+1JK}\left[(Sn_j)_{i+1JK} + (Sn_j)_{i+2JK}\right] - \frac{1}{2}\overline{q}_{IJK}\left[(Sn_j)_{iJK} + (Sn_j)_{i+1JK}\right] \tag{2.97}$$

In particular defining,

$$\begin{aligned} \left[\psi_j^{\mathbf{A}}\right]_{IJK} &= -\left[(Sn_j)_{iJK} + (Sn_j)_{i+1JK}\right]; \\ \left[\psi_j^{\mathbf{A}}\right]_{I+1JK} &= (Sn_j)_{i+1JK} + (Sn_j)_{i+2JK} \end{aligned} \tag{2.98}$$

the expression (2.97) can be finally written as:

$$\mathbf{A} = \frac{\left[\psi_j^{\mathbf{A}}\overline{q}\right]_{IJK} + \left[\psi_j^{\mathbf{A}}\overline{q}\right]_{I+1JK}}{2} \tag{2.99}$$

B : Computation of the up and down terms

The components in the upward direction are first computed by averaging the values of q over the finite volumes enclosing the surface S_{up}: Ω_{IJK}, Ω_{I+1JK}, Ω_{IJ+1K}, $\Omega_{I+1J+1K}$ (cf. Figure 2.20). In particular, the following expression is considered:

$$\begin{aligned} q_{up}\left(Sn_j\right)_{up} = \frac{1}{2}\left[\varepsilon^{Ij+1K}\overline{q}_{IJK} + \left(1-\varepsilon^{Ij+1K}\right)\overline{q}_{IJ+1K}\right]\left(Sn_j\right)_{Ij+1K} + \\ \frac{1}{2}\left[\varepsilon^{I+1j+1K}\overline{q}_{I+1JK} + \left(1-\varepsilon^{I+1j+1K}\right)\overline{q}_{I+1J+1K}\right]\left(Sn_j\right)_{I+1j+1K} \end{aligned} \tag{2.100}$$

The ponderation coefficients ε are calculated by averaging over the magnitude of the different volumes:

$$\varepsilon^{Ij+1K} = \frac{\mid \Omega_{IJK} \mid}{\mid \Omega_{IJK} \mid + \mid \Omega_{IJ+1K} \mid}; \; \varepsilon^{I+1j+1K} = \frac{\mid \Omega_{I+1JK} \mid}{\mid \Omega_{I+1JK} \mid + \mid \Omega_{I+1J+1K} \mid} \tag{2.101}$$

In a similar way, the component in the downward direction is computed by:

$$\begin{aligned} q_{do}\left(Sn_j\right)_{do} = \frac{1}{2}\left[\varepsilon^{IjK}\overline{q}_{IJ-1K} + \left(1-\varepsilon^{IjK}\right)\overline{q}_{IJK}\right]\left(Sn_j\right)_{IjK} + \\ \frac{1}{2}\left[\varepsilon^{I+1jK}\overline{q}_{I+1J-1K} + \left(1-\varepsilon^{I+1jK}\right)\overline{q}_{I+1JK}\right]\left(Sn_j\right)_{I+1jK} \end{aligned} \tag{2.102}$$

where:

$$\varepsilon^{IjK} = \frac{\mid \Omega_{IJ-1K} \mid}{\mid \Omega_{IJ-1K} \mid + \mid \Omega_{IJK} \mid};\ \varepsilon^{I+1jK} = \frac{\mid \Omega_{I+1J-1K} \mid}{\mid \Omega_{I+1J-1K} \mid + \mid \Omega_{I+1JK} \mid}. \tag{2.103}$$

Taking (2.100) and (2.102) into account, the term **B** can be finally written as:

$$\mathbf{B} = \frac{\left[\psi_j^{\mathbf{B}}\overline{q}\right]_{IJK} + \left[\psi_j^{\mathbf{B}}\overline{q}\right]_{I+1JK} + \left[\psi_j^{\mathbf{B}}\overline{q}\right]_{IJ+1K} + \left[\psi_j^{\mathbf{B}}\overline{q}\right]_{I+1J+1K} + \left[\psi_j^{\mathbf{B}}\overline{q}\right]_{IJ-1K} + \left[\psi_j^{\mathbf{B}}\overline{q}\right]_{I+1J-1K}}{2} \tag{2.104}$$

where the different $\psi^{\mathbf{B}}$ coefficients are given by:

$$\begin{aligned} \left[\psi_j^{\mathbf{B}}\right]_{IJK} &= \varepsilon^{Ij+1K}\left(Sn_j\right)_{Ij+1K} - \left(1-\varepsilon^{IjK}\right)\left(Sn_j\right)_{IjK} \\ \left[\psi_j^{\mathbf{B}}\right]_{I+1JK} &= \varepsilon^{I+1j+1K}\left(Sn_j\right)_{I+1j+1K} - \left(1-\varepsilon^{I+1jK}\right)\left(Sn_j\right)_{I+1jK} \\ \left[\psi_j^{\mathbf{B}}\right]_{IJ+1K} &= \left(1-\varepsilon^{Ij+1K}\right)\left(Sn_j\right)_{Ij+1K} \\ \left[\psi_j^{\mathbf{B}}\right]_{I+1J+1K} &= \left(1-\varepsilon^{I+1j+1K}\right)\left(Sn_j\right)_{I+1j+1K} \\ \left[\psi_j^{\mathbf{B}}\right]_{IJ-1K} &= \varepsilon^{IjK}\left(Sn_j\right)_{IjK} \\ \left[\psi_j^{\mathbf{B}}\right]_{I+1J-1K} &= \varepsilon^{I+1jK}\left(Sn_j\right)_{I+1jK}\,. \end{aligned} \tag{2.105}$$

C : Computation of the top and bottom terms

This calculation is performed similarly to the previous one. For example, the volumes enclosing the surface S_{top} are: Ω_{IJK}, Ω_{IJK+1}, Ω_{I+1JK}, $\Omega_{I+1JK+1}$. Therefore, the following expression is considered for $q_{top}\left(Sn_j\right)_{top}$:

$$\begin{aligned} q_{top}\left(Sn_j\right)_{top} = \frac{1}{2}\left[\varepsilon^{IJk+1}\overline{q}_{IJK} + \left(1-\varepsilon^{IJk+1}\right)\overline{q}_{IJK+1}\right]\left(Sn_j\right)_{IJk+1} + \\ \frac{1}{2}\left[\varepsilon^{I+1Jk+1}\overline{q}_{I+1JK} + \left(1-\varepsilon^{I+1Jk+1}\right)\overline{q}_{I+1JK+1}\right]\left(Sn_j\right)_{I+1Jk+1} \end{aligned} \tag{2.106}$$

where:

$$\varepsilon^{IJk+1} = \frac{\mid \Omega_{IJK} \mid}{\mid \Omega_{IJK} \mid + \mid \Omega_{IJK+1} \mid};\ \varepsilon^{I+1Jk+1} = \frac{\mid \Omega_{I+1JK} \mid}{\mid \Omega_{I+1JK} \mid + \mid \Omega_{I+1JK+1} \mid}. \tag{2.107}$$

In a similar way the term in the bottom direction is computed by:

$$\begin{aligned} q_{bot}\left(Sn_j\right)_{bot} = \frac{1}{2}\left[\varepsilon^{IJk}\overline{q}_{IJK-1} + \left(1-\varepsilon^{IJk}\right)\overline{q}_{IJK}\right]\left(Sn_j\right)_{IJk} + \\ \frac{1}{2}\left[\varepsilon^{I+1Jk}\overline{q}_{I+1JK-1} + \left(1-\varepsilon^{I+1Jk}\right)\overline{q}_{I+1JK}\right]\left(Sn_j\right)_{I+1Jk} \end{aligned} \tag{2.108}$$

where:

$$\varepsilon^{IJk} = \frac{\mid \Omega_{IJK-1} \mid}{\mid \Omega_{IJK-1} \mid + \mid \Omega_{IJK} \mid};\ \varepsilon^{I+1Jk} = \frac{\mid \Omega_{I+1JK-1} \mid}{\mid \Omega_{I+1JK-1} \mid + \mid \Omega_{I+1JK} \mid}. \tag{2.109}$$

Taking (2.106) and (2.108) into account, the term **C** can be finally written as:

$$\mathbf{C} = \frac{\left[\psi_j^{\mathbf{C}}\overline{q}\right]_{IJK} + \left[\psi_j^{\mathbf{C}}\overline{q}\right]_{I+1JK} + \left[\psi_j^{\mathbf{C}}\overline{q}\right]_{IJK+1} + \left[\psi_j^{\mathbf{C}}\overline{q}\right]_{I+1JK+1} + \left[\psi_j^{\mathbf{C}}\overline{q}\right]_{IJK-1} + \left[\psi_j^{\mathbf{C}}\overline{q}\right]_{I+1JK-1}}{2} \tag{2.110}$$

where the different $\psi^{\mathbf{C}}$ coefficients are given by:

$$\begin{aligned} \left[\psi_j^{\mathbf{C}}\right]_{IJK} &= \varepsilon^{IJk+1}\left(Sn_j\right)_{IJk+1} - \left(1-\varepsilon^{IJk}\right)\left(Sn_j\right)_{IJk} \\ \left[\psi_j^{\mathbf{C}}\right]_{I+1JK} &= \varepsilon^{I+1Jk+1}\left(Sn_j\right)_{I+1Jk+1} - \left(1-\varepsilon^{I+1Jk}\right)\left(Sn_j\right)_{I+1Jk} \\ \left[\psi_j^{\mathbf{C}}\right]_{IJK+1} &= \left(1-\varepsilon^{IJk+1}\right)\left(Sn_j\right)_{IJk+1} \\ \left[\psi_j^{\mathbf{C}}\right]_{I+1JK+1} &= \left(1-\varepsilon^{I+1Jk+1}\right)\left(Sn_j\right)_{I+1Jk+1} \\ \left[\psi_j^{\mathbf{C}}\right]_{IJK-1} &= \varepsilon^{IJk}\left(Sn_j\right)_{IJk} \\ \left[\psi_j^{\mathbf{C}}\right]_{I+1JK-1} &= \varepsilon^{I+1Jk}\left(Sn_j\right)_{I+1Jk}. \end{aligned} \tag{2.111}$$

Introducing the expressions for **A** (2.99), **B** (2.104), and **C** (2.110) inside the integral (2.95), and using the definition of $\mid \Omega_{i+1JK} \mid$ (cf. (2.93)) we finally obtain the following expression for the gradient of q:

$$\begin{aligned} \left[\frac{\partial q}{\partial x_j}\right]_{i+1JK} = \frac{1}{\mid \Omega_{IJK} \mid + \mid \Omega_{I+1JK} \mid}\{ \left[\left(\psi_j^{\mathbf{A}} + \psi_j^{\mathbf{B}} + \psi_j^{\mathbf{C}}\right)\overline{q}\right]_{IJK} + \left[\left(\psi_j^{\mathbf{A}} + \psi_j^{\mathbf{B}} + \psi_j^{\mathbf{C}}\right)\overline{q}\right]_{I+1JK} + \\ \left[\psi_j^{\mathbf{B}}\overline{q}\right]_{IJ+1K} + \left[\psi_j^{\mathbf{B}}\overline{q}\right]_{I+1J+1K} + \left[\psi_j^{\mathbf{B}}\overline{q}\right]_{IJ-1K} + \left[\psi_j^{\mathbf{B}}\overline{q}\right]_{I+1J-1K} + \\ \left[\psi_j^{\mathbf{C}}\overline{q}\right]_{IJK+1} + \left[\psi_j^{\mathbf{C}}\overline{q}\right]_{I+1JK+1} + \left[\psi_j^{\mathbf{C}}\overline{q}\right]_{IJK-1} + \left[\psi_j^{\mathbf{C}}\overline{q}\right]_{I+1JK-1} \} \end{aligned} \tag{2.112}$$

Defining the coefficients ξ at the different finite volumes as:

$$\begin{aligned}
\xi^j_{IJK} &= \frac{\left[\psi^{\mathbf{A}}_j + \psi^{\mathbf{B}}_j + \psi^{\mathbf{C}}_j\right]_{IJK}}{\mid \Omega_{IJK} \mid + \mid \Omega_{I+1JK} \mid};\ \xi^j_{IJK} = \frac{\left[\psi^{\mathbf{A}}_j + \psi^{\mathbf{B}}_j + \psi^{\mathbf{C}}_j\right]_{I+1JK}}{\mid \Omega_{IJK} \mid + \mid \Omega_{I+1JK} \mid} \\
\xi^j_{\lambda A} &= \frac{\left[\psi^{\mathbf{B}}_j\right]_{\lambda A}}{\mid \Omega_{IJK} \mid + \mid \Omega_{I+1JK} \mid};\ \xi^j_{\lambda B} = \frac{\left[\psi^{\mathbf{C}}_j\right]_{\lambda B}}{\mid \Omega_{IJK} \mid + \mid \Omega_{I+1JK} \mid} \qquad (2.113)
\end{aligned}$$

with $\lambda A = (I, J+1, K)$, $(I+1, J+1, K)$, $(I, J-1, K)$, $(I+1, J-1, K)$ and $\lambda B = (I, J, K+1)$, $(I+1, J, K+1)$, $(I, J, K-1)$, $(I+1, J, K-1)$, we can write (2.112) as:

$$\left[\frac{\partial q}{\partial x_j}\right]_{i+1JK} = \sum_{\beta=1}^{10} \xi^j_\beta \overline{q}_\beta \qquad (2.114)$$

with the domain of dependence being the one illustrated in the Figure 2.10.

Appendix D: Interpolations face to center and center to face

A : Center to Face

Let $\mathbf{\Gamma}$ be a given vector, and $\overline{\mathbf{\Gamma}}_{IJK} = \left(\overline{\Gamma}_1, \overline{\Gamma}_2, \overline{\Gamma}_3\right)_{IJK}$ the corresponding average over the finite volume Ω_{IJK} (cf. (2.45)). Consider for example the face $(i+1, J, K)$ of the Figure 2.2 (the other faces are treated in a similar way).

Knowing the surface S_{i+1JK} and the normal unit vector $\mathbf{n}_{i+1JK}$ at that face, the corresponding interpolated flux of $\mathbf{\Gamma}$ $\left([\mathcal{F}_{\mathbf{\Gamma}}]_{i+1JK}\right)$ is computed as:

$$[\mathcal{F}_{\mathbf{\Gamma}}]_{i+1JK} = \left(\tilde{\mathbf{\Gamma}} \cdot S\mathbf{n}\right)_{i+1JK} \qquad (2.115)$$

where " $\cdot$ " denotes the dot product, and the vector $\tilde{\mathbf{\Gamma}}_{i+1JK}$ is computed as:

$$\begin{aligned}
\left[\tilde{\Gamma}_1\right]_{i+1JK} &= \frac{1}{\mid \Omega_{IJK} \mid + \mid \Omega_{I+1JK} \mid} \left[\mid \Omega_{IJK} \mid \left[\overline{\Gamma_1}\right]_{IJK} + \mid \Omega_{I+1JK} \mid \left[\overline{\Gamma_1}\right]_{I+1JK}\right] \\
\left[\tilde{\Gamma}_2\right]_{i+1JK} &= \frac{1}{\mid \Omega_{IJK} \mid + \mid \Omega_{I+1JK} \mid} \left[\mid \Omega_{IJK} \mid \left[\overline{\Gamma_2}\right]_{IJK} + \mid \Omega_{I+1JK} \mid \left[\overline{\Gamma_2}\right]_{IJ+1K}\right] \\
\left[\tilde{\Gamma}_3\right]_{i+1JK} &= \frac{1}{\mid \Omega_{IJK} \mid + \mid \Omega_{I+1JK} \mid} \left[\mid \Omega_{IJK} \mid \left[\overline{\Gamma_3}\right]_{IJK} + \mid \Omega_{I+1JK} \mid \left[\overline{\Gamma_3}\right]_{IJK+1}\right] \qquad (2.116)
\end{aligned}$$

Remark that (2.116) is a simple volume average of the values of $\overline{\mathbf{\Gamma}}$ at the neighbouring cells along the x direction.

B : Face to Center

Let $\overline{\mathbf{\Gamma}}_{IJK} = \left(\overline{\Gamma}_1, \overline{\Gamma}_2, \overline{\Gamma}_3\right)_{IJK}$ be the average value of a given vector to be computed st the center (I, J, K) (cf. Figure 2.2). Starting from the values of the corresponding fluxes at the neighbouring cells, the following 3×3 system is considered:

$$\left\{ \begin{array}{lcl} \frac{1}{2}\left[(S\mathbf{n})_{iJK} + (S\mathbf{n})_{i+1JK}\right] \cdot \overline{\mathbf{\Gamma}}_{IJK} & = & \frac{1}{2}\left[[\mathcal{F}_{\mathbf{\Gamma}}]_{iJK} + [\mathcal{F}_{\mathbf{\Gamma}}]_{i+1JK}\right] \\ \frac{1}{2}\left[(S\mathbf{n})_{IjK} + (S\mathbf{n})_{Ij+1K}\right] \cdot \overline{\mathbf{\Gamma}}_{IJK} & = & \frac{1}{2}\left[[\mathcal{F}_{\mathbf{\Gamma}}]_{IjK} + [\mathcal{F}_{\mathbf{\Gamma}}]_{Ij+1K}\right] \\ \frac{1}{2}\left[(S\mathbf{n})_{IJk} + (S\mathbf{n})_{IJk+1}\right] \cdot \overline{\mathbf{\Gamma}}_{IJK} & = & \frac{1}{2}\left[[\mathcal{F}_{\mathbf{\Gamma}}]_{IJk} + [\mathcal{F}_{\mathbf{\Gamma}}]_{IJk+1}\right] \end{array} \right. \tag{2.117}$$

where $[\mathcal{F}_{\mathbf{\Gamma}}]_\alpha$ correspond to the flux of $\mathbf{\Gamma}$ through the face α.

Remark that (2.117) states that the values at the center are computed as a mean of the corresponding fluxes at the faces. For every finite volume (I, J, K), $\overline{\mathbf{\Gamma}}_{IJK}$ is therefore determined by solving the system (2.117).

Appendix E: The different solutions for model comparison

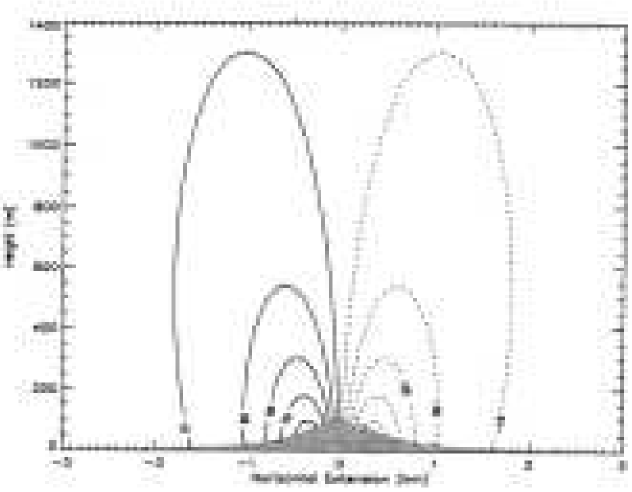

FIGURE 2.21: Analytical solution for vertical velocity field $[\frac{cm}{s}]$ and a 2km wide bell shaped hill under neutral stability conditions (Thunis, 1995).

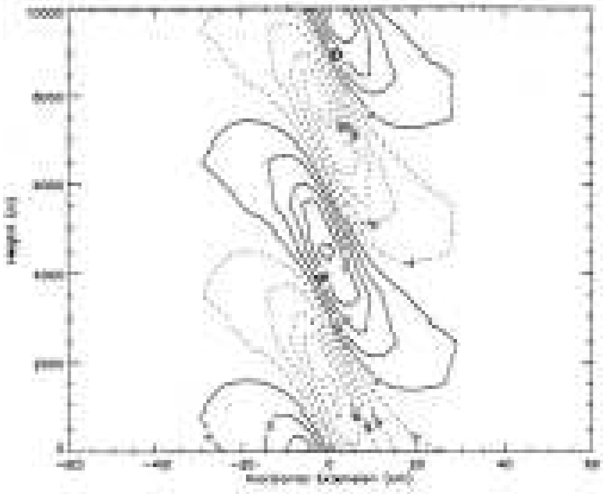

FIGURE 2.22: Analytical solution for vertical velocity field $[\frac{cm}{s}]$ and a 10km wide bell shaped hill under strong stability conditions of $3.5\frac{K}{m}$ (Thunis, 1995).

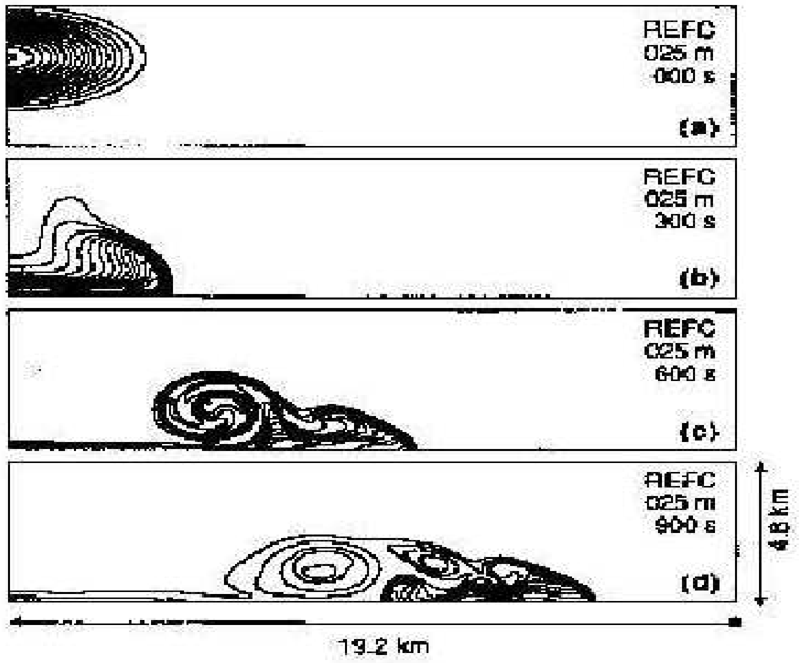

FIGURE 2.23: Compressible reference solution for the buoyant bubble test for the 25m resolution (Straka et al., 1993). Plots indicate θ' at 0, 300, 600 and 900s. Contour interval is $1°C$ and the contours are centered around $0°C$.

Bibliography

[1] Atkinson, B.W.: 1981, 'Meso-scale atmospheric circulations', *Academic Press*, London, 495pp.

[2] Bott, A.: 1989, 'A positive definite advection scheme obtained by non-linear renormalization of the advection fluxes', *Mon. Wea. Rev.*, **118**, 586-612.

[3] Bott, A.: 1992, 'Monotone flux limitation in the area-preserving flux-form advection algorithm', *Mon. Wea. Rev.*, **120**, 2592-2602.

[4] Bougeault, P. and Sadourny, R.: 2001, 'Dynamique de l'atmosphère et de l'océan', *Édition de l'École polytechnique*, Paris, 309pp.

[5] Bougeault, P. and Lacarre, P.: 1989, 'Parameterisation of Orography-Induced Turbulence in a Mesobeta-Scale Model ', *Mon. Wea. Rev.*, **117**, 1872-1890.

[6] Chung, T.J.: 2002, 'Computational Fluid Dynamics', *Cambridge Ucademic Press*, New York, 1012pp.

[4] Clappier, A., Perrochet, P., Martilli, A., Muller, F., Krueger, B.C.: 1996, 'A new non-hydrostatic mesoscale model using a CVFE (control volume finite element) Discretisation technique', in *Proceedings of EUROTRAC Symposium '96.*, Editors: P.M. Borrell et al., Computational Mechanics Publications, Southampton, 527-531, 1996.

[8] Clappier, A.: 1998, 'A correction method for use in multidimensional time-splitting advection algorithms: Application to two and three dimensional transport', *Mon. Wea. Rev.*, **126**, 232-242.

[9] Crowley, W.P.: 1968, 'Numerical advection experiments', *Mon. Wea. Rev.*, **96**, 1-11.

[7] Grell, G.A., Duhia, J. and Stauffer, D.R.: 1994, 'A description of the 5^{th} generation of the Penn State/NCAR mesoscale model', *NCAR Technical Note*, TN 398+STR.

[11] Harten, A.: 1983, 'High resolution schemes for hyperbolic conservation laws', *J. Comput. Phys.*, **49**, 357-393.

[12] Hundsdorfer, W., Koren, M., van Loon and Verwer, J.G.: 1995, 'A positive finite-difference advection scheme', *J. Comput. Phys.*, **117**, 35-46.

[13] Jacobson, M.Z.: 1999, 'Fundamentals of Atmospheric Modeling', *Cambridge University Press*, Washington.

[14] Klemp, J.B., Lilly, D.K.: 1978, 'Numerical simulations of hydrostatic mountain waves', *J. Atmos. Sci.*, **35**, 78-107.

[15] Leonard, B.P.: 1979, 'A stable and accurate convective modeling procedure based on quadratic upstream interpolation.', *Comput. Methods Appl. Mech. Eng.*, **19**, 59-98.

[16] Leveque, R.J.: 2002, 'Finite Volume Methods for Hyperbolic Problems', *Cambridge University Press*, Washington.

[17] Louis, J.F.: 1979, 'A parametric model of vertical eddies fluxes in the atmosphere', *Boundary-Layer Meteorol.*, **17**, 187-202.

[18] Marardel, S.: 2005, 'Fondamentaux de Météorologie', *Cépaduè*.

[19] Martilli, A.: 2001, 'Development of an urban turbulence parameterisation for mesoscale atmospheric models', Phd Thesis $N°$, **2445**, Swiss Federal Institute of Technology, Lausanne.

[20] Martilli, A., Clappier, A., Rotach, MW.: 2002, 'An urban surface exchange parameterization for mesoscale models', *Boundary-Layer Meteorology*, **104**, 261-304.

[21] Masson, V., Grimmond, C.S.B., Oke, T.R.: 2002, 'Evaluation of the Town Energy Balance (TEB) scheme with direct measurements from dry districts in two cities', *J. Applied Meteorol*, **41**, 1011-1026.

[22] NUMERICAL RECIPES IN FORTRAN 77: THE ART OF SCIENTIFIC COMPUTING: 1986-1992, ISBN 0-521-43064-X, Cambridge University Press.

[23] Pielke, R.A., Cotton, W.R., Walko, R.L., Tremback, C.J., Lyons, W.A., Grasso, L.D., Nicholls, M.E., Moran, M.D., Wesley, D.A., Lee, T.J., and Copeland, J.H.: 1992, 'A comprehensive mesoscale modeling system-RAMS', *Meteorology and Atmospheric Physics*, **49**, 69-91.

[24] Pielke, R.A.: 1974, 'A three dimensional numerical model of the see breeze over South Florida', *Mon. Weather Rev.*, **102**, 115-139.

[25] Pielke, R.A.: 2002, 'Mesoscale Meteorological Modeling', *Academic Press*, San Diego.

[26] Roulet, Y.-A.: 2004, 'Validation and application of an urban turbulence parameterisation for mesoscale atmospheric models', Phd Thesis $N°$, **3032**, Swiss Federal Institute of Technology, Lausanne.

[27] Sasamori, T.: 1968, 'Radiative cooling calculation for application to general circulation experiments', *J. Appl. Meteor.*, **7**, 721-729.

[28] Schayes, G.: 1982, 'Direct determination of diffusivity profiles from synoptic reports', *Atmos. Environ.*, **16**, 1407-1413.

[29] Smith, R.B.: 1979, 'The influence of mountains on the atmosphere', *Adv. Geophys.*, **21**, 87-230.

[30] Smolarkievicz, P.K.: 1984, 'A fully multidimensional positive definite advection transport algorithm with small implicit diffusion', *J. Comput. Phys.*, **54**, 325-362.

[31] SNEDDON, I.N.: 1957, 'Elements of Partial Differential Equations', New York: McGrow-Hill.

[32] STRAKA, J.M., WILHELMSON, R.B., WICKER, L.J., DROEGEMEIER, K.K.: 1993, 'Numerical Solutions of a non-linear Density Current: A Benchmark Solution and Comparisons', *Int. Jour. for Numerical Methods in Fluids*, vol. 17, pp 1-22.

[33] STULL, R.B.: 1988, 'An Introduction to Boundary Layer Meteorology', *Kluwer Academic Publisher*, Dordrecht, 670 pp.

[34] SWEBY, P.K.: 1985, 'High resolution TVD schemes using flux limiters', *Lect. Appl. Math.*, **22**, 289-309.

[35] THUBORN, J.: 1996, 'TVD Schemes, Positive Schemes, and Universal Limiter', *Monthly Weather Review*, **125**, 1990-1993.

[36] THUNIS, P.: 1995, 'Formulation and evaluation of a non-hydrostatic vorticity-mode mesoscale model', *Ph. D. Thesis*, Catholic University of Leuven, Belgium.

[37] TREMBACK, C.J., POWELL, J., COTTON, W.R., and PIELKE, R.A.: 1987, 'The forward-in-time upstream advection scheme: Extension to higher orders', *Mon. Wea. Rev.*, **115**, 540-555.

[38] YANEKO, N.A.: 1971, 'The Method of Fractional Steps', Springer-Verlag, 160 pp.

Chapter 3

Development of a Building Energy Model for mesoscale applications

Abstract

The heat generated inside buildings, and the way this heat is exchanged with the exterior can play an important role in urban climate. For example recent studies showed that anthropogenic heat from air-conditioning facilities can increase the exterior ambient temperature, and should be taken into account for a more complete Urban Heat Island (UHI) mitigation study. In this purpose the present work sets its goal as the development and the testing of a new Building Energy Model (*BEM*) to be coupled with an Urban Canopy Parameterisation (UCP) for mesoscale models.

This model takes into account: the diffusion of heat through walls, roofs and floors; the natural ventilation and the radiation exchanges between the indoor surfaces; the generation of heat from occupants and equipments; the consumption of energy from air-conditioning systems. In this work *BEM* is compared with other programs used in the thermal analysis of buildings (*CBS-MASS*, *BLAST*, *TARP*), and another box building model. Results indicate that *BEM* provides good estimations of the physical behaviour of buildings. The chapter closes by carrying out a sensitivity study of different physical parameters.

3.1 Introduction

Nowadays more than half of the global population lives in urban regions, and this proportion is forecasted to increase to three quarters during the next twenty five years. So it is not surprising that these areas have been extensively studied during the last decades. Cities are perhaps one of the most difficult regions for microclimate studies and a complete representation of all the heterogeneities would be a too complex issue. Another approach was therefore needed and induced atmospheric scientists to represent cities with simplified geometries and to parametrise the physical effects generated by urban areas. In this context the increasing computational power of computers (CPU) allowed in the last decades to create more and more sophisticated urban parameterisations, and to introduce them inside mesoscale meteorological models for the study of urban climate (Masson, 2000, Kusaka et al., 2001, Martilli et al., 2002). For example the parameterisation of Martilli et al. (2002) accounted for the impact of urban surfaces (roofs, walls, streets) on wind speed, temperature, turbulent kinetic energy, shadowing, and radiation trapping induced by urban canyons. More in general the models developed in this period allowed a better understanding of the complex interactions between buildings and the atmosphere.

However, the generation of heat in buildings and the corresponding exchanges with the exterior were not explicitly considered. In this context, one of the first works in which these features were taken into account inside a mesoscale model, was the one of Kikegawa et al. (2003, 2006). These recent studies indicated that the heat released by air-conditioning facilities can have an important impact on urban environment, and should be taken into account for a more complete study of urban canopy climate (UHI processes, etc.), as well as for the optimisation of cooling/heating energy demands.

In this contribution, a Building Energy Model (BEM) is developed in this work, to be implemented in an Urban Canopy Parameterisation (UCP) for mesoscale models. It is important to point out, that, due to CPU time costs, the implementation of a very detailed building energy program in a Mesoscale Model (MM) is not consistent with our final goal to simulate and study a whole city. Furthermore, the horizontal grid resolution of a MM ranges between hundreds of meters and few kilometers, implying that BEM cannot be applied to resolve each specific building. For this reason the model has to describe the physical properties of an ideal building which should represent those included inside the mesoscale grid cells. On the contrary, the implementation of a very simple BEM inside MM would not allow a satisfactory representation of the impact generated by buildings on urban climate, air pollution, and cooling/heating energy demands. A compromise is therefore needed.

The Building Energy Model developed in this study is similar to the one considered by Kikegawa et al. (2003). The main differences lie in the computation of solar radiation reaching the indoor walls, the treatment of anthropogenic fluxes needed for cooling/heating purposes, the possibility to consider several floors in a building, and the ability to take the presence of windows into account. In particular the present model considers:

- the diffusion of heat through walls, roofs and floors;
- the natural ventilation and the radiation exchanged between the indoor surfaces;
- the generation of heat due to occupants and equipments;
- the consumption of energy due to different types of air-conditioning systems.

In section 3.2 the physics of the building model is presented. In section 3.3 the verification procedure is carried out. In particular in the paragraphes 3.3.1 and 3.3.2, *BEM* is compared with analytical solutions and with other more sophisticated programs as *CBS-MASS* (Zmeureanu et al., 1987), *BLAST* (BLAST-3.0, 1981), and *TARP* (Walton, G.N., 1983). Finally in section 3.3.3 the total processed loads generated by BEM are compared to the ones obtained by another box building model (Kikegawa et al., 2003). In section 4 some numerical simulations are presented in order to evaluate the impact of different physical parameters. Conclusions are given in section 3.5.

3.2 The Building Energy Model (BEM)

BEM is a box-type heat budget model similar to the one developed by Kikegawa et al. (2003). Each box represents a particular floor in which the heat generated by convection, conduction, ventilation and anthropogenic activities is considered (cf. Figure 3.1). In addition two different air-conditioning systems are taken into account (cf. Figure 3.1):

- **Roof-top**

The heat generated at every floor is evacuated by a single air-conditioning system located at the roof level.

- **Vertical wall**

Air-conditioning systems are located at every floor and corresponding heat fluxes are directly ejected within the canyon.

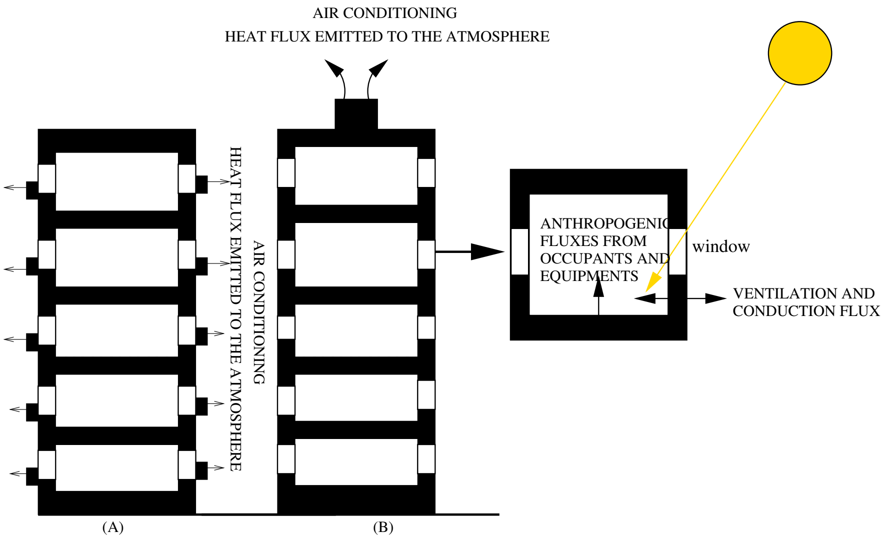

FIGURE 3.1: Representation of the two typical buildings treated by BEM. Different floors can be considered. The diffusion of heat through walls, the natural ventilation, the generation of heat from equipments and occupants are estimated for every floor, as well as the energy fluxes needed for heating and cooling. The heat flux generated by air-conditioning facilities can be emitted at every floor (vertical-wall air-conditioning (A)) or at the roof level (roof-top air-conditioning (B)).

In BEM the time evolution of the room air temperature (T_r) and the room air humidity (q_{V_r}) are computed by solving the following heat budget equations:

$$Q_B \frac{dT_r}{dt} = H_{in} - H_{out} \tag{3.1}$$

$$l\rho V_B \frac{dq_{V_r}}{dt} = E_{in} - E_{out} \tag{3.2}$$

where:

- Q_B $[\frac{J}{K}]$ and V_B $[m^3]$ are the overall heat capacity and the total volume of the indoor air.
- H_{in} $[W]$ and E_{in} $[W]$ are the sensible and the latent heat generated inside the room.
- H_{out} $[W]$ and E_{out} $[W]$ are the sensible and the latent heat that have to be ejected outside the room in order to maintain comfortables conditions.

In particular H_{in} and E_{in} are given by:

$$H_{in} = \underbrace{\sum_j A_j^{wind} h_{wind,j} \left(T_{wind,j} - T_r\right)}_{\text{A}} + \underbrace{\sum_j A_j^{wall} h_{wall,j} \left(T_{wall,j} - T_r\right) +}_{\text{B}}$$

$$\underbrace{(1-\beta)\,\rho C_p V_a \left(T_a - T_r\right)}_{\text{C}} + \underbrace{A_f q_E}_{\text{D}} + \underbrace{A_f P \varphi_P q_{hs}}_{\text{E}} \tag{3.3}$$

$$E_{in} = \underbrace{(1-\beta)\, l\rho V_a \left(q_{V_a} - q_{V_r}\right)}_{\text{C}} + \underbrace{A_f P \varphi_P q_{hl}}_{\text{E}} \tag{3.4}$$

The different terms correspond to:

- TERM A: *heat exchanged between the windows and the indoor air* (j is the index over vertical walls, A_j^{wind} is the window surface, $h_{wind,j}$ is the convective heat transfer coefficient, and $T_{wind,j}$ is the window temperature).

- TERM B: *heat exchanged between the walls, ceiling and pavement and the indoor air* (j is the index over the walls, A_j^{wall} is the wall surface, $h_{wall,j}$ is the convective heat transfer coefficient, and $T_{wall,j}$ is the indoor surface wall temperature).

- TERM C: *heat (sensible and latent) exchanged through ventilation* ($\beta \in (0, 1)$ is the control coefficient for ventilation rate, l is the latent heat of evaporation $[\frac{J}{Kg}]$, V_a $[\frac{m^3}{s}]$ is the total ventilation rate, T_a $[K]$ is the outdoor temperature, and q_{V_a} is the specific humidity of the outdoor air).

- TERM D: *sensible heat generated by equipments* (A_f $[m^2]$ is the floor area and q_E is the sensible heat gains from equipments per floor area $[\frac{W}{m^2}]$).

- TERM E: *heat (sensible and latent) generated from occupants* (P is the peak number of occupants per floor area $[\frac{person}{m^2}]$, q_{hs} and q_{hl} are the sensible and the latent heat generated from occupants $[\frac{W}{person}]$).

To compute the surface temperatures of walls, roofs and floors, a heat diffusion equation is solved in several layers inside the material and an energy budged is computed for every surface. Details of these calculations are presented in the following section.

3.2.1 Computation of walls, roofs, and floors temperatures

Each material (wall, roof, floor) is divided into n different layers. In order to compute the surfaces temperatures the following heat diffusion equation is solved:

$$\frac{\partial T_{mat}}{\partial t} = \frac{\partial}{\partial x}\left[K_s \frac{\partial T_{mat}}{\partial x}\right] \tag{3.5}$$

where T_{mat} is the temperature at the different layers inside the material, and K_s $[\frac{m^2}{s}]$ is the thermal diffusivity.
To solve the problem two different boundary conditions (*b.c.*) are added to (3.5):

- external *b.c.*: the layer is in contact with the exterior climate.

- internal *b.c.*: the layer is in contact with the indoor air.

External b.c.

The following heat budget equation is solved:

$$\frac{\partial T_n}{\partial t} = \frac{1}{\Delta x}\left[\frac{HF_{ext}}{Cs} - K_s\frac{\partial T_{mat}}{\partial x}|_{n-1}\right] \tag{3.6}$$

where T_n is the temperature of the most external layer of the material, Δx is the thickness of the layer, and C_s $[\frac{J}{m^3K}]$ is the specific heat of the layer. The term $K_s\frac{\partial T_{mat}}{\partial x}|_{n-1}$ describes the heat transferred to the layer n through conduction, and HF_{ext} is the external heat budget described by the following equation:

$$HF_{ext} = (1-\alpha_{ext})\,Rs_{ext} + \epsilon_{ext}Rl_{ext} - \epsilon_{ext}\sigma T_n^4 + \mathcal{H}_{ext} \tag{3.7}$$

where α_{ext} and ϵ_{ext} are respectively the albedo and the emissivity of the external layer, σ the constant of Bolzmann, Rs_{ext} the incoming external shortwave radiation, Rl_{ext} the longwave radiation received by the external surface, and $\mathcal{H}_{ext}$ $[\frac{W}{m^2}]$ the sensible heat flux exchanged between the surface and the air. The sensible flux $\mathcal{H}_{ext}$ is given by the following expression:

$$\mathcal{H}_{ext} = \rho C_p \eta_{ext}\,(T_{air} - T_n) \tag{3.8}$$

where η_{ext} $[\frac{m}{s}]$ is the external transfer coefficient. In particular following the work of Clarke (2001), this value is determined by the following expression:

$$\eta_{ext} = c_c\left[a_c + b_c\left(\frac{U^{hor}}{d_c}\right)\right] \tag{3.9}$$

where a_c, b_c, c_c, d_c are constants deduced from laboratory studies, respectively equal to 1.09, 0.23, 5.678 and 0.3048. The term U^{hor} corresponds to the horizontal wind component.

Internal b.c.

The treatement of the internal boundary condition is similar to that of the external. In particular equations (3.5), (3.6) and (3.7) are still valid when the external quantities are replaced with the corresponding internal values.

The main differences consist in the computation of the solar shortwave and longwave radiations (Rs_{int}, Rl_{int}), and the calculation of the transfer coefficient η_{int}. In particular η_{int} has been computed in accordance with *CIBSE* guide (Clarke, 2001), using a value of 1.5 for downward, 3.0 for horizontal, and 4.3 for upward flow directions.

The short wave radiation reaching the indoor walls of a room is the sum of the solar radiation transmitted through the window (Rs_{tr}) and the short wave radiation reflected by other walls. In particular for a given wall i the following expression is considered:

$$Rs^i_{int} = Rs_{tr} + \sum_{j=1,j\neq i}^{6} \overline{\alpha_j} Rs^j_{int} \psi_{ji} \qquad \forall \quad walls \quad \text{i=1,}\cdots,6 \tag{3.10}$$

where $\overline{\alpha_j} = (1 - p_{win})\alpha_{wal_j} + p_{win}\alpha_{win}$ is the averadged albedo of the wall j. The term p_{win} is the window proportion of the wall, and α_{win} is the albedo of the window, which is computed with a polynomial approach based on the work of Roos (1997), and assuming that the solar radiation passing through the window spreads isotropically in all directions. The complete calculation of α_{win} is given in Appendix *A*.

The term ψ_{ji} indicates the view factor from wall j to wall i, and is computed as in Martilli et al. (2002). Note that (3.10) leads to a 6 × 6 linear system easily solved by matrix inversion.

A similar approach is used with respect to the internal longwave radiation. In particular the longwave radiation reaching an indoor wall of a room is the sum of the longwave radiation emitted and reflected by the other walls. For a given wall i the following equation is used:

$$Rl^i_{int} = \sum_{j=1,j\neq i}^{6} \sigma\left(\tilde{\epsilon_j} T^4_{wall,j} + \hat{\epsilon_j} T^4_{wind,j}\right) + \sum_{j=1,j\neq i}^{6} (1 - \epsilon_j)\, Rl^j_{int}\psi_{ji} \qquad \forall \quad \text{walls} \quad i = 1, \cdots, 6 \tag{3.11}$$

where $\tilde{\epsilon_j} = \epsilon_{wal_j}(1 - p_{win})$, $\hat{\epsilon_j} = \epsilon_{win} \cdot p_{win}$, and $\epsilon_j = \tilde{\epsilon_j} + \hat{\epsilon_j}$. This is again a 6 × 6 linear system which is solved by matrix inversion.

For the computation of the surface temperature of windows, a small difference between the two sides of the glass is supposed, and a time dependent energy budget equation is solved. Details of this calculation are presented in the following section.

3.2.2 Window temperature computation

Consider a wall i, having a given percentage of window. For the computation of the window temperature, ($T_{wind,i}$) the following heat budget equation is solved explicitly:

$$\rho_{wind,i} C_{wind,i} \Delta_{wind,i} \frac{dT_{wind,i}}{dt} = \Phi_i \tag{3.12}$$

Take note that (3.12) is only time dependent, which assumes that the temperature difference between the two sides of the glass is small. The term $\rho_{wind,i}$ $[\frac{Kg}{m^3}]$ is the density of the glass, $C_{wind,i}$ $[\frac{J}{KgK}]$ is the specific heat of the glass, $\Delta_{wind,i}$ $[m]$ is the thickness of the window, and Φ_i $[\frac{W}{m^2}]$ is the total flux balance of energy, which is given by:

$$\Phi_i = \epsilon_{wind,i}\left(Rl^i_{ext} - \sigma T^4_{wind,i}\right) + \mathcal{H}^i_{ext} + \epsilon_{wind,i}\left(Rl^i_{ext} - \sigma T^4_{wind,i}\right) + \mathcal{H}^i_{int} \tag{3.13}$$

where $\mathcal{H}^i_{ext}$ and $\mathcal{H}^i_{int}$ are the sensible heat fluxes at the two sides of the window. They are calculated using the expression (3.8) by replacing T_n with the corresponding temperature of the window.

In BEM the indoor air temperature and humidity are controlled thanks to an air-conditioning system. In particular the terms H_{out} and E_{out} in (3.1) – (3.2) correspond to the anthropogenic sensible and the latent heat fluxes that have to be introduced or evacuated in order to heat or cool the room air up to the confort conditions. In the following the mathematical model of the air-conditioning system will be described. A similar method is used to compute H_{out} and E_{out}, so only the derivation of H_{out} will be discussed.

3.2.3 Mathematical model of the air-conditioning system

First consider that if the air-conditioning is not in use, the term H_{out} is set to zero. This means that there is no anthropogenic heat ejected into the atmosphere for cooling or emitted inside the room for heating purposes. On the other hand if the air-conditioning system is on, a comfort target temperature T_{target}, a comfort gap ΔT and a maximum power of cooling/heating δ $[\frac{°C}{s}]$ have to be fixed. Then, starting from the discretised form of (3.1), a first room air temperature $T_r^\star$ is computed by setting H_{out} to zero:

$$T_r^\star = \frac{\Delta t}{Q_B} H^n_{in} + T^n_r \tag{3.14}$$

where Δt is the time step, H^n_{in} and T^n_r are respectively the total sensible heat load and the internal air temperature of the room at time n.
Remark that $T_r^\star$ is the temperature that the indoor air of the room can reach without any anthropogenic control. In particular three different cases can occur:

Case A:$\mid \mathbf{T_r^\star - T_{target}} \mid \leq \mathbf{\Delta T}$
In that case $T_r^\star$ is within the comfort range, then $H^n_{out} = 0$, and $T^{n+1}_r = T^\star_r$.

Case B: $\mathbf{T_r^\star > T_{target} + \Delta T}$
This means that $T_r^\star$ is greater than the target temperature plus the comfort range (cooling period). Then the internal temperature at the following time step is set to $T_r^{n+1} = T_{target} + \Delta T$ and starting from (3.1) the heat flux H_{out}^n is given by:

$$H_{out}^n = H_{in}^n - \frac{Q_B}{\Delta t}\left(T_{target} + \Delta T - T_r^n\right) \tag{3.15}$$

Next a test of efficiency is performed on the air-conditioning system in order to verify its capability to eject this amount of heat. In particular this is the case if the following condition is satisfied (the parameter δ $[\frac{^\circ C}{s}]$ represents the maximum power of heating/cooling of the air-conditioning system):

$$\mid \frac{H_{out}^n - H_{in}^n}{Q_B} \mid \leq \delta \tag{3.16}$$

If (3.16) is not verified, this means that the air-conditioning system cannot evacuate the heat flux H_{out}^n given by (3.15). In that case a new value of H_{out}^n is calculated as:

$$H_{out}^n = H_{in}^n + \delta Q_B \tag{3.17}$$

Starting from H_{out}^n, the internal temperature of the room at the following time step is directly calculated from the discretised form of (3.1):

$$T_r^{n+1} = T_r^n + \frac{\Delta t}{Q_B}\left(H_{in}^n - H_{out}^n\right) \tag{3.18}$$

Case C: $\mathbf{T_r^\star \leq T_{target} - \Delta T}$
In that case $T_r^\star$ is smaller than the target temperature minus the comfort range (heating period). Following a similar procedure as in the previous case, the internal temperature of the room at the following time step is now set to $T_r^{n+1} = T_{target} - \Delta T$. Then, starting from (3.1), the heat flux H_{out}^n is computed by:

$$H_{out}^n = H_{in}^n - \frac{Q_B}{\Delta t}\left(T_{target} - \Delta T - T_r^n\right) \tag{3.19}$$

Following the previous case, H_{out}^n is tested with respect to the condition (3.16). In particular if this equation is not satisfied, a new heat flux is calculated with respect to the parameter δ:

$$H_{out}^n = H_{in}^n - \delta Q_B \tag{3.20}$$

Finally the new room air temperature is computed with the equation (3.18). With a similar procedure focused on the internal humidity, a corresponding latent heat flux E^n_{out} can be calculated.

It is important to point out that H_{out} and E_{out} are the sensible/latent heat needed by the room in order to maintain the internal temperature and humidity inside the comfort range and do not represent the heat emitted into the atmosphere through air-conditioning facilities. Remark in particular that these quantities will be positive only in the case B, which corresponds to the situation where the internal air temperature and humidity need to be decreased. On the other hand C corresponds to a heating and dry period, in which no heat is exchanged between the indoor air and the atmosphere. So, starting from the values of H^n_{out} and E^n_{out} calculated before, the heat ejected into the atmosphere from air-conditioning facilities is computed by:

$$H^n_{atm} = \begin{cases} \left(\frac{COP+1}{COP}\right)(H^n_{out} + E^n_{out}) & \text{if} \quad T^\star_r > T_{target} + \Delta T \\ 0 & \text{else} \end{cases} \tag{3.21}$$

$$E^n_{atm} = \begin{cases} E^n_{out} & \text{if} \quad q^\star_{Vr} > q_{Vtarget} + \Delta q_V \\ 0 & \text{else} \end{cases}$$

where H^n_{atm} $[W]$ and E^n_{atm} $[W]$ are the sensible/latent heat fluxes ejected into the atmosphere at time n and COP is the coefficient of performance of the air-conditioning system.

Remark that every floor of a given building is subject to a different heating/cooling of the indoor air and will consequently generate a different amount of anthropogenic heat. As already mentioned (cf. Figure 3.1), for this building energy model two different air-conditioning systems can be taken into account. In particular if a vertical wall air-conditioning is considered, a different amount of sensible (H^n_{atm}) and latent (E^n_{atm}) heat will be ejected by every floor. On the other hand if a roof-top air-conditioning is in use, the heat generated at every floor is evacuated by a single system located at the roof level. In particular for a typical building of m floors, this leads to:

$$H^{tot,n}_{atm} = \sum_{i=1}^{m} H^{i,n}_{atm}; \quad E^{tot,n}_{atm} = \sum_{i=1}^{m} E^{i,n}_{atm} \tag{3.22}$$

where $H^{tot,n}_{atm}$ and $E^{tot,n}_{atm}$ are the total sensible/latent heat emitted into the atmosphere at time n and $H^{i,n}_{atm}$ and $E^{i,n}_{atm}$ are the ones generated by the floor i.

The air-conditioning fluxes together with those generated from natural ventilation (term

C of (3.3) and (3.4)), are directly linked to the atmosphere and should be taken into account inside an urban canopy parameterisation for mesoscale models. In this context the chapter 4 will be focused on the coupling between BEM and the urban module of Martilli et al. (2002). Numerical results will indicate that the heat generated from anthropogenic activities can produce a non negligent impact on the urban meteorology and allows a more precise study related to UHI mitigation strategies.

3.3 Verification and validation procedure

A combination of analytical, inter-program and empirical testing procedure has been used for the verification and validation of the building energy model. In particular following the work of Zmeureanu et al. (1987) BEM is firstly compared with analytical solutions and with other more sophisticated programs used in the thermal analysis of buildings, as CBS-MASS (Zmeureanu et al., 1987), TARP (Walton, G.N., 1983) and BLAST (BLAST-3.0, 1981). Finally an empirical validation test is performed by comparing BEM with the box building model developed by Kikegawa et al. (2003).

3.3.1 Comparison between BEM and some analytical solutions

The simulations are carried out over a building of five floors. If not specified, the results presented in the following refer to the third floor (intermediate floor). The room dimensions in x, y and z directions are respectively $6.0m \times 6.0m \times 3.6m$, and the windows proportion of the different walls is set equal to zero. Concerning the indoor air of the rooms the main assumptions are the following:

- the indoor air is dry;
- there is no solar radiation, and no sensible/latent heat generated by equipments and occupants;
- the longwave radiation incoming at the exterior walls is constant.

The physical parameters of the building's surfaces (walls, ceiling and floors) are presented in the Appendix B (cf. Table 3.1). Initially the temperatures of those materials, as well as that of the indoor and outdoor air are set to $20°C$. Starting from this configuration, two analytical solutions are studied.

A: Constant internal air temperature and a step change in the outdoor air temperature

For this first test the internal air temperature of the rooms is kept constant at $20°C$ ($H_{in} = H_{out}$ in (3.1)), while the outdoor air temperature undergo a sudden drop to $0°C$.

No air infiltration is considered in this case ($\beta = 1$ in (3.3)). In the Figure 3.2 the inside walls surface temperature of the intermediate room obtained by BEM is compared with the analytical and the CBS-$MASS$ solution.

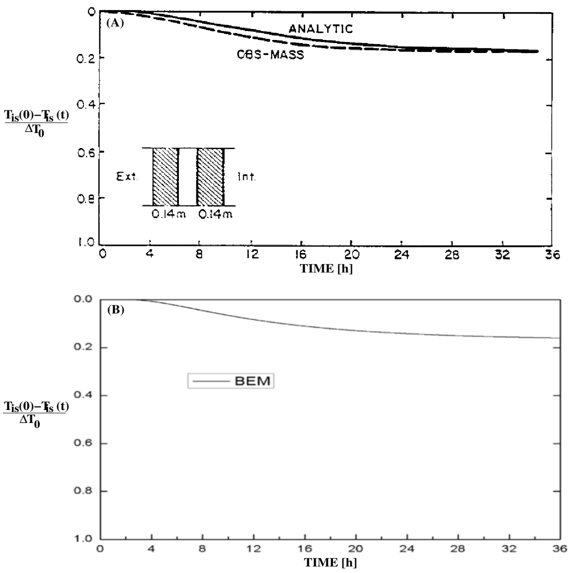

FIGURE 3.2: Comparison of the variation of the inside surface temperature of a $0.28m$ brick wall due to a step change in the outdoor temperature. Figure A indicates the analytical and the CBS-$MASS$ solution (Zmeureanu at al., 1987), while Figure B shows the one obtained by BEM.

Results indicate that the solution of BEM is in good agreement with the analytical and the CBS-$MASS$ one.

B: Effect of air infiltration and internal mass

Starting from the same initial conditions as in the test A, the variation of the intermediate floor air temperature subject to a sudden drop of outdoor air temperature to $0°C$ is analysed. Two main assumptions are done for this simulation:

- The effect of air infiltration is considered by setting the parameter β to zero in (3.3).
- The temperature of the internal mass (i.e. ceilings and floors of the different floors) is set equal to its corresponding room air temperature.

As shown in the Figure 3.3 the analytical, the CBS-$MASS$ and the BEM solutions are in good agreement.

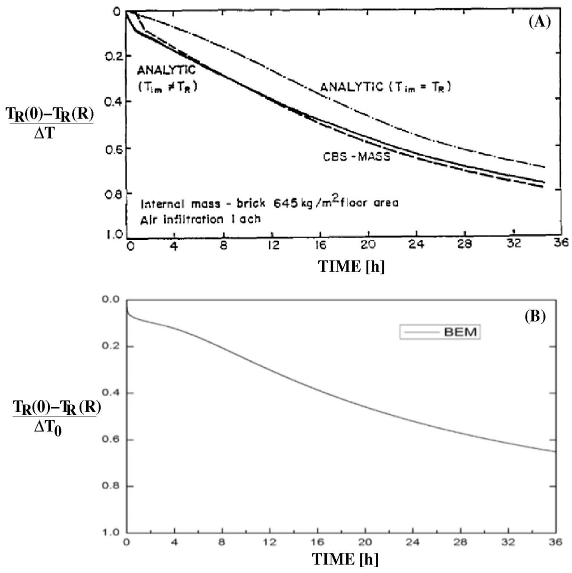

Figure 3.3: Comparison of the variation of the room air temperature due to a step change in outdoor air temperature with air infiltration and internal mass. Figure A indicates the analytical and the *CBS-MASS* solution (Zmeureanu at al., 1987), while Figure B shows the one obtained by BEM.

3.3.2 Inter-program validation

In this section the results of *BEM* are compared with those obtained by three well known programs in the thermal analysis of buildings: *BLAST*, *TARP* and *CBS-MASS*. The simulation is performed in a winter design day (cf. Table 3.2 in the Appendix *B*), over a 5-floor building having an intermediate-floor office space of $30m \times 30m \times 3,6m$, with four exterior walls and windows. The main physical characteristics of the building are also presented in the Appendix *B* (cf. Table 3.3). Following the work of Zmeureanu et al. (1987) the thermal load (i.e. $-H_{out}$ in (3.1)) needed to preserve the internal air temperature constant at $20°C$ is analysed. In particular in the Figure 3.4 the results obtained by *BEM* are compared to that of *BLAST*, *TARP* and *CBS-MASS*. One can see that the heating load simulated by *BEM* is close to the one obtained by the others building energy programs.

The small differences could be linked to uncertainties on the values of some parameters that were not explicitly mentioned in Zmeureanu et al. (incoming longwave radiation at the outdoor surfaces and convective heat transfer coefficient at the exterior walls).

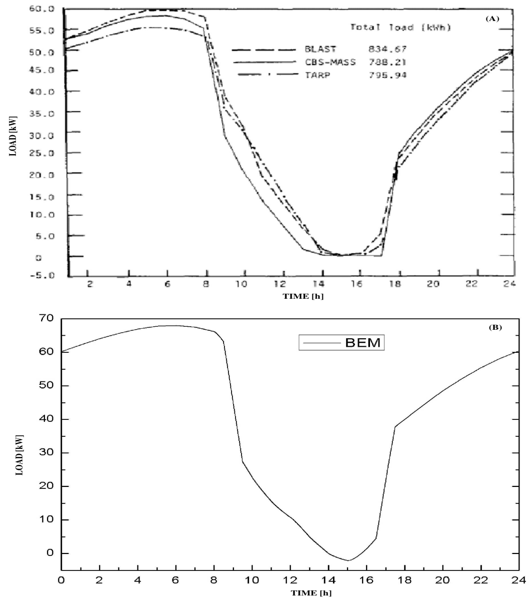

FIGURE 3.4: Comparison between the heating load obtained by *CBS-MASS*, *BLAST*, *TARP* and *BEM* for the intermediate floor of an office building on a winter design day. Dry air is considered in the simulation. Figure A indicates the *TARP*, *BLAST* and the *CBS-MASS* solution (Zmeureanu at al., 1987), while Figure B shows the one obtained by BEM.

3.3.3 Comparison between BEM and another box building model

In this section a comparison is done between *BEM* and the model developed by Kikegawa et al. (2003), starting from data collected in a measurement campaign over Tokyo (Japan). In particular measurements were acquired during August 1998 for a 25−story office building of approximately $100m$ high (building-O) located at the center of a business area (Ootemachi). Measurements include the countinuos acquisition of meteorological data from the rooftop of the building. The dimensions of each floor of the building-O are $47.0m \times 47.0m \times 3.78m$ and the physical parameters of the walls, as well as those corresponding to the air-conditioning system can be found in the Appendix B (cf. Table 3.4). In Figures 3.5 and 3.6 the meteorological data (coming from the measurement campaign) and the temporal evolution of φ_P and q_E (cf. (3.3)) used for the simulation are also presented.

The model of Kikegawa et al. is compared with *BEM* by computing the total processed load (i.e. $H_{out} + E_{out}$ in (3.1) and (3.2)) for the building-O. The simulation is carried out from the 2^{th} August 1998 at 0000 LST to the 5^{th} August 1998 at 2400 LST (typical

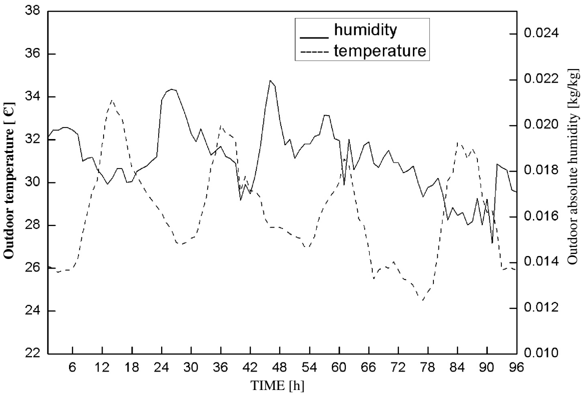

Figure 3.5: Temporal evolution of the outdoor temperature and of the outdoor absolute humidity used for the comparison between BEM and the model of Kikegawa et al. (2003)

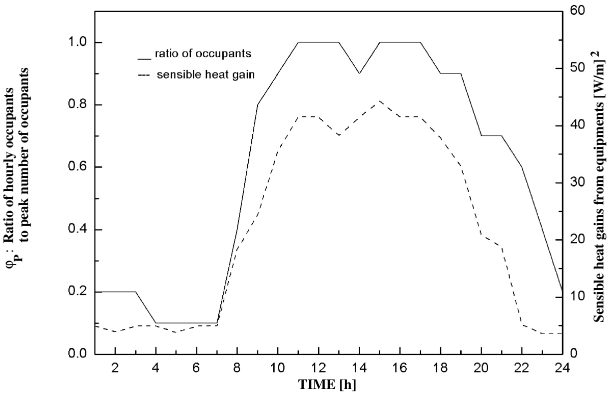

Figure 3.6: Temporal evolution of φ_P and q_E used for the comparison between BEM and the model of Kikegawa et al. (2003)

summer-day conditions). In the Figure 3.7 the comparison between the two simulations is presented.

Results show that when the air-conditioning system is on, *BEM* is able to reproduce pretty well the behaviour of the total load obtained by Kikegawa's model. Some considerations can be done in order to analyse the differences between the two results:

- The total load produced by BEM is a step function which clearly showes when the air-conditioning is on and when it is off. On the other hand the air-conditioning system considered by Kikegawa et al. (2003), is quite different as it assumes that the processed

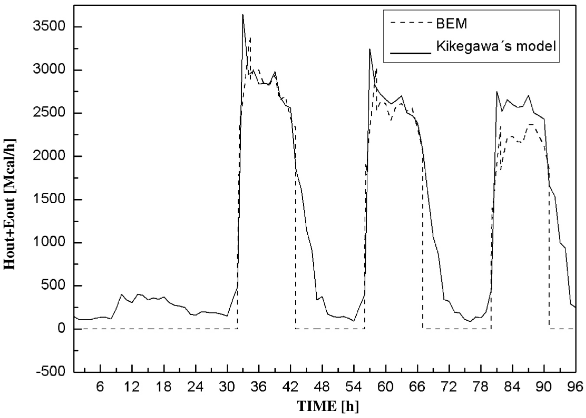

FIGURE 3.7: Comparison between the total load obtained by BEM and that produced by the model of Kikegawa et al. (2003) starting from the meteorological data collected at the roof level of the building-O.

load H_{out} and E_{out} in (3.1) and (3.2) are proportional to H_{in} and E_{in}. More precisely the following equations are adopted:

$$H_{out} = \varphi_P H_{in}; \quad E_{out} = \varphi_P E_{in}$$

where φ_P is the hourly occupancy ratio. As one can see in the Figure 3.6 the parameter φ_P is always greater then zero and consequently the processed load $H_{out} + E_{out}$ follows the same trend.

• The model of Kikegawa et al. (2003), has been directly tested and validated by implementing it on an UCP (Kusaka et al., 2001). In particular the measured outdoor air temperature at the observational altitude over the Ootemachi area has been compared with the temperature obtained by the numerical model (Kikegawa et al., 2003).

In the validation procedure adopted in this chapter BEM is treated separately, i.e. is not connected to a mesoscale model. In particular the result of the Figure 3.7 has been obtained by assuming that the external temparature and humidity (cf. Figures 3.5 and 3.6) are constant with height. On the other hand the result of the Figure 3.7 of Kikegawa's model is obtained with the outdoor conditions given by the mesoscale model.

• The difference between the two results can also be given by the uncertainties in some parameters that are not mentioned in the work of Kikegawa et al. (2003), as the values used for the convective heat transfer coefficient at the surface.

Taking these considerations into account the results obtained by BEM are very satisfactory.

3.4 Study of the processed load sensitivity to different physical processes

Equations (3.1) up to (3.4) show that the temperature and humidity inside a building are influenced by several physical processes:

- heat exchanged between the wall and the air;
- natural ventilation;
- heat generated by equipments and occupants.

The goal in this section is to study the sensitivity of BEM with respect to those parameters. In order to perform this analysis the same building parameters and conditions used in the paragraph 3.3.2 are adopted. The sensitivity of the processed load (i.e. the energy needed to control the internal air temperature and humidity) with respect to the different physical parameters is studied. In particular the following simulations are performed by fixing $H_{out} = H_{in}$ in each floor, which corresponds to the load needed to maintain the internal temperature constant (cf. (3.1)). The results presented in this section are obtained by adding the total load of the different floors. In the following the **base case** test refers to the load presented in the section 3.3.2.

3.4.1 Sensitivity of the load with respect to the physics of the wall

A first test is performed in order to evaluate the impact of the presence of windows. In this context the base-case test is first compared with the corresponding solution obtained by setting the windows proportion to zero, and afterwards with the result obtained by assuming that the internal albedo of the windows is equal to 1 once the radiation is inside the floor (total trapping case). The aim of this last simulation is to evaluate the impact of the internal walls in the building (i.e. the rooms): the effect of internal walls is to trap the external solar radiation inside the building preventing the heat to exit from the windows. The result of this comparison is presented in the Figure 3.8.

Results show that in this winter case the absence of windows reduce the energy consumption during the night and increase it during the day. In fact on the one hand the glasses have a higher heat capacity than the walls which corresponds to a higher load needed during the night. On the other hand the absence of windows during the day prevents the solar radiation to penetrate inside the building, which increases the load

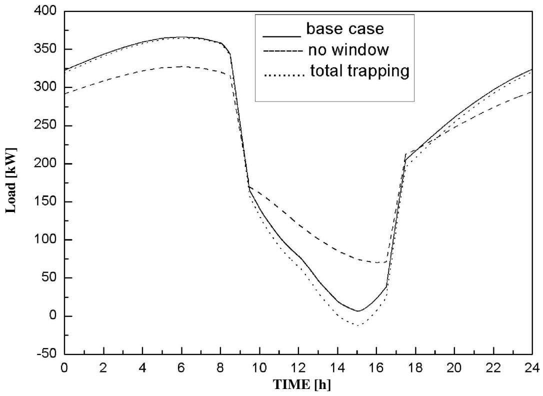

Figure 3.8: Comparison between three different loads obtained by BEM in order to study the impact of windows and indoor walls.

needed to maintain a constant internal temperature. The total trapping test shows that the impact of indoor walls is small and can be neglegted.

A second test is performed in order to study the sensitivity of the load with respect to the external heat transfer coefficient h_{ext} (cf. (3.8)). As one can see in (3.9) this coefficient is usually estimated as a function of wind speed. However there is still a signifiant uncertainty in the determination of such relationship (Masson, 2000, Martilli et al., 2002). In this context the processed load has been computed with respect to three different value of h_{ext}. The result of the Figure 3.9 indicates that the solution is sensitive to this physical parameter with a maximum variability of $50kW$.

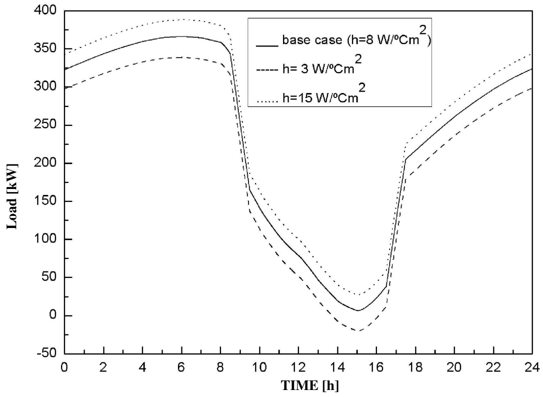

Figure 3.9: Comparison between three different loads obtained by BEM in order to study the impact of the external heat transfer coefficient.

3.4.2 Sensitivity of the load with respect to the heat generated by the presence of people and natural ventilation

The base case test is first compared with a simulation in which the presence of people and equipments has been neglected ($\varphi_P = 0$ and $q_E = 0$ in (3.3)), and then compared to a test performed without the natural ventilation term ($\beta = 1$ in (3)). Results are presented in the Figure 3.10. At first it is possible to see that the heat generated by people and equipments increases the load of about $150kW$ during daytime (the impact is clearly zero during night time when there is no people and equipments inside the building). It is also interesting to observe that in this winter case the presence of natural ventilation contributes to decrease the internal temperature of the building (heat is transferred from inside to outside). In particular one can see in the Figure 3.10 that the lack of natural ventilation decreases the heating load during the night, and generates an internal temperature higher than the comfort target of $26°C$ during the day. This imposes to cool down the internal air by ejecting a certain amount of heat outside the building (the heating load has a negative value during the day).

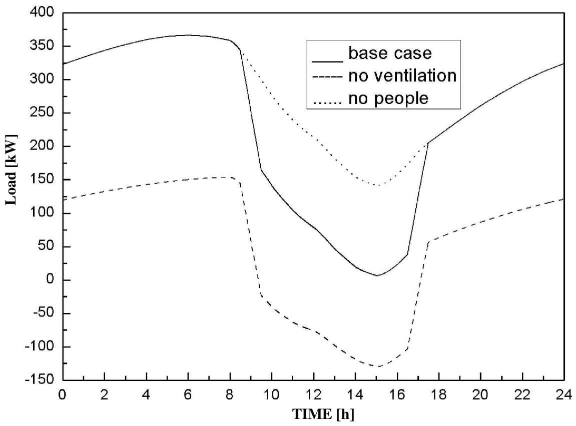

FIGURE 3.10: Comparison between three different loads obtained by BEM in order to study the impact of the presence of people and equipments, and natural ventilation.

3.5 Conclusions and perspectives

In the first part of this work a new Building Energy Model (BEM) has been presented and the governing equations as well as the physical processes taken into account have been described. The model is able to simulate the effects of natural ventilation, heat conduction through walls, heating from equipments and occupants and anthropogenic heating/cooling from air-conditioning facilities.

A combination of analytical, inter-program and empirical testing procedure has been carried out in order to test and validate the model. In particular the different results of the section 3.3.1 show that BEM has accuratly reproduced the basic heat transfer phenomena. Moreover the inter-program and the empirical testing simulations (cf. sections 3.3.2 and 3.3.3) indicate that the model is also able to reproduce the heat fluxes that are exchanged between buildings and atmosphere. This is a very important point as the final goal of this study is to couple BEM with an Urban Canopy Parameterisation (UCP) for mesoscale models. This part of the work will be presented in the following chapter where it will be pointed out that the expected future results are to obtain a new simulating tool able to generate a better representation of urban canopy climate (UHI processes, etc.).

Finally the sensitivity study presented in the section 3.4 evaluated the impact of different physical parameters on the processed load. It has been pointed out that the physics of the walls, as well as the natural ventilation and the heat released by equipments and occupants can have important consequences on the final solution. Different tests will also be considered in the following chapters in order to evaluate the impact of the fluxes generated by BEM on urban meteorology and cooling energy demands.

Appendix A: Calculation of the albedo of the window

Let I be the intensity of the solar radiation and dA a surface element of the glass (cf. Figure 3.11).

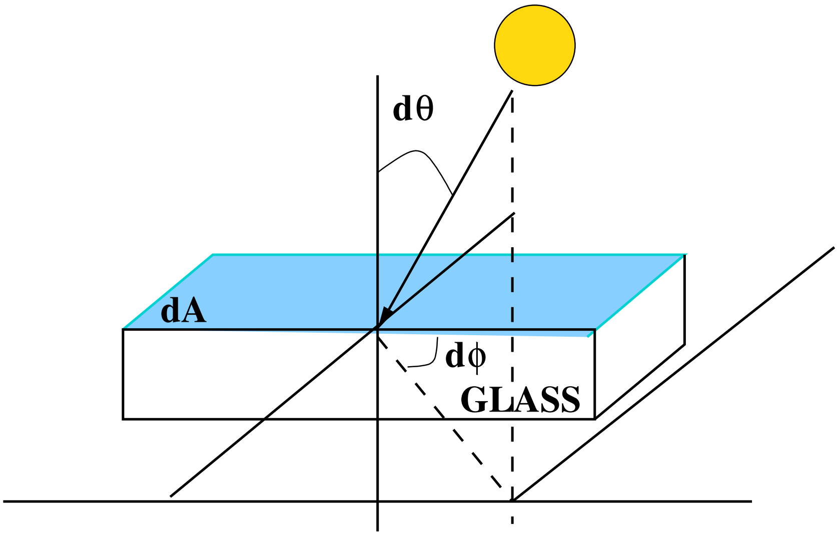

FIGURE 3.11: Representation of a surface element dA of the glass.

The total flux of energy $\mathcal{F}$ reaching the element dA can be written as (Pielke, 1984):

$$\mathcal{F} = \int_0^{2\pi} \int_0^{\frac{\pi}{2}} I(\theta,\phi)\cos\theta\sin\theta d\theta d\phi dA = \pi I dA \tag{3.23}$$

If α_{win} is the albedo of the window, the energy crossing the glass element dA is then given by:

$$\mathbf{E} = (1 - \alpha_{win})\,\mathcal{F}dA \tag{3.24}$$

In order to compute α_{win} another expression is derived for $\mathbf{E}$ based on the **total solar energy transmittance** g. In particular following the work of Roos (1987), and Karlsson et al. (2000), a polynomial approach is used to fit the value of g with the angle of incidence θ. The following expression is used:

$$g(z) = g_0\left(1 - az^{\alpha} - bz^{\beta} - cz^{\gamma}\right) \tag{3.25}$$

where $z = \frac{\theta}{90°}$ (θ is the angle of incidence), and g_0 is the transmittance at the near-normal value. After some fitting tests over different types of windows (Karlsson et al.,

2000) the following coefficients have been considered for (3.25):

$$\begin{gathered} a = 8, \quad b = \frac{0.25}{q}, \quad c = 1 - a - b, \\ \alpha = 5.2 + 0.7q, \quad \beta = 2, \quad \gamma = 5.26 + 0.06p + (0.73 + 0.04p)\, q. \end{gathered} \tag{3.26}$$

with p equal to the number of panes of the window (1, 2, or 3) and q to a 'category' parameter having values between 1 and 10 depending on the type of glass ($q = 4$ for standard glasses).

Taking the value of g into account, the energy **E** crossing the glass elemet dA can be written as:

$$\mathbf{E} = \int_0^{2\pi} \int_0^{\frac{\pi}{2}} I(\theta,\phi) g(\theta) \cos\theta \sin\theta d\theta d\phi dA = \pi I dA \tag{3.27}$$

Considering that I is spread isotropically in all directions (I is a constant) (3.27) can be written as:

$$\begin{aligned} \mathbf{E} &= 2\pi I \int_0^{\frac{\pi}{2}} g(\theta) \cos\theta \sin\theta d\theta dA \\ &= 2\mathcal{F} \int_0^{\frac{\pi}{2}} g(\theta) \cos\theta \sin\theta d\theta dA \end{aligned} \tag{3.28}$$

Equalizing (3.24) and (3.28) leads to the following expression for α_{win}:

$$\alpha_{win} = 1 - 2 \int_0^{\frac{\pi}{2}} g(\theta) \cos\theta \sin\theta d\theta \tag{3.29}$$

With an algebraic manipulation and using the definition of g the expression (3.29) can be finally written as:

$$\alpha_{win} = 1 - g_0 + \frac{g_0}{2} \int_0^{\pi} \left(\frac{a}{\pi^\alpha} x^\alpha + \frac{b}{\pi^\beta} x^\beta + \frac{c}{\pi^\gamma} x^\gamma \right) \sin x dx. \tag{3.30}$$

Remark that (3.30) is a simple expression giving the albedo of the window as a function of the parametes p and q.

Appendix B: Data used for the different simulations

Parameters	**Settings**
Exterior walls	0.28m Brick
Intermediate walls (ceilings and floors)	0.28m Brick
Ground wall	0.28m Brick
Constant surface wall coefficient (indoor and outdoor)	$8\frac{W}{m^2 {}^\circ C}$
Volumetric ventilation rate	$3.6\frac{m^3}{m^2 h}$
Physical properties used for Brick	
Conductivity	$0.73\frac{W}{mK}$
Density	$1.84.10^3\frac{kg}{m^3}$
Specific heat	$900\frac{J}{kgK}$
Emissivity	0.9

Table 3.1: Physical parameters of building's materials (walls, ceiling and floors) used for the simulation in the analytical validation.

Hour (h)	**Outdoor temperature** ($^\circ C$)	**Direct normal radiation** ($\frac{W}{m^2}$)
1	-18.05	-
2	-18.80	-
3	-19.40	-
4	-19.85	-
5	-20.00	-
6	-19.70	-
7	-18.95	-
8	-17.60	-
9	-15.65	398.1
10	-13.40	685.9
11	-10.85	794.5
12	-8.45	833.7
13	-6.65	830.0
14	-5.45	781.2
15	-5.00	652.7
16	-5.45	301.9
17	-6.50	-
18	-8.15	-
19	-10.10	-
20	-12.05	-
21	-13.70	-
22	-15.20	-
23	-16.40	-
24	-17.30	-

Table 3.2: Weather data for the inter-program validation in a winter design day.

Parameters	**Settings**
Exterior walls	0.10m brick 0.10m insulator 0.002m gypsum board
Intermediate walls (ceilings and floors)	0.10m concrete 0.10m insulator 0.002n gypsum board
Ground wall	0.22m concrete
Constant surface wall coefficient (indoor and outdoor)	$8\frac{W}{m^2 {}^\circ C}$
Constant surface window coefficient (indoor and outdoor)	$2.8\frac{W}{m^2 {}^\circ C}$
Air infiltration	$\beta = 0$
Volumetric ventilation rate	$3.6\frac{m^3}{m^2 h}$
Glazing-to-wall-ratio (double standard glazing)	0.5
Internal heat gains	$30\frac{W}{m^2}$ between $9:00$ to $17:00$
Room air temperature	$20^\circ C$
Physical properties used for the materials	
Emissivity	0.9
Concrete	
Conductivity	$1.73\frac{W}{mK}$
Density	$2.35.10^3\frac{kg}{m^3}$
Specific heat	$880\frac{J}{kgK}$
Albedo	0.2
Insulator	
Conductivity	$0.057\frac{W}{mK}$
Density	$13\frac{kg}{m^3}$
Specific heat	$840\frac{J}{kgK}$
Gypsum board	
Conductivity	$0.14\frac{W}{mK}$
Density	$760\frac{kg}{m^3}$
Specific heat	$800\frac{J}{kgK}$
Albedo	0.7

Table 3.3: Physical parameters used for the simulation of the inter-program validation.

Parameters	**Settings**
Exterior vertical walls	0.11m concrete 0.05m insulator 0.11m gypsum board
Intermediate walls (ceilings and floors)	0.22m concrete
Ground wall	0.33m concrete 1.07m soil
Constant surface wall coefficient (indoor and outdoor)	$8\frac{W}{m^2{}^\circ C}$
Constant surface window coefficient (indoor and outdoor)	$2.8\frac{W}{m^2{}^\circ C}$
Duration of air-conditioning on weekdays	$0900-1900\ LST^\star$
Target temperature of room cooling	$26^\circ C$
Target relative-humidity of room cooling	50%
Volumetric ventilation rate per unit floor area	$5.0\frac{m^3}{m^2h}$
Control coefficient for ventilation rate (β)	60%
Floor area per occupant	$5\frac{m^2}{Person}$
Sensible heat generated from occupants (q_{hs})	$54\frac{W}{Person}$
Latent heat generated from occupants (q_{hl})	$64\frac{W}{Person}$
Insolation transmittance through the windows (windows with blinds)	30%
Glazing-to-wall-ratio	30%
Parameters own of BEM	
Comfort range of temperature	$0.1^\circ C$
Power of cooling/heating	$10^{-3}\frac{^\circ C}{s}$
Comfort range of humidity	$10^{-3}\frac{kg}{kg}$
Power of drying/moistening	$10^{-6}\frac{kg}{kg.s}$
Physical properties used for the materials	
Emissivity	0.9
Concrete	
Conductivity	$1.39\frac{W}{mK}$
Volumetric heat capacity	$1,93.10^6\frac{J}{m^3K}$
Albedo	0.2
Insulator	
Conductivity	$0.04\frac{W}{mK}$
Volumetric heat capacity	$0.06.10^6\frac{J}{m^3K}$
Soil	
Conductivity	$1.00\frac{W}{mK}$
Volumetric heat capacity	$1,74.10^6\frac{J}{m^3K}$
$\star$ Pre cooling starts from 0800 LST	

Table 3.4: Parameters used in the validation of BEM against the model of Kikegawa et al. (2003).

Bibliography

[1] BLAST-3.0: 1981, 'The Building Loads Analysis and System Thermodynamics Program Users Manual', U.S. Army Construction Engineering Research Laboratory, Champaign, Illinois, March.

[2] Clarke, J.: 2001, 'Energy Simulation in Building Design', Butterworth-Heinemann, Oxford.

[3] Karlsson, J., Roos, A.: 2000, 'Modelling the angular behaviour of the total solar energy transmittance of windows', *Solar Energy*, **69**: 321-329.

[4] Kikegawa, Y., Genchi, Y., Yoshikado, H., Kondo, H.: 2003, 'Development of a numerical simulation system toward comprehensive assessments of urban warming countermeasures including their impact upon the urban buildings' energy-demands', *Applied Energy* **76**: 449-466.

[5] Kikegawa, Y., Genchi, Y., Kondo,H., Hanaki,K.: 2006, 'Impacts of city-block-scale countermeasures against urban heat island phenomena upon a building's energy-consumption for air conditioning', *Applied Energy* **83**: 649-668.

[6] Kusaka, H., Kondo, H., Kikegawa, Y., Kimura, F.: 2001, 'A simple single-layer urban canopy model for atmospheric models: Comparison with multi layer and slab models', *Boundary-Layer Meteorology* **101**: 329-358.

[7] Martilli, A., Clappier, A., Rotach, MW.: 2002, 'An urban surface exchange parameterization for mesoscale models', *Boundary-Layer Meteorology* **104**: 261-304.

[8] Masson, V.: 2000, 'A physically-based scheme for the urban energy budget in atmospheric models', *Boundary-Layer Meteorol.*, **94**, 357-397.

[9] Oke, T.R.: 1987, 'The surface energy budget on urban areas', in *Modeling the Urban Boundary Layer*, edited by the *American Meteorological Society*, 1-52.

[10] Pielke, R.A.: 1984, 'Mesoscale meteorological modeling', *Academic Press*, Orlando, Florida, 612 pp.

[11] Roos, A.: 1997, 'Optical characterisation of coated glazings at oblique angles of incidence: measurements versus model calculations.', *Journal of Non-Crystalline Solids*, **218**: 247-255.

[12] Sparrow, E.M., Cess, R.D.: 1978, 'Radiation Heat Transfer', *Brooks/Cole Publishing Company Belmont*, CA, 366 pp.

[13] Walton, G.N.: 1983, 'Thermal Analysis Research Program (TARP)', Reference Manual, U.S. Department of Commerce, National Bureau of Standards, National Engineering Laboratory, Washington, DC, March.

[14] Zmeureanu, R., Fazio, P., Haghighat, F.: 1987, 'Analytical and Inter-program Validation of a Building Thermal Model.', *Energy and Buildings* **10**: 121-133.

Chapter 4

Development of a numerical simulation system for the study of UHI mitigation strategies

Abstract

In the present study the Building Energy Model (BEM) described in chapter 3 is coupled with an Urban Canopy Parameterisation (UCP). The resulting parameterisation (UCP-BEM) is then introduced in the finite volume mesoscale model described in chapter 2. The aim of the resulting simulating tool is to allow a more accurate study of the impact of anthropogenic activities on urban microclimate: energy demands for heating in winter and increase of energy consumption generated by artificial air-conditioning in summer.

The coupling between UCP and BEM is presented in detail in the first part of the chapter. In a second time one-dimensional and two-dimensional simulations are performed. One-dimensional simulations provide first interesting informations related to some characteristics of UCP-BEM (e.g. impact of boundary conditions, geomerty). Two-dimensional simulations are carried out for an idealysed case of a city surrounded on both sides by rural areas. In particular the impact of anthropogenic air-conditioning on the urban boundary layer is analysed.

A sensitivity study is also performed with respect to different parameters in order to test the model and evaluate the effectiveness of different UHI mitigation and cooling energy demand control strategies.

4.1 Introduction

In the previous chapters it has been pointed out that anthropogenic heat released by air-conditioning facilities can have an important impact on urban microclimate, and should be taken into account for a more complete UHI mitigation study. For instance the work produced by Kikegawa et al. (2006), during a summer episode in the Tokyo metropolitan area shows that the reduction in the air-conditioning anthropogenic heat leads to a daily and spatially averaged decrease in near-ground air temperature of 0.2-1.2 $°C$. These temperature decreases could result in building-cooling energy savings of 4-40%.
The study of the impact generated by anthropogenic air-conditioning on the urban boundary layer and cooling energy demands, represents also a central point in the present work. With this purpose a particular interest is given to the analysis of the modifications that these fluxes can produce on different meteorological variables (e.g. air temperature, wind, TKE). Note that this can have direct consequences on UHI intensity, CO_2 production, and cloud formation. In particular the identification of possible strategies to control this kind of phenomena represents a very important issue as it directly affects thermal comfort of the inhabitants, air quality, and energy consumption in buildings. In the present work, a sensitivity study is carried out in order to evaluate to which extent the magnitude of air-conditioning fluxes can be controlled by modifying some building parameters (e.g. heat capacity, thermal conductivity, COP, target temperature).

Similarly to Kikegawa et al. (2003), this study is carried out considering a numerical simulation system composed by a Mesoscale Model (MM), an Urban Canopy Parameterisation (UCP), and a Building Energy Model (BEM). Note that the advantage of a numerical tool is to allow a clear distinction and evaluation of the different sources of heat released into the atmosphere. In this work, a particular interest is given to the sources generated by air-conditioning facilities which directly depend on energy consumption inside buildings. Remark that this term is stricly linked to the magnitude of the outdoor air temperature, which in turn is a function of the heat fluxes released into the atmosphere. More in general, this numerical model must be able to take these kind of feed-back phenomena into account, and a coupling between MM, UCP, and BEM is therefore needed.

A set of one-dimensional simulations is first considered in order to test the model and present some basic characteristics (e.g. boundary conditions, geometry). In a second time, the numerical tool MM-UCP-BEM is applied to $2D$ idealised cases of a city surrounded on both sides by rural areas, with the purpose of evaluating the impact of anthropogenic air-conditioning fluxes, and of identifying possible short and long term control strategies. A two-dimensional configuration is chosen as it leads to an easier identification of the possible impacts of anthropogenic air-conditioning fluxes and can be a useful guidance to the interpretation of future more realistic 3D studies. In this context, it is also important to point out that in this work we are not interested in quantitative values, but in identifying a tendency and in evaluating the importance of the different countermeasures.

In section 4.2 the simulation system composed by MM, UCP and BEM is described. The coupling between UCP and BEM is discussed in detail in section 4.3. The numerical tests are presented and analysed in section 4.4, and finally conclusions and perspectives are given in section 4.5.

4.2 Presentation of the numerical model

The urban parameterisation developed by Martilli et al. (2002), represented a clear improvement to the traditional approach and allowed a better understanding of the complex interactions between buildings and the atmosphere. The main features of this UCP include:

- Sink of momentum distributed from the ground surface up to the height of the highest building.
- Shadowing and trapping effects in urban canyons.
- Length scales for the TKE computation modified due to the presence of buildings.

This urban module has been exstensively used and validations have been already carried out for one-dimensional (Roulet et al., 2004), two-dimensional (Martilli, 2002, 2003) and three-dimensional tests (Martilli et al., 2003, Roulet et al., 2004).
As mentioned in Martilli et al. (2002), one of the possible improvements of this model include the representation of the anthropogenic heat fluxes exchanged between buildings and the atmosphere, which are only partially taken into account by fixing the internal temperature of the walls.

In this contribution, the present study aims to develop a new urban parameterisation (UCP-BEM) based on the coupling between the module of Martilli et al. (2002), and the building model presented in the chapter 3. The final goal is to have a more complete urban parameterisation, which should be able to improve the capability of mesoscale models to simulate urban canopy climate (UHI processes, etc.) and air pollution dispersion in the city and its surroundings.

A general view of the simulation system is presented in the Figure 4.1.

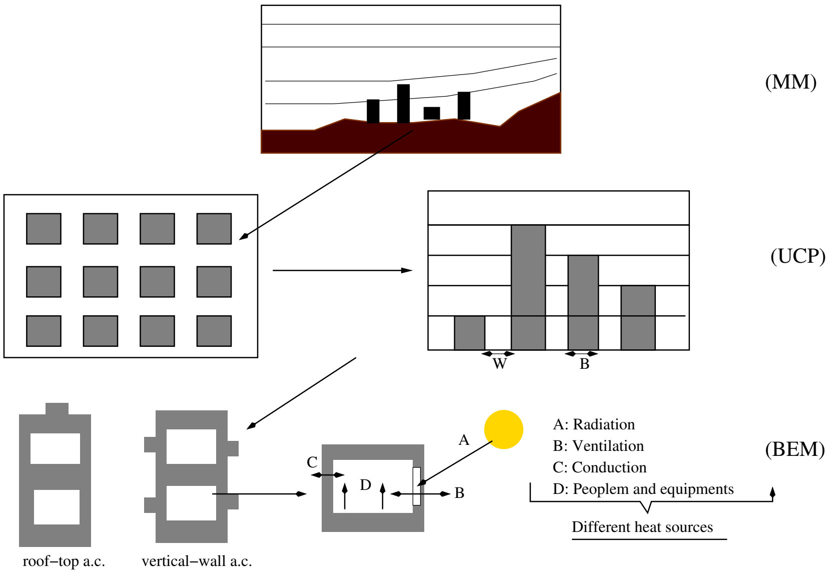

FIGURE 4.1: Representation of the simulation system composed by the Mesoscale Model (MM), the Urban Canopy Parameterisation (UCP) and the Building Energy Model (BEM).

The Mesoscale Model (MM) considered in this study is the finite volumes model described in chapter 2. In the following section the coupling between BEM (cf. chapter 3) and the urban parameterisation of Martilli et al. (2002), is presented in detail. In general the links between the two models are the following:

- UCP gives to BEM the outdoor air temperature, humidity, and radiation reaching the walls and the roof. This allows on the one hand the computation of the radiation entering the building through the windows, and on the other hand it sets the boundary conditions for the calculation of walls and roofs temperatures.
- BEM gives to the UCP walls and the roofs temperatures, the heat flux generated by natural ventilation, and the heat flux due to processes linked with the generation of energy inside the building (e.g. air-conditionning).

4.3 The coupling between UCP and BEM

The urban structure is defined on a numerical grid different from that of the mesoscale model. In the following all the variables located at a center of the urban grid will be described by an index IU, while the variables with index I will refer to the center of the mesoscale grid. For the faces of the two grids, the same notations are employed, but with the index iu for urban, and i for mesoscale quantities. The city is represented as a combination of several urban classes, each of them being characterised by an array of buildings of a given orientation. In addition (cf. Figure 4.2), the present parameterisation UCP-BEM is built in such a way that each building can have four different walls. Each east-west and south-north oriented wall has the same width, given respectively by B_{WE} and B_{SN}. In a similar way the east-west, and the south-north oriented street canyons have a width W_{WE} and W_{SN}. Following the work of Martilli et al. (2002), each class is composed by buildings of different heights, with a probability $\gamma(z_{iu})$ to have a building with height z_{iu}, and a density function $\Gamma(z_{iu})$ of buildings with height z_{iu} or higher (cf. Figure 4.3). In particular if nu is the highest level of the urban grid, $\Gamma(z_{iu})$ is computed by:

$$\Gamma(z_{iu}) = \sum_{ju=iu}^{nu} \gamma(z_{ju})$$

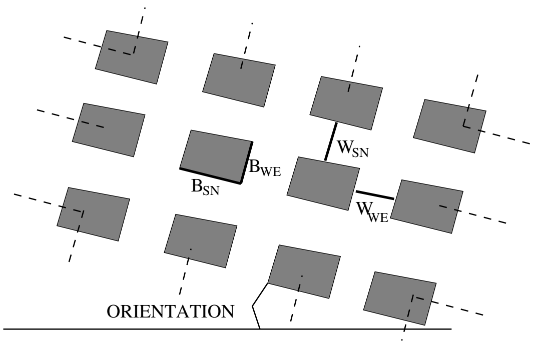

FIGURE 4.2: Representation of a typical urban class.

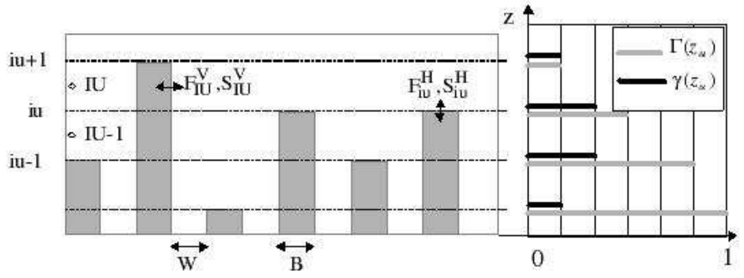

FIGURE 4.3: Schematic representation of the numerical grid in the urban module (Martilli, 2001).

To simplify the formulation, we assume that the length of the west-east and of the south-north oriented canyon is equal to the corresponding horizontal grid size. Starting from these assumptions, it is possible to estimate the areas of every urban surface type for each grid cell:

West-East walls

$$S_{IU}^{V_{WE}} = \underbrace{(\Delta z_{IU} B_{WE}) \frac{S_{TOT}^{H}}{(B_{WE} + W_{SN})(B_{SN} + W_{WE})}}_{\left[S_{IU}^{V_{WE}}\right]_{MAX}} \Gamma(z_{iu+1}) \tag{4.1}$$

South-North walls

$$S_{IU}^{V_{SN}} = \underbrace{(\Delta z_{IU} B_{SN}) \frac{S_{TOT}^{H}}{(B_{WE} + W_{SN})(B_{SN} + W_{WE})}}_{\left[S_{IU}^{V_{SN}}\right]_{MAX}} \Gamma(z_{iu+1}) \tag{4.2}$$

Roofs

$$S_{iu}^{H} = (B_{WE} B_{SN}) \frac{S_{TOT}^{H}}{(B_{WE} + W_{SN})(B_{SN} + W_{WE})} \gamma(z_{iu}) \tag{4.3}$$

West-East canyons

$$S^{CAN_{WE}} = \left[\frac{W_{WE}}{W_{WE} + B_{SN}} - \frac{1}{2}\left(\frac{W_{WE} W_{SN}}{(B_{SN} + W_{WE})(B_{WE} + W_{SN})}\right)\right] S_{TOT}^{H} \tag{4.4}$$

South-North canyons

$$S^{CAN_{SN}} = \left[\frac{W_{SN}}{W_{SN} + B_{WE}} - \frac{1}{2}\left(\frac{W_{WE} W_{SN}}{(B_{SN} + W_{WE})(B_{WE} + W_{SN})}\right)\right] S_{TOT}^{H} \tag{4.5}$$

where Δz_{IU} is the vertical urban grid spacing, S_{TOT}^{H} is the total horizontal area of the cell, $\left[S_{IU}^{V_{WE}}\right]_{MAX}$ and $\left[S_{IU}^{V_{SN}}\right]_{MAX}$ are the maximal surfaces that can be occupied by the walls.

Following the work of Martilli el al. (2002), the impact of every urban surface type (canyon, floor, roof, wall) on the momentum, energy, humidity, and turbulent kinetic energy, is computed separately. Mind that the implementation of BEM inside the UCP does not have neither a direct impact on the calculation of the buildings effects on the momentum nor on the turbulent kinetic energy fluxes. Thus, momentum loss due to friction, and the shear and buoyant production of TKE at the roofs, are calculated with $MOST$ and the classical surface layer theory, with the loss distributed between the ground level and the level of the highest building. In addition, the drag and the increased conversion of Mean Kinetic Energy into Turbulent Kinetic Energy on the vertical surfaces are parametrised following the work of Raupach et al. (1991). The complete calculation of these fluxes can be found in Martilli et al. (2002). All the horizontal fluxes induced by the canyons, are also calculated in the same way as in Martilli's UCP (Martilli et al., 2002).

On the other hand, the presence of BEM has a direct impact on the computation of the sensible and latent heat fluxes from the roofs, as well as those from the walls. In particular, when a roof-top air-conditioning system is in use, building's roofs will exchange with the atmosphere the air-conditioning fluxes H^{tot}_{atm} and E^{tot}_{atm} (cf. equation (3.22)). On the other hand vertical walls will exhcange latent and sensible heat fluxes produced by natural ventilation (cf. equations (3.3) – (3.4)), and (when a verical wall air-conditioning is considered) the fluxes H^{n}_{atm} and E^{n}_{atm} (cf. equation (3.21)).
In order to take those factors into account, BEM is coupled to the UCP by assuming that every urban level IU corresponds to a particular floor (cf. Figures 3.1, 4.1). As in BEM the internal temperature and humidity are changing with time, an urban level IU can have different types of floors according to the height of the corresponding building. For instance in the Figure 4.3, the level IU-1 has two different floors: the first being an intermediate one, and the second being directly in contact with the roof. Typically the latter will heat more the internal air as it will receive more outdoor solar radiation. Starting from these considerations, every urban class is composed by a given number of building types (N_{type}), having the same dimensions (B_{WE} and B_{SN}), and a different number of floors. The parameter N_{type} is calculated starting from the distribution γ: a building type i_{type} of height iu exists only if $\gamma(z_{iu}) \neq 0$. In that case we also define the term $\mathcal{P}_{type}(i_{type})$ ($\forall\ i_{type} = 1, \cdots, N_{type}$) set equal to $\gamma(z_{iu})$ and describing the probability of having a building of type i_{type} (with height iu). In the present UCP the BEM module is run for every type of building. Then for every urban grid level IU, a mean sensible and latent heat flux from the walls is calculated by averaging over all the types of buildings. Remark that for a given urban face iu, there is at most one type of building for which $\gamma(z_{iu}) \neq 0$, thus there is no need to average the fluxes generated at roof level.

Computation of the sensible fluxes

The sensible fluxes at roof level, are given by the fluxes produced by turbulent activities ($F\theta^{tur}$), plus the fluxes ejected to the atmosphere through air-conditioning ($F\theta^{atm}$). In particular for a generic roof located at a height iu, the total horizontal sensible flux $F\theta^{hor}_{iu}$ $[Kg \cdot \frac{K}{s}]$ is given by:

$$F\theta^{hor}_{iu} = \left[F\theta^{tur}_{iu} + F\theta^{atm}_{iu}\right] S^{H}_{iu} \tag{4.6}$$

According to Martilli et al. (2002), the term $F\theta_{iu}^{tur}$ $[\frac{kg}{m^3} \cdot K \cdot \frac{m}{s}]$ is computed using the Louis formulation (Louis, 1979):

$$F\theta_{iu}^{tur} = -\rho_{IU} \frac{k^2}{\left[ln\left(\frac{\frac{\Delta Z_{IU}}{2}}{z_{0,iu}}\right)\right]^2} \mid U_{IU}^{hor} \mid \left(\theta_{IU}^{air} - \theta_{iu}^{rof}\right) fh\left(\frac{\frac{\Delta Z_{IU}}{2}}{z_{0,iu}}, Ri_B\right) \tag{4.7}$$

where U_{IU}^{hor} is the horizontal wind component, Ri_B the bulk Richardson number at the level IU, k the von Karmann constant equal to 0.4, θ_{iu}^{rof} the surface temperature of the roof, and fh the expression used in Louis (1979).
The value of $F\theta_{iu}^{atm}$ $[\frac{kg}{m^3} \cdot K \cdot \frac{m}{s}]$ is given by:

$$F\theta_{iu}^{atm} = \frac{H_{atm,iu}^{tot}}{C_p\left(B_{WE}B_{SN}\right)} \tag{4.8}$$

where $H_{atm,iu}^{tot}$ $[W]$ is calculated according to the expression (3.22). Remark that if a vertical wall air-conditioning is in use the term $F\theta_{iu}^{atm}$ is equal to 0.

The total sensible fluxes from vertical surfaces ($F\theta_{IU}^{ver}$ $[Kg \cdot \frac{K}{s}]$), are given by the sum of the turbulent contribution ($F\theta_{IU}^{tur}$), the heat fluxes exchanged through natural ventilation ($F\theta_{IU}^{vent}$), and the heat emitted from air-conditioning facilities ($F\theta_{IU}^{atm}$). The contributions of the west-east and of the south-north oriented walls are summed together:

$$F\theta_{IU}^{ver} = \left[F\theta_{IU}^{tur} + F\theta_{IU}^{vent} + F\theta_{IU}^{atm}\right]^{WE}\left[S_{IU}^{V_{WE}}\right]_{MAX} + \left[F\theta_{IU}^{tur} + F\theta_{IU}^{vent} + F\theta_{IU}^{atm}\right]^{SN}\left[S_{IU}^{V_{SN}}\right]_{MAX} \tag{4.9}$$

The calculation of $F\theta_{IU}^{tur}$ $[\frac{kg}{m^3} \cdot K \cdot \frac{m}{s}]$ is done with a similar method used by Martilli et al. (2002), in which the sensible heat coefficient is computed as a function of the between-building wind speed (Arnfield and Grimmond, 1998, Clarke, 2001). The difference lies in the fact that the presence of windows has to be taken into account, and that the value of $F\theta_{IU}^{tur}$ is obtained by averaging over all the building types. In particular for a north-south oriented canyon we have:

$$\begin{aligned}\left[F\theta_{IU}^{tur}\right]^{WE} = -\frac{h_{c,IU}}{C_p} \sum_{i=1}^{N_{type}} \mathcal{P}_{type}(i) \Big\{ p_{win} \Big[\left(\theta_{IU}^{air} - \theta_{i,IU}^{west^{win}}\right) + \left(\theta_{IU}^{air} - \theta_{i,IU}^{east^{win}}\right) \Big] \\ + \left(1 - p_{win}\right) \Big[\left(\theta_{IU}^{air} - \theta_{i,IU}^{west^{wall}}\right) + \left(\theta_{IU}^{air} - \theta_{i,IU}^{east^{wall}}\right) \Big] \Big\}\end{aligned} \tag{4.10}$$

where p_{win} is the window proportion, θ_{IU}^{air} $[K]$ is the outdoor air potential temperature, $\theta_{i,IU}^{west^{wall/win}}$ $[K]$ and $\theta_{i,IU}^{east^{wall/win}}$ $[K]$ are the surface potential temperatures of the west and the east walls/windows of the building type i at level IU. The term $h_{c,IU}$ $[\frac{W}{m^2K}]$ is the convective heat transfer coefficient which is calculated in the same way as in (3.9) by replacing U^{hor} with the corresponding horizontal velocity at the level IU (Clarke, 2001). The calculation of the term $\left[F\theta_{IU}^{tur}\right]^{SN}$ is done in the same way by replacing in (4.10) the east-west potential temperatures with their corresponding south-north values.

The terms $\left[F\theta_{IU}^{vent}\right]^{WE}$ and $\left[F\theta_{IU}^{vent}\right]^{SN}$ have also to be computed by averaging over the different types of building. In particular for a given building type i, the sensible heat flux exchanged through natural ventilation is given by (cf. equation (3.3)):

$$H_{IU}^{vent,i} = -(1-\beta)\rho_{IU}C_pV_a\left(\theta_{IU}^{ext} - \theta_{IU}^{int,i}\right) \tag{4.11}$$

where $\theta_{IU}^{int,i}$ is the internal potential temperature of the floor located at the level IU and of the building type i. Starting from (4.11), the averaged sensible heat flux exchanged through natural ventilation at the level IU (H_{IU}^{vent} $[W]$) is computed by:

$$H_{IU}^{vent} = \sum_{i=1}^{N_{type}} \mathcal{P}_{type}(i)H_{IU}^{vent,i} \tag{4.12}$$

We will assume that the flux H_{IU}^{vent} is spread homogeneously along the west-east and the south-north directions. With this assumption, the terms $\left[F\theta_{IU}^{vent}\right]^{WE}$ $[\frac{kg}{m^3}\cdot K\cdot\frac{m}{s}]$ and $\left[F\theta_{IU}^{vent}\right]^{SN}$ $[\frac{kg}{m^3}\cdot K\cdot\frac{m}{s}]$ are finally given by:

$$\begin{aligned}\left[F\theta_{IU}^{vent}\right]^{WE} &= \frac{1}{2}\left[\frac{H_{IU}^{vent}}{C_pB_{WE}\Delta Z_{IU}}\right]; \\ \left[F\theta_{IU}^{vent}\right]^{SN} &= \frac{1}{2}\left[\frac{H_{IU}^{vent}}{C_pB_{SN}\Delta Z_{IU}}\right]\end{aligned} \tag{4.13}$$

where ΔZ_{IU} is the vertical size of the urban cell IU.

Finally the heat flux generated from air-conditioning facilities at the level IU ($F\theta_{IU}^{atm}[\frac{kg}{m^3}\cdot K\cdot\frac{m}{s}]$) is calculated in a similar way. In particular the equations (4.12) and (4.13) are still valid by replacing $H_{IU}^{vent,i}$ with $H_{IU}^{atm,i}$ given by (3.21). Remark that if a roof-top air-conditioning is in use, the terms $H_{IU}^{atm,i}$ are equal to zero.

For every building type, the surface temperatures of roofs, walls and windows are computed inside the BEM module. Details of these calculation are given in chapter 3. The calculation of the shortwave and the longwave radiation reaching the urban surfaces (needed for the computation of the energy budget for every surface) is performed following the work of Martilli et al. (2002). In particular a $2D$ radiation module is used, in which view factors are computed for each urban grid layer in order to take into account shadowing and radiation trapping in the street canyon. Moreover multiple reflections of the incident solar radiation and longwave emissions between walls and canyon floors are also considered at each urban grid (Figure 4.4).

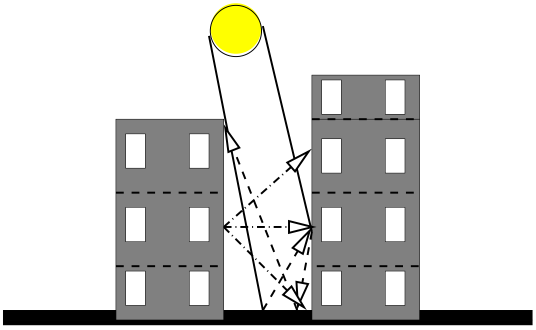

FIGURE 4.4: Representation of the radiation trapping effects in the urban module, including the directly incident solar radiation (solid lines), reflected solar radiation (dashed lines), and longwave reemissions from surfaces (dash-dotted lines).

In UCP-BEM, some modifications have been introduced in order to take into account the presence of windows on the vertical surfaces. In particular the reflected solar radiation from walls have been computed using an averaged albedo (α_{wal}^{AV}):

$$\alpha_{wal}^{AV} = (1 - p_{win})\,\alpha_{wal} + p_{win}\alpha_{win} \tag{4.14}$$

Note also that the longwave radiation emitted from a surface is a function of the emissivity and the temperature of that surface. For this reason the calculation of the longwave emissions from vertical surfaces have also been modified by separating the contribution of the walls (with a probability $(1 - p_{win})$) from that of the windows (with probability p_{win}). The complete calculation of the radiation at the different walls is presented in the Appendix *A*. For every urban class, the radiation calculation is performed twice: at first the west-east oriented walls are considered and then the south-north (cf. Figure 4.5).

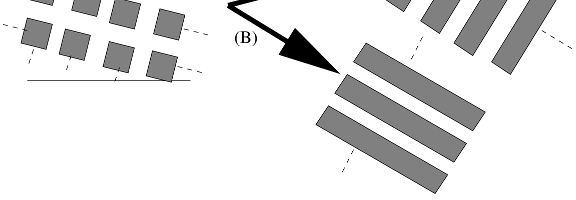

FIGURE 4.5: Representation of the radiation computation. A first calculation is performed over a west-east oriented canyon (A), and then over a south-north one (B). In the two cases a mean surface wall temperature T_M^{wal} is calculated by performing an average over all the building types.

Remark that this $2D$ approach is less CPU demanding than a three-dimensional calculation but leads to some errors as the interactions between the west-east an the south-north oriented walls are not taken into account. We also point out that on one hand, the present UCP deals with different building types, each being characterised by different wall temperatures. On the other hand, the two-dimensional radiation calculation needs a homogeneous temperature along each west-east and south-north oriented street canyon. Taking this into account, a mean temperature is computed along the walls of every street canyon by averaging the longwave emissions from the walls of the different building types. In particular for a vertical level IU and for every direction the following expression is used for the mean wall temperature:

$$\epsilon\sigma\left(T^{wal}_{M,IU}\right)^4 = \frac{1}{N_{type}}\sum_{i=1}^{N_{type}}\epsilon\sigma\left(T^{wal}_{i,IU}\right)^4$$

$$\Rightarrow T^{wal}_{M,IU} = \left[\frac{1}{N_{type}}\sum_{i=1}^{N_{type}}\left(T^{wal}_{i,IU}\right)^4\right]^{\frac{1}{4}} \tag{4.15}$$

where $T^{wal}_{M,IU}$ is the surface averaged temperature of the wall at the level IU (cf. Figure 4.5) and $T^{wal}_{i,IU}$ is the surface wall temperature of the building type i at the level IU.

Computation of the humidity fluxes

The humidity fluxes at the roof level $\left(F\mathcal{H}^{hor}\ [\frac{Kg}{s}]\right)$ are given by the latent heat fluxes ejected into the atmosphere through air-conditioning $\left(F\mathcal{H}^{atm}\right)$. In particular, at a given height iu this is computed by:

$$F\mathcal{H}^{hor}_{iu} = F\mathcal{H}^{atm}_{iu} S^{H}_{iu} \tag{4.16}$$

The term $F\mathcal{H}^{atm}_{iu}\ [\frac{Kg}{m^3}\cdot\frac{m}{s}]$ is given by:

$$F\mathcal{H}^{atm}_{iu} = \frac{E^{tot}_{atm,iu}}{l\left(B_{WE}B_{SN}\right)} \tag{4.17}$$

where the latent heat $E^{tot}_{atm,iu}$ $[W]$ is calculated following the expression (3.22). Remark that if a vertical wall air-conditioning system is in use the term $F\mathcal{H}^{atm}_{iu}$ is set to zero.

The total humidity fluxes from vertical surfaces $\left(F\mathcal{H}^{ver}_{IU}[\frac{Kg}{s}]\right)$ are given by the latent heat fluxes exchanged through natural ventilation $\left(F\mathcal{H}^{vent}_{IU}\ [\frac{Kg}{m^3}\cdot\frac{m}{s}]\right)$ and those emitted from air-conditioning facilities ($F\mathcal{H}^{atm}_{IU}\ [\frac{Kg}{m^3}\cdot\frac{m}{s}]$). In particular, similarly to the sensible heat flux contribution, this can be computed by:

$$F\mathcal{H}_{IU}^{ver} = \left[F\mathcal{H}_{IU}^{vent} + F\mathcal{H}_{IU}^{atm}\right]^{WE} S_{IU}^{V_{WE}} + \left[F\mathcal{H}_{IU}^{vent} + F\mathcal{H}_{IU}^{atm}\right]^{SN} S_{IU}^{V_{SN}} \tag{4.18}$$

The terms $\left[F\mathcal{H}_{IU}^{vent}\right]^{WE}$ and $\left[F\mathcal{H}_{IU}^{vent}\right]^{SN}$ are given by:

$$\begin{aligned} \left[F\mathcal{H}_{IU}^{vent}\right]^{WE} &= \frac{1}{2}\left[\frac{E_{IU}^{vent}}{lB_{WE}\Delta Z_{IU}}\right] \\ \left[F\mathcal{H}_{IU}^{vent}\right]^{SN} &= \frac{1}{2}\left[\frac{E_{IU}^{vent}}{lB_{SN}\Delta Z_{IU}}\right] \end{aligned} \tag{4.19}$$

where E_{IU}^{vent} is the averaged latent heat flux exchanged through natural ventilation at the level IU. It is calculated similarly to (4.12) by replacing $H_{IU}^{vent,i}$ with $E_{IU}^{vent,i}$. In particular this last term describes the latent heat exchanged through ventilation by a building type i at the level IU, and (following (3.4)) it is given by:

$$E_{IU}^{vent,i} = -(1-\beta)\,\rho_{IU} l V_a \left(q_{V_{IU}}^{air} - q_{V_{IU}}^{int,i}\right) \tag{4.20}$$

here $q_{V_{IU}}^{air}$ is the specific humidity of the outdoor air at the urban height IU, and $q_{V_{IU}}^{int,i}$ that of the indoor air of the building of type i.

The term $F\mathcal{H}_{IU}^{atm}$ is calculated in a similar way by replacing E_{IU}^{vent} with E_{IU}^{atm} inside (4.19). Finally note that for a roof-top air-conditioning system this last term is equal to zero.

Calculation of the urban sources

The implicit and explicit sources of momentum, energy, humidity, and turbulent kinetic energy, are calculated with the same method used in Martilli et al. (2002). In particular for a given variable Γ we have:

$$a_{\Gamma,I}\Gamma + b_{\Gamma,I} = \frac{F_{\Gamma,I}^{H} + F_{\Gamma,I}^{V}}{V_I^A} \quad \forall \quad \textit{mesoscale cell } I \tag{4.21}$$

where V_I^A is the volume of air in the mesoscale grid cell I, and $F_{\Gamma,I}^{H}$ and $F_{\Gamma,I}^{V}$ are the horizontal and vertical urban sources interpolated to the grid of the mesoscale model. The methodology used to connect the two grids is explained in detail in Martilli et al. (2002).

In the present work the calculation of V_I^A has been modified in order to follow the geometry of the Figure 4.2:

$$V_I^A = Vtot_I \left[1 - \left(\frac{B_{WE} B_{SN}}{(B_{WE} + W_{SN})\,(B_{SN} + W_{WE})} \right) \frac{1}{(z_{i+1} - z_i)} \cdot \right.$$
$$\left. \sum_{iu=iub}^{iu=iue} \Gamma(z_{iu+1})\,(\min(z_{i+1}, z_{iu+1}) - \max(z_i, z_{iu})) \right] \tag{4.22}$$

where *iub* and *iue* are the first and the last urban grid levels inside the mesoscale cell I (cf. Figure 4.6) and $Vtot_I$ is the total volume of the cell (building+air).

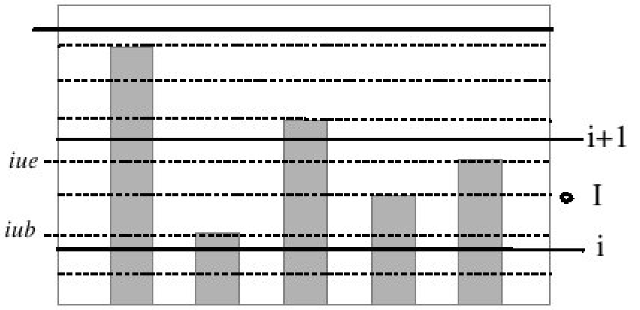

FIGURE 4.6: Representation of the connection between the urban module grid (dashed lines) and the mesoscale model grid (solid lines). *iub* and *iue* are the lowest and the highest urban model levels in the mesoscale level I (Martilli, 2001)

4.4 Numerical results

One and two-dimensional simulations are applied to MM-UCP-BEM in order to test the model and study the impact of anthropogenic air-conditioning fluxes on urban climate (e.g. air temperature, wind, TKE). Furthermore, in section 4.4.2.2 the $2D$ configuration is used to carry out a sensitivity study. The goal is to evaluate the effectiveness of different strategies for the control of the negative effects that these heat sources can produce: UHI intensification, cooling energy demands, air quality, CO_2 production, etc. It is important to point out that the two-dimensional simulations presented in this section have qualitative interests, and do not intend to perform a quantitative analysis of the impacts of anthropogenic air-conditioning since there are no measurements of it. On the other hand remark that the possibility to estimate informations that cannot be directy measured is a clear advantage of numerical modelling. Furthermore, the different parts of the present simulation system (MM, UCP, and BEM) have been already tested and successfully compared to measured data. Thus, the following results are also expected to give reliable informations concerning the impact of anthropogenic air-conditioning fluxes, and cooling energy demands control strategies

4.4.1 1D simulations

One-dimensional simulations are performed over a $1km \times 1km$ wide cell with 100% urban soil coverage. In particular a base-case simulation is built up with the physical parameters of different urban surfaces (wall, roof, street) being those originally used in the context of Martilli's UCP for theoretical applications (Martilli et al., 2002), one-dimensional off-line simulations (Roulet et al., 2005), and for the Athens case (Martilli et al., 2003). In addition for the present urban parameterisation, the properties of the floors have been set equal to those of the roofs (cf. Table 4.1).

Surface	K$[10^6 m^2 s^{-1}]$	C$_s[MJm^{-3}K^{-1}]$	$\varepsilon[-]$	$\alpha[-]$	z$_0[m]$
Street	0.286	1.4	0.95	0.2	0.01
Wall	0.67	1.0	0.90	0.2	-
Roof/Floor	0.67	1.0	0.90	0.2	0.01

Table 4.1: Physical parameters adopted for the $1D$ test simulations: thermal diffusivity K, specific heat capacity C_s, emissivity ε, albedo α, and roughness length z_0 (Martilli et al., 2002).

The other input parameters defined for the base-case simulation are:

- building orientation (cf. Figure 4.7): 0° west-east and 90° south-north.
- street and building width: $15m$ for both ($B_{WE} = B_{SN} = W_{WE} = W_{SN} = 15m$).
- building height distribution: 100% at $15m$. No intermediate floors are considered.
- windows proportion: $p_{win} = 0.3$.

The simulation period is from 00 LT 25 June to 00 LT 28 June 2002.

A: Comparison between different geometries

This first test aims to verify that the present UCP is able to reproduce similar results to the parameterisation of Martilli et al. (2002), when the same kind of geometry is considered, and the fluxes generated from air-conditioning facilities are not taken into account. For this purpose we impose a constant internal air temperature of 20°C, but the corresponding sensible and latent heat fluxes generated from anthropogenic air-conditioning are not ejected into the atmosphere. As one can see in the Figure 4.7, Martilli's parameterisation with two street orientations (Figure 4.7-A) is compared to the base-case solution (Figure 4.7-B) and to the result obtained with the present UCP by setting two urban classes with a very low west-east and south-north oriented canyon (Figure 4.7-C).

In all cases the urban parameters of the Table 4.1 are considered and the geometrical properties of buildings and streets (dimension, orientation) are those of the base-case configuration except for the width of the small canyons in the case C which is set to $0.5m$.

From Figure 4.8 one can first observe that the air potential temperature generated by Martilli's urban parameterisation is higher than the one obtained with the base-case configuration. In fact expressions (4.6), (4.9) and (4.21) indicate that the sensible fluxes are directly proportional to the magnitude of urban surfaces (roof, wall, street) and inversely proportional to the volume of air in the mesoscale grid. In this context one can observe from Figure 4.7 that the surface and the volume occupied by buildings is greater in the configuration A (Martilli's UCP geometry) than in B (base-case configuration). This statement of fact explains the difference between the two temperatures.
Figure 4.8 also indicates that the present UCP can reproduce the two-dimensional geometry of Martilli's urban parameterisation. In fact the two near ground temperatures converge to very similar solutions if the configuration C (cf. Figure 4.7) is considered.

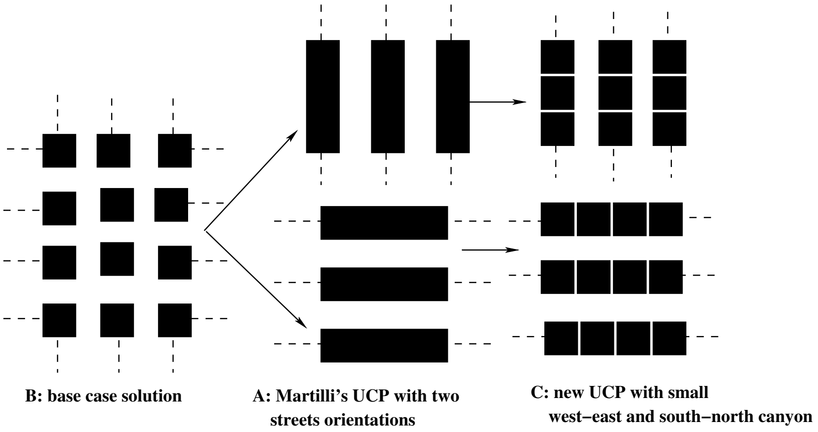

FIGURE 4.7: **A**: Martilli's UCP with 0° west-east and 90° south-north oriented canyons. **B**: base case geometry. **C**: new UCP with small west-east and south-north canyons.

B: Comparison between different types of boundary conditions

The major difference between the two UCP lies in the treatment of the internal wall boundary condition: in the parameterisation of Martilli et al. (2002), the internal temperature is fixed, while in the present model its value can vary with time. In particular when there is no artificial heating/cooling by the air-conditioning system, a free floating condition is generated and the internal air temperature varies with time in correspondance to the heat flux produced inside/outside the room. In Figure 4.9 the free floating and the fixed internal boundary conditions are compared accordingly to the base-case configuration, and the effect on the near-ground air potential temperature is analysed.

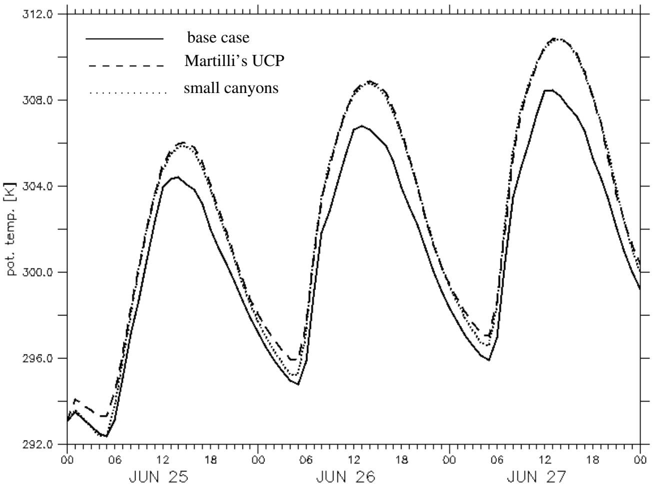

FIGURE 4.8: The potential temperature at $5m$ above ground as a function of time from 00 LT 25 June to 00 LT 28 June for the base case simulation (solid lines), the case A (dashed lines) and the case C (dotted lines) of the Figure 4.7.

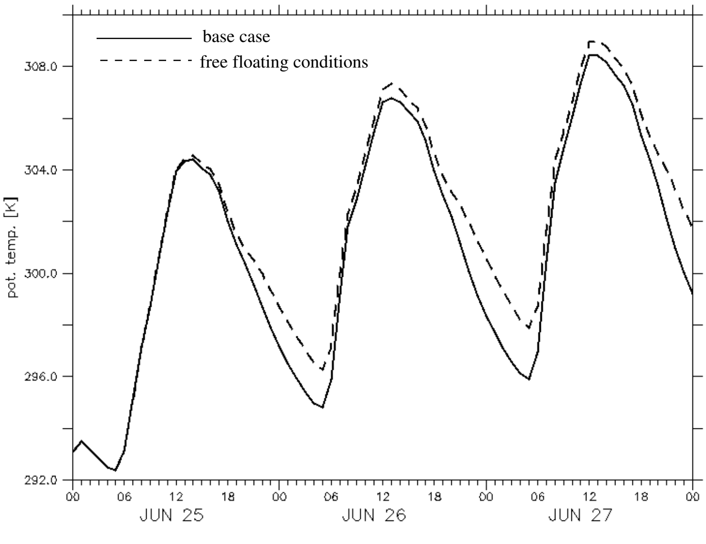

FIGURE 4.9: The potential temperature at $5m$ above ground as a function of time from 00 LT 25 June to 00 LT 28 June for the base case simulation with a fixed internal temperature of 20°C (solid lines), and for the free floating conditions (dashed lines).

Figure 4.9 indicates that the potential temperature in free floating conditions is higher than the one obtained by setting a fixed internal temperature. In fact, for this summer condition the free floating case generates a progressive heating of the indoor air during the day. This leads to an increase of walls' temperature generating a net conductive sensible heat flux from the walls to the exterior air. Remark that the temperature difference generated by the two boundary conditions is higher during night-time with peak values of more than $1°C$.

The result of the Figure 4.9 has been obtained by considering a single floor of $15m$ height (base-case assumption) which leads to an homogenous air temperature inside all the building. On the other hand if different floors are considered, the corresponding internal air temperature will not remain constant with height: every floor is subject to a different solar radiation leading to a differential heating/cooling of the indoor air and consequently to different anthropogenic sensible and latent heat fluxes for cooling and heating purposes. In particular the following results indicate that the number of floors can have an important impact on the amount of heat generated from air-conditioning facilities.

C: The impact of floors on the air-conditioning fluxes

In the next test the physical parameters related to the base-case configuration are applied to a three-floors building, each floor being $5m$ height. The internal temperature and humidity are fixed inside a comfort range, and a roof-top air-conditioning system is considered. The internal heat sources generated by the presence of people and equipments are also taken into account. All the physical parameters related to anthropogenic heat sources are summarised in the Table 4.2.

As one can see in the Figure 4.10, the temporal evolution of the occupancy ratio (φ_P) adopted for the test is a simple step function in which the maximal presence of people is supposed to be between 09.30 LT and 18.30 LT.

In order to preserve the internal temperature and humidity inside the comfort conditions, every floor has to eject a certain quantity of sensible and latent heat flux into the atmosphere. In particular the time evolution of sensible heat presented in the Figure 4.11 indicates that every floor produces a different amount of heat.

Note that while the energy released by the first and the second floor is comparable, the one ejected by the third is much higher. This is because the third floor is directly submitted to the solar radiation coming from the roof, leading to a more important heating of the indoor air with a consequent increase of cooling-energy needs.

Parameters	**Settings**
Duration of air-conditioning	00-24 LT
Temperature comfort range	$[21.5°C, 22.5°C]$
Relative humidity comfort range	$[0.49, 0.51]$
Thermal efficiency of the total heat exchanger (β)	1.0
Sensible heat generated from occupants (q_{hs})	$54.7 \frac{W}{Person}$
Latent heat generated from occupants (q_{hl})	$64.0 \frac{W}{Person}$
Sensible heat generated from equipments (q_E)	$20 \frac{W}{m^2}$
Air-conditioning system	roof-top
COP of the air-conditioning system	3.5

TABLE 4.2: Representation of the parameters used for the air-conditioning calculation. The temperature comfort range is taken from Roulet (1987) while the internal relative humidity value, as well as the sensible and latent heat released by occupants, from the work of Kikegawa et al. (2003). The sensible heat generated from equipments is derived from Jacobs et al. (2005). The natural ventilation term is not taken into account ($\beta = 1$). Based on the work of Aschie et al. (1999) a standard COP for office buildings of 3.5 has been considered.

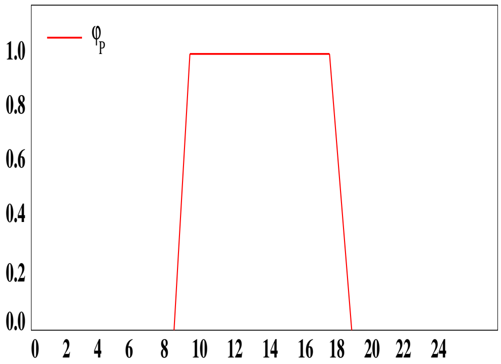

FIGURE 4.10: Time evolution of the occupancy ratio (φ_P).

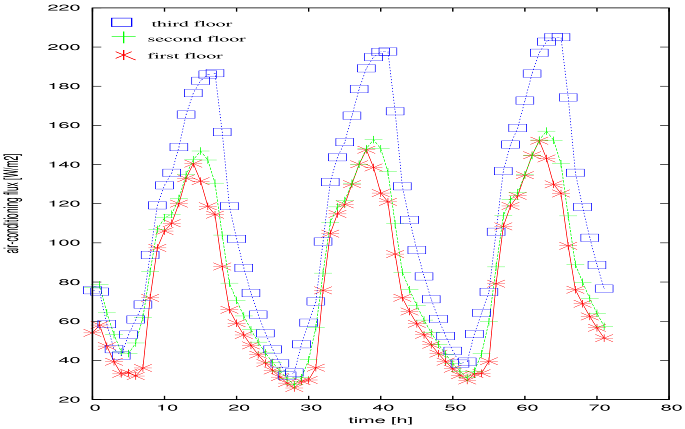

FIGURE 4.11: The sensible heat fluxes ejected from air-conditioning facilities by the different floors as a function of time from 00 LT 25 June to 00 LT 28 June.

Remark that when vertical wall air-conditioning systems are considered, a higher amount of heat will therefore be ejected at the higher levels inside the urban canopy.

In order to evaluate the impact of the fluxes generated by BEM on the exterior microclimate, a set of two-dimensional simulations is presented in the following section. The whole model composed by MM, UCP and BEM is tested over different theoretical cities surrounded on both sides by rural areas. In this context the impact of air-conditioning fluxes is analysed with respect to different meteorological variables (temperature, wind speed, TKE). Furthermore, in section 4.4.3 a sensitivity analysisis is performed over a summer episode with the purpose of identifying the effectiveness of different UHI mitigation strategies and of evaluating the corresponding impact on the total cooling-energy demands.

4.4.2 2D simulations

The domain is similar to the one considered by Martilli et al. (2002), with a horizontal extension of $100km$, a resolution of $1km$ and a flat topography in which a city is surrounded on both sides by rural areas. The model extends vertically up to $12000m$ above ground level with a vertical resolution varying from $5m$ close to the ground to $1000m$ at the top of the domain. The physical parameters of the rural soil are those used by Martilli et al. (2002), for theoretical applications and for the Athens case (Martilli et al., 2003). Furthermore concerning the urban area, two base-case conditions are considered based on North American ($base_{USA}$) and European ($base_{EU}$) cities. The physical parameters for walls (external walls and floors), roofs, and streets adopted for $base_{USA}$ are those used by Dupont et al. (2004), for the city of Philadelphia. The ones considered for $base_{EU}$ are taken from the work of Roulet over the city of Basel (Roulet, 2004). All the cities are divided into a downtown-commercial area with tall buildings, surrounded on both sides by a residential area in which smaller residences are considered. For the two cases ($base_{USA}$, $base_{EU}$) the following input parameters are considered (index $''C''$ refers to a commercial building and $''R''$ to a residential one):

$\mathbf{base_{USA}}$

• building orientation: 0° west-east and 90° south-north;

• $40km$ wide city with 8 commercial cells surrounded on both sides by 16 residentials;

• $B^C_{WE} = 30m$, $W^C_{WE} = 60m$, $B^C_{SN} = 30m$, $W^C_{SN} = 0m$, $B^R_{WE} = 20m$, $W^R_{WE} = 40m$, $B^R_{SN} = 20m$ and $W^R_{SN} = 0m$;

• commercial building-height distribution: 100% at $50m$ with $5m$ height floors;

• residential building height distribution: 5% at $5m$, 25% at $10m$, 40% at $15m$, 25% at $20m$ and 5% at $25m$ height. Every building type is composed by a $5m$ height floor;

- windows proportion: $p^C_{win} = 0.3$, $p^R_{win} = 0.2$.

$\mathbf{base_{EU}}$

- building orientation: 0° west-east and 90° south-north;
- $30km$ wide city with 8 commercial cells surrounded on both sides by 11 residentials;
- $B^C_{WE} = 25m$, $W^C_{WE} = 25m$, $B^C_{SN} = 25m$, $W^C_{SN} = 0m$, $B^R_{WE} = 20m$, $W_R = 21.25m$, $B^R_{SN} = 20m$ and $W^R_{SN} = 0m$;
- commercial building-height distribution: 100% at $20m$ with $5m$ height floors;
- residential building height distribution: 5% at $5m$, 25% at $10m$, 40% at $15m$, 25% at $20m$ and 5% at $25m$ height. Every building type is composed by a $5m$ height floor;
- windows proportion: $p^C_{win} = 0.3$, $p^R_{win} = 0.2$.

Remark that the corresponding plane area density (λ_P) are of the order of 0.5 for the European and 0.3 for the North American base-case. These values are in the range of real cities (Grimmond and Oke, 2000, Ratti et al., 2003).

It is assumed that the buildings inside the commercial areas have an air-conditioning system in use from $08LT$ to $20LT$ (working period). On the other hand any anthropogenic cooling is considered inside the residentials. All the physical parameters related to anthropogenic heat sources produced by residential and commercial buildings are summarised in the Table 4.3 (the same values are used for $base_{USA}$ and $base_{EU}$).

Parameters	**Settings (C)**	**Settings (R)**
Duration of air-conditioning	08-20 LT	-
Temperature confort range	$[21.5°C, 22.5°C]$	-
Relative humidity confort range	$[0.49, 0.51]$	-
Thermal efficiency of the total heat exchanger (β)	1.0	0.6
Sensible heat generated from occupants (q_{hs})	$54.7\frac{W}{Person}$	$54.7\frac{W}{Person}$
Latent heat generated from occupants (q_{hl})	$64.0\frac{W}{Person}$	$64.0\frac{W}{Person}$
Sensible heat generated from equipments (q_E)	$20\frac{W}{m^2}$	$20\frac{W}{m^2}$
Air conditioning system	roof-top	-
COP of the air-conditioning system	3.5	-

Table 4.3: Representation of the parameters used for the air-conditioning calculation. The temperature comfort range is taken from Roulet (1987), while the internal relative humidity value, as well as the sensible and latent heat released by occupants, from the work of Kikegawa et al. (2003). The sensible heat generated from equipments is derived from Jacobs et al. (2005). The commercial buildings have no natural ventilation ($\beta = 1$), while for the residentials the ventilation rate β is set to 0.6 (Kikegawa et al., 2003). Based on the work of Aschie et al. (1999), a standard COP for office buildings of 3.5 has been considered. No air-conditioning systems are considered for the residential buildings.

For both, the American and the European base-case, the occupancy ratio inside the commercial areas (φ_P^C) is the same step function presented in the Figure 4.10 in which the maximal presence of people ($\varphi_P^C = 1$) is supposed to be between $09.30LT$ and $18.30LT$. Assuming that the total population of the city remains constant during the day, the corresponding occupancy ratio for residential areas can be derived by the following expression:

$$\varphi_P^R(t) = 1 - \varphi_P^C(t) \tag{4.23}$$

In a similar way starting from a peak number of occupants per unit of floor area in the commercial cells (P_C), a corresponding peak number can be derived for residential areas (P_R):

$$P_R = P_C \frac{N_C G_C}{N_R G_R} \tag{4.24}$$

where N_C, N_R are respectively the number of commercial and residential cells in the city and G_C, G_R are "geometric factors" related to commercial and residential areas. The complete derivation of (4.23) and (4.24), as well as the expressions for G_R and G_C are presented in the Appendix B. In the following simulations P_C for the American base-case is set to $0.125\frac{person}{m^2}$ and the one for the European city to $0.0625\frac{person}{m^2}$. Assuming a square city configuration, one can derive that the corresponding total population reaches realistic values with 8×10^6 inhabitants for the American city and 4.5×10^6 for the European (cf. Appendix B).

The meteorological initial conditions are a wind speed from the West of $1\frac{m}{s}$ and a relative humidity equal to 50% in the first $1000m$ and then reducing with height. A ground initial potential temperature of $298K$ is considered with an atmospheric stability of $3.5\frac{K}{km}$. A hot climate summer condition is chosen with the simulation day being 15 July 2005 and a latitude of $40.26N$ (Madrid latitude). Finally similarly to the work of Martilli et al. (2002), the column boundary conditions are adopted (one-dimensional vertical resolution of the mesoscale model equations).

4.4.2.1 2D results

Figure 4.12 first shows for the American and European base-case conditions, the comparison between the heat emitted through air-conditioning and the total sensible flux generated at the roof. Observe that in both cases the air-conditioning flux is higher than zero from $08LT$ to $20LT$. In that period this heat is ejected into the atmosphere and a comfort temperature between $21.5°C$ and $22.5°C$ is preserved inside the building (cf. Table 4.3). On the other hand the total sensible flux follows the day cycle of the sun reaching a maximum between $12LT$ and $13LT$. In both cases observe that the heat released by the air-conditioning system generates more than half of the total sensible heat emitted from the roof. In addition as the volume of the air occupied by the American commercial buildings is greater than the one handled by the Europeans, the corresponding air-conditioning flux is also more important leading to a peak value being more than 17% higher.

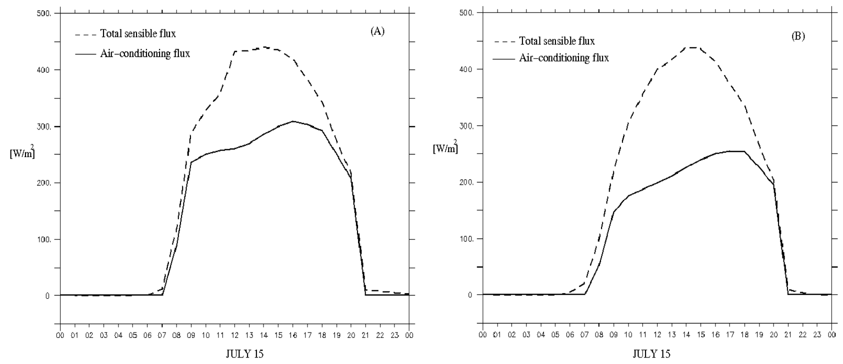

FIGURE 4.12: Air-conditioning flux (solid lines) and total sensible heat flux (dashed lines) at the roof level for $base_{USA}$ (A) and $base_{EU}$ (B). The results refer to an urban cell located at the center of the commercial area.

This amount of anthropogenic heat released into the atmosphere will have a non negligent impact on urban meteorology. For instance Figure 4.13 illustrates that in both cases ($base_{USA}$ and $base_{EU}$) the emission of air-conditioning heat, is directly followed by an increase in the air potential temperature (the same internal comfort conditions are kept in the two simulations).
Remark that the temperature difference between the two simulations (with and without air-conditioning) is zero when the air-conditioning system is not in use. The figure indicates that the potential temperature at the roof-top level is almost $1°C$ higher in the American base-case than in the European one. In addition, at this height the temperature difference between the air-conditioning and the non air-conditioning simulations reaches quite high values with a peak of $1.74°C$ for $base_{USA}$ and of $1.52°C$ for $base_{EU}$.

As it is shown in Figure 4.14, one of the most important effects produced by this temperature increase lies in the intensification of the diurnal UHI. Remark in particular that the air-conditioning heat flux emissions from the roof-top of the commercial buildings generate a neighbouring temperature difference lying between $1°C$ and $2°C$. In addition due to vertical diffusion, a temperature gradient is also generated above and below the roof level.

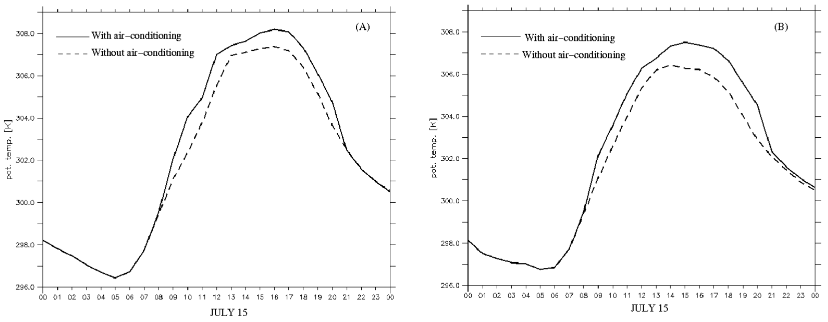

FIGURE 4.13: Roof-top time evolution of the air potential temperatures with (solid lines) and without (dashed lines) the heat emitted through air-conditioning facilities (e.g. heat released into the soil). The $base_{USA}$ case (A) and the $base_{EU}$ (B) are represented. The results refer to an urban cell located at the center of the commercial area.

This aspect is confirmed by the vertical profiles of potential temperature presented in Figure 4.15 in which it has been observed that even if in both, the American and the European base-case, the maximal temperature gradients are located above the roof-top of the commercial buildings, a non negligent impact is also produced on the near-ground air temperature. In particular at this level during the air-conditioning period (from $08LT$ to $20LT$) the temperature increases (averaging along the commercial area) of $0.40°C$ for $base_{USA}$ and $0.70°C$ for $base_{EU}$, with maximal differences achieving more than $1.0°C$.

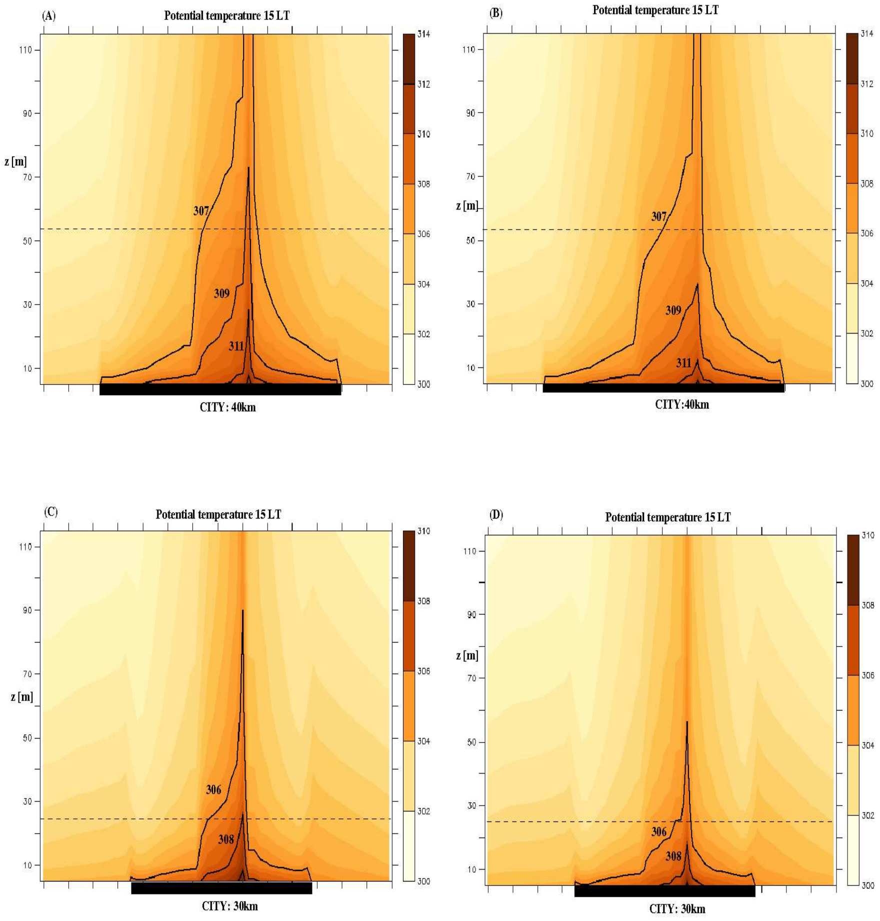

Figure 4.14: Vertical section of the air potential temperature over the American base-case city (A and B), and over the European one (C and D). The air-conditioning (A and C) and the non air-conditioning results are represented and the height of the commercial buildings is scatched in dashed straight lines.

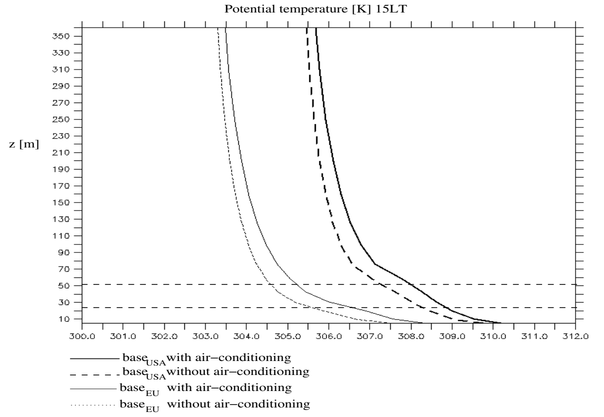

FIGURE 4.15: Vertical profiles of potential temperature at $15LT$ with and without the heat emitted through air-conditioning facilities. The $base_{USA}$ and $base_{EU}$ case are considered and the figure refers to a cell located at the center of the commercial area. The dashed straight lines indicate the heights of the American and European commercial buildings.

Remark that even if the heat emitted from air-conditioning facilities is lower for a building in the European configuration (cf. Figure 4.12), the total increase produced on the external potential temperature is higher for $base_{EU}$ than for $base_{USA}$. This is due to the fact that the plane area density (and consequently the total number of buildings) considered for the commercial area of the American base-case is lower than the one of the European. In this context the vertical profiles of the Figure 4.16 illustrate that by dividing the canyon width of the American base-case commercial area by a factor of two (leading to a λ_P coefficient equal to 0.5) and keeping the same total population, the corresponding impact produced by the air-conditioning flux on the external temperature is much more important. Observe that in both cases the peak temperature difference is clearly located above the roof level and then smoothed in the upward and downward directions. Moreover the case with a higher building density ($W^C_{WE} = W^C_{SN} = 30m$) leads at $15LT$ to a peak temperature increase of more than $1°C$ with a near ground difference of nearly $0.7°C$.

In general this kind of temperature increase inside the urban canopies, can lead to important consequences on the pedestrian comfort and on the building cooling-energy demands (feedback effect). The vertical profiles of the Figure 4.17 indicate that the effect is even more important if vertical wall air-conditioning systems are adopted. In fact in that case the heat is directly emitted inside the street canyons (cf. Figure 3.1) and (due to the presence of buildings) spread within a smaller volume of air. In particular it has been observed that between $08LT$ and $20LT$ the application of a vertical wall air-conditioning system increases the mean near-ground temperature along the commercial area of $1.49°C$ for $base_{EU}$ and $1.24°C$ for $base_{USA}$.

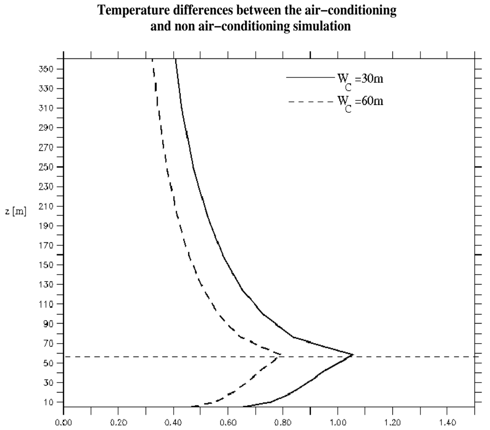

FIGURE 4.16: Vertical profiles at $15LT$ of the difference in the air potential temperature between the air-conditioning and the non air-conditioning simulation. The figure refers to a building located at the center of the commercial area and the $base_{USA}$ case (dashed line) is compared to the one obtained by setting $W_C = 30m$ (solid line). The dashed straight line indicates the height of the American commercial buildings.

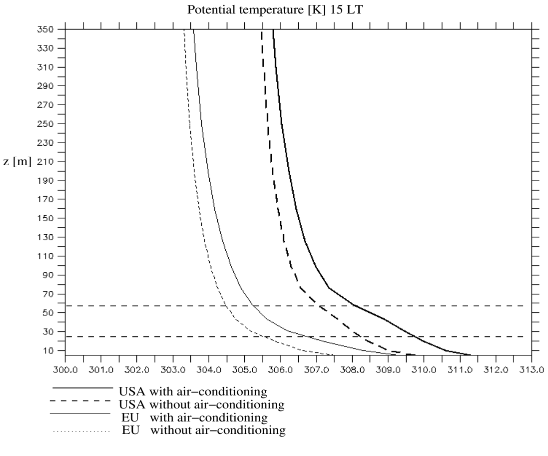

FIGURE 4.17: Vertical profiles of potential temperature at $15LT$ with and without the heat emitted through air-conditioning facilities. The American and the European case are considered supposing a vertical wall air conditioning. The figure refers to a cell located at the center of the commercial area. The dashed straight lines indicate the heights of the American and European commercial buildings

The modification produced by anthropogenic air-conditioning on the magnitude of the total sensible fluxes ejected into the atmosphere can also generate important consequences on other meteorological variables. For instance, as explained in detail in the work of Martilli et al. (2002), the modification of the sensible fluxes from horizontal surfaces has a direct impact on the buoyant production of TKE. This aspect is presented in Figure 4.18 in which one can observe that for both, the American and the European base-case conditions, the generation of air-conditioning fluxes is followed by an increase in the TKE production above the building's roofs of the commercial cells. Also remark that the buoyant production of TKE at the roof-top of the residential buildings is not affected as the air-conditioning flux is only emitted from the commercial areas. In this region during the air-conditioning period, a peak TKE difference of more than 20% has been observed above buildings' roofs. Note that this increase in the TKE production can also have important consequences on pollutant dispersion. In addition, the vertical profiles of Figure 4.19 indicate that this TKE difference can be observed up to the boundary layer height. Remark that the TKE generated by the American base-case is higher than that of the European with the boundary layer rising from $2000m$ to $2400m$.

As explained in Martilli et al. (2002), the momentum fluxes due to horizontal surfaces (roofs and canyons) depend on the bulk Richardson number which is a function of the wind speed and of the air temperature. For this reason the increase in the potential temperature generated by the anthropogenic air-conditioning fluxes, will also have an impact on the magnitude of the wind speed. This aspect is presented in Figure 4.19 in which one can observe that the vertical profiles of horizontal wind speed are greater when the fluxes from air-conditioning facilities are considered. Also remark that in both cases ($base_{USA}$ and $base_{EU}$) the main differences are generated above the roof level as the momentum sources generated by vertical walls do not directly depend on the air potential temperature (Martilli et al., 2002). Finally for the two base-case simulations it has been observed that depending on the hour of the day and on the commercial cell under consideration, this wind speed increase can achieve peak values lying between 5% and 20%.

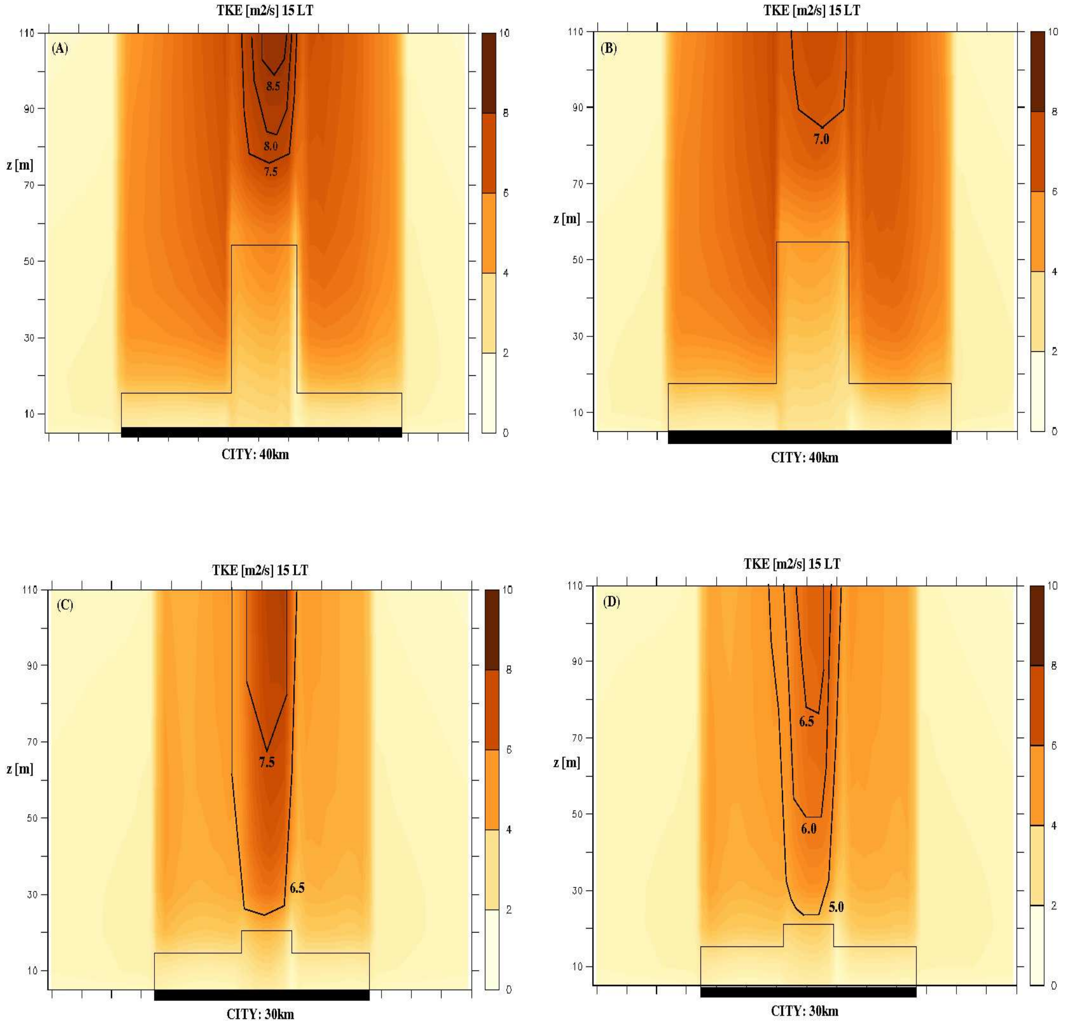

FIGURE 4.18: Vertical profiles of TKE at 15*LT* with (*A* and *C*) and without (*B* and *D*) the air-conditioning flux. The American base-case (*A* and *B*) and the European one (*C* and *D*) are represented.

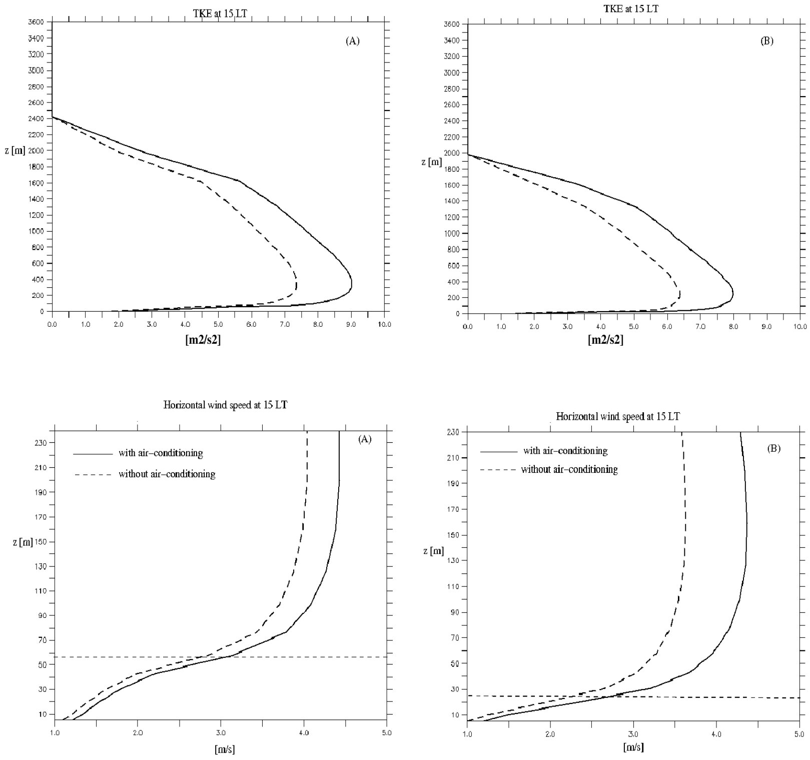

FIGURE 4.19: Vertical distribution of turbulent kinetic energy ((A) and (B)) and of horizontal wind velocity ((C) and (D)) at $15LT$ for a building located at the center of the commercial area. The American ((A) and (C)) and the European ((B) and (D)) base-cases are represented and the air-conditioning simulation (solid lines) is compared to the one in which no air-conditioning flux is emitted (dashed lines). The heights of the American and European buildings are also represented with dashed straight lines.

4.4.2.2 Sensitivity tests

In order to improve the welfare and the comfort of the inhabitants of a city, it is important to identify some long and short term strategies that could reduce the summertime energy consumption generated by air-conditioning facilities and consequently mitigate the UHI formation. For instance, in the study produced by Kikegawa et al. (2003), over the Tokyo area, it is mentioned that for a peak daily temperature increase of $1°C$, $1.5GW$ of new energy cooling demand is required. In this context, the following of this chapter will be focused on a sensitivity study in which the magnitude of the peak energy cooling demands and the temperature differences produced by air-conditioning heat emissions are analysed with respect to different physical parameters. Only the American configuration is considered, but similar results can be obtained with the European simulation. In Table 4.4 the different configurations adopted for the study are resumed. The factors of change in the thermal diffusivity and the specific heat capacity used for this sensitivity analysis (that is, an increase or decrease by a factor of 10 in each parameter) are arbitrary chosen, but they are not unrealistic (Masson et al., 2002, Dupont, 2004). The COP coefficient considered in the case C is taken from the work of Kikegawa et al. (2003). The decrease in the internal comfort temperature of $4°C$ (case B) leading to a comfort range of $18 \pm 0.5°C$ is also not unrealistic as indicated in Roulet (1987).

Case	**Settings**
A	base-case conditions
B	internal comfort temperature lowered by $4°C$
C	COP of the air-conditioning system lowered to the value of 1.2
D	thermal diffusivity of roofs and walls increased by a factor of 10
E	thermal diffusivity of roofs and walls lowered by a factor of 10
F	heat capacity of roofs and walls increased by a factor of 10
G	heat capacity of roofs and walls lowered by a factor of 10

Table 4.4: Representation of the different cases used for the sensitivity analysis (all the physical parameters related to the cases $B, \cdots, G$ are derived from those of the base-case condition A).

Figure 4.20 compares the differences (in %) between the peak energy cooling demands generated by the base-case conditions, and those obtained with the configurations $B, \cdots, G$. Similar persentages have been observed for a vertical wall air-conditioning system.

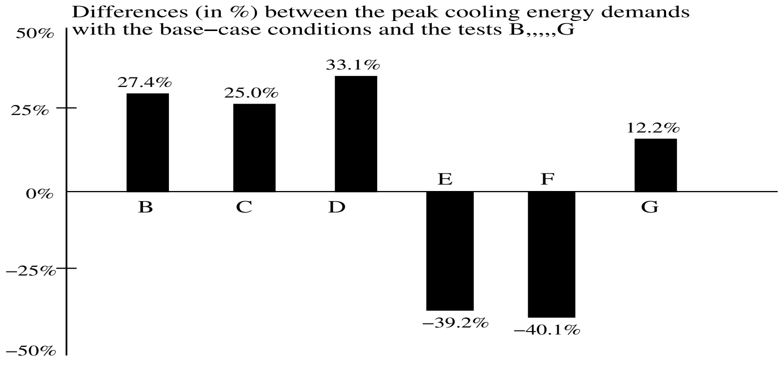

Figure 4.20: Differences in the peak cooling energy demands between the base-case configuration (A), and the tests $B, \cdots, G$. The results have been obtained by averaging the persentages of all the commercial cells.

First remark that a decrease in the internal comfort temperature of $4°C$ generates an air-conditioning heat surplus of more than 27% into the atmosphere. As shown in Table 4.5 this energy produces a non negligent impact on the external near-ground temperature (and consequently on the magnitude of the UHI) leading to a mean increase along the commercial area of $0.51°C$ for a roof-top air-conditioning system and of $1.72°C$ for a vertical wall one. Note also that Table 4.5 follows the result of Figures 4.15-4.17 showing that the near-ground level temperature increase is more important with a vertical wall air-conditioning system.

Case	**Roof-top** $[°C]$	**Vertical-wall** $[°C]$
A	0.40	1.24
B	0.51	1.72
C	0.49	1.65
D	0.53	1.75
E	0.26	0.97
F	0.35	1.11
G	0.42	1.37

Table 4.5: Near ground air temperature differences between a simulation with ejects the air-conditioning fluxes into the atmosphere and another which does not (for example heat released into the soil). Results have been obtained by averaging in space along the commercial area and in time from $08LT$ to $20LT$ (air-conditioning period).

Case C illustrates that a similar behaviour can be obtained if the base-case COP is lowered to the value of 1.2. In particular results indicate that such a decrease in the performance of the air-conditioning system can generate 25% of energy surplus released into the atmosphere, which leads to a mean near-ground temperature increase between $0.49°C$ and $1.65°C$ depending on the system being in use.

The following tests $(D, \cdots, G)$ illustrate that the physical properties of the materials used for the construction of the buildings, can also have a strong impact on the magnitude of the heat generated by air-conditioning systems. For instance in summertime conditions an increased thermal diffusivity of roofs and walls, allows a more important heat transfer between the outdoor and the indoor air. In particular case D indicates that for $base_{USA}$, this measure contribute to increase the internal temperature of the building (heat is transferred from outside to inside) leading to a more important use of anthropogenic air-conditioning. Results show that a thermal diffusivity of roofs and walls rised by a factor of 10, can generate more than 33% of cooling energy surplus along the commercial area, and consequently a near-ground temperature difference between $0.53°C$ and $1.75°C$. As shown in the test D, and opposite effect is obtaind with the thermal diffusivities decreased by a factor of 10, leading to a cooling energy saving of more than 39% and a lower near-ground temperature increase than that observed with the base-case conditions (cf. Table 4.5). The cases F and G treat a similar test with respect to the specific heat capacity. Remark in particular that an opposite behaviour is obtained than that observed with the thermal diffusivity: a higher heat capacity enables to store a bigger amount of heat inside the material (walls and roof) and consequently leads to a smaller heating of the indoor air of the room. In this context the test F indicates that if the heat capacity of the roof and the walls is increased by a factor of 10, the corresponding peak cooling-energy demand decreases by more than 40%. In addition the effect produced on the external temperature is lower than the one obtained with the base-case conditions. Finally observe that an opposite behaviour is produced with a specific heat lowered by a factor of 10 with an increase of more than 12% of the peak coolin-energy demands, and a higher impact on the external near-ground temperature. Results $D, \cdots, G$ indicate that different physical properties of the building's materials impact the way with which the heat is exchanged between the exterior and the interior, and can consequently affect the magnitude of the air-conditioning fluxes. In the same way the feedback produced by the cut-off of air-conditioning waste-heat into the atmosphere is also modified. For instance, it has been observed that the peak cooling-energy savings can vary from $0.45\%/^{\circ}C$ to $4.75\%/^{\circ}C$ of outdoor air temperature depending on the material being in use. Remark in particular that a lower conductivity and a higher heat capacity will generate a lower feedback as they reduce the heat transfer from the outside to the inside air.

4.5 Conclusions

In this chapter we first described a new urban module based on the coupling between the Building Energy Model (BEM) presented in chapter 3 and the Urban Canopy Parameterisation (UCP) of Martilli et al. (2002). The new model UCP-BEM was implemented inside the Mesoscale Model (MM) described in chapter 2 leading to a numerical simulation system that can evaluate the impact of anthropogenic activities generated by buildings inside urban areas: air-conditioning cooling in summer or heating in winter. In a second time a serie of one and two-dimensional simulations was carried out with the purpose of testing the model and of enchancing the understanding of the impact of anthropogenic fluxes generated by BEM.

One-dimensional results first indicated that (as expected) UCP-BEM is equivalent to the parameterisation developed by Martilli et al. (2002) if we consider a two-dimensional geometry and a fixed internal boundary condition, without taking the fluxes of BEM into account. Furthermore the comparison between the fixed and the free floating case indicated that the internal conditions of the buildings (temperature, humidity) can lead to important consequences on the exterior microclimate. The impact of internal heat capacity was also underlined by showing that an increase in the number of intermediate floors can modify the magnitude of the total anthropogenic fluxes emitted from air-conditioning facilities.

Two-dimensional simulations were applied to a typical summertime episod, and the effect of air-conditioning cooling was studied over idealised American and European urban areas. Numerical tests first indicated that the heat released by air-conditioning facilities can have a non negligent impact on the exterior temperature and contribute to increase the UHI formation with further consequences on the magnitude of the cooling energy demands. In this context we observed that inside the urban canopies, vertical wall generate more important effects than roof-top air-conditioning systems, with a mean near-ground temperature difference rising in base-case conditions from $0.40°C$ to $1.24°C$. In addition simulations indicated that there are different factors that can modify the magnitude of the air-conditioning fluxes and consequently the impact produced on the external air temperature. For instance it was observed that an increase of $4°C$ in the comfort temperature inside the buildings, or the introduction of a more efficient air-conditioning system, can generate more than one-forth of cooling-energy savings with further positive consequences on the external temperature. Remark that the modification of these two quantities could represent an efficient short term strategy for the UHI mitigation and the reduction of the air-conditioning consumptions. Concerning other possible countermeasures, it was observed that the physical properties of the urban surfaces (roofs, floors and walls) could also have important effects on the magnitude of the cooling-energy demands. In particular for these summer conditions, materials with a low thermal diffusivity and a high heat capacity enable a smaller heat transfer from the outside to the inside air, generating up to 40% of air-conditioning heat savings. On the contrary materials with high conduction and low heat capacities need up to one-third of cooling energy surplus which enhance the outdoor temperature rise and consequently the UHI phenomena. It was observed that these modifications can also produce very important differences on the feedback which was ranging between $0.45\%/°C$ and $4.75\%/°C$ of outdoor air temperature, depending on the material being in use.

Numerical results indicated that anthropogenic air-conditioning fluxes not only influence the outdoor air temperature, but also the others meteorological variables. In particular it was first observed that for both, the American and the European urban areas, they can generate a non negligent increase in the buoyant production of TKE, with peak differences of more than 20%. In the vertical direction, the impact produced on the TKE was observed up to the boundary layer height. Results also showed that the temperature rise generated by the air-conditioning fluxes leads to an increase in the wind speed, especially above the roof-top of the buildings.

In general looking at the European and the American base-case results, it was observed that the impact of BEM on meteorological quantities can be rather different from one urban area to another. In particular numerical simulations indicated that the urban microclimate can be very sensitive to the density of the urban areas (measured by the λ_P coefficient): a high densified city requires higher cooling-energy needs, and consequently generates a more important impact on the outdoor meteorology.

In conclusion this work shows that the numerical simulation system MM-UCP-BEM is able to simulate the links between anthropogenic fluxes in buildings and urban canopy climate. We observed in particular that the impact of air-conditioning should be taken into account for a complete study of the UHI intensity. The model also proved his capability to perform a detailed sensitivity study for the evaluation of the impact and the effectiveness of different UHI and cooling energy demands control strategies. This is an essential point as the aim in the near future is to utilize this kind of tool as a support for urban planners for the development of more comfortable and less energy-consuming cities.

In the next chapter we intend to extend this kind of study and apply the new simulating tool (MM-UCP-BEM) to a real city. The goal is to show that the model is able to perform a more complete analysis of the complex interactions between urban climate and energy demands for buildings.

Appendix A: Computation of the radiation reaching the external surfaces

Long wave radiation

The long wave radiation Rl reaching a vertical wall W (which can be west, east, south or north oriented) is given by a summation of the following terms:

- long wave radiation coming from the sky (Rl_{sky}).
- fraction of long wave radiation emitted and reflected by the opposite wall and window (Rl_{wal}).
- fraction of long wave radiation emitted and reflected by the street (Rl_{str}).

For example the long wave radiation reaching a west wall W_w at a vertical level iu is given by:

$$Rl_{iu}^{W_w} = Rl_{sky,iu} + Rl_{wal_e,iu} + Rl_{str,iu} \tag{4.25}$$

where $Rl_{sky,iu}$ is computed as in Martilli et al. (2002). The others quantities are given by:

$$\begin{aligned} Rl_{wal_e,iu} = (1-p_{win}) & \left[\sum_{ju=1}^{nu} \psi_{ju,iu}\Gamma(z_{ju+1}) \left(\varepsilon_{wal}\sigma T^4_{wal_e,ju} + (1-\varepsilon_{wal})\, Rl_{wal_e,ju}\right) \right] + \\ p_{win} & \left[\sum_{ju=1}^{nu} \psi_{ju,iu}\Gamma(z_{ju+1}) \left(\varepsilon_{win}\sigma T^4_{win_e,ju} + (1-\varepsilon_{win})\, Rl_{wal_e,ju}\right) \right] \end{aligned} \tag{4.26}$$

$$Rl_{str,iu} = \varepsilon_{str}\psi_{str,ju}\sigma T^4_{str} + (1-\varepsilon_{str})\,\psi_{str,iu}Rl_{str} \tag{4.27}$$

where nu is the number of levels in the urban grid.

In a similar way the long wave radiation at the street level is the sum of the one coming from the sky ($Rl_{sky,str}$) and the one emitted and reflected by the walls at the two sides of the canyon. For example for the south-north canyon we have:

$$Rl_{str} = Rl_{sky,str} + Rl_{wal_{we},str} \tag{4.28}$$

where:

$$Rl_{sky,str} \quad = \quad \psi_{sky,str}Rl_{sky} + \sum_{ju=1}^{nu} \psi_{ju,str}Rl_{sky}\left(1-\Gamma(z_{ju+1})\right) \tag{4.29}$$

$$
\begin{aligned}
Rl_{wal_{we},str} = (1-p_{win})\,[\sum_{ju=1}^{nu}\Gamma(z_{ju+1})\,&\left(\varepsilon_{wal}\psi_{ju,str}\sigma\left(T^4_{wal_e,ju}+T^4_{wal_w,ju}\right)+\right.\\
&\left.(1-\varepsilon_{wal})\,\psi_{ju,str}\left(Rl_{wal_e,ju}+Rl_{wal_w,ju}\right)\right)]+\\
p_{win}[\sum_{ju=1}^{nu}\Gamma(z_{ju+1})\,&\left(\varepsilon_{win}\psi_{ju,str}\sigma\left(T^4_{win_e,ju}+T^4_{win_w,ju}\right)+\right.\\
&\left.(1-\varepsilon_{win})\,\psi_{ju,str}\left(Rl_{wal_e,ju}+Rl_{wal_w,ju}\right)\right)]
\end{aligned}
\tag{4.30}
$$

The parameters $\psi_{[-]}$ correspond to the *view factors* and are calculated as in Martilli et al. (2002). The expression (4.25) is a system of $2n+1$ equations and $2n+1$ unknowns (the long wave radiation at the walls and street, with n being the number of levels below the roof height) which is solved by a matrix inversion.

Short wave radiation

The short wave radiation reaching a vertical wall W is the sum of the direct radiation coming from the sky and the radiation reflected by the other surfaces of the canyon (vertical walls, windows and floors). For example the short wave radiation reaching a west wall at a urban level iu ($Rs^{W_w}_{iu}$) is given by:

$$
Rs^{W_w}_{iu} = Rs_{sky,iu} + Rs_{str,iu} + Rs_{wal_e,iu} \tag{4.31}
$$

The different terms are given by:

$$
Rs_{sky,iu} = Rs^{s}_{wal_w,iu} + \sum_{ju=1}^{nu}\psi_{ju,iu}Rs^{s}_{wal_w,ju}\left(1-\Gamma(z_{ju+1})\right), \tag{4.32}
$$

$$
Rs_{str,iu} = \alpha_{str}\psi_{str,iu}Rs_{str}, \tag{4.33}
$$

$$
Rs_{wal_e,iu} = \sum_{ju=1}^{nu}\Gamma(z_{ju+1})\left[(1-p_{win})\alpha_{wal}\psi_{ju,iu}Rs_{wal_e,ju} + p_{win}\alpha_{win}\psi_{ju,iu}Rs_{wal_e,ju}\right] \tag{4.34}
$$

In a similar way the short wave radiation reaching the street (Rs_{str}) is given by the sum of the radiation coming from the sky and the one coming by the vertical walls around the canyon. For example for a south-north oriented canyon we have the following expression:

$$
\begin{aligned}
Rs_{str} = Rs^{s}_{str} + \sum_{ju=1}^{nu}\psi_{ju,str}\left(Rs^{s}_{wal_w,ju}+Rs^{s}_{wal_e,ju}\right)\left(1-\Gamma(z_{ju+1})\right)+\\
\sum_{ju=1}^{nu}\Gamma(z_{ju+1})\psi_{ju,str}\left(Rs_{wal_w,ju}+Rs_{wal_e,ju}\right)\left[p_{win}\alpha_{win}+(1-p_{win})\,\alpha_{wal}\right]
\end{aligned}
\tag{4.35}
$$

This is again a linear system of $2n+1$ equations and $2n+1$ unknowns which is solved by a matrix inversion.

The quantities $Rs^s_{[-]}$ in (4.32) and (4.35) correspond to the direct radiation reaching the surface (street or wall). This value is computed as in the work of Martilli et al. (2002), by taking into account the obstruction of the canyon elements.

Appendix B: Computation of the presence of people in commercial and residential areas

Assuming that the total population inside a city is constant we have that:

$$N^{people}_{city} = N^{people}_{R} + N^{people}_{C} \tag{4.36}$$

In particular the total number of people in the city (N^{people}_{city}) is given by:

$$N^{people}_{city} = \rho_P \left(N_C + N_R\right) \Delta x \Delta y \tag{4.37}$$

where ρ_P $[\frac{inhab.}{m^2}]$ is the density average of the population in the city, N_C and N_R are respectively the number of commercial and residential cells in the city, and $(\Delta x \Delta y)$ is the area of the cell (commercial and residential cells have the same area).

The number of people in residential areas (N^{people}_{R}) is given by:

$$N^{people}_{R} = N_R \left(\Delta x \Delta y\right) \lambda^R_P \Phi_R(t) \left[\sum_{k=1}^{N^{type}_R} nlev_{R_k} \gamma_{R_k}\right] \tag{4.38}$$

The term $\Phi_R(t)$ $[\frac{Persons}{m^2}]$ is the temporal evolution of the number of occupants in a floor for a residential area. Then N^{type}_R is the number of types of residential buildings (i.e. the number of residential buildings of different heights), γR_k is the probability to have a building of type k, and finally $nlev_{R_k}$ is the number of floors in a building of type k.

The number of people in commercial areas is obtained in a similar way by replacing the different terms in (4.38) with their corresponding commercial values.

Defining the following **geometric values** for commercial and residential areas

$$G_R = \lambda^R_P \sum_{k=1}^{N^{type}_R} nlev_{R_k} \gamma_{R_k};\ G_C = \lambda^C_P \sum_{j=1}^{N^{type}_C} nlev_{C_j} \gamma_{C_j} \tag{4.39}$$

equation (4.36) can be written as:

$$\rho_P \left(N_C + N_R\right) = N_C G_C \Phi_C(t) + N_R G_R \Phi_R(t) \tag{4.40}$$

We assume now that there exists a time t for which $\Phi_C(t) = 0$ (all the commercial cells are empty). In particular in this situation the corresponding residential parameter $\Phi_R(t)$ reaches a maximal value that is defined as the **peak number of occupants** in the residential cells ($P_R[\frac{inhab.}{m^2}]$). In particular from (4.40) one can derive that:

$$P_R = \rho_P \frac{(N_C + N_R)}{N_R G_R} \tag{4.41}$$

and in a similar way:

$$P_C = \rho_P \frac{(N_C + N_R)}{N_C G_C} = P_R \frac{N_R G_R}{N_C G_C} \tag{4.42}$$

Finally writing $\Phi_C(t)$, $\Phi_R(t)$ as $\Phi_C(t) := P_C \varphi_C(t)$ and $\Phi_R(t) := P_R \varphi_R(t)$ and replacing it in (4.40), the relation between the temporal evolution of the **ratio of occupants** in the different cells can be derived:

$$\varphi_C(t) + \varphi_R(t) = 1 \tag{4.43}$$

Bibliography

[1] Arnfield, A.J., Grimmond, C.S.B.: 1998, 'An urban canopy energy budget model and its application to urban storage heat flux modelling', *Energy and Buildings*, **27**, 61-68.

[2] Clarke, J.: 2001, 'Energy Simulation in Building Design', Butterworth-Heinemann, Oxford.

[3] Dupont, S., Otte, T.L., Ching, J.K.S.: 2004, 'Simulation of meteorological fields within and above urban and rural canopies with a mesoscale model ($MM5$)', *Boundary-Layer Meteorol.*, **113** (1), 11-58.

[8] Grimmond, C.S.B., Oke, T.R.: 2000, 'Aerodynamic Properties of urban areas derived from analysis of surface form', *J. Appl. Meteor*, **38**, 1262-1295.

[5] Jacobs, A., Nicol, F., Wilson, M. and Solomon, J.: 2005, 'CLEAR, A multimedia package for Comfortable Low Energy Architecture', *International Conference "Passive and Low Energy Cooling for the Built Environment"*, Santorini, Greece.

[6] Kikegawa, Y., Genchi, Y., Yoshikado, H., Kondo, H.: 2003, 'Development of a numerical simulation system toward comprehensive assessments of urban warming countermeasures including their impact upon the urban buildings' energy-demands', *Applied Energy* **76**: 449-466.

[7] Kikegawa, Y., Genchi, Y., Kondo, H., Hanaki, K.: 2006, 'Impacts of city-block-scale countermeasures against urban heat island phenomena upon a building's energy-consumption for air conditioning', *Applied Energy* **83**: 649-668.

[8] Louis, J.F.: 1979, 'A parametric model of vertical eddies fluxes in the atmosphere', *Boundary-Layer Meteorol.*, **17**, 187-202.

[11] Martilli, A., Clappier, A., Rotach, MW.: 2002, 'An urban surface exchange parameterization for mesoscale models', *Boundary-Layer Meteorology* **104**: 261-304.

[10] Martilli, A.: 2002, 'Numerical study of urban impact on the boundary layer structure: sensitivity to wind speed and and urban morphology, and rural soil moisture', *J. of Appl. Meteorol.*, **41**: 1247-1267.

[11] Martilli, A., Roulet, Y.-A., Junier, M., Rotach, M.W. and Clappier, A.: 2003, 'On the impact of urban exchange parameterisation on air quality simulations: the Athens case', *Atmos. Environ.* **37**: 4217-4231.

[12] Masson, V., Grimmond, C.S.B., Oke, T.R.: 2002, 'Evaluation of the Town Energy Balance (TEB) scheme, with direct measurements from dry districts in two cities', *J. Applied Meteorol.* **41**: 1011-1026.

[13] Ratti, C., Di Sabatino, S., Britter, R., Brown, M., Caton, F., Burian, S.: 2002, 'Analysis of $3-D$ urban databases with respect to pollution dispersion for a number of European and American cities', Water, Air and Soil Pollution: Focus 459-469.

[14] Raupach, M.R.: 1992, 'Drag and drag partition on rough surfaces', *Boundary-Layer Meteorol.*, **60**, 375-395.

[15] Roulet, C.-A.: 1987, 'Energétique du bâtiment II', Presses Polytechniques romandes, Lausanne, Switzerland.

[16] Roulet, Y.-A., Martilli, A., Rotach, M.W., Clappier,A.: 2005, 'Validation of an urban surface exchange parameterization for mesoscale models $-1D$ case in a street canyon', J. of Appl. Meteorol., **44**, 1484-1498.

[17] Roulet, Y.-A.: 2004, 'Validation and Application of an urban turbulence parameterisationscheme for mesoscale atmospheric models', *PhD Thesis N°* 3032, Swiss Federal Institute of Technology, Lausanne.

Chapter 5

Application of a numerical model for the study of urban warming countermeasures over the region of Basel

Abstract

The main objective of the present work is to test and evaluate the applicability of the simulation system presented in the previous chapters to a realistic three-dimensional domain. For this purpose, the model is runned over Basel urban area and its surroundings, taking advantage of the large measuring campaign (BUBBLE) that have been conducted in 2001 and 2002. With those measurements, the Urban Heat Island (UHI) over Basel area is evaluated and compared to simulation results. In this context, the impact of the Building Energy Model (BEM) is also studied. In general, the numerical tool has proved its capability to simulate this important phenomenon generated by the presence of cities.

In a second time, a sensitivity study is carried out for a summertime episode in order to evaluate the model's capability to study different urban warming countermeasures and cooling energy demands control strategies. Results indicate that anthropogenic fluxes generated by air-conditioning facilities impact local meteorology over Basel, and should be taken into account for a more precise study of UHI mitigation strategies.

Possible future appllications are finally mentioned in the concluding part of the chapter.

5.1 Introduction

The aim of the present work is first to evaluate the applicability of the simulation system MM-UCP-BEM, detailed in the previos chapters of the thesis, to a real three-dimensional configuration. Secondly, we will study the capability of the numerical tool in representing different physical processes linked to urban climate (e.g. heat island processes), and in allowing detailed analysis of different strategies for the generation of more comfortable, and less energy-consuming cities.

The model is applied to the city of Basel which is located in the North-Western part of Switzerland on the Rhine river, surrounded in the north-east by the German Black Forest, in the south by the Jura range, and in the west by the French Vosges mountains. These surrounding mountains generate formation of diurnal slope winds, and the corresponding topographic situation makes the area of Basel as one of the warmest (and incidentally most polluted) Switzerland' regions.
Another important point which makes Basel attractive for three-dimensional testing, is the fact that it was subjected to an intense measuring period that took place from August 2001 to July 2002. The main goal of this project called UrBan Boundary Layer Experiment (BUBBLE) was to study boundary-layer and surface-exchange processes over different types of surfaces (urban, sub-urban, and rural), and the impact on the transport and diffusion of air pollution. A detailed description of the BUBBLE campaign can be found in Rotach et al. (2005), as well as on the corresponding website.
The possibility to have a direct access to a wide range of measured data, gave a great opportunity to compare numerical mesoscale models to real observations. In this context, the studies of Roulet (2004), Roulet et al. (2005), Muller (2007), Germano (2006), and Salamanca and Martilli (2008), supply a very important and useful basis for the present work.

Section 5.2 first describes the specific model setup adopted in the study. In particular the forcing and nesting procedures are detailed, as well as the origin of meteorological, topography, and land use data. The characteristics of the different urban surfaces are also described, and an overview of the BUBBLE measuring stations is given.
Average measured and simulated urban and rural temperatures are then computed and compared in section 5.3. In this context, the time evolution of the Urban Heat Island (UHI) is analysed over a simulated three-day episode lasting from 25 June to 27 June 2002. As it will be stated in the following, the main objective concerning this part of the work is not to perform a detailed validation of the model MM-UCP-BEM, but to verify the impact of the urban fluxes generated by BEM on the outdoor temperature.

In this context, a study of the impact of BEM on urban microclimate (temperature, wind speed, TKE) is also considered in paragraph 5.4. This is performed following a similar procedure to the one adopted in Chapter 4 for two-dimensional idealized configurations.

Finally, in paragraph 5.5 we analyse the applicability of the simulation system MM-UCP-BEM in evaluating the effectiveness of different UHI mitigation and cooling energy demands control strategies over the Basel area. Conclusions are given in section 5.6.

5.2 Setup of the simulation

In this paragraph we present the characteristics of the mesoscale domain defined for the study. At first, we will describe the forcing procedure adopted for the generation of initial and boundary conditions, and in a second time, the characteristics of the urban area over the region of Basel will be detailed.

5.2.1 Domain features and nesting procedure

The domain considered for the study has a horizontal resolution of $1.5\text{k}m \times 1.5\text{k}m$, with an extension of 52.5km in the x-direction (35 grid points), and 60km in the y-direction (40 grid points). The model extends vertically up to 12 000m above ground level with a vertical resolution stretched from 10m close to ground to 1000m at the top of the domain (total of 30 grid points). For this application the mesh is deformed in order to take topographic features into account (cf. Chapter 2). In particular, topographic data are extrapolated from a worldwide Digital Elevation Model (DEM), collected by the U.S. Geological Survey (GTOPO30[1]) with a resolution of 1km × 1km. As one can see in Figure 5.1, the domain of interest includes the city of Basel and its more immediate surroundings, as well as part of the Black Forest and Jura Mountains.

In order to apply the Finite Volumes Mesoscascale model (FVM) presented in Chapter 2 over the domain of Figure 5.1, initial and boundary conditions have to be provided by a *forcing* procedure reading and interpolating the meteorological data of a larger scale model. In this work, an Inverse Distance Weighted interpolation method (IDW) is considered. It assumes that the value of an interpolated point (P_{FVM}) should be influenced more by the near large-scale model values than the more distant points (Chang, 2006, Germano, 2006). In particular, for N neighbouring points of the larger scale model, a

---

[1] a detailed description of GTOPO30 with the corresponding downloadable data can be found in: *http://edc.usgs.gov/products/elevation/gtopo30/gtopo30.html*

given meteorological variable ψ at the point P_{FVM} is computed by:

$$\psi\left(P_{FVM}\right)=\sum_{i=1}^{N}\omega\left(P_{FVM};P_{MOD}^{i}\right)\psi\left(P_{MOD}\right) \tag{5.1}$$

where P_{MOD}^{i} are the large scale model points, and $\omega\left(P_{FVM};P_{MOD}^{i}\right)$ the weights given to P_{MOD}^{i} $\forall$ $i=1,\cdots,N$.

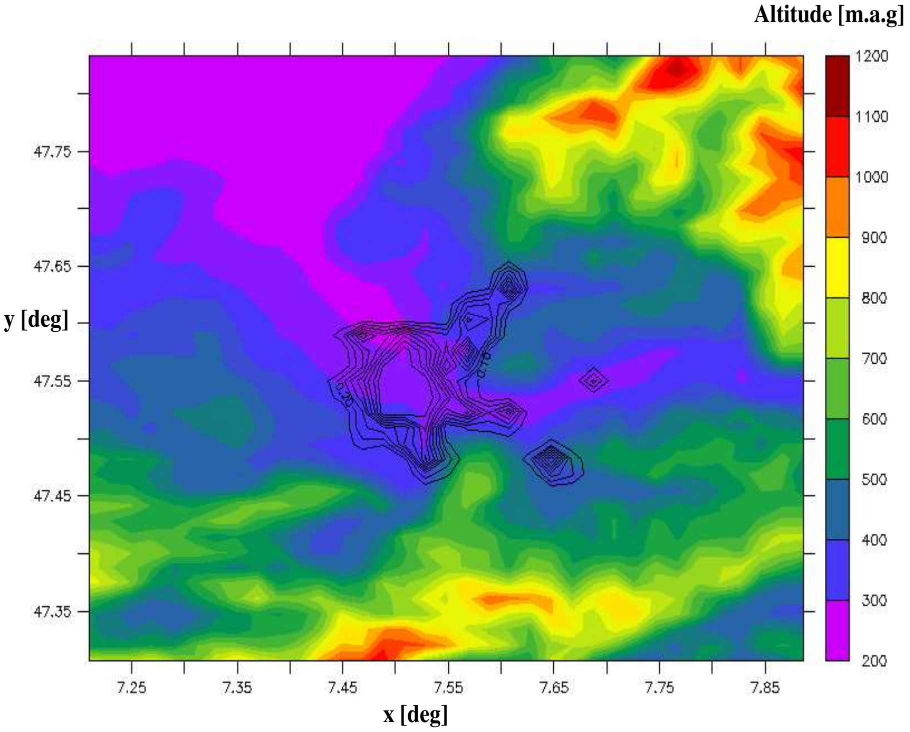

Figure 5.1: Topography of the simulation domain. Contour black lines delimit the Basel area.

In particular, for the forcing model considered in this work we set $N=4$ in (5.1), and the corresponding weights ω are computed with the following bilinear interpolation:

$$\begin{cases} \omega\left(P^1_{MOD}\right) & = & \left(1-\xi^1\right)\left(1-\xi^4\right) \\ \omega\left(P^2_{MOD}\right) & = & \xi^3\left(1-\xi^2\right) \\ \omega\left(P^3_{MOD}\right) & = & \xi^2\left(1-\xi^3\right) \\ \omega\left(P^4_{MOD}\right) & = & \xi^1\xi^4 \end{cases} \tag{5.2}$$

where the ξ coefficients are computed by:

$$\begin{cases} \xi^1 = \frac{d_1}{d_1+d_3} \\ \xi^2 = \frac{d_2}{d_1+d_3} \\ \xi^3 = \frac{d_3}{d_1+d_3} \\ \xi^4 = \frac{d_4}{d_2+d_4} \end{cases} \tag{5.3}$$

and d_i $i = 1, \cdots, 4$ is the distance between P_{FVM} and P^i_{MOD}.

In the vertical direction, a straightforward interpolation according to height is considered for the upper atmosphere. At low levels, a similar procedure is adopted, but the colums of the input model are shifted to the height of the higher resolution topogtaphy of FVM. In that way, the influence of the earth's surface in the boundary layer is conserved, and no artificial atmospheric stabilities are generated (Roches, 2007).

The input model considered in the present work is the Fifth-Generation NCAR/Penn State Mesoscale Model MM5 (Grell et al., 1994). With respect to FVM, MM5 provides a more detailed land-use data set with up to 24 soil categories (vegetation, desert, water, ice, etc.). In addition, microphysical schemes for the treatment of cloud and precipitations are taken into account. Thus, forcing FVM with MM5 meteorological data consent an "indirect" consideration of these physical phenomena at the boundaries of the simulation domain in Figure 5.1.

The MM5 grid utilised for the forcing of meteorological data on the FVM domain in Figure 5.1 has a horizontal resolution of 4km × 4km, and covers a square domain of $244km$ by $244km$ (61×61 grid points). As one can see in Figure 5.2 (cf. $D04$), the domain includes part of Swiss Prealps at the Southern boundary, part of the German Black Forest at the east, the tail of the Swiss Jura Mountains (south-west of the domain), the French (Alsatian) Vosges mountains in the west, and the Rhine valley east and north of Basel.

Following the work of Roulet (2004), a forcing parameter is considered in order to define the strength of the MM5 forcing on the FVM domain. In particular, in the vertical direction a forcing of 100% is introduced at the boundaries of the grid, and decreases

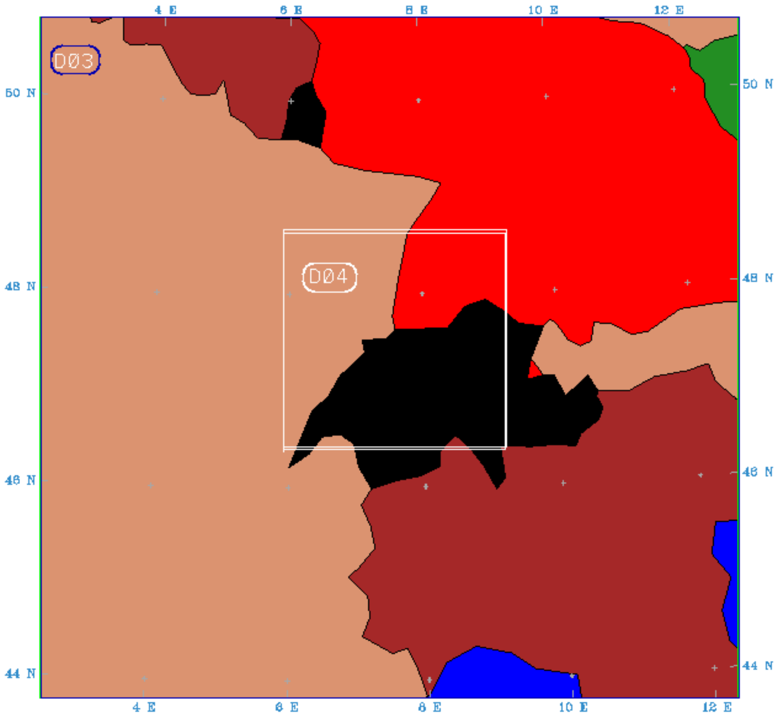

FIGURE 5.2: Visualisation of the MM5 domain D04 used to force the meteorological variables on the FVM domain.

in steps of 20% per row of cells toward the interior of the domain. In the horizontal, a forcing of 100% is considered at the boundaries, and decreases to 50% and 20% toward the interior grid points. The zone of influence will then be limited to the first three cells at each horizontal domain boundary (East, West, North, South), and to five cells at the top of the domain.

As one can see in Figure 5.3, the meteorological data on the MM5 domain D04, have been obtained by applying the MM5 mesoscale model to three *nested* domains (D01, D02, D03).
The size of the different domains, as well as the nesing characteristics[2] are summarized in Table 5.1.

Meteorological data at the boundaries of the largest domain D01 are forced using

---

[2] A detailed desciption of the different nesting procedures considered in the MM5 model (e.g. one/two way) can be found in: *http://www.mmm.ucar.edu/mm5/*.

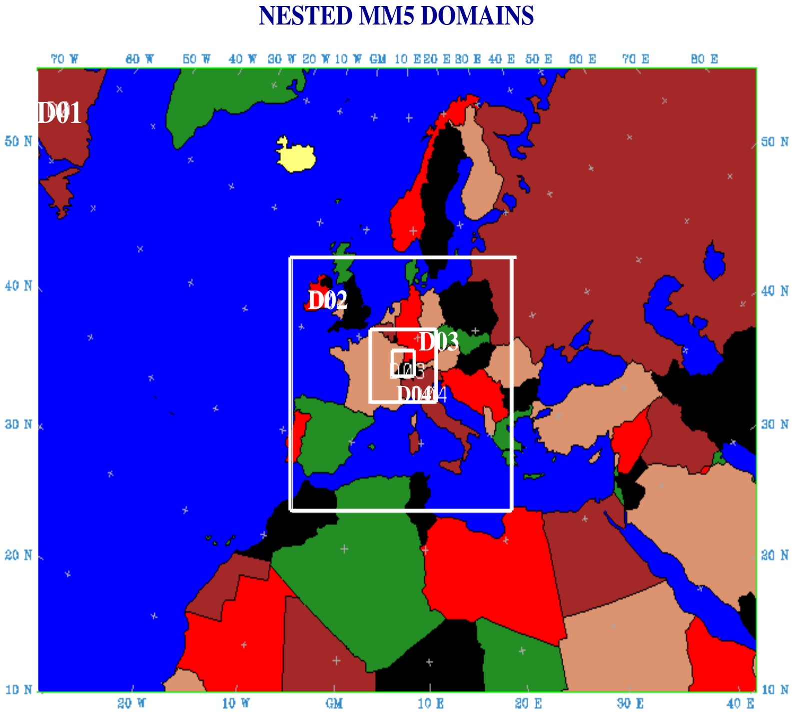

FIGURE 5.3: Visualisation of the nesting procedure on MM5. Four nested domains are considered: D01, D02, D03, D04.

Domain	**Δx [km]**	**Δy [km]**	**Nx**	**Ny**	**Nesting type**
D01	108	108	80	60	one-way
D02	36	36	73	73	two-way
D03	12	12	64	64	two-way
D04	4	4	61	61	two-way

TABLE 5.1: Characterostics of the different nested domains of MM5: resolution (Δx, Δy), number of grid points in the horizontal direction (Nx, Ny), and type of nesting.

NCEP/NCAR Reanalysis data[3]. These data cover all the Earth's surface with a spatial resolution of 2.5° latitude by 2.5° longitude, and a time resolution of six hours. Remark that, due to the coarse resolution of the NCEP data set, the largest domain considered for the nesting procedure should also have a low spatial discretisation. In fact, in order

---

[3] A detailed description of the NCEP/NCAR reanalysis data set can be found in: *http://www.cdc.noaa.gov/data/reanalysis/reanalysis.shtml*

to increase the accuracy of the final result, the spatial resolution difference between two nested domains has to be controlled. As one can see in Table 5.1, a maximal nesting ratio of 3 : 1 is considered in the MM5 nesting procedure. The horizontal resolution difference between D04 ($4km$), and the FVM domain ($1.5km$) is also maintained below this value.

5.2.2 Urban soil definition and measurements

The percentage of urban and rural soil coverage are determined from the KABA[4] project data base (Fehrenbach, 1999). Among the different maps, the KABA data base also provides a very detailed land coverage description deviding the region of Basel into 15 different land-use classes with a resolution of 100m. For the purpose of the simulation, all rural and urban classes have been aggregated to define a rural and urban land-use percentage. Furthermore, following the work of Roulet, (2004), three urban classes are defined in terms of specific building parameters (width, height, density), based on the informations from the 15 land-use classes defined in the KABA database:

- dense urbanised area: mean building height over 11m, building density higher than 50% (class 1)
- transition zone (suburban and industrial areas): mean building height between 8 and 11m, building density between 40 and 50% (class 2)
- village cores and single houses: mean building height below 8m, building density lower than 40%.

In the present study, only the Basel agglomeration is considered when counting urban soil coverage. In particular, the other cities that should be part of the domain of Figure 5.1 (e.g. Mulhouse, Strasbourg in France) are supposed to have no influence on the climate over the region of Basel, and are treated as 100% rural areas. We also remark that this type of urban soil coverage has only been considered in the FVM simulation, and not in the MM5 nesting procedure.

The physical characteristics of the building materials are established using data from the BUBBLE[5] measuring campaign (Rotach et al., 2005). The BUBBLE project consisted in a large Urban Planetary Boundary Layer (PBL) experiment carried out under the auspices of the European COST 715 action. Its aim was to investigate the exchange processes occurring near the urban surface as well as the flows occurring in the upper

---

[4] Homepage of the KABA project: *http://pages.unibas.ch/geo/mcr/Projects/KABA/index.en.htm*

[5] Detailed informations concerning the BUBBLE project can be found in: *http://pages.unibas.ch/geo/mcr/Projects/BUBBLE/*

part of the Urban Boundary Layer (UBL).

From the 15th June until the 12th July 2002, a so-called Intensive Operation Period (IOP) took place. As one can see in Figure 5.4, different measuring weather stations were in use, located either on urban, suburban, or rural sites. A detailed list of the different stations is presented in Appendix A. The time resolution was 10 min for most of the stations and meteorological parameters. A few stations had a resolution of 30 min. The principal urban site was "Basel-Sperrstrasse" (Ue1 in Figure 5.4), and was of particular interest due to its location within an urban canyon. A detailed description of the characteristics of this measuring site can be found in Roulet et al. (2005).

The thermal characteristics of building materials considered in this work are taken from the data collected at the Sperrstrasse station. The different values are presented in the Appendix B (more details concerning the characteristics of urban surfaces can be found in Christen, 2005, Salamanca and Martilli, 2008).

In particular, all the three urban classes that have been previously defined, have the same physical properties of the different materials (roof, wall, street). Following the work of Roulet (2004), identical building orientations are also defined with two perpendicular street orientations with angles of 70° and 160° (two-dimensional configuration of the UCP in Chapter 4). As indicated in Table 5.2, the differences between the three urban types, only lie in the distribution of building-height density and street width.

Building height [m]	**Percentage of buildings with this height [%]**		
	Class 1	*Class 2*	*Class 3*
3.65	-	-	-
7.30	10	25	75
10.95	15	50	25
14.60	50	25	-
18.25	15	-	-
21.90	10	-	-
Building width [m]	15	15	15
Street width [m]	12.75	20	30

Table 5.2: Building-height distribution, building width and street width for the three urban classes.

The values of Class 1 in Table 5.2 are related to the data of the Basel Sperrstrasse measuring station (Christen, 2005, Salamanca and Martilli, 2008). Remark that a mean

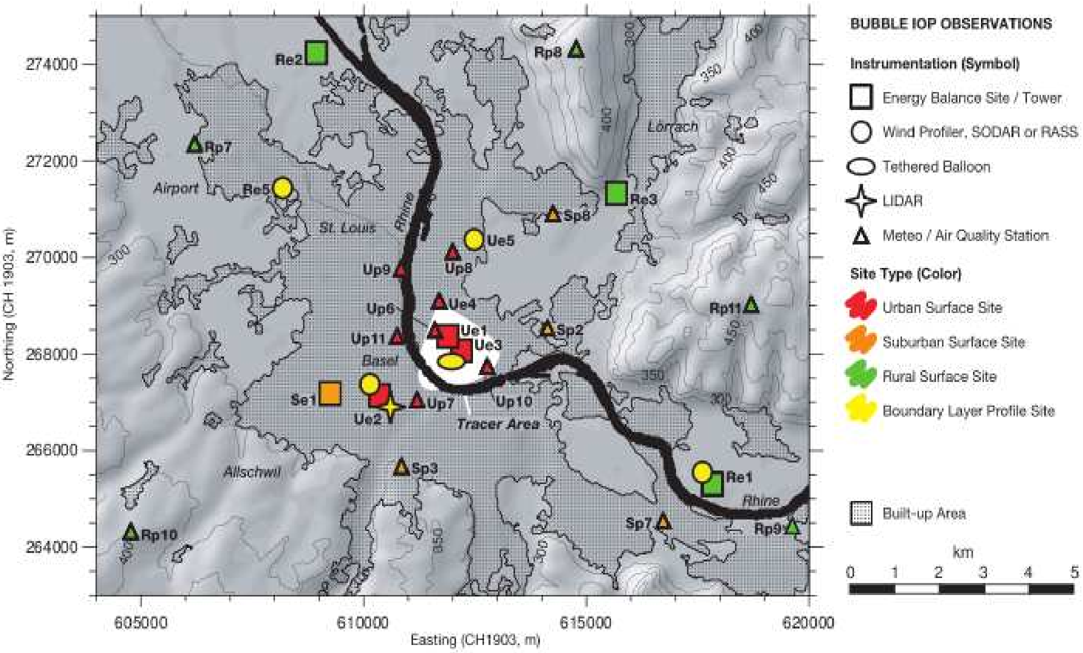

FIGURE 5.4: Map of the measurement stations during the BUBBLE-IOP (some rural sites are out of map). The Figure is taken from the BUBBLE websity: *http://pages.unibas.ch/geo/mcr/Projects/BUBBLE/*

building height of 14.6m is considered, and that the building and street width correspond to a plane area density (λ_P) of 0.54. On the other hand, the data for the transition zone (class 2) and village cores (class 3) are derived from the work of Roulet (2004). Observe that the corresponding λ_P parameters lie between 0.33 and 0.42, which is in the range of real cities (Grimmond and Oke, 2000, Ratti et al., 2003).

5.3 Comparison with measured data

Starting from the configuration and the urban characteristics presented in section 5.2, a first set of simulations is considered in order to test the MM-UCP-BEM model with respect to the three-dimensional real simulation test of the city of Basel.

Previous one-dimensional (Roulet et al., 2005), and three-dimensional (Roulet, 2004, Germano, 2006, Muller, 2007) studies have already been carried out in order to evaluate the effectiveness of the coupling between the urban parameterisation of Martilli et al. (2002), and the mesoscale model developped by Clappier et al. (1996). In particular, these works verified that the results generated by the model are comparable to those provided by the BUBBLE measuring campaign. In the present section, the BUBBLE data are utilised as a comparison helping to evaluate the behaviour of the simulation system composed by the finite volume model of Chapter 2, and the UCP-BEM parameterisation presented in Chapter 4. At first, the temperature inside buildings is maintained constant at $24°C$, without taking anthropogenic impact generated by the fluxes of BEM into account. As already mentioned in section 4.4.1, for this configuration the UCP-BEM model of Chapter 4 is equivalent to the parameterisation developped by Martilli et al. (2002).

Following the work of Muller (2007), mean near-ground urban and rural air temperatures are first determined by averaging the corresponding values available from the BUBBLE measuring campaign over different measuring sites. In this context, it is important to observe that the vertical resolution of the mesoscale model provides a first vertical level at 10m height. Yet, the reader should keep in mind that the BUBBLE measurements were not made at the same height, and that the corresponding average urban and rural temperatures have been computed by considering the measured values closest to 10 meters. In particular, the corresponding stations considered for the averaging procedure are presented in the Appendix A.
A three days simulation period is considered going from 00LT 25 June to 00LT 27 June 2002. This episode is included inside the IOP and is characterised by a constant meteorological situation with a very strong daily cycle.

Figures 5.5 and 5.6 show the corresponding comparison between simulated and measured average near-ground temperatures in the urban and rural case.

Note that the main tendency of the evolution of urban and rural air temperatures is well reproduced. Still, simulated daytime temperature estimated by the model appear too high. This can be especially observed during the third day in which the temperature differences reach more than $2°C$, both in rural, and urban sites. Similar behaviours were also observed in Germano's work, (2005), and could be due to the fact that the soil module considered in the model does not compute evapo-transpiration processes which could produce cooling of the outdoor air.

Differences between urban and rural temperatures (Figures 5.7 and 5.8), indicate that the model is able to simulate the UHI formation. One can also observe that this is not the case when the urban source terms computed by the urban parameterisation are not

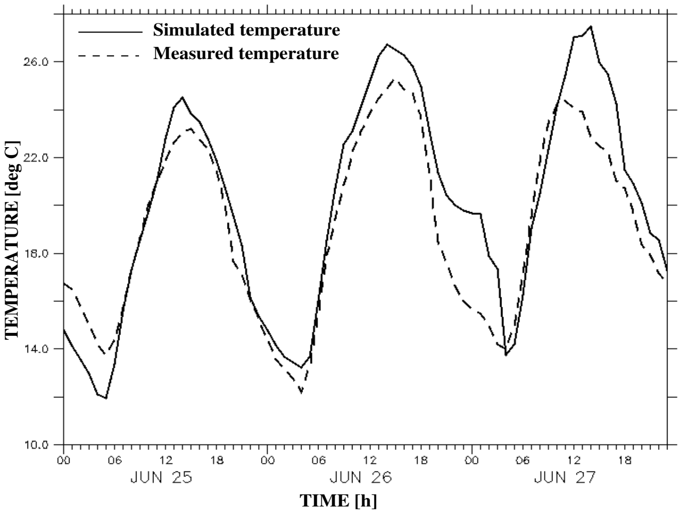

FIGURE 5.5: Comparison between simulated (solid lines) and measured (dashed lines) near-ground averaged rural temperatures.

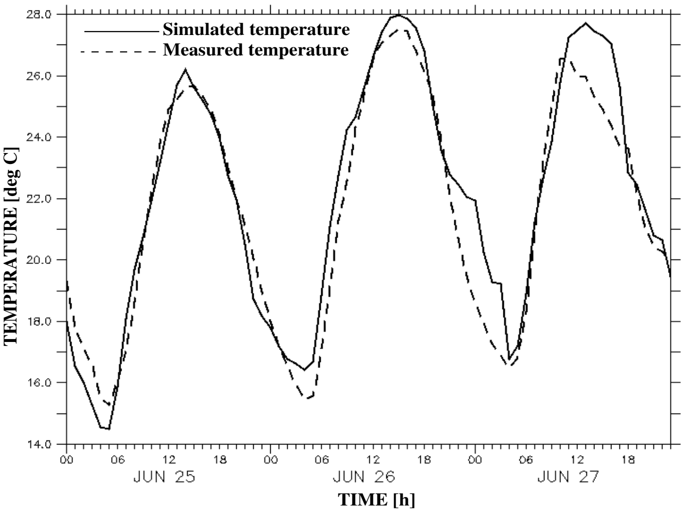

FIGURE 5.6: Comparison between simulated (solid lines) and measured (dashed lines) near-ground averaged urban temperatures.

taken into account. In general, measurements and simulated results indicate that peak UHI values are generated during night-time when surface cooling through longwave radiation releases heat to the surface layer. Figure 5.7 illustrates that the peak measured

UHI is reached at 20LT on 26 June with a value of nearly 6°C. Remark that this peak is not captured by the model which, in general, under-estimates the measured UHI. As one can see in Figure 5.7, the average UHI generated by the simulation is around 0.5°C lower. Similar behaviours were also observed in Muller's work, (2007), in which the author analysed the impact of the coupling between the UCP of Martilli et al. (2002), and the weather forecast model alMo (the operational numerical weather prediction model of MeteoSwiss).

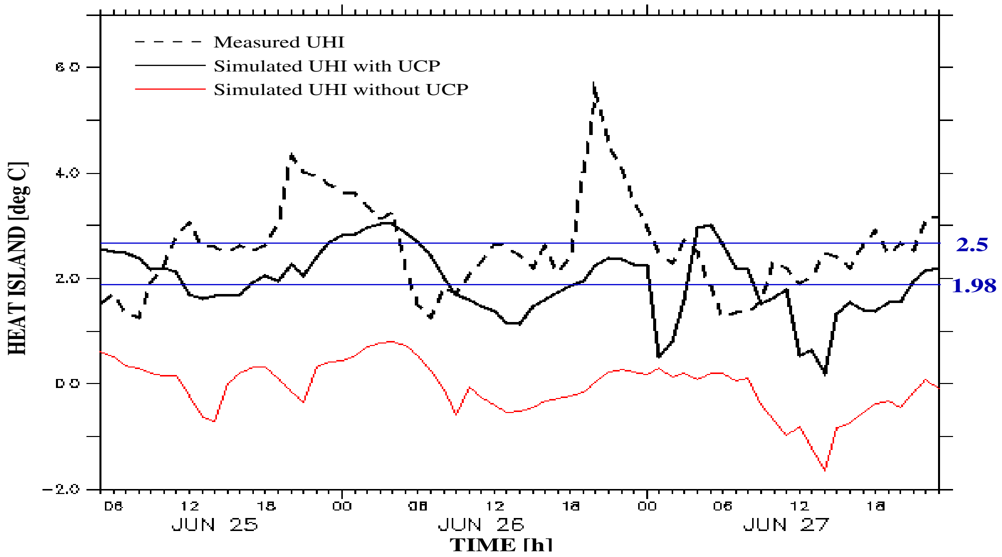

FIGURE 5.7: Time evolution of the UHI over the city of Basel. A comparison is done between average near-ground UHI obtained with measurements (dashed line), simulation with UCP (solid black lines), and without UCP (solid red line). Measured and simulated average UHI are given by straight solid lines.

In this context, observe that the physics of the urban system in the parameterisation of Martilli et al., (2002) is simplified, and does not take some urban fluxes into consideration, which could modify the urban energy balance. In particular, as presented in Chapter 4 of the present thesis, anthropgogenic fluxes produced by air-conditioning facilities can have a non negligent impact on the external temperature, and should be taken into account for a more complete UHI study. This was also one of the conclusions of Salamanca and Martilli's study, (2008), which was mainly focused on the comparison between the UCP of Martilli et al. (2002), and the corresponding counterpart UCP-BEM (cf. Chapter 4). The two models were tested in a one-dimensional off-line configuration and evaluated against measurements obtained in the BUBBLE campaign over the Sperrstasse station during the IOP period. At this time, temperature sensors

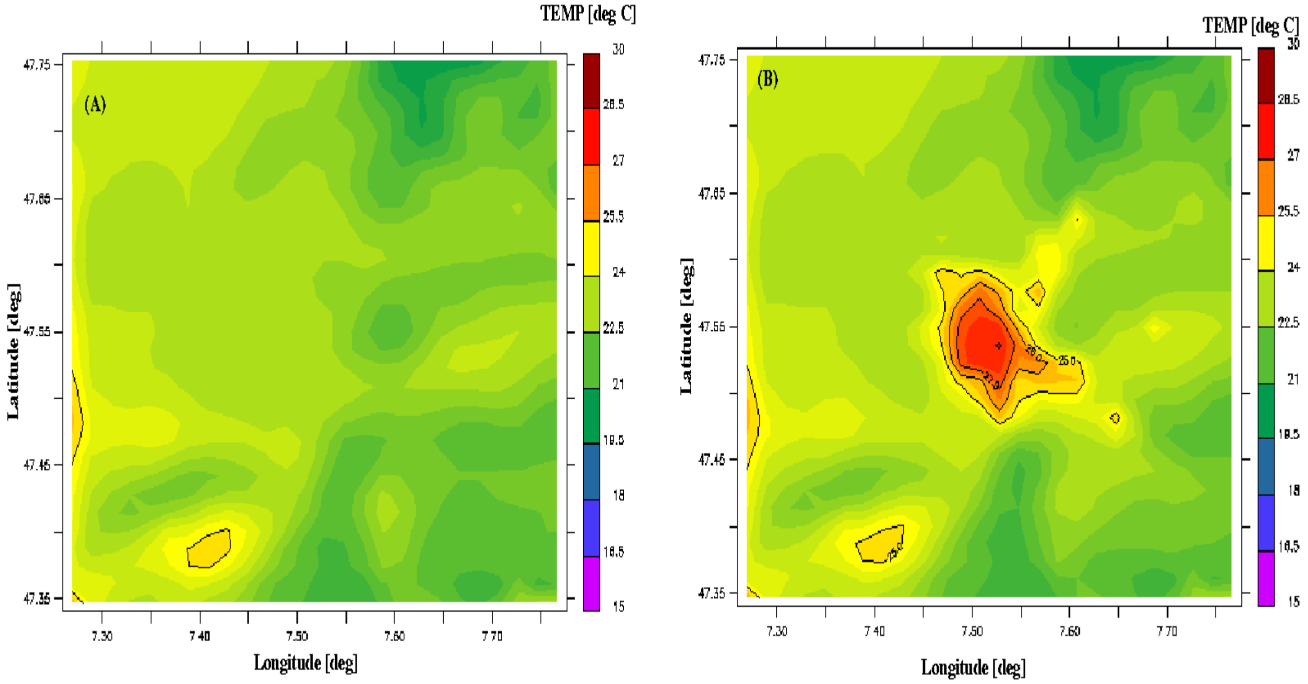

FIGURE 5.8: Simulated temperature on 26 June 2002 at 12LT without (A) and with (B) the presence of the UCP.

were installed in the stairwells of some buildings and suggested that the internal temperature was close to 24°C. This value was taken as the comfort temperature, and the corresponding anthropogenic fluxes generated by BEM were released by roof-top air-conditioning systems (cf. Chapter 3). The result of the study indicated that the coupling between UCP and BEM allows a better representation of the physics of the system, and of the corresponding urban fluxes.

Taking this into consideration, our idea was to try to apply the coupling UCP-BEM to the present three-dimensional configuration, and evaluate the corresponding impact on the UHI formation. It should be pointed out, that this test has mainly qualitative interests, and does not aim to validate the coupling UCP-BEM for three-dimensional appilications. In fact, there are no available data indicating the energy consumption from air-conditioning facilities over the city of Basel during the IOP period. Furthermore, it is not clear if the comfort temperature of 24°C evaluated in the Basel Sperrstrasse (Salamanca and Martilli, 2008) is available for all the city, while percentage of buildings which are effectively equipped with air-conditioning systems is not known. Finally, as indicated in Chapter 4 for two-dimensional configurations, these anthropogenic fluxes can be very sentitive to different physical parameters (buildings materials, COP, etc.), that can only be approximated when considering the city as a whole (it is not possible to represent all the features of urban areas). Taken this into consideration, it is generally very difficult to perform an accurate validation of UCP-BEM for three-dimensional real case simulations. Again, this is not the final goal in the present chapter, in which we are mainly interested in evaluating the impact and the possible applications of this model. Clearly, a more detailed three-dimensional validation procedure has to be considered in future studies. Ideally, the model should be applied to hot climate cities where the use of air-conditioning systems is known, and the data concerning the corresponding anthropogenic fluxes are available.

The different parameters considered for the air-conditioning simulation are those of section 4.4.2 for commercial buildings (cf. Table 4.3), except for the internal comfort temperature ($24°C$), and a constant ratio of occupants of $0.0116\frac{\text{person}}{m^2}$ of floor area (Salamanca and Martilli, 2008). It is supposed that air-conditioning systems are working from 08LT to 20LT over all the urban area of Basel. Following Table 4.2, we set the height of the different buildings' floors to 3.65m.

Starting from this configuration, we compare in Figure 5.9 the time evolution of the average near-ground UHI (at 10m height) with and without taking the effects of BEM into account. Measured UHI is also presented for comparison.
Observe that (as expected) the UCP and UCP-BEM results are comparable when the air-conditioning system is not in use (from 20LT to 08LT). On the other hand, when the air-conditioning system is on, the UCP-BEM heat island becomes higher than the UCP one, as a net anthropogenic flux is emitted into the atmosphere, with a consequent heating of the outdoor air (more details are given in paragraph 5.4). Remark that the corresponding three-days' average UHI is closer to the one generated with measured data.

This test indicates that the implementation of BEM inside the UCP affects the UHI formation in a non negligent way. In particular, as it will be presented in the following of this chapter, the corresponding UCP-BEM parameterisation can improve the applicability of the model to simulate Urban Boundary Layer (UBL) climate (section 5.4), and provides a more complete UHI formation and mitigation study (section 5.5).

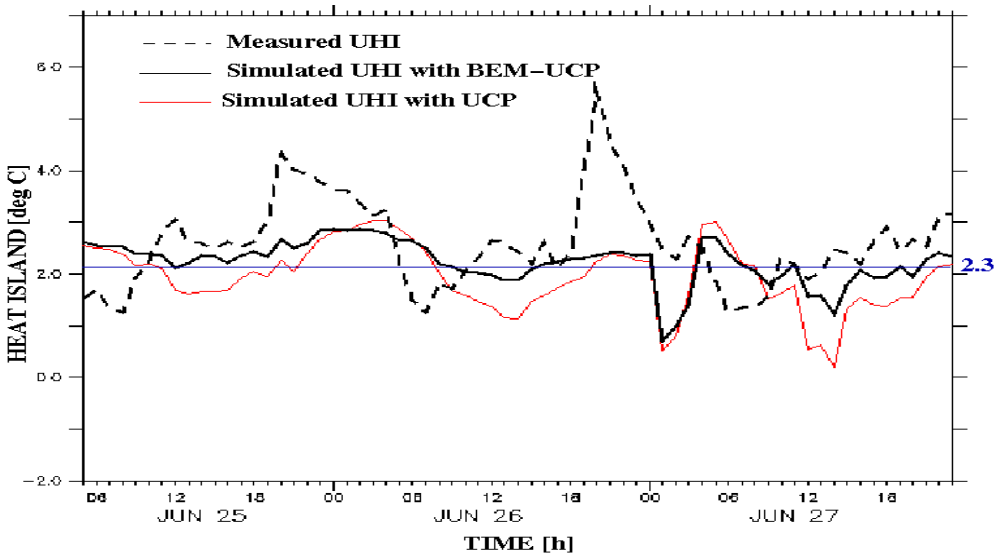

FIGURE 5.9: Time evolution of the UHI over the city of Basel. Comparison between average near-ground UHI obtained with measurements (dashed line), simulation with UCP-BEM (solid black lines), and with UCP only (solid red line). The blue straight line indicates the average value for the UCP-BEM simulation.

5.4 Impact of anthropogenic air-conditioning on meteorological variables

The study discussed in the present paragraph aims at evaluating the impact of BEM on the urban microclimate over the Basel area. A similar procedure is considered in Chapter 4 (section 4.4.2.1). In particular, the effects on temperature, wind speed, and TKE will be discussed. Next, a *base-case* simulation, corresponding to the air-conditioning configuration of the previous paragraph, will be considered. Thus, it is assumed that buildings maintain a comfort internal temperature of 24°C from 08LT to 20LT, by ejecting the corresponding air-conditioning fluxes through a roof-top system.

The results presented in the following are focused on the second simulation day (26 June 2002).

5.4.1 Temperature

Following equation (4.6), the total sensible fluxes emitted at roof level are computed by a summation of the turbulent contribution and the heat generated from air-conditioning facilities. In particular, we observed in Chapter 4 that air-conditioning contribution can generate more than half of the total sensible heat emitted from the roof.

As one can see in Figures 5.10, 5.11, and 5.12, this behaviour can also be observed in the present three-dimensional configuration of the city of Basel. In particular, these figures illustrate the percentage of emitted anthropogenic roof-top air-conditioning fluxes at 10m (Figure 5.10), 20m (Figure 5.11), and 30m (Figure 5.13) height, at 12LT. Note that the roof-top air-conditioning fluxes acting on the exterior microclimate at the first vertical level, are those of buildings being less than 10m height. In fact, as presented in section 5.2.2, this corresponds to village cores and transition zones where the maximal building density is 50%. Taken this into account, Figure 5.10 clearly shows that the corresponding anthropogenic fluxes are located at the surroundings of the central area of Basel. Observe that the corresponding magnitudes can reach values being between 20% and 40% of the total fluxes emitted at the roofs, and that (due to transport processes) this effect is also generated in urban and rural neighbouring areas.

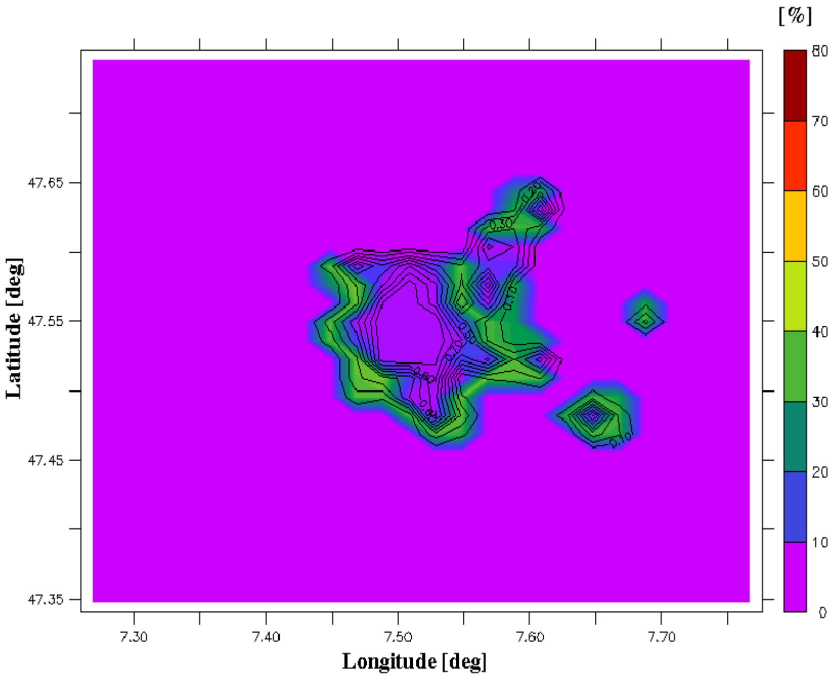

FIGURE 5.10: Urban flux percentage at 12LT 26 June 2002 at 10m above ground level. The city of Basel is represented in contour black lines.

Figure 5.11 illustrates the percentage of anthropogenic air-conditioning fluxes for buildings being 10m to 20m height (three to five-floors buildings). As indicated in Table 5.2, this includes all the transition zone, and most of the dense urbanised area. Note that the fluxes are now more concentrated at the central area of Basel. The values are greater than those of Figure 5.10 with percentages being between 40% and 60%. Remark in fact that as a roof-top air-conditioning is in use, the fluxes generated at every floor are evacuated by a single system located at the roof level (cf. equation (3.22)). As higher buildings are considered, we can expect that more important anthropogenic heat sources than those observed in the Figure 5.10 are generated.

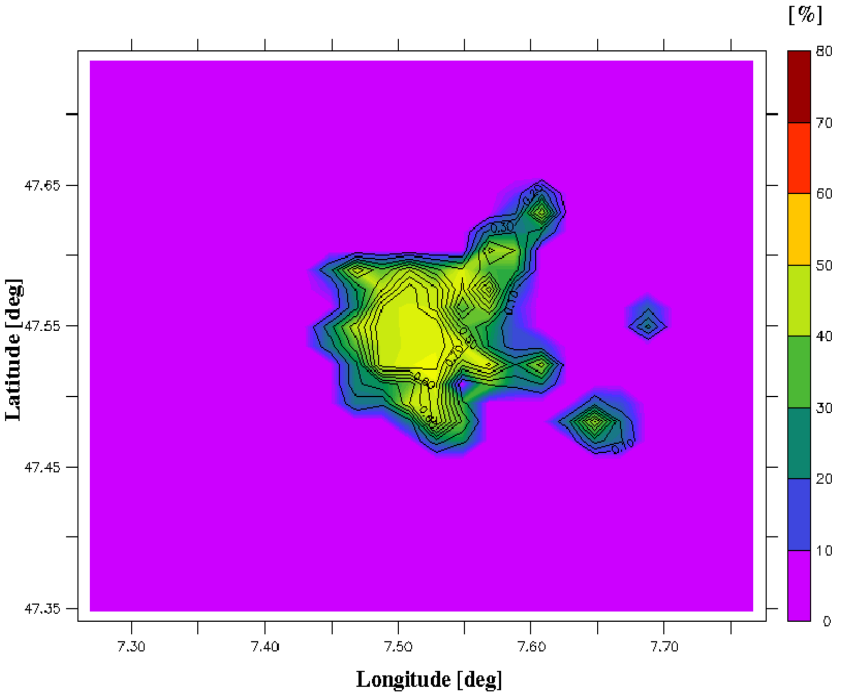

FIGURE 5.11: Urban flux percentage at 12LT 26 June 2002 at 20m above ground level. The city of Basel is represented in contour black lines.

Similar to previous cases, Figure 5.12 evaluates the percentage of anthropogenic air-conditioning for buildings more than 20m high. This includes 10% of the dense urbanised area. Remark that these fluxes can reach very important values with percentages ranging between 60% and 80% of the total heat emitted from the roofs.

These anthropogenic sensible heat fluxes will have a direct influence on the urban source term $\mathcal{D}_\theta$ in the energy conservation equation (2.13) (cf. Chapter 4 for more details). In particular, this will generate a consequent heating of the outdoor air. Furthermore, advection and diffusion processes propagate this effect in the horizontal and vertical directions. For instance, Figure 5.13 illustrates the above-ground temperature differences generated over the city of Basel when the base-case result is compared to the same simulation, but without ejecting the heat into the atmosphere (e.g. heat released into the soil). Observe that in the most urbanised areas, the emission of anthropogenic air-conditioning generates a temperature increase between $0.8°C$ and $1°C$.

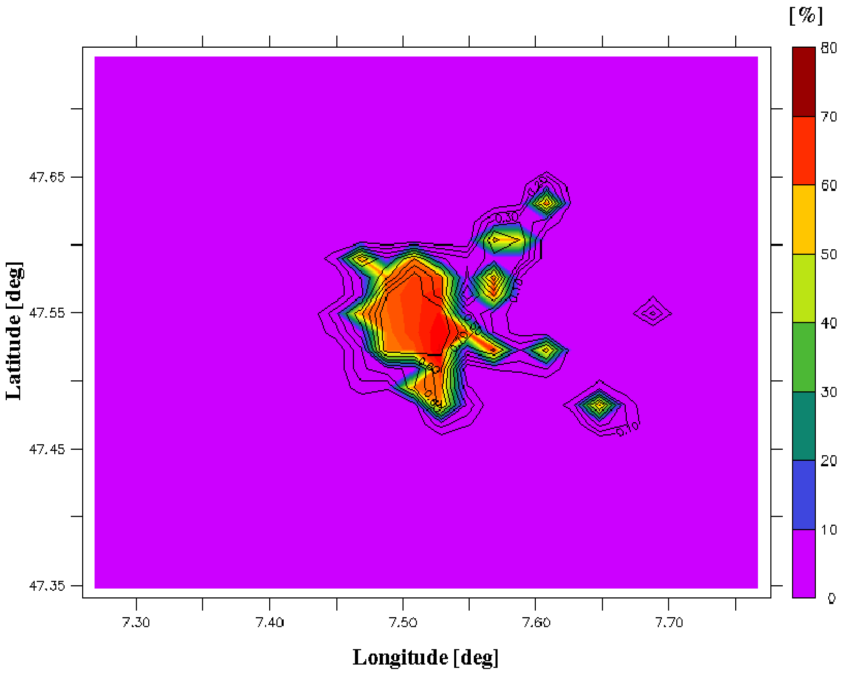

FIGURE 5.12: Urban flux percentage at 12LT 26 June 2002 at 30m above ground level. The city of Basel is represented in contour black lines.

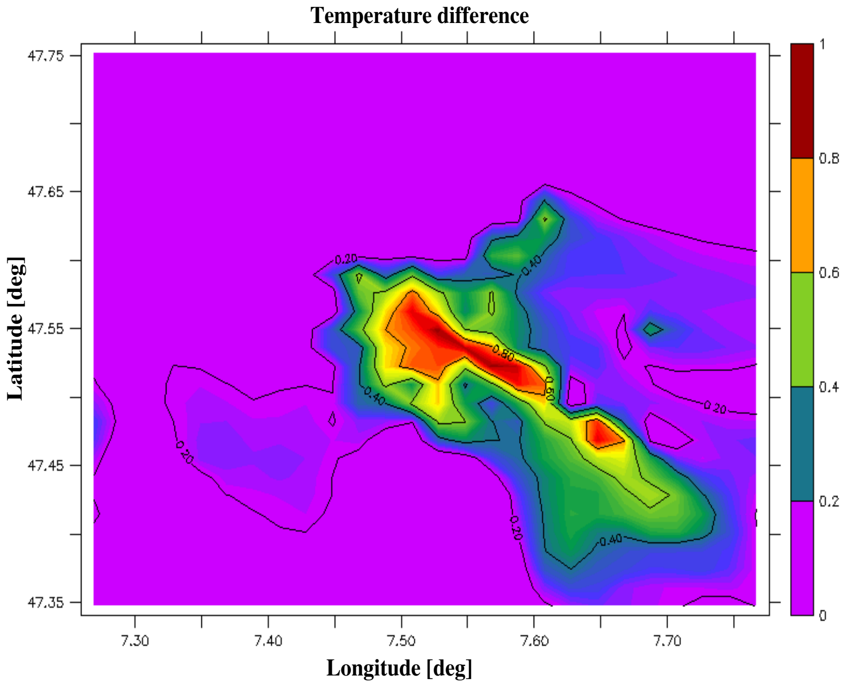

FIGURE 5.13: Temperature difference at 12LT 26 June 2002 at 10m above ground level between the base-case and non air-conditioning simulation.

Remark that these temperature gradients are advected by the mean wind, which at 12LT is blowing in the south-east direction. As already observed in Figures 5.7 and 5.9, one of the most important consequences of this temperature increase is given by an intensification of the diurnal UHI.

Figure 5.14 illustrates for the Sperrstrasse location, the vertical propagation of the temperature differences generated by air-conditioning facilities. As indicated in Table 5.2, in this site 80% of buildings are between 10m and 20m high. Thus, the most important anthropogenic heat flux is emitted at the second mesoscale vertical level. In particular, it is at this height that the peak temperature difference can be observed. Similar to the result of Figure 4.17 for the two-dimensional simulation, this gradient is then smoothed in the upward and downward directions.

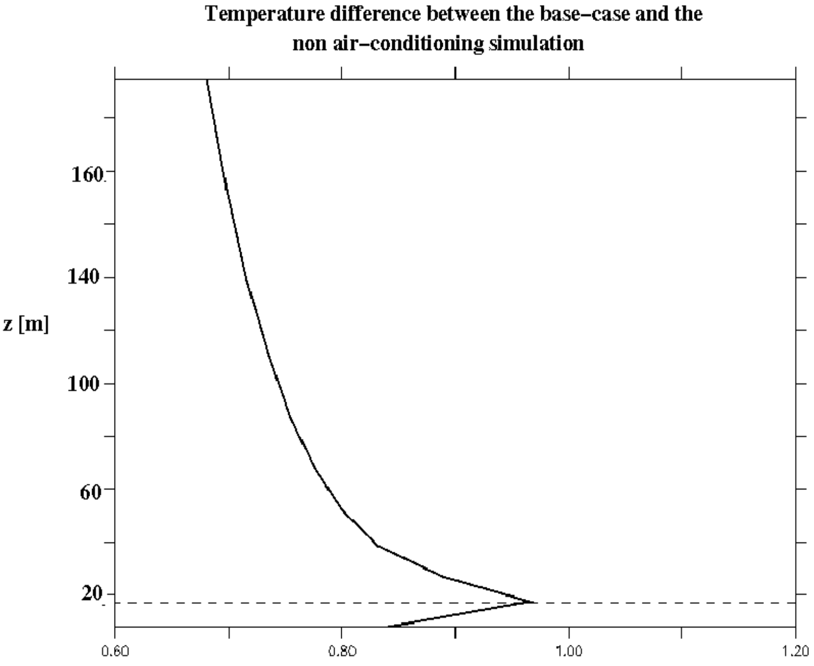

Figure 5.14: Vertical profile at 12LT 26 June 2002 of the difference in the air temperature between the base-case and non air-conditioning simulation. The figure refers to buildings located at the Sperrstrasse dense urbanised area. The straight dashed line indicates buildings heights.

Remark that the peak temperature difference reaches almost $1°C$, with a non-negligent near-ground gradient of more than $0.80°C$. Furthermore, by averaging along the air-conditioning period (08LT to 20LT), a corresponding mean near-ground temperature difference of more than $0.6°C$ was observed at the Sperrstrasse area on the 26 of June 2002.

The vertical profiles of Figure 5.15 finally show that (accordingly to the result of Figure 4.18 for two-dimensional simulations), this temperature gradient can be considerably increased by the application of vertical wall air-conditioning systems.

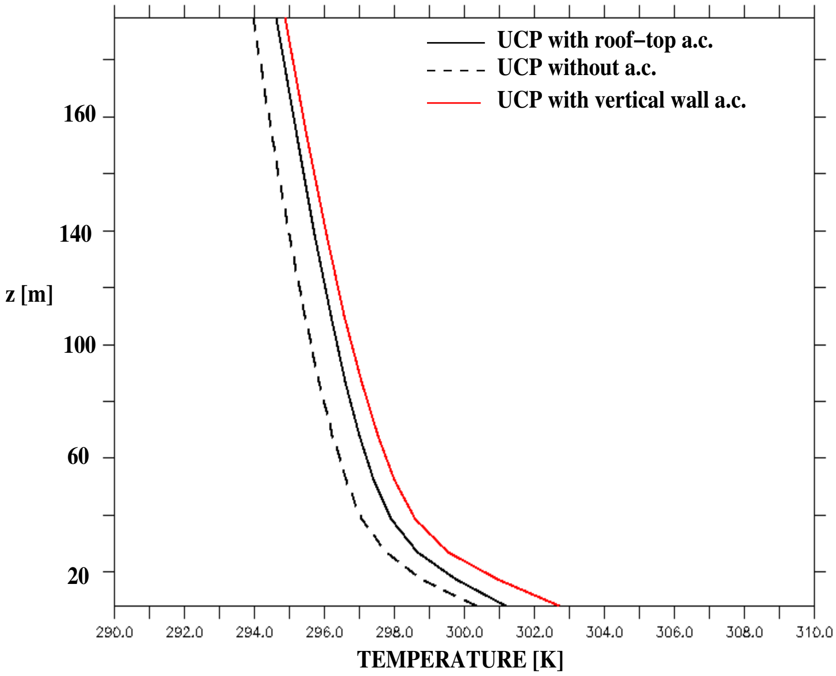

Figure 5.15: Vertical temperature profiles at 12LT 26 June 2002 at the Sperrstrasse dense urbanised area. The roof-top air-conditioning (black line), vertical wall air-conditioning (red line), and non air-conditioning case (dashed line) are represented.

Note that the application of a vertical wall air-conditioning system can lead to a near-ground temperature increase of more than $2°C$. Moreover, by averaging over the air-conditioning period we have observed that, compared to a roof-top system, the mean temperature gradient over the Sperrstrasse location has reached on the 26 of June 2002 nearly $1.2°C$.

5.4.2 Wind speed

Figure 5.16 first compares the difference in horizontal wind speed between the simulation with (non air-conditioning case), and without UCP (only rural soil). Remark that an average decrease of $2[\frac{m}{s}]$ can be observed inside the urban area of Basel, due to drag effects of buildings. This is an important modification generated by the presence of cities on exterior microclimate.

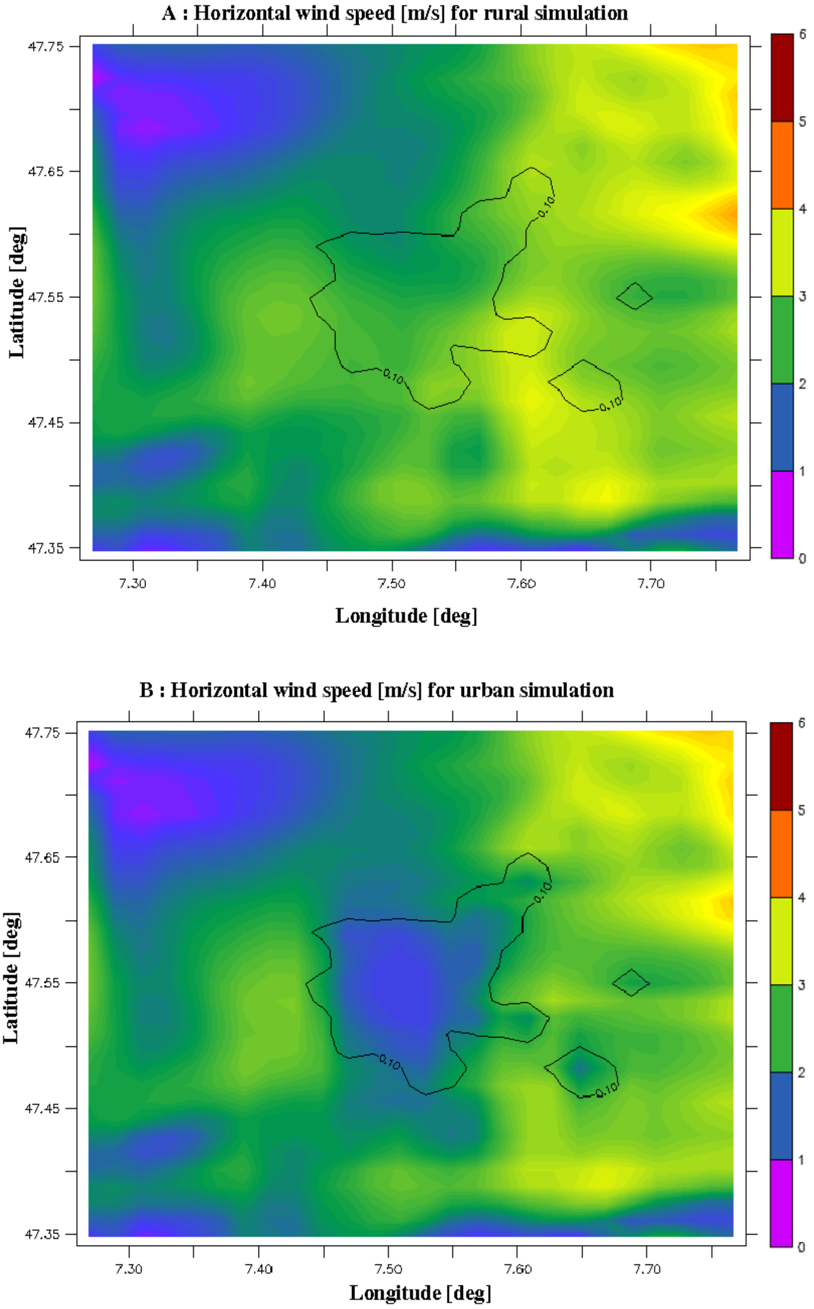

FIGURE 5.16: Horizontal wind speed at 10m height at 12LT 26 June 2002. The simulation without UCP (A) and with UCP (B) are compared. Contour black lines indicate the Basel region.

As already mentioned in Chapter 4 (section 4.4.2.1), the increase in air temperature generated by the air conditioning fluxes, will also have an impact on the magnitude of wind speed.

In this context, Figure 5.17 illustrates the vertical profiles of horizontal wind speed (in the x-direction) at the Sperrstrasse location for the base-case simulation, and the result without taking air-conditioning fluxes into account. Similar to the result of Chapter 4 (Figure 4.20), the main differences are generated above the roofs. Furthermore, the gradient is less important at near-ground level. In particular, by averaging over the air-conditioning period (08LT to 20LT), we observed at this height a mean difference of the order of 5%, and peak values reaching 12%.

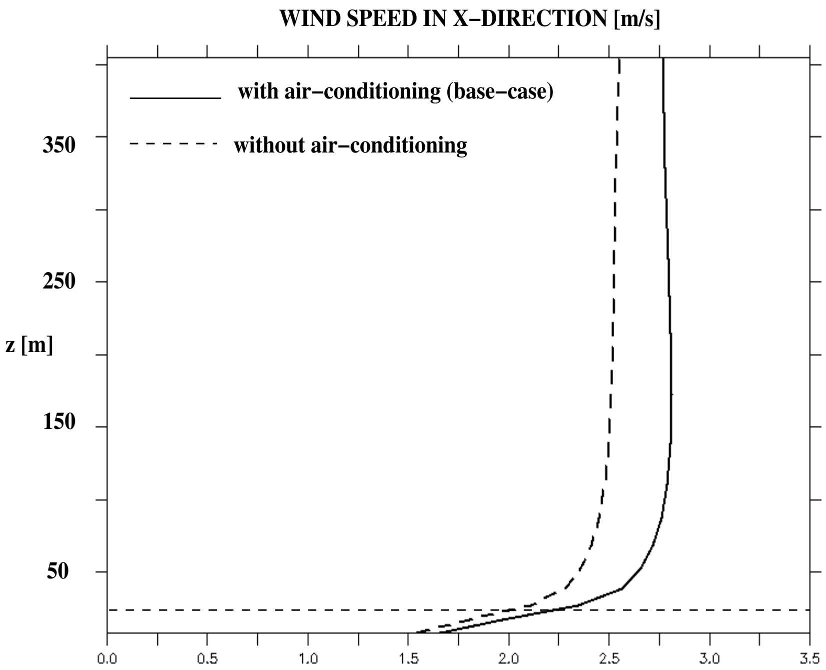

FIGURE 5.17: Vertical profiles of wind speed in the x-direction at the Sperrstrasse location at 12LT 26 June 2002. The base-case result (solid line) is compared to the non air-conditioning simulation (dashed lines). Buildings' height is represented by the dashed straight line.

5.4.3 Turbulent Kinetic Energy

Figure 5.18 indicates that (accordingly to the results of Chapter 4), air-conditioning fluxes generate an increase in the buoyant production of TKE above the buildings roofs.

In particular, during the air-conditioning period, a TKE difference of more than 30% has been observed at 20m height at the Sperrstrasse location.

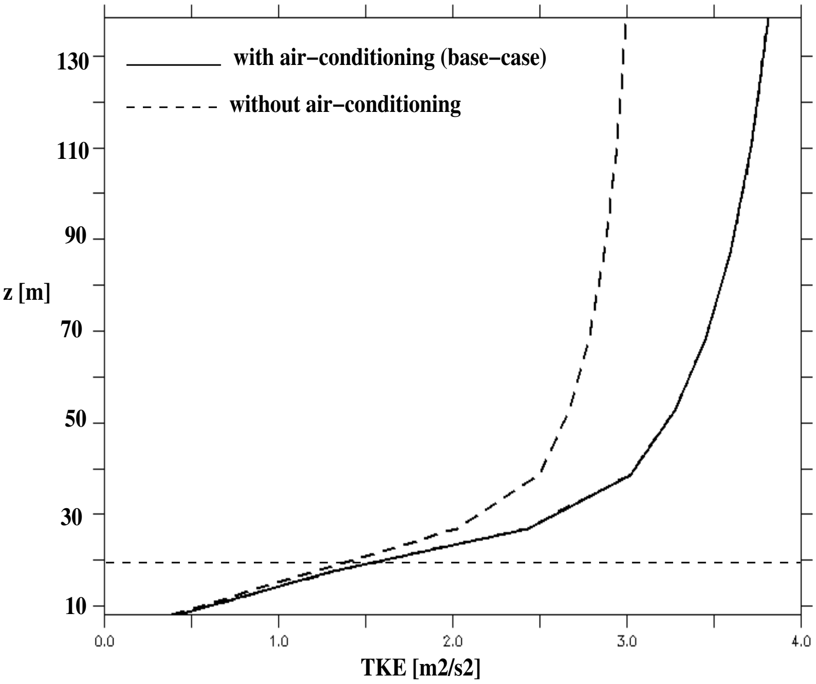

FIGURE 5.18: Vertical profiles of TKE at the Sperrstrasse location at 12LT 26 June 2002. The base-case simulation (solid line) is compared to the one with no air-conditioning fluxes emitted into the atmosphere (dashed line). The straight dashed line indicates roofs height.

As a consequence, the increase in buoyant turbulent kinetic energy leads to a stronger vertical mixing. Similar to the result in Figure 4.20, it has been observed that this effect can occur up to the boundary layer height.

It is interesting to observe that this different turbulent activity can also have consequences on pollutant dispersion. For example, Figure 5.19 shows the near-ground concentration difference related to a constant tracer emission generated at the first vertical mesoscale level over the urban area of Basel, and subjected to transport and diffusion processes.
Remark that the increased turbulent activity generated by air-conditioning facilities, leads to a more important mixing of the pollutant, and consequently to a lower near-ground concentration. In this context, it has been observed that along the Basel area, and during the air-conditioning period, this peak near-ground concentration differences lies between 3% and 9%.

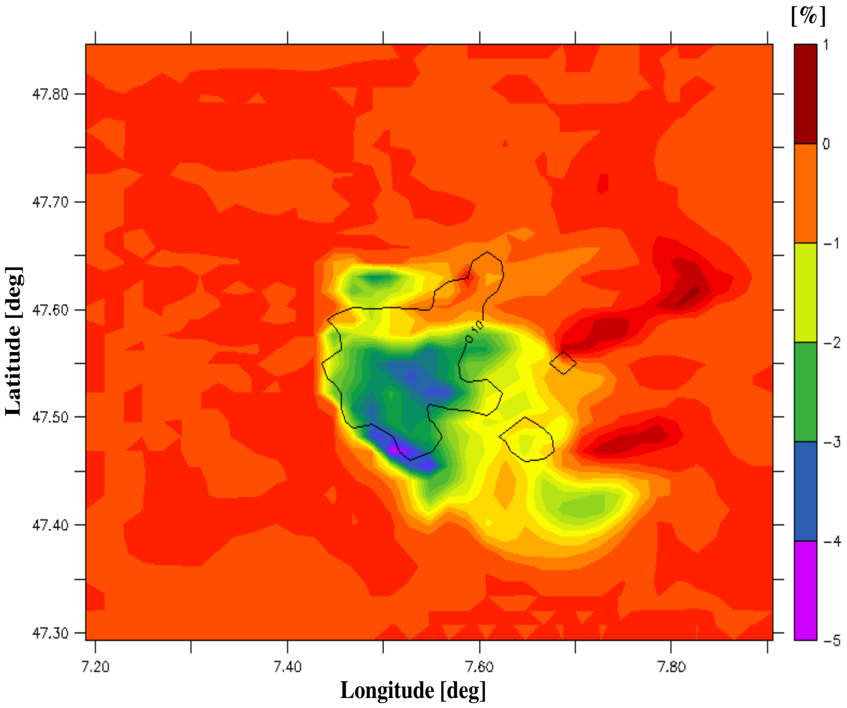

FIGURE 5.19: Near-ground concentration difference (in [%]) at 12LT 26 June 2002, of a constant source emitted along the Basel urban area. The result indicate the difference between the base-case simulation and the non air-conditioning result. Contour black line indicates the Basel urban area.

5.5 Analysis of different urban warming countermeasures

The aim of the present paragraph is to discuss the applicability of the simulation system MM-UCP-BEM in evaluating UHI control strategies, reduce summertime energy consumption from air-conditioning facilities, and in general increase human comfort inside urban areas.

5.5.1 Sensitivity tests

As already presented in Chapter 4 (section 4.4.2.2), an important study that this model can provide lies in a sensitivity analysis of the physical parameters characterising urban surfaces. In fact, identifying how different materials are able to modify urban microclimate (UHI processes, etc.), and cooling/heating energy demands, we can evaluate the effectiveness of long and short term strategies for the optimisation of human comfort in cities. In this context, the sensitivity analysis considered in Chapter 4 for two-dimensional applications, is also applied in the present section with respect to the urban area of Basel. The different configurations considered for the study are recoverred from those of Table 4.4.

Case	**Settings**
A	base-case conditions
B	internal comfort temperature lowered by 4°C
C	COP of the air-conditioning system lowered to the value of 1.2
D	thermal diffusivity of roofs and walls increased by a factor of 10
E	thermal diffusivity of roofs and walls lowered by a factor of 10
F	heat capacity of roofs and walls increased by a factor of 10
G	heat capacity of roofs and walls lowered by a factor of 10

Table 5.3: Representation of the different cases used for the sensitivity analysis (all the physical parameters related to the cases $B, \cdots, G$ are derived from those of the base-case condition A).

Similar to the study performed in Chapter 4, we at first compare in Figure 5.20 the differences (in %) between the peak cooling energy demands generated by the base-case condition, with those obtained with the configurations $B, \cdots, G$. Results refer to 26 of June 2002, and are produced by averaging over the Basel area the differences between the configurations $B, \cdots, G$, with the base-case result A. The peak is then obtained by considering the corresponding maximal values over the air-conditioning period (08LT to 20LT).

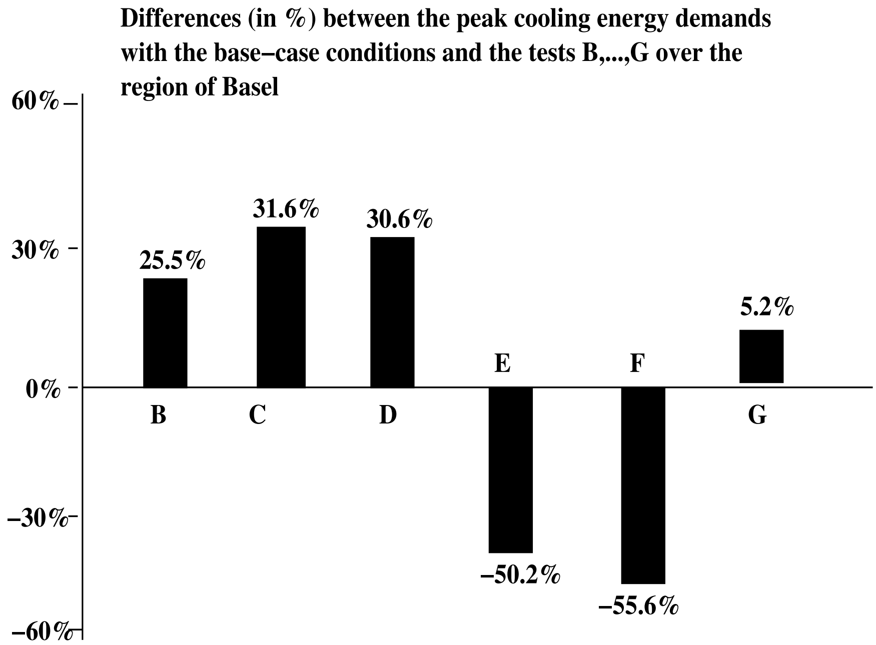

Figure 5.20: Differences in the peak cooling energy demands between the tests $B, \cdots, G$, and the base-case configuration (A).

Remark that similar behaviours are obtained compared to those of Figure 4.2.1 for two-dimensional applications. Thus, for a more detailed explaination of the results of Figure 5.20 we refer to section 4.4.2.2. In general, the following considerations can be made:

- paying attention to the efficiency of the air-conditioning system (COP), and accepting a higher internal comfort temperature, can have very positive effects on cooling-energy demands.
- physical properties of built materials modify the heat exchanges between indoor and outdoor air, and, therefore, can have important consequences on cooling energy demands. In particular, well insulated and higher heat capacity materials can provide very important summertime cooling energy savings.

As already mentioned in Chapter 4, in all these cases the anthropogenic fluxes emitted into the atmosphere for cooling purposes will have a direct impact on external temperature. It could be seen in Table 5.4, that the corresponding variations in the average near-ground air temperature can be more or less important, with a range going from $0.11°C$, to $1.32°C$, depending on the chosen condition, and the air-conditioning system being in use.

Case	**Roof-top** [$°C$]	**Vertical-wall** [$°C$]
A	0.20	0.88
B	0.22	0.92
C	0.25	0.96
D	0.42	1.32
E	0.11	0.43
F	0.12	0.47
G	0.31	1.03

Table 5.4: Mean near ground air temperature differences between the simulation ejecting the air-conditioning fluxes into the atmosphere (base-case) and another which does not (for example heat released into the soil). Results refer to 26 June 2002, and were obtained averaging in space along the Basel area and in time from $08LT$ to $20LT$ (air-conditioning period).

Note that according to the results of Figure 5.15 and the conclusions of Chapter 4, the external temperature is more affected by vertical wall than roof-top air-conditioning systems.

Results $A, \cdots, G$ indicate that there are different strategies with which one can modify the magnitude of anthropogenic heat emitted from air-conditioning facilities, and the corresponding effects on urban microclimate. Similarly, the feedback produced by the cut-off of air-conditioning waste heat into the atmosphere is also modified. In this context, feedback values can be important in evaluating in different case-settings the cooling energy surplus needed to maintain the internal temperature of buildings within comfort conditions. In particular, following the work of Büyükalaca et al. (2001), the feedback will be evaluated by the Degree-Days (DD) value, which is a measure indicating the demand for energy to heat (HDD) or cool (CDD) buildings' environments. The method assumes that the energy needs for buildings are proportional to the difference between the mean daily temperature, and a base temperature. Taking this into account, the feedback value (in %) at every point (I,J,K) of the mesoscale grid (cf. section 2.3) is computed with the following expression:

$$\text{feedback}_{IJK} := \left[\frac{CDD_{AC} - CDD_{NAC}}{CDD_{AC}}\right]_{IJK} .100 \tag{5.4}$$

where CDD_{AC} defines cooling degre-days for the simulation which ejects air conditioning heat into the atmosphere, while CDD_{NAC} refers to the result in which the internal temperature is maintained inside comfort conditions, without emitting the corresponding heat (e.g. heat released into the soil). For a given number D of days, the general expression for CDD is given by (more details are given in Büyükalaca et al., 2001):

$$CDD = (1 \text{ day}) \sum_{\text{days}=1}^{D} (T_m - T_b)^+ \tag{5.5}$$

where T_m is the daily mean outdoor temperature, and T_b the base outdoor temperature. This value defines the temperature above which cooling is needed. Traditionally, CDD are computed by setting the base temperature to $22°C$ (Büyükalaca et al., 2001). This is also considered in the present calculations, but it should be kept in mind that there can be different parameters that can modify this constant (personal preferences, buildings characteristics, etc.), and that the value of $22°C$ should be rearranged from one application to another (Kreider et al., 1994).

For the present application feedbacks are only computed for 16 June 2002. The corresponding values aim to give a first idea of the magnitude and the way with which this quantity can vary with respect to different settings. Clearly future works should consider longer periods of time (months, year) in order to provide more complete and concluding results.

Table 5.5 resumes the feedbacks related to the different settings $A, \cdots, G$. These values refer to the first mesoscale level (10m height), and are calculated by averaging the percentages over the Basel urban area.

The graphics showing the corresponding near-ground feedbacks over Basel for the different situations are presented in the Appendix C.

Case	**Feedback values** [%]
A	3.8
B	4.6
C	5.4
D	9.2
E	2.4
F	2.7
G	5.8

Table 5.5: Mean near-ground feedback values over the Basel urban area on 26 June 2002 for the different settings $A, \cdots, G$.

Note that accordingly to the previous results, the feedbacks computed as CDD difference between the air-conditioning and the non air-conditioning case, can also lead to important variations based on the characteristics of the air-conditioning system (COP, internal comfort temperature), and the physical properties of buildings. In particular for these summer conditions, materials with high thermal diffusivity and low heat capacity, enable a higher heat transfer from the outside air to the inside air, generating very important feedback surplus.

Remark 1

For all cases $A, \cdots, G$, it has been assumed that the air-conditioning system is working from 08LT to 20LT. Figure 5.21 illustrates (for the setting A) that if the system is switched on throughout the day, an important feedback surplus is produced. It has been observed that this modification can increase the mean near-ground feedback value from 3.8% to 8.2%. Even if this represents only an indicative result, it clearly shows that an excessive air-conditioning activity increases the magnitude of heat fluxes emitted into the atmosphere, increasing the mean outdoor temperature, and consequently the CDD value.

Remark 2

It has been previously pointed out that inside urban canopies, vertical wall air-conditioning systems generate more important effects than roof-top ones. As it could be seen in Figure 5.22, this is directly followed by an increase in CDD values and consequently of the feedback defined by expression (5.4). In particular it has been observed that for the setting A, the application of a vertical wall air-conditioning system increases the mean near-ground feedback over Basel from 3.8% to 9.6%.

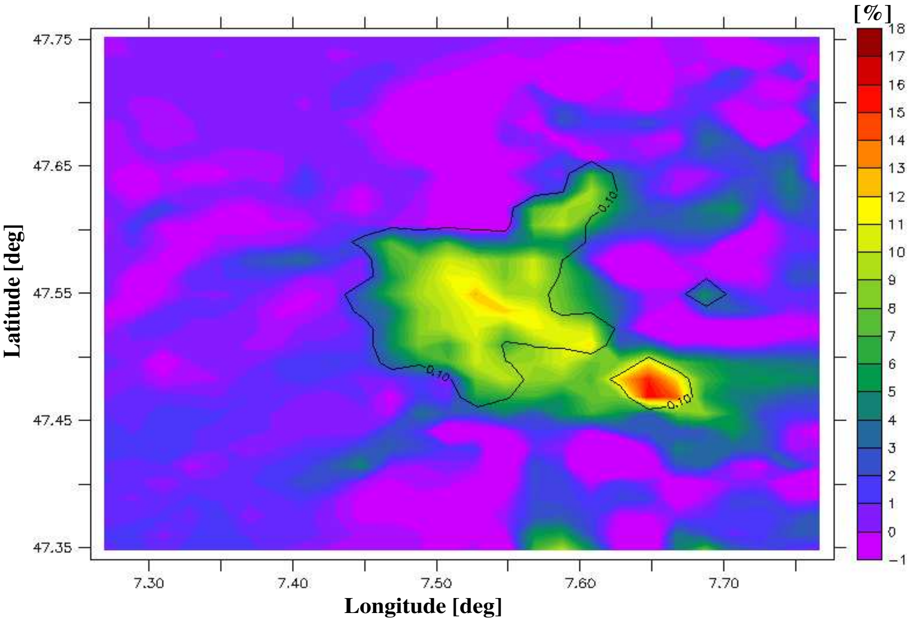

FIGURE 5.21: Average near-ground feedback over Basel with setting A, and a roof-top air-conditioning system working during all the day. The result refers to 26 June 2002, and the limits of the Basel urban area are represented with the contour black line.

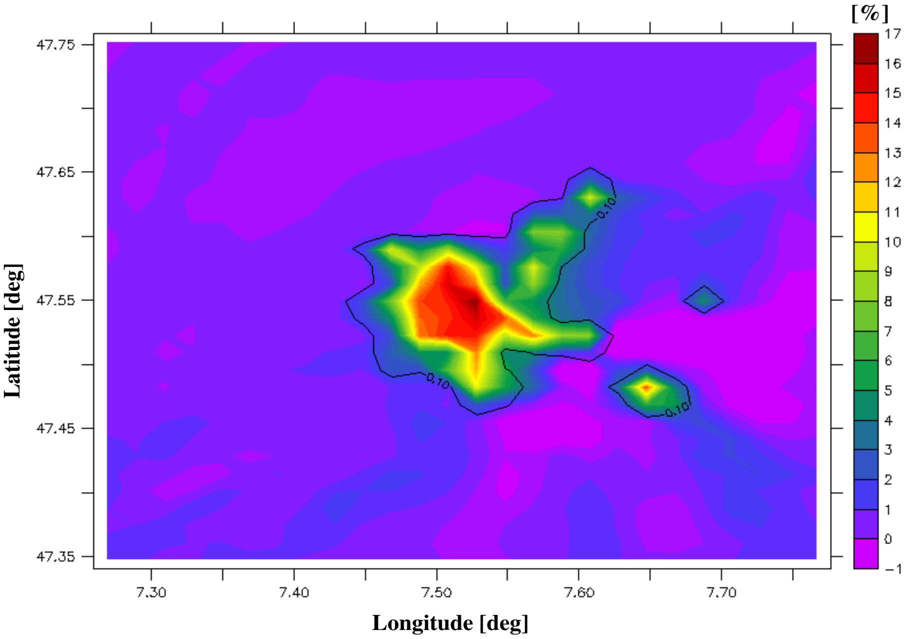

FIGURE 5.22: Average near-ground feedback over Basel with setting A, and a verical wall air-conditioning system. The result refers to 26 June 2002, and the limits of the Basel urban area are represented with the contour black line.

As already mentioned, these are first indicative results, but further improvements have to be done in order to expand the present study to longer periods. In this context, winter conditions should also be considered in order to evaluate the impact of summertime countermeasures on heating energy demands and in order to find strategies for optimising heating performances.

5.5.2 On the impact of future urban planning guidelines

In future works the intent is to apply the simulation system MM-UCP-BEM over longer periods of time in order to evaluate the effects of different countermeasures against UHI formation, energy saving, and global warming. In particular, year-long simulations are needed to evaluate if summertime UHI countermeasures do not excessively affect pedestrian comfort in winter time conditions. In this context, recent studies produced by Ihara et al. (2007), suggest the applicability and the effectiveness of this type of numerical model to perform these kind of studies.

In a near future, these modelling tools could be an important support for urban planners, helping them to evaluate the most effective policies to obtain more comfortable, and less energy-consuming cities. In addition, models could help to test, and understand which are the best ways to organise and expand developping cities. For example, Figure 5.23 gives an idea of a theoretical study concerning the city of Basel. The aim would be to evaluate how the city should be expanded (to the north-west (A), or to the south-east (B)) in order to maximize pedestrian comfort, and minimize energy demands and urban warming. Clearly, in this case year-long simulations will be needed for taking into account both winter and summertime conditions, and for permiting a more complete insight into local meteorological conditions around the city.

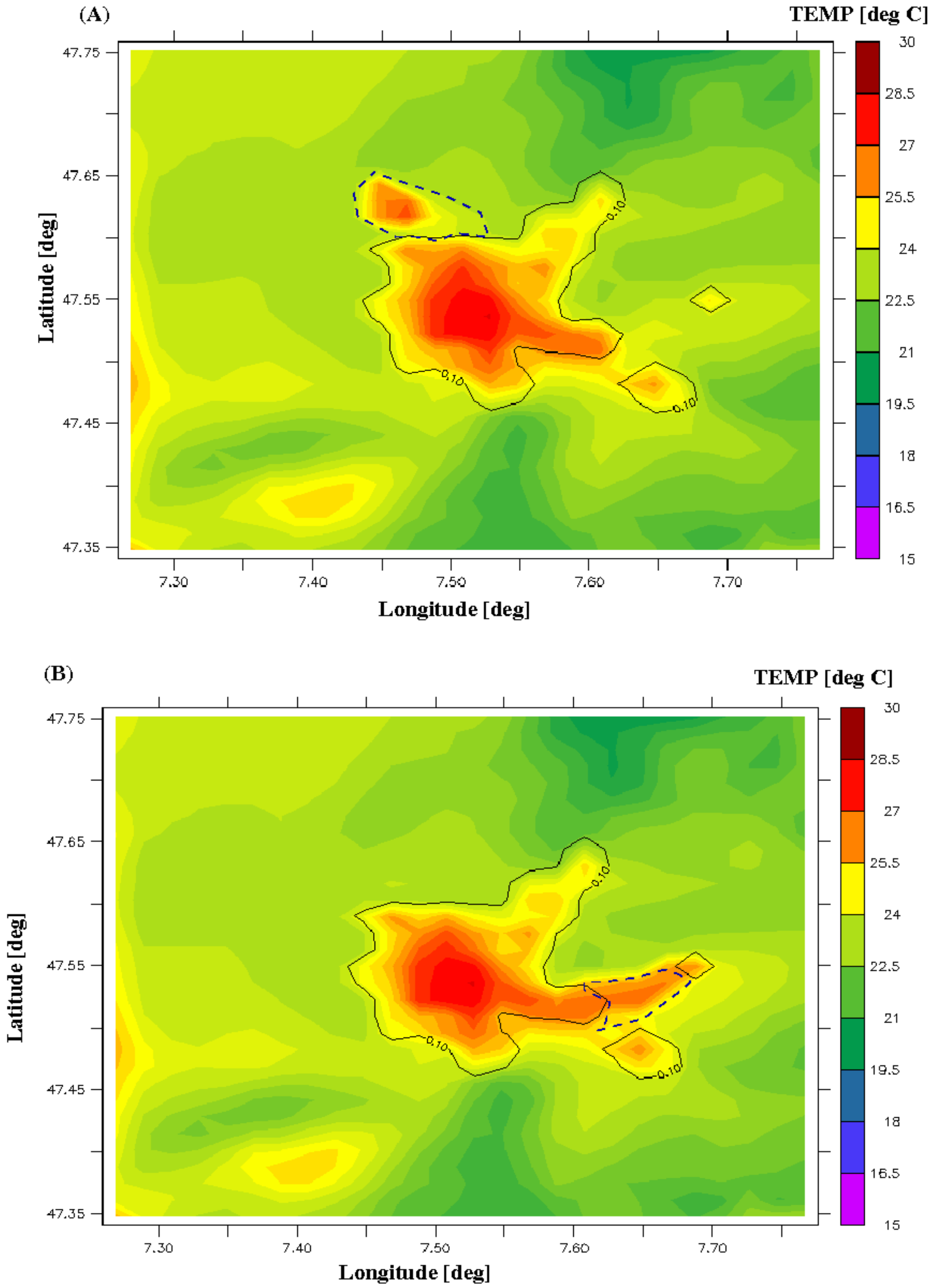

FIGURE 5.23: Heat Island over the city of Basel on 26 June 2002. Hypotetical extensions of the city in the north (A), and in the south (B) directions are represented in dashed lines. The contour of the Basel urban area is given in black solid lines.

5.6 Conclusions

The numerical simulation system MM-UCP-BEM was applied over the three-dimensional realistic configuration including the city of Basel and the surrounding areas.

Comparisons with measured external temperatures provided by the BUBBLE campaign, initially indicated that the model could reasonably well reproduce the daily variations of outdoor air temperature. Still, simulated daytime average temperatures estimated by the model appeared too high, for both urban and rural sites. In this context, a future improvement of the soil module by taking evapo-transpiration processes into account should be considered. In addition, the radiation model adopted in this work does not include the effects generated by cloud formation. Neglecting clouds and the related decrease of incoming radiation can lead to overestimating outdoor temperature. This aspect should be taken into account in future developments, especially as longer simulation periods are planned.

The urban scheme proved its capability to capture urban-induced processes, such as the decrease in wind speed inside the city induced by drag forces or the formation of the urban heat island. In particular, the implementation of the building energy model indicated that anthropogenic air-conditioning fluxes produce an increase of this phenomenon. We have observed that this behaviour is more pronounced when vertical wall air-conditioning systems are adopted.
The study of the impact of BEM on other meteorological quantities confirmed the results obtained in Chapter 4 with two-dimensional configurations. In this context, an increase in wind speed and turbulent kinetic energy was observed. We underlined, that this turbulent activity generates a higher vertical mixing, and can lead to a decrease in near-ground air pollution.

The second part of the chapter was focused on evaluating the applicability of the simulation system MM-UCP-BEM with respect to the three-dimensional configuration, in performing urban warming countermeasures, and cooling energy demands control strategies. For this purpose, we first considered a similar sensitivity analysis as the one in Chapter 4 concerning 2D idealised cities. Simulations indicated that there are different strategies and physical parameters that can modify the magnitude of air-conditioning fluxes, and the corresponding impact on urban meteorology. Results follow the same trend compared to those presented in Chapter 4. In particular, we observed that low thermal diffusivity and high heat capacity materials can generate very important cooling energy savings. Similarly, the implementation of efficient air-conditioning systems and the application of an ”energy-saving policy” (an increase in the internal comfort temperature, switching off air-conditioning system during the night-time) can also lead to positive effects.

The analysis of the differences in cooling degree-days between air-conditioning and non air-conditioning simulations (i.e. heat flux not released into the atmosphere), indicate that anthropogenic air-conditioning fluxes can produce non negligent feedbacks on the exterior temperature. These values are sensitive to the physical properties of built materials (roofs, walls), as well as to the air-conditioning system being in use. In this context, we have observed that at ground level, vertical wall air-conditioning systems produce more important feedbacks than roof-top ones.

In conclusion, we showed in this work that the numerical model MM-UCP-BEM can be applied for the study of realistic three-dimensional configurations. In addition, the introduction of BEM inside the UCP allows computation of the heat released into the atmosphere by air-conditioning facilities, as well as the corresponding feedbacks produced on different meteorological variables. In our findings, the impact of anthropogenic heat fluxes on the outdoor temperature is not negligible, and should also be taken into account for a more complete summertime UHI mitigation strategy. In general, the implementation of BEM increased the efficiency of the urban parameterisation in providing more detailed studies of urban warming countermeasures and cooling energy demands in real cities.

It should be stated that the different results presented in this work have mainly qualitative interests, and do not intend to lead to quantitative conclusions. In fact, a more complete three-dimensional verification has to be conducted, ideally in hot-climate cities, where different measured data concerning air-conditioning fluxes are available. Nevertheless, the correspondance between two (Chapter 4), and three-dimensional results, as well as the separate verifications of MM (Chapter 2), BEM (Chapter 3), and UCP-BEM (Salamanca and Martilli, 2008), increases the reliability of the different conclusions concerning the impact of anthropogenic air-conditioning fluxes and cooling energy demands.

In future works, winter conditions should also be considered in order to permit a more precise evaluation of the impact of summerime countermeasures on heating energy demands and to find strategies for the optimisation of heating performances. In this context, further improvements have to be done in order to be able to expand the present study to longer periods.

Finally, we underlined that in a near future, such numerical models could be utilised as a support for urban planners, helping them to specify appropriate policies for the maximisation of human comfort in urban areas. In this context, for developping countries, they could help evaluate the most efficient options to expand cities.

Appendix A: List of the different BUBBLE measuring stations

The following table lists the different stations available during the BUBBLE IOP. They are divided into Urban (U), Rural (R), and Sub-Urban (S) areas. The different urban and rural stations used for the averaging procedure in the section 5.3 are emphasised.

Code on map (Figure 5.4)	**Station name**	**Heights [mASL]**
Rp6	Aesch Schlatthof	353
Se1	Allschwil	277
Rp7	Airport Basel-Mulhouse	
Sp2	Basel-Bäumlihof	289
Sp3	Basel-Binningen (ANETZ, NABEL)	316
Up6	Basel-Feldbergstrasse	255
Ue4	Basel-Horburg	254
Re3	Basel-Lange Erlen	275
Up7	Basel-Leonhard	273
Ue5	Basel-Kleinhüningen	265
Up8	Basel-Novartis Klybeck	255
Ue3	Basel-Messe	255
Up9	Basel-Novartis St. Johann	257
Up10	Basel-Roche	255
Ue2	Basel-Spalenring	278
Ue1	Basel-Sperrstrasse	255
Up11	Basel-St. Johann	260
Rp11	St. Chrischonaturm	490
Sp4	Dornach	325
Re4	Gempen	710
Re1	Grenzach	265
Sp5	Liestal LHA	320
Rp8	Oetlingen	450
Rp9	Pratteln Hardwasser	272
Sp6	Rheinfelden	285
Rp10	Schönenbuch	400
Sp7	Schweizerhalle	270
Re5	St. Louis	250
Re2	Village Neuf	240
Sp8	Weil am Rhein	250

Appendix B: Thermal properties of the building materials

The following table illustrates the physical characteristics of the different layers for roofs, walls, and streets (thickness d [m], heat capacity of the layer C [$\frac{MJ}{m^3K}$], thermal conductivity λ [$\frac{W}{mK}$]). The physical properties of floors is set equal to those corresponding to the walls. Layer 1 corresponds to the most internal, and 3 to the most external.

Roof Layer	1	2	3	4
d	0.02	0.02	0.02	0.04
C	1.128	0.276	0.382	1.745
λ	0.614	0.129	0.090	0.984
Street Layer	1	2	3	4
d	0.010	0.040	0.025	0.975
C	1.940	1.940	1.550	1.350
λ	0.750	0.750	0.934	0.275
Wall Layer	1	2	3	4
d	0.01	0.03	0.08	0.02
C	1.778	1.780	1.764	1.779
λ	1.070	1.076	1.071	0.651

Appendix C: Near-ground average feedbacks for the different situations.

The different cases presented in Figures 5.24, $\cdots$,5.30 are those considered in Table 5.3. In all the Figures, countour black lines indicate the limits of the Basel urban area. Results refer to 26 June 2002.

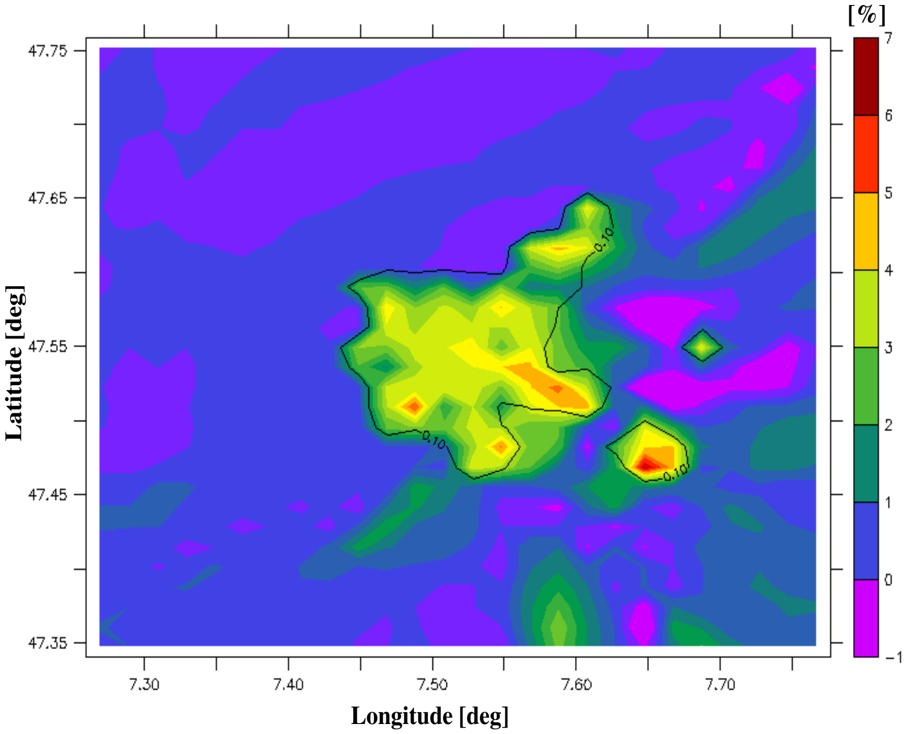

FIGURE 5.24: *Case A*

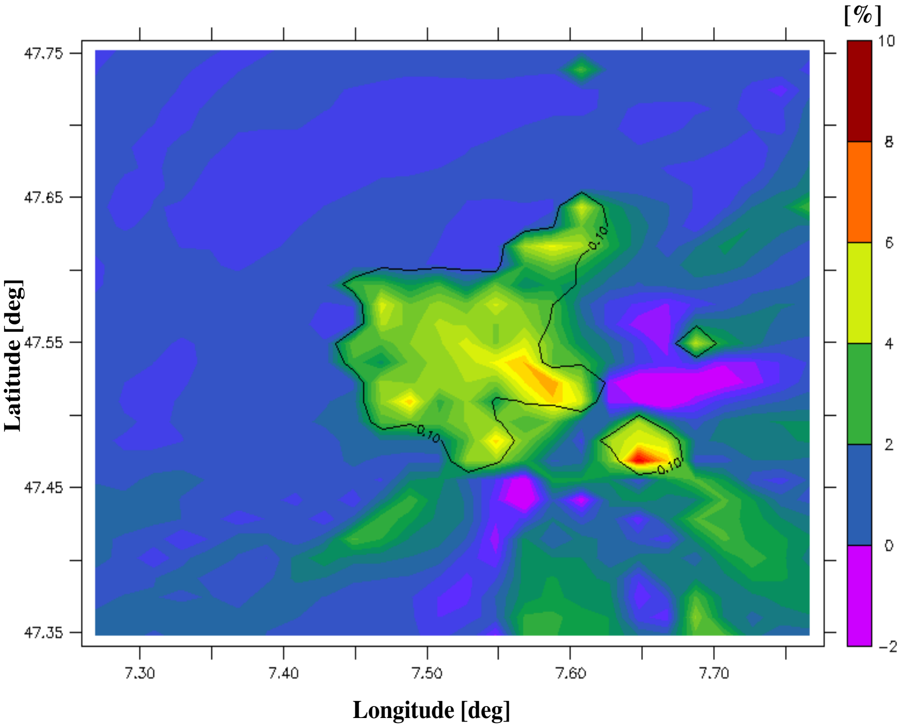

FIGURE 5.25: *Case B*

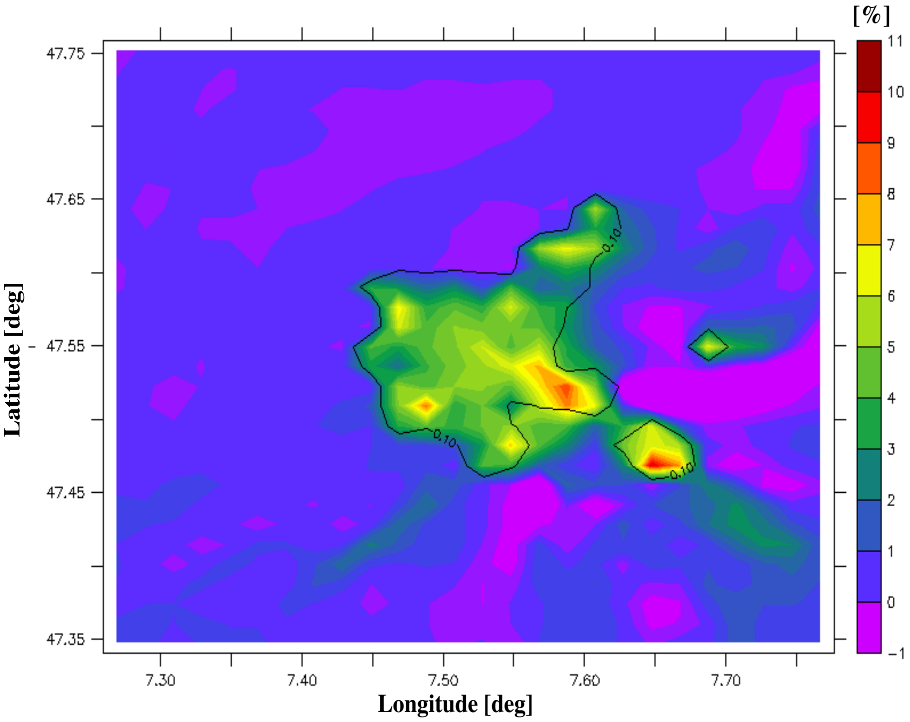

FIGURE 5.26: *Case C*

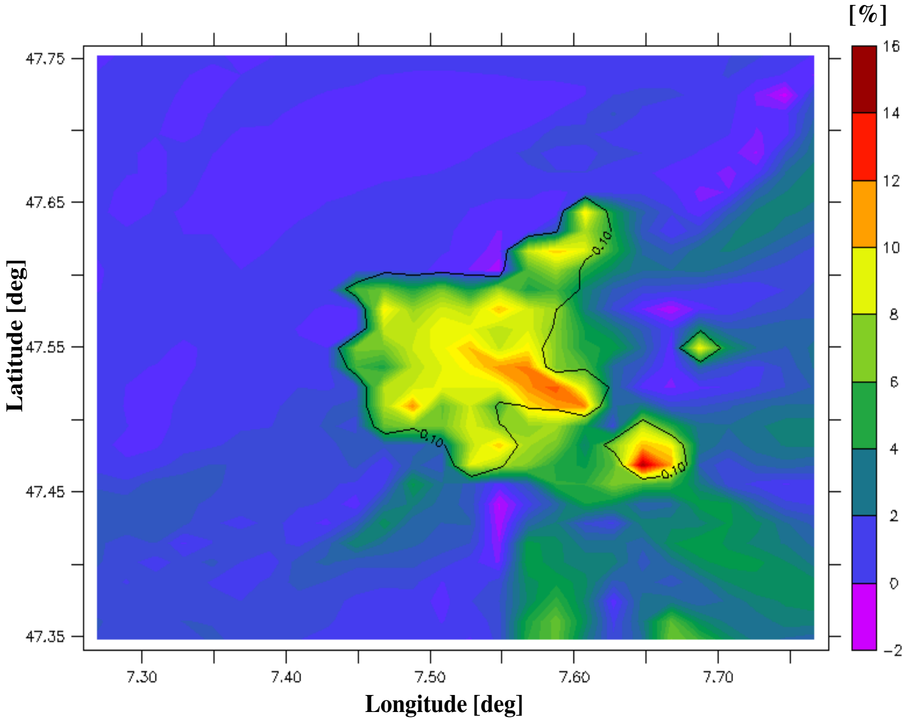

FIGURE 5.27: *Case D*

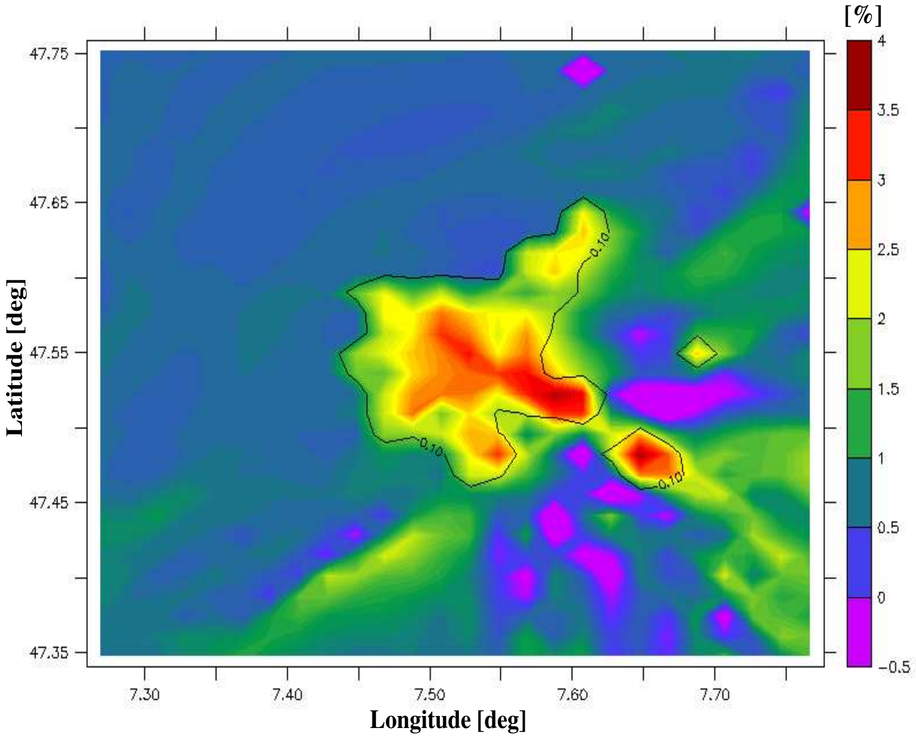

FIGURE 5.28: *Case E*

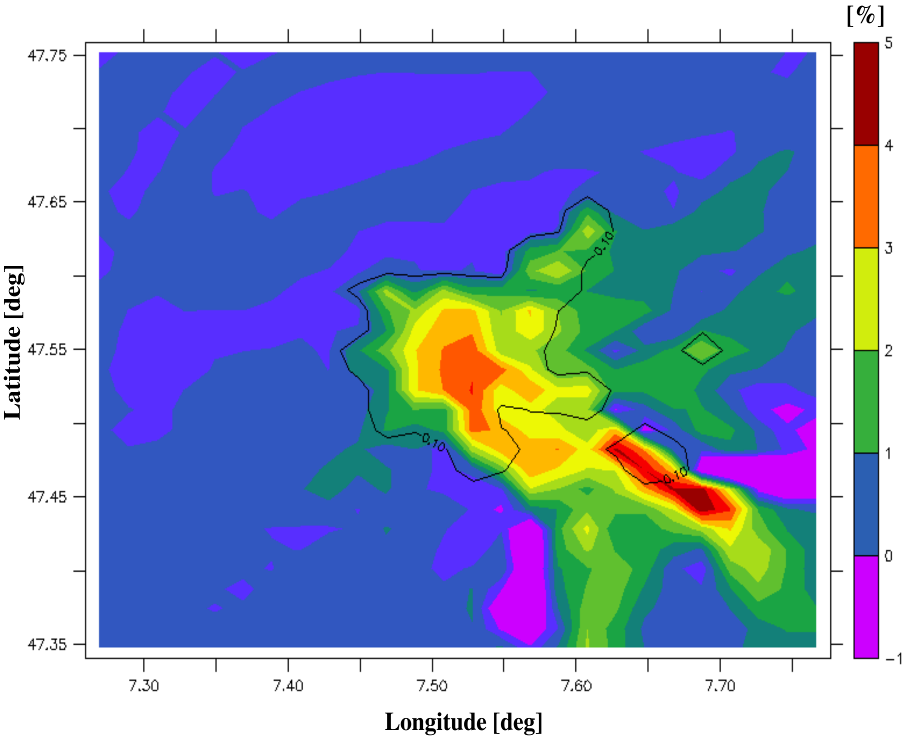

FIGURE 5.29: *Case F*

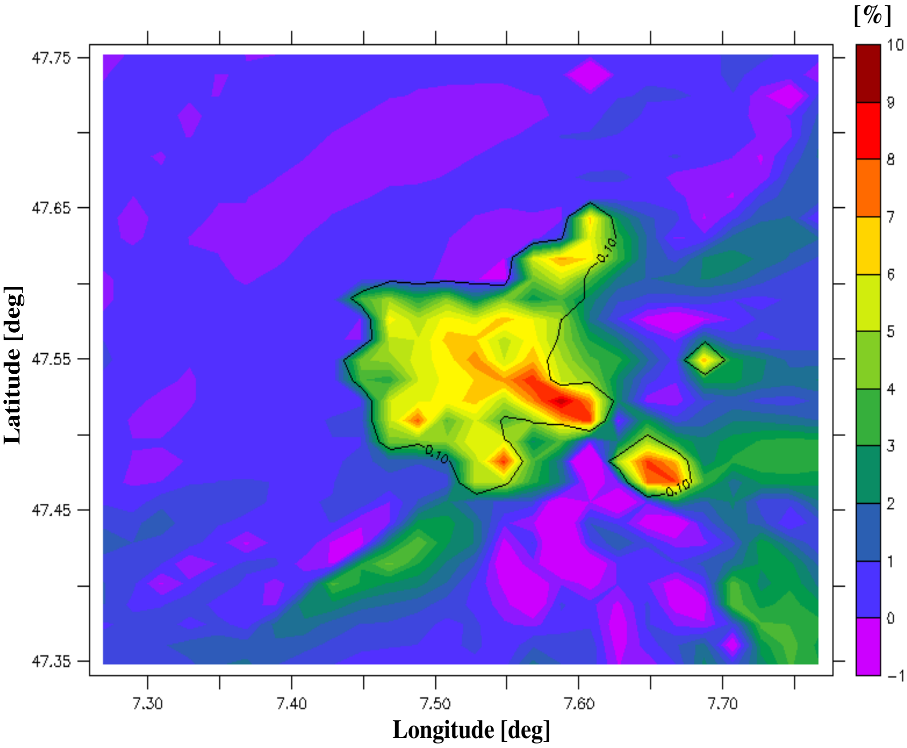

FIGURE 5.30: *Case G*

Bibliography

[1] Büyükalaca, O., Hüsammettin, B., Tuncay, Y.: 2001, 'Analysis of variable-base heating and cooling degree-days for Turkey', *Applied Energy*, **69**, 269-283.

[2] Chang, C.L.: 2006, 'The parameter optimization in the inverse distance method by genetic algorithm for estimating precipitation', *Environmental Monitoring and Assessment*, **117**, 145-155.

[3] Christen, A.: 2005, 'Atmospheric Turbulence and Surface Energy Exchange in Urban Environments. Results from the Basel Urban Boundary Layer Experiment (BUBBLE)', Diss. Phil.-Nat.Fak. Univ Basel, ISBN 3-85977-260-X.

[4] Clappier, A., Perrochet, P., Martilli, A., Muller, F., Krueger, B.C.: 1996, 'A new non-hydrostatic mesoscale model using a CVFE (control volume finite element) Discretisation technique', in *Proceedings of EUROTRAC Symposium '96.*, Editors: P.M. Borrell et al., Computational Mechanics Publications, Southampton, 527-531.

[5] Fehrenbach, U.: 1999, 'Analyse und Bewertung lokal- und regionalklimatishc wirksamer Faktoren in der Region Basel', Diss. Phil.-Nat.Fak. Univ Basel, ISBN 3-85977-245-7.

[6] Germano, M.: 2006, 'Qualitative modelling of the natural ventilation potential in urban context', *PhD Thesis N°* 3482, Swiss Federal Institute of Technology, Lausanne.

[7] Grell, G.A., Duhia, J. and Stauffer, D.R.: 1994, 'A description of the 5^{th} generation of the Penn State/NCAR mesoscale model', *NCAR Technical Note*, TN 398+STR.

[8] Grimmond, C.S.B., Oke, T.R.: 2000, 'Aerodynamic Properties of urban areas derived from analysis of surface form', *J. Appl. Meteor*, **38**, 1262-1295.

[9] Ihara, T., Kikegawa, Y., Asahi, K., Genchi, Y., Kondo, H.: 2007, 'Changes in year-round air temperature and annual energy consumption in office building areas by urban heat-island countermeasures and energy-savings measures', *Applied Energy*, **85**, 12-25.

[10] Kreider, J.F., Rabl, A.: 1994, 'Heating and cooling of buildings', New-York, McGraw Hill.

[11] Martilli, A., Clappier, A., Rotach, MW.: 2002, 'An urban surface exchange parameterization for mesoscale models', *Boundary-Layer Meteorology* **104**: 261-304.

[12] Muller, C.: 2007, 'Improvement of an urban turbulence parameterization for meteorological operational forecast and air quality modeling', Phd Thesis $N°$, **3766**, Swiss Federal Institute of Technology, Lausanne.

[13] Ratti, C., Di Sabatino, S., Britter, R., Brown, M., Caton, F., Burian, S.: 2002, 'Analysis of $3-D$ urban databases with respect to pollution dispersion for a number of European and American cities', Water, Air and Soil Pollution: Focus 459-469.

[14] Roches, A.: 2007, 'Développement d'un préprocesseur de modèles météorologiques', *Msc Thesis*, Swiss Federal Institute of Technology, Lausanne.

[15] Rotach, M.W., Vogt, R., Bernhofer, C., Batchvarova, E., Christen, A., Clappier, A., Feddrsen, B., Gryning, S.E., Martucci, G., Mayer, H., Mitev, V., Oke, T.R., Parlow, E., Richner, H., Roth, M., Roulet, Y.-A., Ruffieux, D., Salmond, J., Schatzmann, and Voggt, J.: 2005, 'An urban boundary layer meteorology project', *Theor. Appl. Climatol.* DOI: 10.1007/s00704-004-0117-9.

[16] Roulet, Y.-A., Martilli, A., Rotach, M.W., Clappier, A.: 2005, 'Validation of an urban surface exchange parameterization for mesoscale models $-1D$ case in a street canyon', J. of Appl. Meteorol., **44**, 1484-1498.

[17] Roulet, Y.-A., 2004, 'Validation and Application of an urban turbulence parameterisationscheme for mesoscale atmospheric models', *PhD Thesis N°* 3032, Swiss Federal Institute of Technology, Lausanne.

[18] Salamanca, F. and Martilli, A.: 2008, 'A new Building Energy Model coupled with an Urban Canopy Parameterization for urban climate simulations-Part II. Validation with one-dimensional off-line simulations', Submitted to *Theor. Appl. Climatol.*.

Chapter 6

Conclusions and perspectives

Pushed by an increasing economic development, as well as important population growth, urban regions include nowadays more than half of the total population and, in the next twenty five years, this proportion is expected to increase to three quarters. Consequently, cities are submitted to a continuing expansion, and to more and more important anthropogenic activities (e.g. traffic emissions, heating from air-conditioning facilities). This increasing stress placed on urban environment can modify local climate in many different ways, generally leading to a progressive degradation of exterior microclimate. By now, there are different cities in which inhabitants are forced to live in unhealthy conditions.

Cities replace natural land cover with pavement, buildings, and other infrastructures. These modifications differentiate urban with respect to rural areas, by both, geometrical and thermal aspects. In particular, geometrical factors are generated by the high roughness of urban surfaces, leading to an intense drag and shear layer at the top of the canopy. In that way, mean kinetic energy is transformed into turbulent kinetic energy, and wind speed is decreased. In addition, buildings' geometry produces a radiation trapping effect in street canyons with consequent heat storage surplus in buildings. On the other hand, thermal modifications appear as materials commonly used in urban regions bear different thermal properties (heat capacity, thermal conductivity), and surface radiative properties (albedo, emissivity) than material substrates typical of the surrounding rural areas. Both, thermal and physical aspects cause cities to become relatively dry environments, with higher temperatures than rural surrounding areas. This phenomenon of urban area warming up, called the Urban Heat Island (UHI), can have important consequences on human comfort and local meteorology, represents one of the most important and studied processes caused by the presence of cities.

In chapter 1 of the present thesis, we mentioned that UHI contributes to increase summertime heat waves' strength, with important consequences on mortality rate, and human health in general. Furthermore, different studies indicate that this phenomenon can lead to an increase in precipitations rate, as well as cloud and fog development. The impact of smog generated by factories and traffic emissions is also made more important, with very relevant effects on air quality and human health. In summertime conditions, urban warming can also lead to a higher cooling demand from air-conditioning facilities, with further economic consequences.

Taking these aspects into account, there is nowadays a real need for efficient urban planning guidelines and sustainability policies in order to improve life quality in urban areas. In this context, several points should be considered including urban warming, air pollution, human health, economic, and cooling energy needs.
The work conducted in the present thesis goes in this direction, aiming at to developing a numerical simulation system which allows a more complete representation of the complex interactions between buildings and the atmosphere. A major interest was given to the study of UHI processes, and control strategies, as well as to the optimization of buildings' energy demands. In near future, the aim is to utilise this kind of model as a support for urban planners, helping them to identify appropriate policies for the optimization of human comfort in urban areas. In particular, with the term "comfort" one shoud include all the different aspects mentioned above.

One of the first and major difficulties in representing urban canopy climate and related air pollution problems, lays in the fact that city scale (tens of kilometers) and mesoscale (hundreds of kilometers) processes are strictly linked, and interactions between them must be taken into account. Furthermore, as presented in chapter 2, the system of equations describing atmospheric flows, and UHI processes is highly non-linear, making the use of numerical models a common technique to handle these types of problems. It is also important to mention that due to limited computational power of computers (CPU), and the lack of measured data, a complete representation of all features of a real city would be too complex. Thus, city structure cannot be resolved in detail, but the effects generated by urban areas have to be parametrized. In this context, we mentioned in chapter 1 that different parameterisation techniques can be adopted, based on Empirical Models, adapted vegetation schemes, and Urban Canopy Parameterisations (UCP). In the present work, a UCP method has been considered (chapter 4), and introduced inside a mesoscale meteorological model (chapter 2).

Based on previous works performed at the Air and Soil Pollution Laboratory (LPAS) at EPFL, a non-hydrostatic mesoscale model was first developed as part of this thesis. The governing equations, with the corresponding resolution techniques, have been presented in detail in chapter 2. It was mentioned, that the mesoscale system can be represented as a combination of advective and diffusive processes, together with implicit and explicit source terms contributions. A fully finite volumes numerical method has been used to solve the different equations, in which the mesocale domain was treated by a structured and deformable (terrain-following) grid, in order to take topographic features into accoount. At first, a set of numerical tests was considered in order to evaluate the behaviour of the advection and diffusion algorithms. In a second time, we performed series of benchmark simulations, with the purpose of testing the complete mesoscale model with respect to analytical, numerical, and observed results cited in the literature. In this context, we have observed that the model was able to reproduce correctly different mesoscale processes like the formation of mountain and lee waves as well as the production of Kelvin-Helmolts instabilities related to non-linear Density Current.

In order to take physical processes generated by cities into account an urban canopy parameterisation (UCP) has been introduced inside the Mesoscale Model (MM). This urban scheme has been extensively used in previous works, and validations have been carried out for one, two, and three-dimensional configurations. The model represents a city as a combination of different urban classes in which mechanical (drag and shear forces), and thermal (radiation trapping) effects produced on meteorological quantities are separately computed for walls, roofs, and streets, and added as implicit and explicit source terms to the mesoscale model equations. The model composed by MM and UCP (MM-UCP) was applied to two-dimensional idealized configurations (chapter 4), and over the three-dimensional domain covering the city of Basel and its surroundings (chapter 5). Results demonstrates the capability of MM-UCP to reproduce different features of urban canopy climate (e.g. decrease in wind speed due to drag and shear forces, formation of the UHI).

One of the possible improvements of the UCP model, included a more complete representation of anthropogenic heat fluxes exchanged between buildings and the atmosphere, which were only partially taken into account by fixing the internal temperature of the walls. In this context, different studies pointed out that for summertime conditions, anthropogenic fluxes released by air-conditioming facilities can have an important impact on urban microclimate and should be taken into account by mesoscale models for a more complete UHI mitigation study and a related analysis of cooling energy demands. Considering the initial motivations of this work, a numerical simulation system aiming at performing complete urban warming countermeasures studies, should be able to take these different aspects into account. To this purpose, a Building Energy Model (BEM) was developped and coupled to the urban canopy parameterisation.

The governing equations and the physical processes considered by BEM have been presented in detail in chapter 3. This is a box-type heat budget model, each box representing a particular floor in which sensible and latent heat generated by convection, conduction, ventilation, people, and equipments is taken into account. Presence of windows is also considered, as well as the consumption of energy due to air-conditioning, that can be generated by both, a single roof-top, or a series of vertical wall systems located at the different floors of the building.

In order to verify the behaviour of this building model a necessary validation procedure was initially carried out. It consisted in a combination of analytical, inter-program, and empirical testing procedure, in which the model was compared to other programs used in the thermal analysis of buildings, as well as to the behaviour of a similar box-building model. Results indicated that BEM was able to simulate accurately the basic heat transfer phenomena and to reproduce the heat fluxes exchanged between buildings and the atmosphere. Note that this is a very important point as we had a major interest in evaluating the impact of these heat fluxes on urban canopy climate.

In a second time, a sensitivity analysis was carried out which indicated that physical characteristics of the walls, as well as heat released by equipments and occupants can have important consequences on cooling/heating energy demands.

The characteristics of the coupling between UCP and BEM were presented in detail in chapter 4. In particular, we described how the natural ventilation, roof-top, and vertical wall air-conditioning fluxes generated by BEM, modify the calculation of sensible and latent heat sources from roofs and walls.

In a second time, the whole simulation system composed by MM, UCP, and BEM was applied to a series of one, and two-dimensional configurations. One-dimensional simulations first compared the new urban scheme UCP-BEM with its counterpart without building energy model (UCP). The aim was to verify if the two parameterisations led to equivalent results for fixed internal wall boundary conditions without taking anthropogenic air-conditioning fluxes into account. In a second time, the importance of considering buildings with different floors was also taken in account, by showing that buildings of same height with different number of floors led to different cooling/heating energy needs.

In the second part of chapter 4, the simulation system composed by MM-UCP-BEM was applied to a set of two-dimensional idealized configurations of cities surrounded on both sides by rural areas. The aim was to evaluate the capability of the model in simulating the links between anthropogenic fluxes in buildings and urban canopy climate. In this context, we observed that the heat released by air-conditioning facilities can have a

non negligent impact on the exterior temperature which can contribute to increase the UHI formation. Furthermore it was observed that inside urban canopies, vertical wall air-conditioning systems generate more important effects than those systems situated at roof tops. Simulations also indicated that these anthropogenic heat fluxes can produce a non negligent impact on the other meteorological variables by both, increasing wind speed as well as the buoyant production of TKE.
The second part of the study was focused on evaluating the applicability of the simulation system MM-UCP-BEM in performing urban warming countermeasures and cooling energy demands control strategies. To this purpose, a sensitivity study was carried out which indicated that there are dfferent strategies and physical parameters that can modify the magnitude of air-conditioning fluxes. Results have shown that low thermal diffusivity and high heat capacity of roofs and walls can generate very important cooling energy savings. Similarly, the implementation of an efficient air-contioning system, and an increase in internal comfort temperature, can also produce very positive effects.

In chapter 5, two-dimensional results have been used as a guidance for the interpretetion and the application of MM-UCP-BEM to the three-dimensional realistic configuration including the city of Basel and the surrounding areas. In general, three-dimensional results proved the applicability of the model to real cities, and indicated that the implementation of BEM inside the UCP increases the effectiveness of the urban parameterisation in providing more realistic studies of urban warming countermeasures, and cooling energy demands.

In a first step, measured data provided by the BUBBLE campaign have been used in order to compute average rural and urban near ground temperatures. These values were compared to simulation results which indicated that the model could reasonably well reproduce the daily variations of outdoor air temperature. Still, a general trend to overestimate this value for both, rural, and urban sites was noted. In this context, in future studies, a more complete soil description, which includes also cooling effects generated by evapo-transpitation processes, should be considered. Moreover, the mesoscale model described in this study does not account for the presence of clouds on humidity and radiation budget. In particular, this can lead to an overestimation of outdoor air temperature, as cooling effects produced by higher humidity, and lower incoming radiation are not taken into account. Note that these aspects should be considered in future developments, especially for longer simulation periods where the presence of clouds cannot be neglegted anymore.

Numerical results have shown that the model was able to reproduce urban-induced processes. In particular, following two-dimensional tests, the introduction of BEM inside the UCP, indicated that anthropogenic air-conditioning fluxes contribute to imcrease the UHI phenomenon, especially if vertical wall systems are in use. Moreover, a study of the impact of BEM on other meteorological quantities confirmed the results obtained with the two-dimensional configuration, with an increase in wind speed, and turbulent kinetic energy. In this context, the introduction of a constant tracer over the urban area of Basel, suggested that the major turbulent activity, could generate a higher vertical mixing, leading to a decrease in near ground air pollution.

In the second part of the study, the sensitivity analysis considered for two-dimensional configurations was used as a guidance for the three-dimensional case of Basel. The goal was to verify the capability of the numerical model MM-UCP-BEM to evaluate the effectiveness of different urban warming countermeasures. Results confirmed that well insulated materials, as well as the implementation of efficient air-conditioning systems, can lead to very important cooling energy savings. Moreover, we observed that the introduction of an "energy-saving policy", by increasing the internal comfort temperature, or switching off air-conditioning systems during night-time, can also lead to positive effects regarding energy consumptions in buildings.

Finally, the study of the differences in cooling degree-days (CDD) between air-conditioning and non air-conditioning simulations, suggested that the increase in outdoor air temperature generated by anthropogenic air-conditioning, can lead to a non negligent increase of the CDD values. These feedbacks are sensitive to the physical properties of built materials (roofs and walls), as well as to the quality of air-conditioning system being in use. Typically, we observed that vertical wall air-conditioning systems generate more important consequences than roof-top systems. These considerations lead to similar conclusions as those presented in other studies, highlighting the importance of considering coupled systems.

Again, we would like to stress that the results presented for these two, and three-dimensional studies have mainly quantitative intersts. In fact, the primary goal in this work was to develop a numerical model that allows a more complete analysis of the complex interactions between buildings and the atmosphere, as well as a more detailed study of urban warming countermeasures, and cooling energy demands in real cities. In this context, we proved that the implementation of BEM inside the UCP increases the effectiveness of the mesoscale model in providing these kind of studies.

We would also like to point out, that even if a more detailed three-dimensional validation is needed, different necessary verification tests have been performed in the present work, as well as in other studies, in order to compare MM, UCP, and BEM, with other programs and measured data. These verifications, together with the correspondances between two, and three-dimensional simulations, increase the reliability of the results presented in this work.

In this respect, as the first important future study would be to perform a more complete three-dimensional validation of MM-UCP-BEM, ideally, in hot climate cities, and where more measured data concerning the use of air-conditioning facilities are available. In this context, it should be pointed out that the access to a complete set of these types of measures is not easy to obtain.

There is also a real need to extend the present study to winter conditions, and in general, to longer periods of time (months, year). In fact, for a complete evaluation of UHI processes and energy demands in buildings, it is very important to verify the impact of summertime countermeasures on wintertime urban climate and heating energy demands. In this respect, we observed in chapter 1 that, especially for cold climate cities, UHI can lead to positive effects in winter, as it reduces heating energy needs, and may help melt ice and snow on road.
As previously mentioned, for performing these types of longer period studies, the mesoscale model should be able to take water and clouds formation into account.

The present numerical tool could also be utilised in order to provide precise boundary conditions for microscale models, for the study of more specific districts.

Finally, concerning the representation of urban warming, air pollution, human health, economic, and cooling energy needs in cities, the introduction of heating from vehicle and factories, as well as the possibility to take the effects of urban greening into account, should give in the future a larger applicability to the present urban parameterisation in providing more efficient studies of urban planning guidelines.

Andrea Krpo
Avenue de Morges 18a 1004 Lausanne
Phone: (+41) 076 339 58 52
e-mail: andrea.krpo@gmail.com

Date of birth: 27.12.1979
Civil status: Single
Citizenship: Swiss

EDUCATION

2005-Present

Phd student in the Atmospheric Modelling group of the Air and Soil Pollution Laboratory (LPAS) at EPFL.
Phd Thesis: *Development and application of a numerical simulation system to evaluate the impact of anthropogenic heat fluxes on boundary layer climate*.
(Supervisor: Prof. Alain Clappier).

2004-2005

Master Thesis at the Chair of Modelling and Scientific Computing (CMCS) at EPFL.
MSc Thesis: *Modélisation par des modèles 1D de l'écoulement du sang et du transport de masse dans des artères avec bifurcation.*
(Supervisor: Prof. Alfio Quarteroni).

1999-2005

MSc Degree in Mathematical Engineering at the Swiss Federal Institute of Technology (EPFL) Lausanne. Emphasis on n*umerical analysis.*

1995-1999

High school focusing on sciences, Liceo Cantonale Bellinzona (TI).

PROFESSIONAL EXPERIENCE

Sept05-Present

Phd work in the modelling group of the Soil and Air Pollution Laboratory (LPAS) at EPFL.
The aim of the work is the development of a numerical simulating tool for the study of the climate generated over large urban areas. This work is done in collaboration with the Solar Energy and Building Physics Laboratory (LESO) at EPFL, and the Centro de Investigationes Energéticas Medioambientales y Technológicas (CIEMAT), Madrid (Spain).

Assistanship work in the school of Architecture, Civil and Environmental Engineering (ENAC), at EPFL.

- Master and semester Project supervision.
- Teaching to graduate and under-graduate EPFL students.

Informatic administrator of the Soil and Air Pollution Laboratory (LPAS).

Participation to international conferences and compilation of scientific papers.

2003-2005

Assistantship work in Mathematics at EPFL.

LANGUAGES

Italian	Mother tongue.	**French**	Fluent oral and written.
English	Very good oral and written.	**German**	Intermediate oral and written.
Spanish	Good oral skills.		

COMPUTER SKILLS

Programming	Fortran 77, Fortran 90, C++.
Operating Systems	Windows, Unix.
Document edition	Word, LATEX, PowerPoint. Exel.
Mathematical tools	Matlab, Maple V., Mathematica.

OTHER INTERESTS

Sports (tennis, judo, swimming), guitar playing, travel and discovering new cultures.